PHENOMIC AND GENOMIC APPROACHES TO UNDERSTAND PHOTOPERIOD ASSOCIATED FLOWERING, PLANT HEIGHT AND YIELD IN SOUTHERN MAIZE (ZEA MAYS L.)

A Dissertation

by

ALPER ADAK

Submitted to the Graduate and Professional School of
Texas A&M University
in partial fulfillment of the requirements for the degree of

DOCTOR OF PHILOSOPHY

Chair of Committee,	Seth C. Murray
Committee Members,	Oscar Riera-Lizarazu
	William Rooney
	Hongbin Zhang
Head of Department,	David D. Baltensperger

May 2022

Major Subject: Plant Breeding

ABSTRACT

Tropical maize germplasm holds a wealth of diversity that could be used for crop improvement. Phenomic and genomic tools can help characterize phenotypes associated with both crop improvement as demonstrated here. Phenomics and genomics were used in this dissertation to characterize maize for crop improvement. Chapter I identified 7 loci, including three novel loci, that were linked to photoperiod-associated flowering in a novel recombinant inbred line (RIL) population derived from Tx773 and three temperate adapted lines (LH195, LH82 and PB80) grown in Texas, Wisconsin and Iowa in over three years. Chapter II showed that allelic effect sizes of economically valuable loci are both dynamic in temporal growth, resulting in characterizations of phenotypic variability overlooked traditional laborious phenotyping methods. Chapter III demonstrated how unoccupied aerial systems (UAS)-based phenotyping can reveal novel and dynamic relationships between time-specific associated loci with complex traits. These relationships were previously impractical to evaluate but doing so demonstrated many candidate genes putatively involve in the regulation of plant architecture even in early stages of maize growth and development. Chapter IV is among the first to demonstrate an ability to predict yield in elite hybrid maize breeding trials using temporal UAS image-based phenotypes and supports the benefit of phenomic selection approaches in estimating breeding values before harvest. Chapter V showed that (i) it is possible to predict complex traits using high throughput phenomic data between different managements and years, and that (ii) temporal phenotype data can reveal time-dependent association between RILs and abiotic stresses, to select resilient plants. Chapter VI

showed that (i) complex traits can be predicted using the high throughput phenomic data between different managements and years, and (ii) temporal phenotype data can reveal time-dependent association between RILs and abiotic stress, which can help to select resilient plants. Chapter VII showed that when weather data was combined with temporal phenomic data, prediction abilities increased and were found to be more effective in yield prediction when tested and untested environments were less similar. Overall, temporal phenomic and weather data could moderately predict grain yield under the most challenging predictive breeding scenario of untested genotypes in untested environments.

DEDICATION

I am very honored and proud to dedicate my doctorate to my family, who impressed the love of agriculture and nature on me. I also dedicate my doctorate to Mustafa Kemal Atatürk who said that “our true mentor in life is science”.

ACKNOWLEDGEMENTS

Throughout my research I have received a great deal of support and assistance from many people.

I would like to thank my academic advisor, Prof. Dr. Seth C. Murray whose expertise and mentorship were invaluable that always inspired me during my academic progress. Your insightful guidance elevated me and brought my ability of critical thinking to a higher level. I sincerely believe that what I have learned from you will be my prime guides for the rest of my life.

I would like to thank my committee members Prof. Dr. Oscar Riera-Lizarazu, Prof. Dr. William Rooney and Prof. Dr. Hongbin Zhang, for their valuable contribution during my PhD education.

Growing and evaluating populations in different environments is critical to dissect the genotype-environment interaction, I would like to thank to Prof. Dr. Jianming Yu, Prof. Dr. Natalia de Leon and Prof. Dr. Jason Wallace, and their labs for helping us by growing our population in Iowa, Wisconsin, and Georgia.

I would like to thank all graduate students, post-doctoral researchers, student workers and crew in Quantitative Genetics and Maize Breeding Lab in Texas A&M University. Without their helps it was impossible to finalize any of research I included. I would like to thank to Turkish Education Attaché, Republic of Turkey Ministry of National Education and Republic of Turkey Ministry of Agriculture and Forestry for supporting my PhD education.

I would like to thank my parents and brother for their wise advice and sympathetic ear. Without their contributions, I would not be motivated during my PhD education. I have come this far, feeling that you are always with me.

Genomic and Bioinformatic Service (TxGen) in Texas A&M University genotyped our breeding lines, I would like to thank their generous support and expertise level of service for my PhD projects. I also would like to thank to AgriGenomics Lab where I received help in conducting DNA extraction and KASP genotyping.

I would like to thank to Dr Annalise N. Binette who always showed her sincere friendship to me. I would like to thank to Dr Steven Anderson, Dr Yuanyuan Chen and Dr Ivan D Barrero Farfan whose data from their previous projects trained me a lot during PhD education.

I would like to thank Prof. Dr. Cengiz Toker for his patience and time spent in training me in academic writing during the initial years of my graduate education. His early guidance played a crucial role in my academic journey.

Finally, I would like to thank to Texas A&M AgriLife the Vice Chancellor's Awards committee for recognition of our research results and nominated me as awardee in the graduate student research section. I also would like to thank to Crop Science Society of America C-1 division judges for recognition of my PhD project as first place in the Crop Breeding and Genetics division.

CONTRIBUTORS AND FUNDING SOURCES

Contributors

This work was supervised by a dissertation committee consisting of Prof. Dr. Seth C. Murray, Prof. Dr. Oscar Riera-Lizarazu, Prof. Dr. William Rooney and Prof. Dr. Hongbin Zhang.

Funding Sources

Scholarship of graduate study was supported by a fellowship from Turkish Education Attaché, Republic of Turkey Ministry of National Education and Republic of Turkey Ministry of Agriculture and Forestry.

Studies in the chapters of this dissertation were made possible in part by USDA–NIFA–AFRI under Grant Numbers: 2017-67013-26185, 2020-68013-32371, and 2021-67013-33915, USDA–NIFA Hatch funds, Texas A&M AgriLife Research, the Texas Corn Producers Board, the Iowa Corn Promotion Board, the Eugene Butler Endowed Chair in Biotechnology and Genome to Field (G2F) project.

NOMENCLATURE

BLUE	Best Linear Unbiased Estimate
BLUP	Best Linear Unbiased Prediction
CHM	Canopy Height Model
CIMMYT	The International Maize and Wheat Improvement Center
CV	Cross Validation
DAP	Days After Planting
DTA	Days to Anthesis
DTS	Days to Silking
EH	Ear Height (from ground to first ear)
Ex-PVP	Expired Plant Variety Protection
FH	Flag Leaf Height (from ground to flag leaf)
FHTP	Field Based High-Throughput Phenotyping
G2F	Genome to Field Project
G2FD	Optimal Planting Time Without Irrigation
G2FI	Optimal Planting Time with Irrigation
G2LA	Late Planting Time
GA	Georgia
GAPIT	Genome Association and Prediction Integrated Tool
GBLUP	Genomic Best Linear Unbiased Prediction
GBS	Genotyping by Sequencing

GCP	Ground Control Point
GDD	Growing Degree Day
GLM	General Linear Model
GP	Genomic Prediction
GWAS	Genome Wide Association Study
GxE	Genotype-by-Environment Interaction
HIF	Heterogeneous Inbred Families
HTP	High-Throughput Phenotyping
IA	Iowa
K	Kindship
KASP	Kompetitive Allele-Specific PCR
LD	Linkage disequilibrium
LM	Linear Model
MAE	Mean Absolute Error
MAF	Minor Allele Frequency
MAS	Marker Assistant Selection
MLM	Mixed Linear Model
NAM	Nested Associated Mapping Population
NID	Normal and Independent Distribution
PAF	Photoperiod Associated Flowering
PCA	Principal component Analysis
PCR	Polymerase Chain Reaction

PEBV	Phenotypically Estimated Breeding Value
PLSR	Partial Least Square Regression
PTT	Photothermal time
QC/QA	Quality Control/Quality Assurance
QTL	Quantitative Trait Loci
REML	Restricted Maximum Likelihood
RF	Random Forest
RGB	Red-Green-Blue
RIL	Recombinant Inbred Line
RMSE	Root Mean Square Error
SNP	Single Nucleotide Polymorphism
TAMU	Texas A&M University
TBLUP	Temporal Best Linear Unbiased Prediction
TH	Terminal Plant Height
TPP	Temporal Phenomic Prediction
TX	Texas
UAS	Unoccupied/Unmanned Aerial System
VI	Vegetation Index
VIF	Variation Inflation Factor
WAASB	Weighted Average of the Absolute Scores
WI	Wisconsin

TABLE OF CONTENTS

Page

LIST OF FIGURES

FIGURE Page

LIST OF TABLES

TABLE Page

CHAPTER I

INTRODUCTION

For over three decades genomics tools have been developed to provide the genome wide markers used in genetic mapping studies to predict traits of interest (e.g. yield) of untested genotypes (José Crossa et al., 2017; Heffner, Lorenz, Jannink, & Sorrells, 2010). Phenotyping technologies have lagged behind genomic technologies; traditional phenotyping has been low throughput in scale and time-dimensions, impeding the biological understanding of complex trait (Araus & Cairns, 2014). However, recent advances in phenotyping are providing high-dimensional phenotype data, which has become a key component to increase understanding of the biology of complex traits (Araus & Cairns, 2014; Shi et al., 2016). This dissertation addresses how to integrate high throughput phenotyping data with high throughput genotyping data, and provides applications in quantitative genetics and maize breeding. In the first chapter, photoperiod driven late flowering was phenotyped across southern and northern environments of the U.S.A and genetic markers are aimed to discover via genome wide association study. The output of this discovery will be a potential to eliminate the extended flowering from tropical maize germplasm which suffers from extended flowering causing adaptation problem in northern environments (Teixeira et al., 2015). In the second chapter, temporal effect sizes of genome wide markers are aimed to monitor growth across time of maize hybrids using unoccupied aerial surveys (UAS). Early growth variation has not been well investigated at either the genomic and phenomic level. In the third chapter, the goal will be to build on a past genome wide association study (GWAS) (Farfan et al.,

2015) and a linkage mapping confirmation study (Y. Chen, 2016) to confirm two loci of interest using new heterogenous inbred families and new UAS tools for monitoring height (Shi et al., 2016). In the third chapter, temporal plant height data obtained from multiple UAS surveys will be used as predictors to predict yield and, temporal phenotype data in both GWAS and temporal genomic prediction. The goal of the third chapter is to discover the candidate genes in GWAS that play a role in regulation of plant architecture across growth as well as temporal marker effects. In addition, temporal plant height is also investigated to determine whether it has an association with grain yield in maize to confirm previous reports (Anderson et al., 2019; Miao, Xu, Liu, Schnable, & Schnable, 2020; Pauli, Andrade-Sanchez, et al., 2016; Xiaqing Wang et al., 2019). In the fourth chapter, temporal phenomic data containing the temporal vegetation index and plant height is aimed to use as predictors for yield and flowering times in maize. This is modeled after genomic prediction (Meuwissen, Hayes, & Goddard, 2001) and terminal trait phenomic prediction (Holly M. Lane et al., 2020; Rincent et al., 2018; Weiß et al., 2022). This novel approach of temporal phenomic prediction introduces how to generate and use to predict the grain yield with different machine learning algorithms (López, López, & Crossa, 2022). In the fifth chapter, temporal phenomic prediction conducted between years tests temporal dimension reduction to address the problem of unmatched flight times between years. In addition, high throughput phenomic data will be integrated with high throughput genomic data as has so far been done in very few studies (Adak, Conrad, et al., 2021; Adak, Murray, & Anderson, 2021; Adak, Murray, Anderson, et al., 2021; Anderson et al., 2020; Jinyu Wang et al., 2021; Xiaqing Wang et

al., 2019). As a special case study in the fifth chapter, time-dependent relationship between genotype, time and weather will be examined. Crop modeling and experience suggests it is logical that these factors interact (Xianran Li et al., 2022; Xin Li, Guo, Mu, Li, & Yu, 2018; Q. Mu, Guo, Li, & Yu, 2022; Pigliucci, 2005). In the sixth chapter, temporal phenomic prediction is aimed to compare with genomic prediction to assess the prediction ability of phenomic data. This has been done for near infrared spectroscopic phenomic prediction (Rincent et al., 2018), as well as in wheat (Krause et al., 2019), but has not yet been looked at in maize or using this depth of temporal phenotypes. In the seventh chapter, a three-way interaction (pedigree*flight*management) design will be introduced in analyzing the temporal data derived from UAV surveys; an extension from traditional analysis models for each time points (Anderson et al., 2019; Pugh et al., 2018). In addition, temporal phenomic data and weather data will be assessed in the prediction of grain yield, this integrates much of the work in previous chapters.

Photoperiod associated flowering (PAF) is a major obstacle impeding U.S. production of southern, tropical and exotic derived hybrids. This is because their parent inbred lines flower too late in the US Corn Belt, where nearly all hybrid seed for the U.S. is produced. In more extreme cases of PAF, even Southern U.S. maize breeding programs can be limited in their use of tropical lines due to cryptic extended flowering time caused by PAF under longer day circumstances; this could be caused by photoperiod and/or associated thermal times which require many environments of screening to separate (Xin Li et al., 2018). PAF triggers delayed flowering in tropical derived germplasm but it is not currently possible to visually select for using only one

southern location (e.g. Texas), because it cannot be separated from insensitive flowering without screening at other latitudes. To determine the underlying genetic cause(s) of PAF in different germplasm pools, phenotyping is needed in both southern production environments along with northern production environments where day lengths are longer combined with genomic analysis tools for mapping. Determining loci affecting PAF could increase the efficiency of Southern U.S. maize breeding programs to selectively eliminate PAF from advanced lines and breeding stocks without having to phenotype each line flowering across multiple locations.

While many late flowering and PAF loci are known, diverse tropical germplasm is expected to vary in the loci causing their quantitative variation. The “LAMA” pool of lowland Bolivian derived, Texas adapted lines demonstrates PAF, which is a barrier for U.S. seed production (Murray et al., 2019). As a source for PAF loci, an elite breeding line (Tx773) derived from LAMA with the latest flowering time, even in Texas, was used. Tx773 is notable for being one of two parents by pedigree of Tx777 (Murray et al. 2019) and is one of the most foliar disease resistant lines in the Texas A&M maize breeding program. Through previous tests conducted with the Genomes to Fields (G2F) project, three Corn Belt adapted lines were selected as parents based on their diverse responses to flowering times and their ability to perform well as inbred lines per se. Of these, LH195 (Holden's Foundation Seeds, 1991) showed a reverse response to PAF, referring late flowering in Texas and early flowering in Wisconsin and Iowa while LH82 (Holden's Foundation Seeds, 1985) and PB80 (DeKalb-Pfizer Genetics, 1988) were

shown to flower with more stability at early and moderate flowering times in each environment, respectively.

Domestication of maize occurred in southern Mexico c. 9000 year ago from teosinte (*Zea mays* ssp. *parviglumis*) which is the wild progenitor of maize (Matsuoka et al., 2002). Throughout the domestication process, flowering time has been subjected to many dramatic alterations compared to teosinte (Doebley, 2004). Specifically, maize enlarged its growing area towards the north where day light is shorter and temperatures cooler during the maize growth periods while teosinte remained restricted to tropical environments in Mexico and Central America (C. Huang et al., 2018; Hung et al., 2012). In maize (*Zea mays* L.), one of the important constraints triggering aberrant phenotypic plasticity is caused by photoperiod sensitivity (Teixeira et al., 2015). Photoperiod sensitivity prevents utilizing exotic genetic diversity of tropical germplasm (K. Liu et al., 2003; Ochs, 2005; Wahl et al., 2017). This is because tropical germplasm is generally characterized by later flowering, weak standability and especially extended plant height with higher numbers of leaves. These problems are exacerbated by photoperiod sensitivity when tropical maize germplasm is grown in temperate regions where daylengths exceeds the 10-13.5 h in the north during the growing season (Warrington & Kanemasu, 1983b), as well as by cooler temperatures delaying the triggering of the flowering response (Goodman, 1999; Tarter & Holland, 2006). In contrast, major maize production areas in the Southern United States encounter the serious problems in maize production as well as in breeding with the temperate-adapted germplasm used by industry. Temperate-adapted germplasm has impeded maize production because it is not

well-adapted to the Southern US, including susceptibility to drought stress and aflatoxin; temperate germplasm is often poor for these problems (F. J. Betrán, Bhatnagar, Isakeit, Odvody, & Mayfield, 2006; KL Mayfield, Murray, Rooney, Isakeit, & Odvody, 2011). Taken together, in order to manipulate the aberrant plasticity by photoperiod sensitivity in southern-exotic germplasm, understanding the PAF mechanism to develop new tropical derived varieties adapted to Northern US climate conditions is important.

Flowering time has been diagnosed as complex trait, orchestrated by many genes of small effects (Buckler et al., 2009). Light is a deterministic factor on maize flowering in addition to temperature. Maize germplasm that was adapted to temperate climate has an ability to flower early which is associated with reduced response to day light (Markelz et al. 2003). Many successive research studies have been conducted to understand this complex trait through discovering roles of underlying genes during the transition from vegetative to reproductive development (Dong et al., 2012). Gene regulatory networks were previously developed by Dong et al. (2012) to examine flowering time related genes interactions in maize in different pathways, namely, light transduction, circadian clock, photoperiod transduction, aging, gibberellin and pathway integrators.

The transition of a plant from the vegetative to the reproductive phase can be manipulated by multiple environmental factors especially photoperiod (Kiniry, Ritchie, & Musser, 1983; Warrington & Kanemasu, 1983a), and flowering time can vary significantly between different genotypes of a plant species. The phenotypic differences between these genotypes may result in delayed or absent flowering (Gouesnard,

Rebourg, Welcker, & Charcosset, 2002). Tropical germplasm that are not photoperiod sensitive have been studied before (Gouesnard et al., 2002; Weldekidan et al., 2022), but the timely flowering of this germplasm in temperate regions remains an important but challenging subject needed for plant breeding between the northern and southern regions. Combination of environmental factors are key determining factors that manipulate the flowering times, such as temperature (Ellis, Summerfield, Edmeades, & Roberts, 1992), growing degree days (C. Huang et al., 2018), photothermal time (Xin Li et al., 2018) and diurnal times (Q. Mu et al., 2022). Environmental parameters affecting flowering times and photoperiod can be modeled to dissect confounding factors across environments.

So far, many QTLs affecting flowering related biological pathways directly or indirectly have been identified and some have been cloned (Aukerman & Sakai, 2003; Bomblies & Doebley, 2006; Bomblies et al., 2003; Colasanti, Yuan, & Sundaresan, 1998; Danilevskaya, Meng, Hou, Ananiev, & Simmons, 2008; Danilevskaya, Meng, Selinger, et al., 2008; C. Huang et al., 2018; Hung et al., 2012; Lawit, Wych, Xu, Kundu, & Tomes, 2010; Lazakis, Coneva, & Colasanti, 2011; Liang et al., 2019; Malcomber, Preston, Reinheimer, Kossuth, & Kellogg, 2006; X. Meng, Muszynski, & Danilevskaya, 2011; Salvi et al., 2007; Sawers et al., 2002; Thornsberry et al., 2001; Q. Yang et al., 2013; Zhu & Helliwell, 2011). The majority of QTLs found have been loci that helped maize to adapt to temperate climates while others have been found to be related to the regulation of hormones. From the plant breeding standpoint, a cloned gene is not necessary if a linked marker can be used to selectively eliminate the PAF out of

tropical derived germplasm. Knowing the functional polymorphism might allow us to go beyond this to further optimize flowering.

Previous literature has defined adaptation phenomena of maize from southern to northern climates and identified QTL conditioning these phenotypes (Hung et al., 2012). However, to our knowledge, no markers to date have been used in marker assisted selection to eliminate PAF out of tropical germplasm. This is in contrast to the modern sorghum conversion program which first phenotypically eliminated photoperiod sensitivity from exotic material but now uses markers for a few major cloned genes (Klein, Miller, Bean, & Klein, 2016).

Ex PVP inbreds LH82 (Holden's Foundation Seeds, 1985), PB80 (DeKalb-Pfizer Genetics, 1988) and LH195 (Holden's Foundation Seeds, 1991) were evaluated during 2014 and 2015 and selected based on flowering responses on 19 environments (Figure 1) within to Genome to Field (G2F) project (Bridget A. McFarland et al., 2020). LH82 flowered the earliest consistently across evaluated environments, PB80 flowered moderately (between LH195 and LH82) and LH195 flowered later then PB80 (Figure 1).

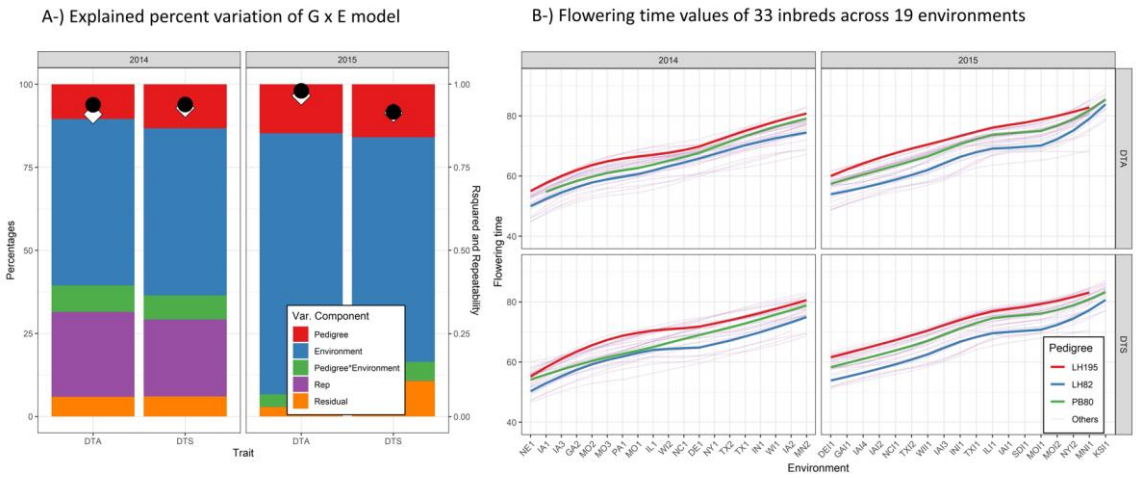

Figure 1 Genotype by environment (G x E) model (equation 1) was implemented todays to anthesis (DTA) and silking (DTS) of 33 different inbreds in 2014 and 2015, and LH195, LH82 and PB80 were chosen as candidate parental lines because of diverse flowering response. A-) Explained percent variation by each component of G x E model for DTA and DTS in 2014 and 2015. B-) DTA and DTS values of inbreds across environments in 2014 and 2015. Black round is Rsquared of G x E model and white diamond is repeatability value.

The primary objective of this study was to identify loci responsible for photoperiod associated flowering in Texas LAMA germplasm for future marker assisted selection or possibly gene cloning. The scope of this project was to (i) develop and advance NAM population during 2018, 2019, 2020 and 2021 (ii) collect flowering times from recombinant inbred lines (RILs) in Texas (TX), Wisconsin (WI) and Iowa (IA) with environmental data during 2018, 2019, 2020 and 2021 (iii) identify (map) key loci controlling PAF and (iv) annotate discovered loci to determine possible candidate gene(s). A secondary aim of this study was to evaluate the NAM population in terms of lesion mimic phenotype that was opportunistically and dramatically observed in the in NAM-RILs.

Materials and Methods

Experimental Population

LH82, PB80, LH195 were then crossed with Tx773 parents beginning in 2013 to construct recombinant inbred lines (RILs) for further investigation. Until 2018, the single seed descent method was applied to develop RILs in each population. Generally, in the F_3 generation, three ears from a single row plot were grown as different rows in successive generations. In summer of 2018, 67 F_4's from Tx773 x LH195, 64 F_4's from Tx773 x LH82 and 37 F_4's from Tx773 x PB80 were grown along with two counts from

each parental line in 2018. In total, 178 RILs were grown in the summer of 2018 in TX, WI and IA, most were in the F_4 generation. The F_4's were planted in Weslaco in 2018 as a fall off-season nursery to advance the generation (F_5) of inbreeding as well as the amount of seed. In 2019, 235 F_6 RILs from Tx773 x LH195, 66 RILs from Tx773 x LH82 and 41 RILs from Tx773 x PB80 (342 RILs in total) were grown along with two counts from each parental line. Then 252 RILs from Tx773 x LH195, 158 RILs from Tx773 x LH82 and 130 RILs from Tx773 x PB80 (540 RILs in total the latest being F_7) were grown along with four counts from each parental line in 2020. New RILs (mostly $F_{4:5}$) from another related breeding nursery were responsible for the increase. Finally 254 RILs from Tx773 x LH195, 159 RILs from Tx773 x LH82 and 125 RILs from Tx773 x PB80 (538 RILs in total) were grown along with four counts from each parental line in 2021 ; generation was reached up to F_8 in 2021 (Table 1).

Table 1 Number of RILs belonging to each sub-population across years, phenotypic measurements and growing environments.

	2018	2019	2020	2021
Tx773 x LH195	67	235	252	254
Tx773 x LH82	64	66	158	159
Tx773 x PB80	37	41	130	125
Phenotypic measurements	DTA, DTS	DTA, DTS	DTA, DTS	DTA, DTS, Lesion mimic
Environment	TX, IA and WI	TX, IA and WI	TX	TX, WI and GA

*TX, IA, WI and GA are Texas, Iowa, Wisconsin and Georgia respectively. DTA and DTS are days to anthesis and silking respectively. Only lesion mimic phenotype was observed in GA.

Growing Areas and Trait Evaluation

In 2018, 178 RILs were grown in College Station, TX, Ames, IA and Madison, WI with planting times of March 28th in TX (both reps in TX), May 8th (first rep in IA), June 1th

(second rep in IA) and May 29th in WI (both reps in WI). In 2019, 342 RILs were grown again in the three locations with the planting times of April 3th (both reps in TX), May 16th (first rep in IA), June 6th (second rep in IA) and May 13th (both reps in WI). In 2020, 540 RILs with enough seed were grown in College Station, TX planted March 17th (both reps in TX). In 2021, same 538 RILs, which were grown in 2020, were also grown in College Station, TX and Madison, WI with the planting time of March 22th in TX (both reps in TX) and May 28th (both reps in WI). One rep was grown in Athens, GA with the planting time of first week of April in 2021. (Figure 2). A randomized complete block design with two replicates were used in all environments across 2018 to 2021 with one replicate in Georgia in 2021.

All environment flowering times (days to anthesis and silking: DTA and DTS) were collected except for Georgia in 2021. DTA and DTS were recorded as days from planting to time to 50% of the plants in a plot had anthers or silks respectively. An intense lesion mimic mutant was also observed segregating in the population and scored on a one to five scale. 538 RILs were scored for lesion mimic mutant phenotype in College Station, TX, Athens, GA (one rep) and Madison, WI in only 2021. An example of the scoring used is in Figure 3.

Statistical Interference

All model components were chosen random using Restricted Maximum Likelihood (REML) in LME4 package in R (Bates, Mächler, Bolker, & Walker, 2014). Two models were used to analyze the flowering times and the lesion mimic phenotype. The first model was the single environment model based on equation 1 as follow:

Figure 2 A-) Growing areas were given with their longitude and latitude information. B-) the population structure derived from genotype by sequencing data.

$$y = \mu + Xg + Zb + Tr + Wi + \varepsilon \qquad \text{[Equation 1]}$$

Where y is the response vector of flowering times (days to anthesis; DTA and silking; DTS), μ is grand mean, g is the vector of recombinant inbred lines ($g \sim NID(0, \sigma_g^2)$), b, r and i are replication ($b \sim NID(0, \sigma_b^2)$), range ($r \sim NID(0, \sigma_r^2)$) and row ($i \sim NID(0, \sigma_i^2)$) effects respectively, accounting for the randomized complete block design, ε is the vector of error ($\varepsilon \sim NID(0, \sigma_\varepsilon^2)$). X, Z, T and W are incidence matrices.

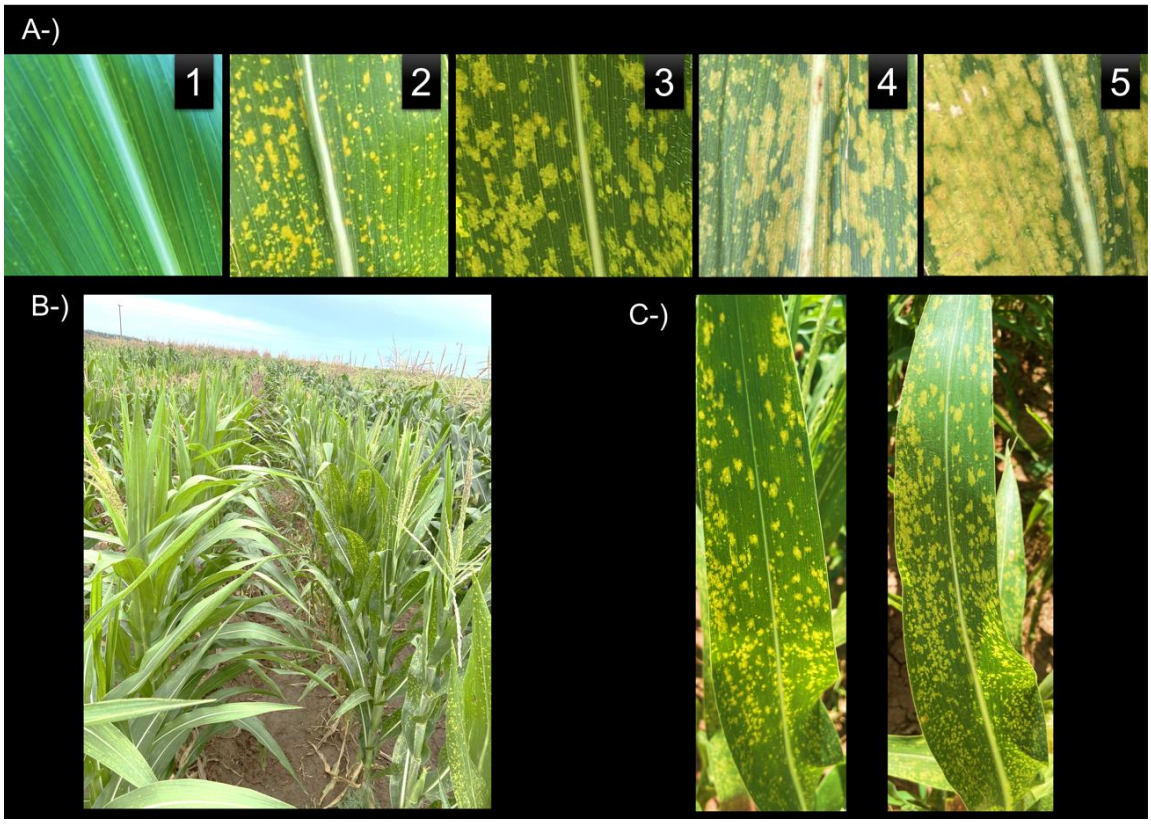

Figure 3 A-) lesion mimic severity; severity level increased from 1 to 5 and used in College Station, TX, Athens, GA and Madison, WI in 2021. B-) Appearance of lesion mimic mutant based on plot level. C-) Appearance of lesion mimic mutant based on leaf level.

Heritability (h_s) was estimated based on single environment model as follows (Equation 2):

$$h_s = \frac{\sigma_g^2}{\sigma_g^2 + \frac{\sigma_\varepsilon^2}{no.of\ reps}} \qquad \text{[Equation 2]}$$

The second model is the multiple environments model based on equation 3 as follow:

$$y = \mu + Xg + Zb + X * Z(g * b) + Tr + Wi + \theta l + \varepsilon \qquad \text{[Equation 3]}$$

Where y is the response vector of flowering times (days to anthesis; DTA and silking; DTS and lesion mimic phenotype), μ is grand mean, g is the vector of recombinant inbred lines ($g \sim NID(0, \sigma_g^2)$); b is the environments ($b \sim NID(0, \sigma_b^2)$); $g *$

b is the interaction terms between RILs and environments (($g * b \sim NID(0, \sigma^2_{g*b})$); r, i and l are replication ($r \sim NID(0, \sigma^2_r)$), range ($i \sim NID(0, \sigma^2_i)$) and row ($l \sim NID(0, \sigma^2_l)$) effects respectively, accounting for randomized complete block design, ε is the vector of error ($\varepsilon \sim NID(0, I\sigma^2_\varepsilon)$). $X, Z, T, W and\ \theta$ are incidence matrices. The multiple environment model was run separately for 2018, 2019 and 2021 because the number of lines were different and at different generations. TX, IA and WI environments were available in 2018 and 2019 while TX, WI and GA were available in 2021. Heritability (h_m) was estimated based on the multiple environment model as follows (Equation 4):

$$h_m = \frac{\sigma^2_g}{\sigma^2_g + \frac{\sigma^2_{g*b}}{no.of\ environments} + \frac{\sigma^2_\varepsilon}{no.of\ reps * no\ of\ environments}} \quad \text{[Equation 4]}$$

Genotyping

In total, genome wide data of 450 RILs (out of 530 RILs) were sequenced using SkimSeq technique (Scheben, Batley, & Edwards, 2017). This was conducted by genotyping by sequencing data (GBS) using a NovaSeq 6000 sequencing platforms (https://www.illumina.com/systems/sequencing-platforms/novaseq.html). Single nucleotide (SNP) were called using the DRAGEN pipeline at TxGen in that Zm-B73-REFERENCE-NAM-5.0 were used as reference genome (Johnson, 2019). In total 559,288 SNP and InDel calls were generated from the raw sequence.

Genome Wide Association Study

To map the loci controlling the PAF, differences of flowering days of RILs between TX and WI, and TX and IA were used as phenotype data accounting for PAF

the genome wide association study (GWAS). To minimize the field spatial and environmental variation, best linear unbiased prediction (BLUP) derived flowering times were used from the models described above [Equation 1 and 3] as suggested by (Kump et al., 2011).

GBS data was filtered as follows: (i) all heterozygote calls were treated as missing, (ii) markers with higher than 20 percent missing values were removed, (iii) markers with lower than 5 percent minor (secondary call) allele frequency were removed. After filtering 39,611 SNPs were retained and were used in GWAS. GWAS was conducted in GAPIT (version 3) by implementing MLM (including PCA + K) and GLM (including K) models in R (X. Liu, Huang, Fan, Buckler, & Zhang, 2016; Jiabo Wang & Zhang, 2021). Two Bonferroni correction were applied as -log(0.01/ no. of markers) and -log(0.05/no of markers). The false positive discovery rate was also set as 5. Three types of thresholds were used in discovery of loci linked to phenotype of interest. LD heatmap package were used to visualize and determine the LD region around the discovered loci and used in the determination of candidate genes (Shin et al. 2006).

QTL Mapping

Quantitative trait locus(QTL) mapping was also run for the lesion mimic mutant phenotype to identify QTL intervals linked to lesion mimic separately in TX, WI and GA. IciMapping software was used to run QTL (L. Meng, Li, Zhang, & Wang, 2015). First each marker in filtered hapmap format GBS (explained in *Genome Wide Association Study)* data was converted into A and B codded GBS data. The allele was

coded A if it belonged to Tx773 (LAMA), while B was coded if the others belonged to LH195, LH82, or PB80. Linkage groups as centimorgan were constructed by "By Anchor Only" setting, and the marker were ordered depending on their physical locations by the "By Input" function. Then MAP function of IciMapping were used to run the QTL analysis for three lesion mimic phenotypes belonging to TX, WI and GA.

Genomic Prediction

Genomic prediction was conducted using the rrBLUP package in R (Endelman, 2011) to predict the PAF as well as flowering times. In the first genomic prediction, PAF was calculated as the differences of flowering times (both DTA and DTS) of RILs between TX and WI, and TX and IA. Then PAF was predicted using the genome wide markers in rrBLUP in that 65 percent of total RILs were used tested RILs and hold-out 35 percent RILs were used as untested RILs. After this model was trained, tested and untested RILs were predicted, and correlation between predicted and actual breeding values of flowering times were used as two types of predictions. In the second genomic prediction, flowering times of RILs grown in TX were used to train the model and flowering items were predicted in WI and IA. 65 percent of total RILs were used as tested RILs and hold-out 35 percent RILs were used as untested RILs. After the model was trained, tested and untested RILs were predicted in TX, WI and IA. Correlation between predicted and actual breeding values of flowering times were used as a prediction ability. In addition, environmental parameters (given below in *Environmental Modelling*) from planting to the first 100 days after planting were merged with GBS data

to run the second genomic prediction to examine the contribution of environmental parameters on the prediction of flowering times.

Environmental Modelling

To understand the environmental parameters causing the PAF, eleven environmental parameters were obtained from the National Oceanic and Atmospheric Administration National Centers for Environmental Information (https://www.ncdc.noaa.gov/). These environmental parameters were temperature (minimum, average and maximum; °C), dew point (minimum, average and maximum; °C), humidity (minimum, average and maximum, %), wind speed (minimum, average and maximum; mph), atmospheric pressure (minimum, average and maximum; millibars), precipitation (cm), photoperiod (day light as hours). From these, the diurnal temperature range ($Temp_{max} - Temp_{min}$), growing degree days ($\frac{Temp_{max}+Temp_{min}}{2} - T_{base}; T_{base}\ is$ 10°C), and photothermal time ($GDD * photoperiod$) were calculated. The environmental models were used as predictors to classify the environments. Mean DTA was calculated by the multiple environments model (equation 3) and environmental parameters from planting date to the mean DTA for each environment (TX, WI and IA) were used as predictors while TX, WI and IA were used as dependent variables. A random forest algorithm was used to classify the environments based on the environmental variables using the 10-fold with three repeat cross validation in *caret* package in R. *mtry* vale was set 4 while *ntree* was set as 1500. Variable importance scores (*varImp*) were calculated to identify the most important environmental parameters causing PAF, and partial dependence plots were used to visualize the probability of

environments depending on changing environmental parameters with high variable importance scores using *edarf* package in R.

Results

Variance Component Results

Results for flowering times

In the single environment model (equation 1), pedigree (RILs) always explained the highest variance for DTA and DTS, changing between ~ 68 to 89 percent of total variation in TX and WI but between ~27 to 53 percent of total variation in IA (caused by different plating times of replications) across four years (2018 to 2021). Broad-sense heritabilities were calculated between ~0.80 to 0.93 for DTA and DTS across four years (Figure 4). Overall, DTA was slightly more heritable (Figure 4). In the multiple environment model (equation 3), pedigree (RILs) explained the ~40 percent of total experimental variance in 2018 and ~50 percent in 2021 but explained only ~10 percent in 2019. This was because the environment explained ~75 percent of total experimental variance in 2019, by far higher than those in 2018 (~40 percent) and 2021 (~1 percent) (Figure 4). Because variation due to environment alone is not included in calculation, heritability ranged between ~0.74 to ~0.92 in the multiple environment model (Figure 4). Different planting times were practiced across years thus RILs were exposed to different environmental parameters in each year that allowed capture of PAF, a genetic by environmental interaction. Differences in planting dates resulted in late flowering caused by PAF to reach up to ~20 and ~9 days in WI and IA respectively in 2019 (Figure 5). So, 2019 was considered the best year to dissect PAF in GWAS.

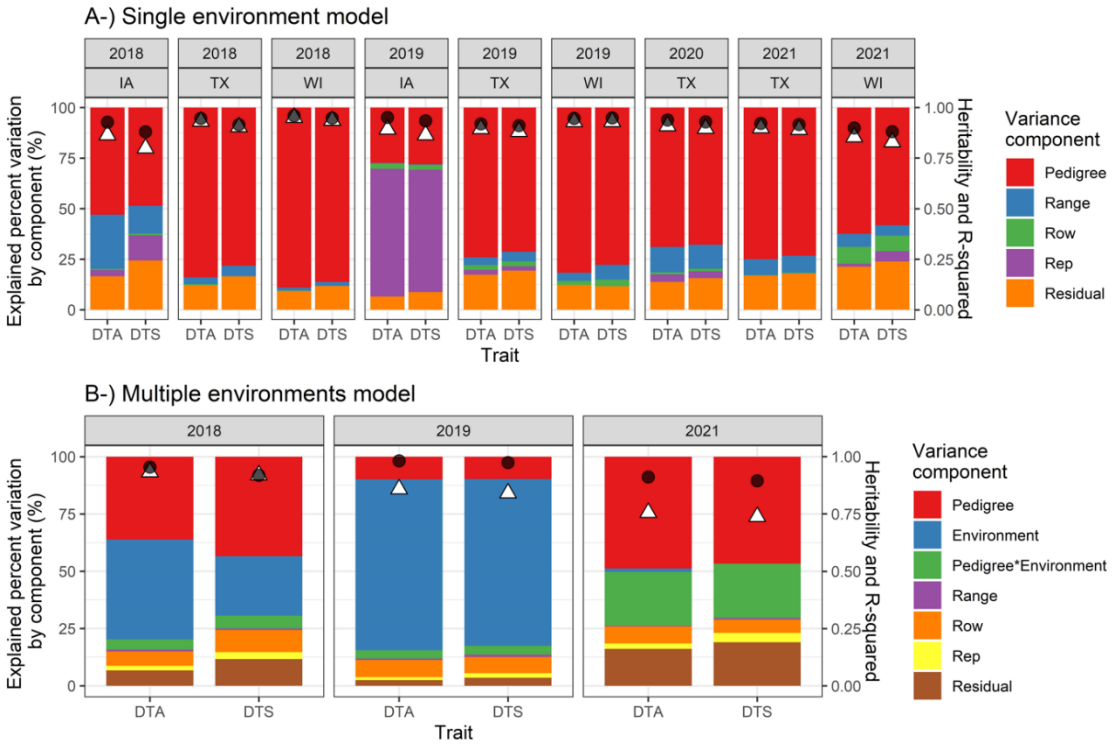

Figure 4 A-) explained percent variation by each component of single environment model by equation 1 for days to anthesis (DTA) and silking (DTS). B-) Explained percent variation by each component of single environment model by equation 3 for DTA and DTS. Black round is R-squared for each model while white triangle is heritability value calculated by equation 2 and 4 for single and multiple environments models respectively.

Results for lesion mimic phenotype

Lesion mimic phenotypes were evaluated using the multiple environment model (Equation 3) to assess the heritability and genotype by environment interactions. Pedigree (RILs) explained the 40 percent of total variation followed by 16 percent by pedigree environment interaction. Heritability was calculated as 0.76 for the lesion mimic phenotype. Lesion mimic phenotypic values of RILs were visualized across TX, GA and WI (Figure 6). Overall, individual RILs showing the lesion mimic phenotype were consistently observed in three environments, although their specific scoring

differed. Although the majority of lesion mimic plants were seen in the Tx773 x LH195 population, none of the four parents showed the lesion mimic in any environment.

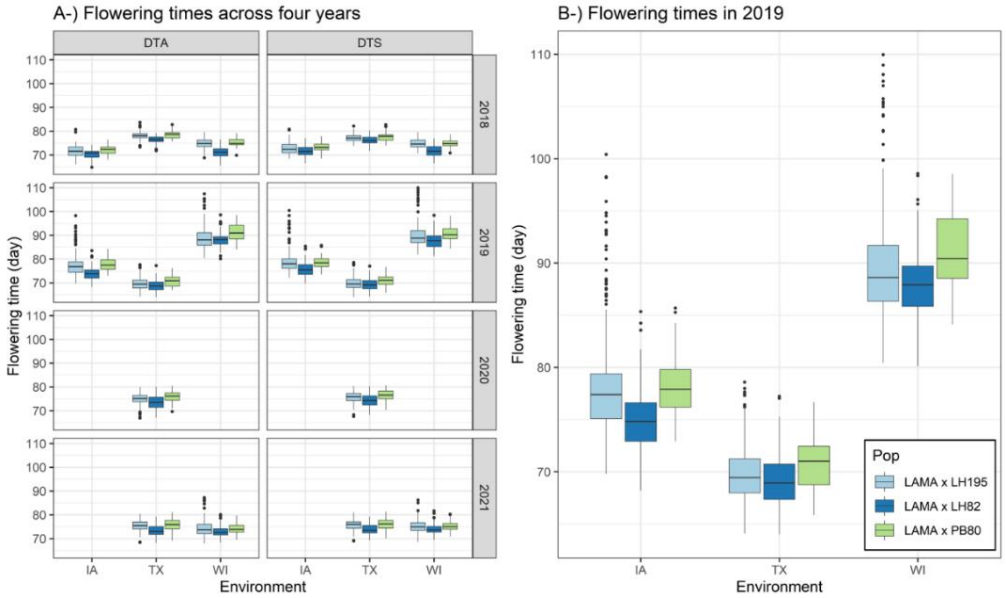

Figure 5 A-) Flowering times of days to anthesis (DTA) and silking (DTS) of RILs across four years. B-) Expanded panel to show flowering times of DTS in 2019, the most discriminatory environment; the latest flowering was observed in 2019.

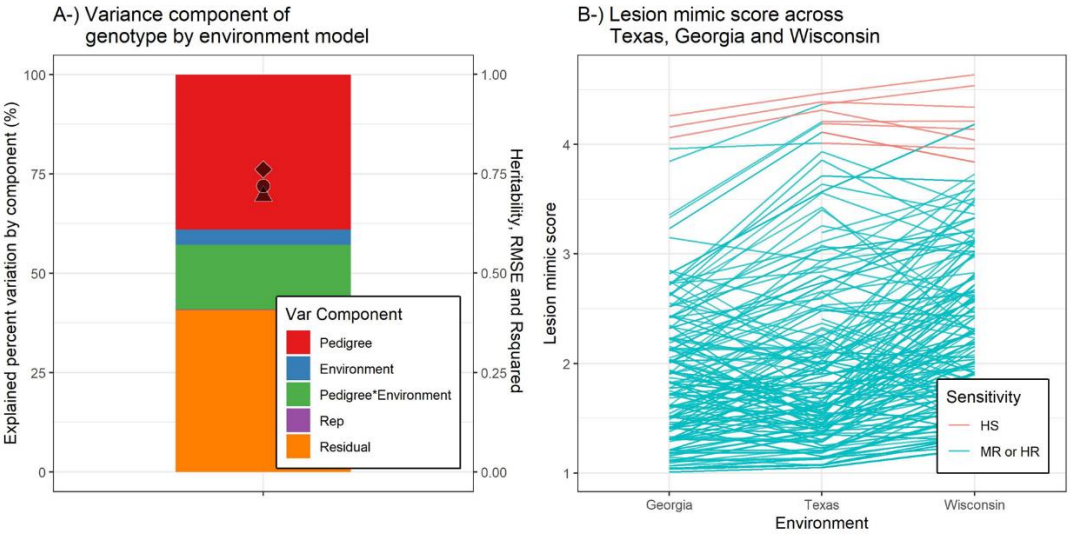

Figure 6 A-) Lesion mimic percent variation explained by the multiple environment model (Equation 3). Black diamond, round and triangle are heritability, Rsquared and root mean square error respectively. HS, MR and HR are highly susceptible, moderate

resistance and highly resistance. HS was considered if the score was higher than 4 in each environment and colored red.

Results of Environmental Modelling

Random forest classification was performed within years and across years. In 2019, when PAF was observed most strongly, random forest prediction had an accuracy of 0.86 with 0.78 Kappa coefficient value over all environmental parameters used as predictors. This high accuracy and Kappa coefficient were the indicators of accurate classification results. Variable importance scores showed that photoperiod, air pressure, wind speed, humidity and PTT were nominated the most important environmental parameters (Figure 7A). Daylength with more than 14 hours and air pressure lower than 990 millibars were nominated as the environmental characteristics of WI and IA in 2019 that caused the PAF (Figure 7B).

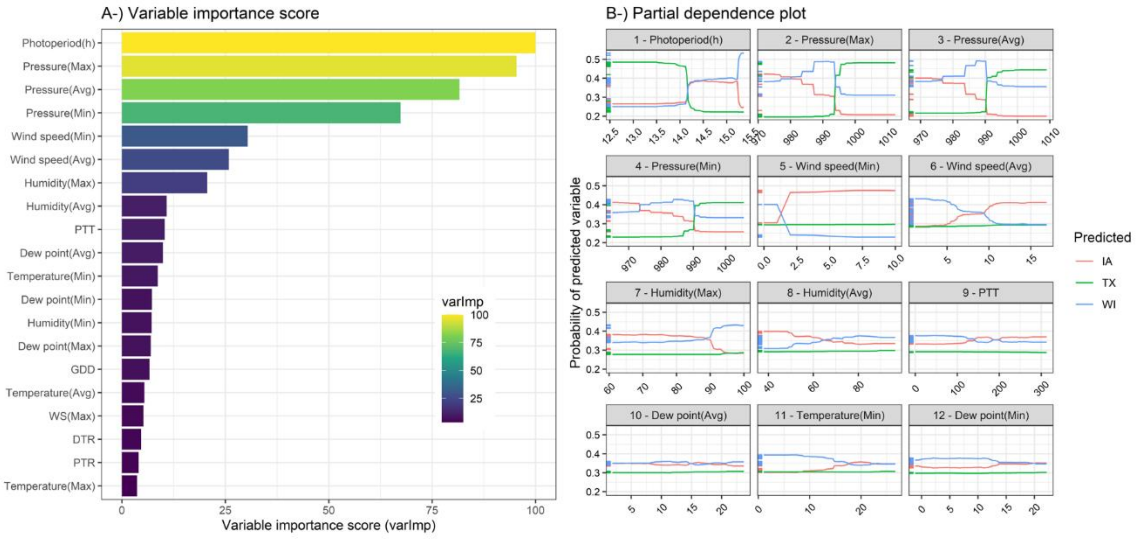

Figure 7 A-) variable importance scores (*varImp*) of environmental parameters provided by random forest algorithm, B-) partial depended plot shows the probability of TX, IA and WI for 2019 based on values of environmental parameters. Number on the top of environmental parameters show the importance ranks determined by *varImp*.

Loci Discovered the Photoperiod Associated Flowering

Genome wide association nominated several loci associated with PAF. PAF estimates for each RIL were calculated between TX and IA, TX and WI for DTA and DTS in 2019, and associated with GBS through the MLM and GLM model. PAF calculated in 2021 between TX and WI were also associated with GBS to examine the consistency in terms of discovery of same loci across years (Figure 8 and 9). Genomic regions associated with PAF were visualized in figure 12; LD regions (>0.8) around the markers controlling the PAF nominated two regions each in chromosome 1, 9 and 10, and one region in chromosome 4 and 7 (Figure 12). Markers associated with PAF are given in Table 1A.

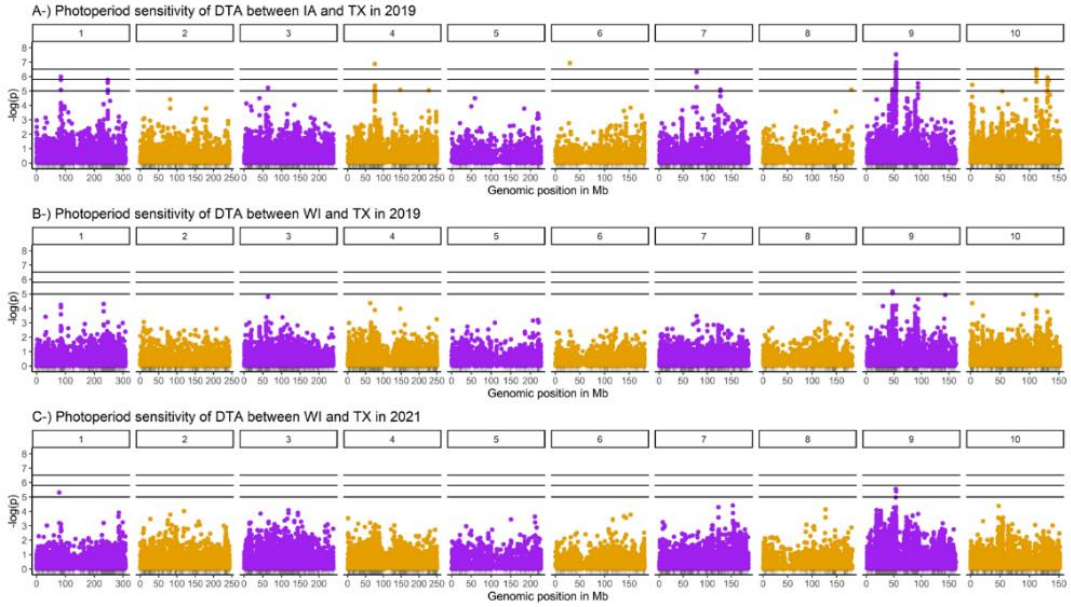

Figure 8 Manhattan plot shows the loci linked to photoperiod associated flowering (PAF) of days to anthesis (DTA) in 2019 and 2021. A-) Manhattan plot for PAF between IA and TX in 2019. B-) Manhattan plot for PAF between WI and TX in 2019 and C-) Manhattan plot for PAF between WI and TX in 2021.

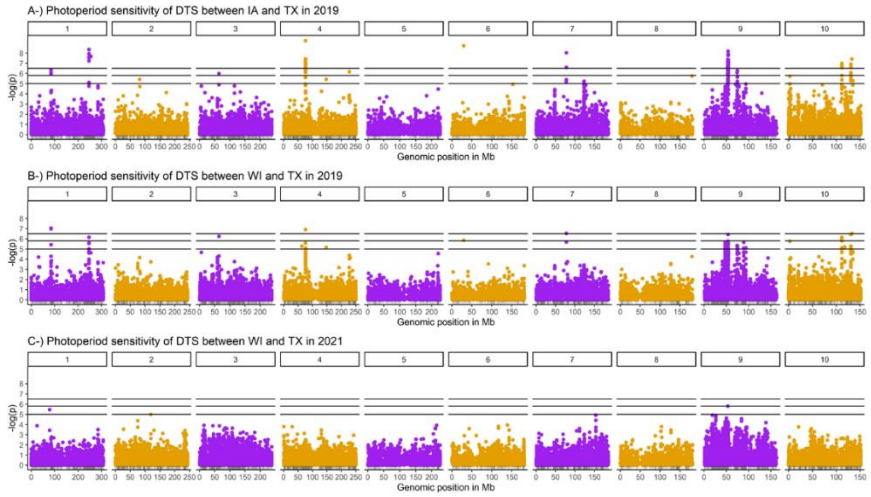

Figure 9 Manhattan plot shows the loci linked to photoperiod associated flowering (PAF) of days to silking (DTS) in 2019 and 2021. A -) Manhattan plot for PAF between IA and TX in 2019. B-) Manhattan plot for PAF between WI and TX in 2019 and C-) Manhattan plot for PAF between WI and TX in 2021.

Genome wide association study were also conducted for the flowering times (DTA in DTS) of 2019, and there were no associated loci discovered in TX, but discovered in WI and IA (Figure 10 and 11). The loci discovered in WI and IA were also consistent with the loci discovered for PAF.

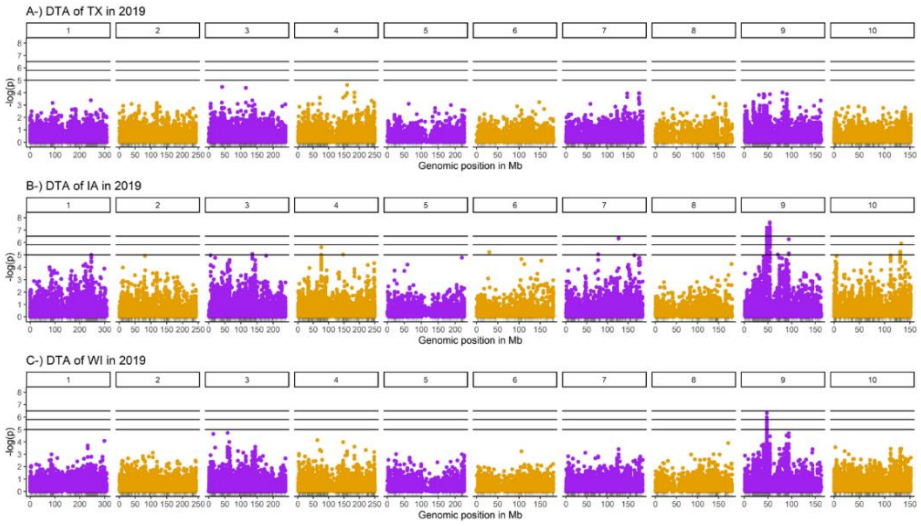

Figure 10 Manhattan plot shows the loci linked to days to anthesis (DTA) in 2019. A-) Manhattan plot for DTA of TX in 2019. B-) Manhattan plot for DTA of IA in 2019 and C-) Manhattan plot for DTA of WI in 2019.

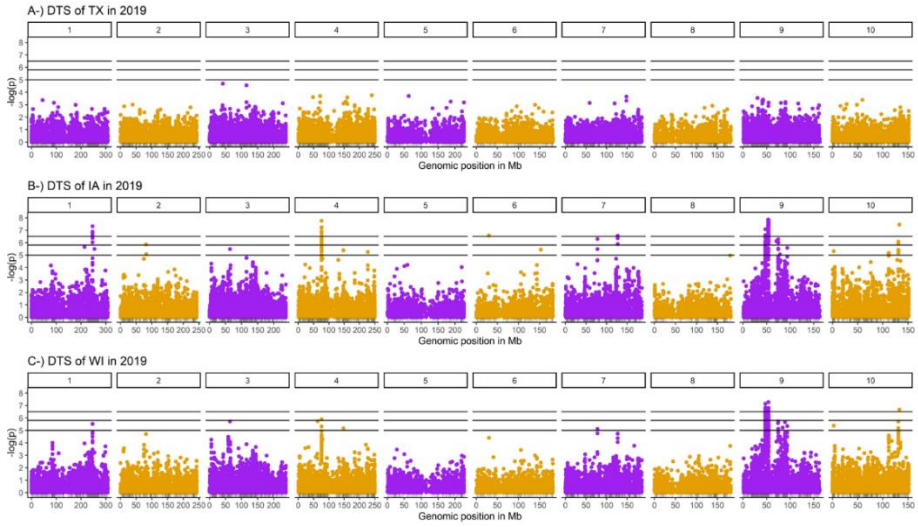

Figure 11 Manhattan plot shows the loci linked to days to silking (DTS) in 2019. A-) Manhattan plot for DTS of TX in 2019. B-) Manhattan plot for DTS of IA in 2019 and C-) Manhattan plot for DTS of WI in 2019.

Genomic Prediction Results for Flowering Time and Photoperiod Associated Flowering

Flowering times (DTA and DTS) were predicted with genome wide markers by training the genomic prediction model in TX and predicting the flowering times in IA and WI to select RILs that had no PAF, causing the late flowing in WI and IA in 2019. Flowering times were predicted with ~0.77 accuracy in TX and 0.47 in both IA and WI for tested RILs (used in training model), however there were ~0.01 percent increases (~0.78 in TX and ~0.48 in WI and IA) in prediction of flowering times of tested RILs when genomic and weather data used together (Figure 13A). Flowering times were predicted between 0.10 to 0.16 for untested RILs in TX, IA and WI and combined data (genome and weather data) did not increase the prediction ability (Figure 13A).

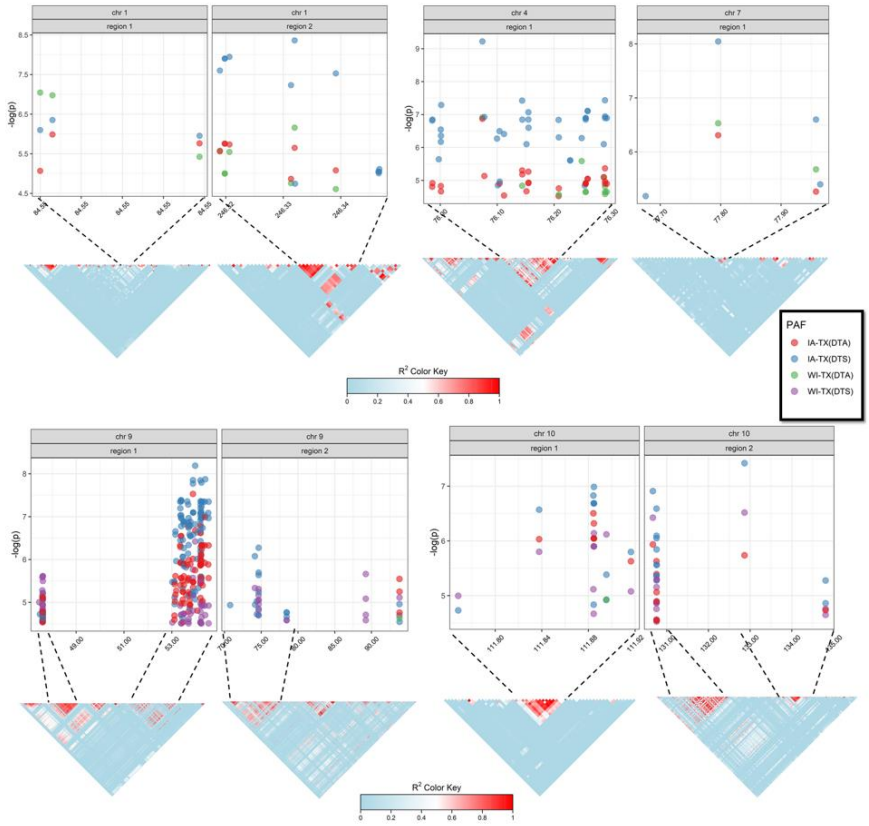

Figure 12 Zoom-in Manhattan plots of associated genomic regions with delayed flowering in 2019 and 2021.

PAF were predicted using genome wide markers. PAF of DTA, which were calculated between WI and TX, were predicted with an accuracy of ~0.81 and ~0.20 for tested and untested RILs (Figure 13B). PAF of DTA, which were calculated between IA and TX, were predicted with the prediction accuracy of ~0.91 and ~0.24 for tested and untested RILs. PAF of DTS, were calculated between WI and TX, were predicted with the prediction accuracy of ~0.93 and ~0.27 for tested and untested RILs. PAF of DTS, which were calculated between IA and TX, were predicted with the prediction accuracy of ~0.95 and ~0.33 for tested and untested RILs (Figure 13B).

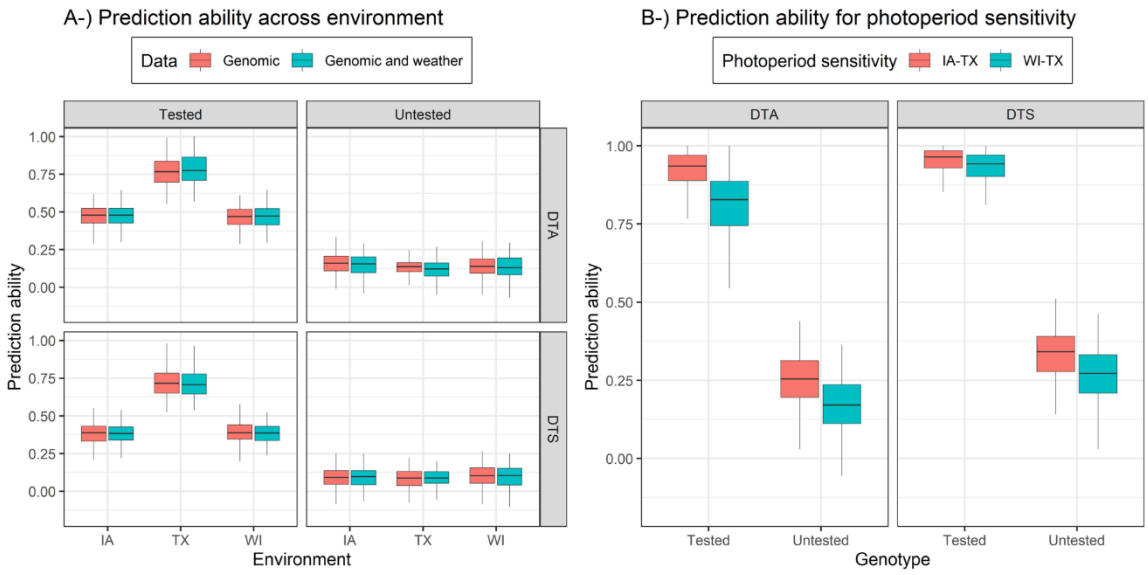

Figure 13 Genomic prediction results for flowering times across three environment and photoperiod associated flowering. A-) Results of the first genomic prediction model where flowering times were trained in Texas (TX) and predicted in Iowa (IA) and Wisconsin (WI). B-) Results of the second genomic prediction model where photoperiod associated flowering (photoperiod sensitivity) were calculated between TX and WI, TX and IA. DTA and DTS are the days to anthesis and silking respectively.

Locus Discovered for the Lesion Mimic Phenotype

The lesion mimic phenotype was associated with genome wide markers that nominated the locus 70,643,531 base pairs (based Zm-B73-Refgen-NAM-5.0) on chromosome 7 (Figure 14A, 14B and 14C). This locus was discovered consistently in TX, WI and IA. The locus segregated at this position for Adenine (A) and Guanine (G) in that A cause the lesion mimic mutant phenotype while G had a normal leaf appearance. The adenine (A) allele is supplied by LH195 parent while PB80, LH82 and Tx773 parents had the G allele. The RILs haplotypes segregating in terms of this locus were also contrasted, and resulted in that RIL haplotypes with A had higher score of

lesion mimic mutant than those with G (Figure 14D). The locus explained the 20, 37 and 46 percent of the lesion mimic phenotype in WI, IA and TX respectively.

Discussion

Maize flowering times differ for the male (silking, DTS) and female (anthesis, DTA) organs but both tend to be well correlated across genotypes. DTA and DTS are polygenic traits in maize (Boyle, Li, & Pritchard, 2017; Buckler et al., 2009; Chardon et al., 2004; Xin Li et al., 2018; Y. x. Li et al., 2016; Salvi, Castelletti, & Tuberosa, 2009; J. Xu et al., 2012), and show high plasticity across different latitudes and altitudes (Kusmec, Srinivasan, Nettleton, & Schnable, 2017; Xin Li et al., 2018; Y. x. Li et al., 2016); but remain relatively heritable traits, with low GxE and error in most germplasm across all conditions (Buckler et al., 2009; Navarro et al., 2017).

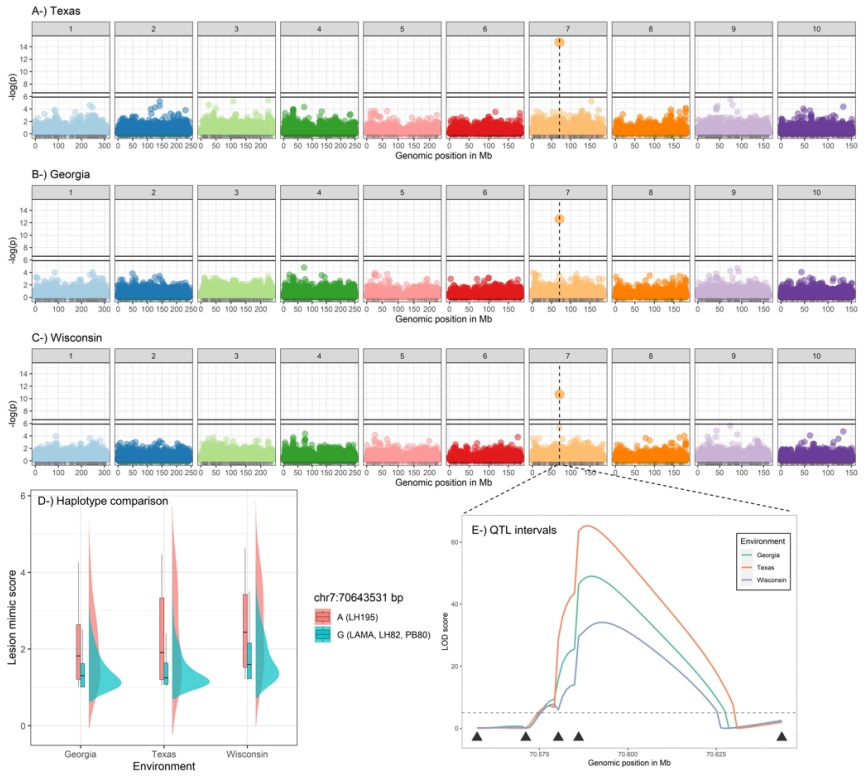

Figure 14 Manhattan plots for lesion mimic phenotype. A-) Manhattan plot results fir TX, B-) Georgia and C-) Wisconsin. D-) haplotype comparison between RILs having adenine (A) and guanine (G). E-) QTL analysis revealed the QTL intervals of genomic region linked to lesion mimic on chromosome 7.

A constant flowering time, reflecting insensitivity to environmental changes across different altitude and latitude, is an important selection standard in maize breeding; critical for temperate breedings program to introduce tropical derived inbreds to northern environments. Photoperiod (also known as day length) is a primary trigger of flowering time in maize causing late flowering under long day circumstances (Buckler et al., 2009; C. Huang et al., 2018; Hung et al., 2012; Xin Li et al., 2018; Teixeira et al., 2015; Q. Yang et al., 2013). Yet various other environmental parameters have an impact on flowering (Briggs, McMullen, Gaut, & Doebley, 2007; D. Li et al., 2016) that require further investigation. Therefore, this study also aimed to discover environmental parameters that lead the late flowering and discover genomic regions that control the late flowering.

Key Environmental Factors Triggering Late Flowering

Photoperiod (also known as day length) is the best identified environmental factor leading the late flowering in maize; especially tropical maize germplasm which has propensity to flower late under long day circumstance (>13.5h day light) (Teixeira et al., 2015). Photoperiod was the primary factor nominated by the random forest classification in this study (Figure 7A) and ~14 hour was proposed as critical threshold; greater than 14 hours represent WI and IA environments where late flowering was observed (Figure 7B). Air pressure was nominated second most important environmental parameters leading the late flowering, which was unexpected. There is a reverse

correlation between altitude and atmospheric pressure (air pressure); WI and IA had higher elevation than TX meaning that WI and IA had lower atmospheric pressure than TX across growth period of RILs. It might be speculated that gas exchange between air and plant was affected adversely; rate of CO_2 intake reduced that caused decrease in rate of photosynthesis resulting in delay in crop growth. Overall, flowering time was delayed because of extended vegetative stage referring the maladaptive syndrome of tropical or tropical derived maize (Teixeira et al., 2015).

This study examined the late flowering of tropical derived RILs across different latitudes to select the most stable (least plastic) RIL candidates to introduce the novel genetic resources that are supplied by the tropical parent (Tx773). The genotype by environment effect explained smaller percent of phenotypic variation of flowering times as compared to environmental main effects that explained majority of percent of phenotypic variation of flowering times (Figure 4). That result underlines the importance of change in environmental parameters that were nominated by random forest classification (Figure 7). Allelic variation was tried to maximize by using three different linkage population in this study, and response of genome wide markers allowed us to predict late flowering (caused by Tx773) positively that was driven by changes in environment parameters from TX to IA and WI (Figure 13). Overall, we can nominate the most stable (least plastic) RILs across three environments. Thus, these candidate RILs has a potential to enhance the genetic diversity of temperate adapted germplasm.

Determining Candidate Genes Linked to PAF

FLOWERING LOCUS (aka, *FT*) genes are well studied gene families (*phosphatidylethanolamine-binding* (*PEBP*) genes) in Arabidopsis and *FT*-like genes contribute the flowering times in maize (Danilevskaya, Meng, Hou, et al., 2008; X. Meng et al., 2011; Pin & Nilsson, 2012). One of the well-known *FT*-like genes, *ZCN8*, act as floral activator coding florigen hormone in maize, and involves the photoperiod sensitivity related flowering in maize (X. Meng et al., 2011). We discovered a locus (chr8: 127,275,201) that is ~0.5 kb away from *ZCN8* (chr8:126,678,560..126,680,664, Zm-B73-Refgen-NAM-5.0) gene in our GWAS results only in 2021 with the ~4.0 p-values and explained 3 percent variation of PAF of DTA between WI and TX that corresponded to ~ 1 day PAF. *ZCN8* was only discovered in 2021 plausibly because 433 RILs were used in 2021 GWAS analysis, which allowed greater statistical power to detect the *ZCN8*. In contrast 290 RILs were used in 2019 which may have been too few to discover *ZCN8* from noise, though it is also possible that environmental variation or the effects of other large loci masked *ZCN8*. The *PEBP* gene family is diverse gene family that harbors many (26) known flowering related genes in maize, *PEBP* genes were used primary source in this study to compare our GWAS hits based on most updated reference genome of maize (Zm-B73-Refgen-NAM-5.0). One GWAS hit was discovered on 111,884,305 bp on chromosome 10 in 2019 (Figure 8, 9 and 10), and 4.6 kb away from *ZCN5* (chr10:116,536,722..116,538,239). This locus explained up to 10 percent variation for DTA and DTS of TX-IA and TX-WI PAF and it corresponds to ~2-day PAF in these location comparisons as well as in delayed flowering within locations (Figure 8, 9, 10 and 11). Another GWAS hit was discovered on 130,667,200 bp on

chromosome 10 in 2019 (Figure 8, 9,10,11), and 1.2 kb away from *ZCN19* (chr10:129,434,908..129,439,219). This locus explained up to 10 percent variation for DTA in TX-IA, and DTS in TX-AI and TX-WI and it also corresponds ~ 2-day PAF in these location comparisons as well as in delayed flowering within locations (Figure 8, 9, 10 and 11).

Another GWAS hit was discovered on 2,691,247 bp on chromosome 10 in 2019 (Figure 8, 9,10,11 and 12), and 0.6 kb away from *MYB69* (chr10:2,009,030..2,010,379). This locus explained up to 8 percent variation for DTA in TX-IA, and DTS in TX-AI and TX-WI and corresponding ~2-day PAF, in these location comparisons, as well as in delayed flowering within locations. *MYB69* positively regulates the gibberellin synthesis in Arabidopsis (Song et al., 2012) that affect the *FT*-like gene under the different latitudes in maize (Li et al., 2016).

Another GWAS was 93,292,309 on chromosome 10 that is ~2.8 kb away from one of *ZmCCT* (cct1: chr10:96,175,404..96,178,980) genes or PAF of DTA between TX and IA (Figure 8). *ZmCCT* was positionally cloned gene, and is considered one of the major loci involved in PAF in maize. The *ZmCCT* allele in teosinte expressed at high level and cause late flowering under long day circumstances (Dong et al., 2012; Hung et al., 2012). This GWAS hit explained 8 percent variation with p value of 4.5 and it corresponds ~1.4-day flowering delay for DTA between TX and IA in 2019.

The most consistent major GWAS hit across all locations and years for late flowering is 246,319,812 bp on chromosome 1 and is ~ 1 kb away from the *ID1* gene (chr1:245,247,265..245,251,918), explaining ~8 percent phenotypic variation

corresponding 2.1 day PAF in this study as well as in delayed flowering within locations. *ID1* is responsible for encoding zinc transcription factor and expressed in immature leaves (Coneva, Zhu, & Colasanti, 2007; Dong et al., 2012), and a mutant (loss-of-function) *id1* triggers the production of more leaves and cause late flowering along with abnormal floral organs (Colasanti et al., 1998; Coneva et al., 2007). This indicates that *ID1* is related to autonomous pathway of flowering times and aids the transporting of *ZCN8* from leaves to phloem, which is not controlled by photoperiod (Coneva et al., 2007; Dong et al., 2012; Wong & Colasanti, 2007). This was strongly supported in our study that our GWAS peak corresponding to *ID1*, was discovered in 2019 and 2021 for both DTA and DTS consistently (Figure 8, 9,10,11 and 12) in TX, WI and IA, and supporting that this peak was not affected by photoperiod or other environmental factors since it is related to floral induction in autonomous pathway of regulation flowering time. Our another major GWAS hit was 76,074,057 on chromosome 4 explaining ~10 percent of phenotypic variation of PAF corresponding to ~2.4 days as well as late flowering; the LD region (extending from ~76,100,000 to 76,300,000 kb with >.80 R^2) of this hit was given in Figure 12; GRMZM2G031846 (chr4:76,027,784..76,034,921) is the only gene in this LD region that was not previously reported involving any of conceptual regulatory network of flowering time in maize (Dong et al., 2012). Another major GWAS hit is located on 53,979,643 bp on chromosome 9 and located in LD extending ~53,000,000 bp to ~ 54,300,000 bp on chromosome 9 (Figure 8, 9,10,11 and 12). This GWAS hit explained the ~12 percent variation corresponding ~2.6 days PAF delayed flowering as well as late flowering.

GRMZM2G001454 (chr9:54,000,483..54,029,870) is located in this LD and coding the putative RING zinc finger domain super family protein, Another gene within LD of this SNP is *GRMZM2G319760* (chr9:53,179,359..53,192,366) a gene with unknown function. Based on our literature review, these two candidate genes have not been previously reported for flowering or delayed flowering related function involving any of conceptual regulatory network of flowering time in maize as described in (Dong et al., 2012). Another GWAS hit is located on 77,795,828 bp on chromosome 7 explaining the ~ 9 percent of PAF and corresponding ~ 2.1 days PAF as well as late flowering (Figure 8, 9, 10 ,11 and 12). This GWAS was not previously associated with flowering pathway in maize before.

When major SNPs discovered for PAF, these 7 SNPs (2,691,247 bp, 111,884,305 bp, 130,667,200 bp on chromosomes 10; 246,319,812 bp on chromosome 1; 76,074,057 bp on chromosome 4; 53979643 bp on chromosome 9; 77795828 bp on chromosome 7) loci could explained up to 63 percent variant of PAF combined corresponding 15.2 days PAF, however, there might be some overfitting (Beavis, 2019). These loci and genes have potential to manipulate late flowering; using these loci in a KASP (Kompetitive Allele-Specific PCR) assay has the potential to develop maize lines without late flowering in temperate maize breeding program locations where late flowering cannot be accurately separated from PAF observed/scored visually. In addition, late flowering were predicted using genome wide markers (Figure 13); so that RILs, which were predicted in terms of showing least/no late flowering, can be used as novel genetic sources in a maize breeding program.

Determining the Candidate Genes Linked to Lesion Mimic Phenotype

Lesion mimic mutants (denoted *les* and *Les* for recessive or dominant allelic state) are very diverse maize mutants that usually display diverse phenotypes similar to maize diseases (Johal, Hulbert, & Briggs, 1995; Neuffer, Jones, & Zuber, 1968). Lesion mimic mutants are likely controlled more than 200 loci (Walbot, 1991); however, several have been cloned or mapped so far. For example, *lethal leaf spot 1* (*lls1*) and *Rp1 (Resistance to P sorghi-D21)* are the mutants providing resistance against to *Cochliobolus heterostrophus* and *Puccinia sorghi* infections in maize (Hu, Richter, Hulbert, & Pryor, 1996; Simmons, Hantke, Grant, Johal, & Briggs, 1998; S. M. Smith, Steinau, Trick, & Hulbert, 2010). 32 *Les* mutants were mapped previously; of those *Les2, Les5, Les-2552* and *lls1* are located on short arm of chromosome 1; *Les7* is located on long arm of chromosome 1, *Les1, Les11* and *Les15* are located on short arm of chromosome 2; *Les4* and *Les10* are located on long arm of chromosome 2; *Les14, Les17* are located on long arm of chromosome 3; *Les13* is located on long arm of chromosome 6; *Les9* is located on short arm of chromosome 7; *Les8* is located on short arm of chromosome 9; *Les3* is located on long arm of chromosome 10; *Les6, Les12, Les16* and *rp1* are located on short arm of chromosome 10 (Johal et al., 1995; Neuffer et al., 1968). Most of those mutants were obtained by EMS (*Ethyl methanesulfonate*) or mutator (a transposable element in maize) and they were dominant except for *Rp1* and *lls1*(Johal et al., 1995; Neuffer et al., 1968). *Les* genes are known to be responsible for the programmed cell death (Bruggeman et al., 2015). Especially, *Les4*, *Les10* and *Les17* mutants had diverse differentially expressed genes as compared to their wild type (not

carrying *Les* allele) that were responsible for defense related genes in maize (X. Mu et al., 2021). These results imply that *Les* mutants activate the plant defense against to disease in early stages of infection. Novel source of *Les* mutants are valuable for dissecting and underlying the resistance mechanisms against to diseases in maize. Our GWAS hit for lesion mimic is located on 70,643,531 bp on chromosome 7; only *Les9* was mapped on the chromosome 7 near to *ra1* gene (chr7:114,958,643..114,959,398) but that is ~45,000,000 bp away from the our GWAS hit and not within the QTL interval given in Figure 12. Allelic segregation of our GWAS hit across RILs showed that Adenine (A) provided by LH195 parent contribute the lesion mimic mutant and Guanine (G) provided by other parents cause the normal phenotype (Figure 15). In addition, we did not observe any lesion mimic mutant phenotype in any of the hundreds of maize hybrids that have been made from these lines (data not shown) in 2020 or 2021. Overall, this lesion mimic is likely a novel spontaneous lesion mimic phenotype supplied by LH195 parent showing recessive inheritance.

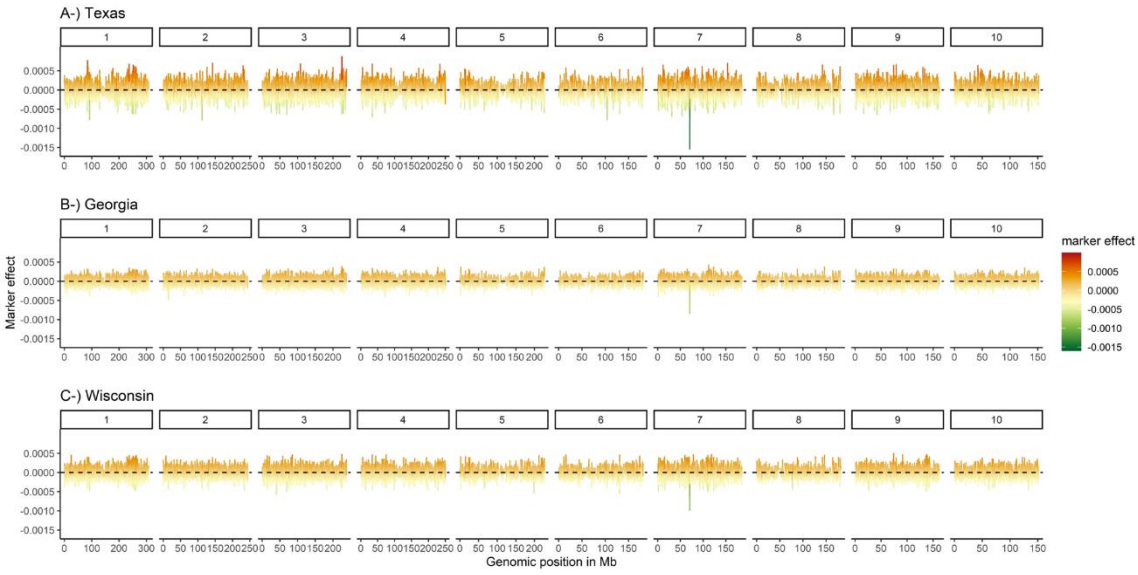

Figure 15 Marker effects (zero center) across calculated by rrBLUP all chromosomes in A-) Texas, B-) Georgia and C-) Wisconsin. GWAS hit discovered for lesion mimic phenotype (70,643,531 bp) on chromosome 7 had negative marker effects across three environments.

Candidate genes were scanned within the 5 kb proximal region (Wallace et al., 2014) within the given LD (Figure 14). Zm00001eb308050 (chr7:69369648..69372362), Zm00001eb308070 (chr7:69475864..69477768), Zm00001eb308090 (chr7:69884969..69885647), Zm00001eb308100 (chr7:70151131..70156945), Zm00001eb308110 (chr7:70325754..70326263), Zm00001eb308120 (chr7:70627651..70635362) and Zm00001eb308130 (chr7:70754766..70766777) are located in the LD and given in Figure 14. These candidate genes were positioned in reference genome 5 of maize (Zm-B73-Refgen-NAM-5.0) and their function are unknown; each these genes have a potential to govern the lesion mimic mutant in maize; function of these genes might shed the light on elevating the early plant defense mechanism in maize when their functions are revealed and used in marker assisted selection.

CHAPTER II

VALIDATION OF FUNCTIONAL POLYMORPHISMS AFFECTING MAIZE PLANT HEIGHT BY UNOCCUPIED AERIAL SYSTEMS DISCOVERS NOVEL PHENOTYPES[1]

Plant height (PHT) in maize has been subjected to many phenomic and genomic investigations since it influences plant architecture and agricultural performance, relating to other agronomically and economically significant traits in maize (*Zea mays* L.) (Anderson et al., 2019; Farfan, Murray, Labar, & Pietsch, 2013; Lima, de Souza, Bento, De Souza, & Carlini-Garcia, 2006; Peiffer et al., 2014; Sari-Gorla, Krajewski, Di Fonzo, Villa, & Frova, 1999; Sibov et al., 2003). A key component of success to the green revolution was the manipulation of PHT in wheat (Triticum spp.) and rice (Oryza Sativa) through the introduction of dwarf loci, initially used as a breeding strategy to maintain grain yield lost through lodging (Khush, 2001; J. Peng et al., 1999). However, an important postscript has been that taller PHT leads to better yields in a number of cereal crops including rice (Y. Zhang et al., 2017), sorghum (S. C. Murray et al., 2008; Shukla, Felderhoff, Saballos, & Vermerris, 2017), wheat (Navabi, Iqbal, Strenzke, & Spaner, 2006), and maize (Farfan et al., 2013); as long as lodging can be avoided. Specifically,

---

Adak, A., Conrad, C., Chen, Y., Wilde, S. C., Murray, S. C., Anderson II, S. L., & Subramanian, N. K. (2021). Validation of functional polymorphisms affecting maize plant height by unoccupied aerial systems discovers novel temporal phenotypes. G3, 11(6), jkab075. https://doi.org/10.1093/g3journal/jkab075

(Farfan et al., 2013) found that manual measured terminal PHT was positively correlated ($r = 0.61$) with grain yield in commercial hybrids over subtropical environments. They proposed that an optimal taller PHT is a desirable maize ideotype with respect to yield, especially under subtropical heat and drought stress, as long as lodging is not an issue. The wealth of studies on maize PHT has demonstrated the complexity, dynamic pattern, and polygenic inheritance of this trait; a trait governed by a large number of loci but with minor effects (Peiffer et al., 2014; Wallace et al., 2016a; Xiaqing Wang et al., 2019). Thus far at least 219 quantitative trait loci (QTLs) have been identified as controlling the PHT in maize (http://archive.gramene. org/qtl/). Very few of these to our knowledge have been confirmed as QTL in independent studies across different genetic backgrounds and environments. In contrast, the large effect genes identified with maize PHT have been associated with novel mutant alleles in hormone pathway genes; alleles rare or absent in landrace and elite cultivars because they are deleterious to plant fitness in nature. For instance, the dwarfing genes dwarf 8 and dwarf 9 encode DELLA proteins, which repress gibberellin (GA)-induced gene transcriptions in the absence of GA signaling (Lawit et al., 2010); the Dwarf3 gene (D3) of maize has significant sequence similarity to the cytochrome P450, which encodes one of the early steps in GA biosynthesis (Winkler & Helentjaris, 1995); brachytic2 mutants, the polar movement of auxins was hindered, which resulted in compact lower stalk internodes (Multani et al., 2003), and nana plant1 effects brassinosteroid synthesis (Hartwig et al., 2011). That quantitative genetic loci discovered for PHT diversity still segregating in maize have not been cloned, let alone manipulated has likely been due to (i) limitations in detection

ability of height related QTLs in diverse structure of mapping populations (Y. Xu, Li, Yang, & Xu, 2017), (ii) different growth pattern under different plant architectures and genetic backgrounds (El-Soda, Malosetti, Zwaan, Koornneef, & Aarts, 2014; Pigliucci, 2005), (iii) reaction norms across varying environments and genetic-by-environmental interactions (El-Soda et al., 2014; Gage et al., 2017), and (iv) antagonistic pleiotropy of major genes (Peiffer et al., 2014). This is likely compounded by the use of inbred lines in genetic mapping as opposed to testcrossed hybrids. Maize evolved as a heterogenous and heterozygous outcrossing species and inbred lines expose weakly deleterious alleles uncommonly exposed in nature which are detected but which heterosis in hybrids can again mask (J. Yang et al., 2017). Hybrids tend to reduce phenotypic variance, especially when topcrossed to a common tester. A genome wide association study (GWAS) on testcrossed hybrids made between a diversity panel and topcrossed to a line from the Stiff Stalk heterotic group (Tx714; (F. Betrán, Bockholt, Fojt III, Mayfield, & Pietsch, 2004)) under variable management discovered three significant loci associated with both terminal PHT and yield (Farfan et al., 2015). These loci explained up to 5.6 cm per variant (4.6% of total), two of which (Chr2: 27,482,431kp and Chr7: 164,955,163 kp; maize refgen_v2) also ranged from 0.14 ton/ha to 0.59 ton/ha effects on grain yield (4.9% of total). While (Farfan et al., 2015) suggest possible candidate genes, they did not calculate the linkage disequilibrium (LD) from these single nucleotide polymorphisms (SNPs) or exhaustively examine linked candidates, which we do here in this article. The two candidate genes suggested by Farfan et al. (2015) include GRMZM2G035688 and GRMZM2G009320. GRMZM2G035688 is an important crop improvement gene in

maize that is responsible for arrangement the maize leaves around stem (referring the aberrant phyllotaxy (*abph1*) in maize) (Hufford et al., 2012; Jackson & Hake, 1999). GRMZM2G009320, a housekeeping gene and acts as a glycose-related enzyme, encodes the glyceraldehyde-3-phosphate dehydrogenase (GAPDH) enzyme to regulate the energy metabolism in maize (Bustos, Bustamante, & Iglesias, 2008; X.-H. Zhang, Rao, Shi, Li, & Lu, 2011). Even if the metabolic and developmental-related functions of these genes have been identified, the temporal effect sizes of native alleles on phenotype across maize development stages and under different genetic populations remain unknown. Past GWASs have shown false positives due to cryptic population structure, familial relatedness, allele variants with low frequency or various allelic variants, as well as spurious associations between phenotypic variations and unlinked markers. For this reason, loci must be validated using different populations, environments (Larsson, Lipka, & Buckler, 2013), and, where relevant, growth stages. Next to transformation or gene editing, near isogenic lines (NILs) remain the standard for the validation of effect sizes of loci on phenotype, crucial for plant breeders and geneticists to measure effect sizes of these loci. Outside of (Farfan et al., 2015), hybrid maize populations have been used in relatively few other GWASs to discover SNPs. GWAS can comprise both additive and nonadditive SNP effects for the traits controlled by both overdominance and dominance conditions (Galli, Alves, Morosini, & Fritsche-Neto, 2020; Vidotti et al., 2019; H. Wang et al., 2017; Warburton et al., 2015). So that validation of SNPs discovered in maize hybrid GWAS populations over multiple genetic backgrounds is important to find pure additive effects of candidate genes.(Y. Chen, 2016) found effects

consistent with (Farfan et al., 2015) in constructed recombinant inbred line (RIL) populations as both inbred and hybrids; however, due to various field issues, this study did not have enough power to determine significance. RILs were thus used as the basis for developing the heterogenous inbred families (HIFs), a type of NIL, tested in this study. In this study for the first time (i) validated the temporal loci effects, first discovered using hybrid genetic background in GWAS, in HIFs generated from different parental crosses; (ii) implemented an unoccupied aerial system (UAS) platform to detect temporal changing of these loci effects on PHTs of HIFs; (iii) examined epistasis between these two loci; and (iv) characterized genetic architecture of their pleotropic effects on flowering times.

Materials and Methods

Development of HIF Populations

The two target SNPs were first validated to segregate across elite breeding lines by means of Sanger sequencing, as expected from the genotyping calls in the previous GWAS (Farfan et al., 2015). These calls were further confirmed using F1 hybrids on-hand that were derived from these parents (Y. Chen, 2016). The primers for Sanger sequencing were developed by Primer 3 (Untergasser et al., 2012), using the B73 maize genome (Schnable et al., 2009) as reference; the primer information is provided in Supplementary Table S1. All polymorphisms within the linkage populations were identified using ClustalX 2.1 (Larkin et al., 2007). As a result, LH82, LAMA, Tx740, Ki3, and NC356 were used as parental lines in four linkage populations (Y. Chen, 2016) and HIFs since their genotyping calls were validated to segregate (Supplementary Figure

S1). The four linkage populations, segregating for the two SNPs of interest, were developed from crosses (1) LH82 LAMA, (2) Ki3 NC356, (3) NC356 Ki3, and (4) Tx740 NC356 (recurrent parent donor parent for populations 1 to 4), respectively, and selfed to generate F5 RILs (Y. Chen, 2016). RILs were selected based on having the desired donor SNPs on a mostly recurrent parent background and backcrossed to the recurrent parent to create F1 hybrids. First, F1 hybrids were further backcrossed with recurrent parents (four to five times) and selfed (three to five times) up to obtaining NILs as HIFs. Until obtaining NILs, both loci (SNP1: 27,482,431 kp in Chr2; SNP2: 164,955,163 kp in Chr7 based on Maize Refgen_v2) were maintained as heterozygote calls in each population (seen as X: Y; i.e., donor allele: recurrent parent allele in Kompetitive Allele-Specific PCR (KASP) genotyping results (below and Figure 16). Second, individuals were selected in each population to have both opposite (XX: YY and/or YY: XX) and identical (XX: XX and/or YY: YY) to determine the HIFs within each population (Figure 16).

DNA Extraction and KASP Genotyping of HIFs

Total genomic DNA was extracted from the frozen (60C) plant flag leaf tissue using a modified cetyltrimethylammonium bromide method (D.-H. Chen & Ronald, 1999). To design the unique markers targeting the SNP1 and SNP2, around 100 bp surrounding the two SNPs on either side were selected to determine allelespecific primers and allele general SNPs using BatchPrimer3 v1.0 (You et al., 2008).

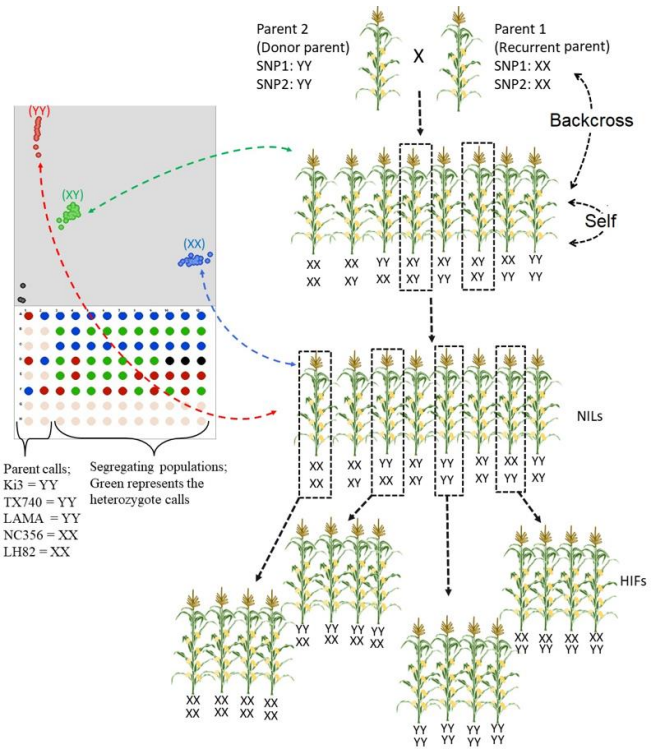

Figure 16 Breeding scheme of generating HIFs based on two SNP models and selection stages of pedigrees via KASP technology (http:// www.kbioscience.co.uk/). Ten to 20 plants from each plot were randomly selected or aided by markers for multiple generations until obtaining NILs (BC3F2 or more recurrent parent crosses or selfs). Only those having heterozygous loci (XY) were selected each generation and their ears were grown as rows (ear-to-row selection). After obtaining NILs, homozygous calls from both SNPs were selected as both identical (XX:XX, YY:YY) and opposite (XX:YY, YY:XX) to generate HIFs. All parents were genotyped (left). Parents; Ki3, NC356, Tx740, and LH82, calls (SNP1: SNP2) are YY:YY, XX:XX, YY:YY, and XX:XX, respectively. No template controls, black color in KASP figure, were used in each plate as negative controls. Reprinted from Adak, Conrad, et al., 2021.

Sequence information of primers was obtained from (Y. Chen, 2016). Loci implemented into KASP (http://www.kbio science.co.uk/) assays by (Y. Chen, 2016) were used in marker-assisted backcrossing to develop HIFs across different NIL backgrounds and used to detect SNP calls (XX, XY, and YY) for developing HIFs during 2016 to 2019 (Figure 16).

Determining LD

Farfan et al. (2015) did not provide LD estimates, so the data were reanalyzed and are reported here. Tassel software (version 5) (Bradbury et al., 2007) was used to obtain LD (LD windows size = 10 markers). First, LD decay plots were generated per chromosome using 61.402 total polymorphic markers used in (Farfan et al., 2015) to determine the LD decay rate. Especially, LD decay plots were generated to assess distances of LD decay pattern in chromosomes 2 and 7 where SNP1 and SNP2 were discovered. (Supplementary Figure S9). Second, nearby LD patterns of SNP1 (Chr2: 27,482,431 kp) and SNP2 (Chr7: 164,955,163 kp) were visualized using LD heatmap in R (Shin et al. 2006). LD calculated based on R2 and lower than 0.2 LD was ignored. The MaizeGBD (http://www.maizegdb.org/) genome browser was used to determine plausible genes linked to SNPs. The Gramene database (http://www.gramene.org) was used for the identification of candidate genes.

Allele Frequency Estimates in Elite Germplasm

The Panzea (https://www.panzea.org/) website was used to extract sequence information of genes from publicly available maize germplasm to evaluate how the allele frequency of these SNPs differs over germplasm and time. For elite temperate material, the information on the years when germplasm was developed were obtained from expired plant variety protection (ExPVP) certificates available on the USDA-ARS Germplasm Resources Information Network (https://www.ars-grin.gov). Allele shift of the loci were illustrated as count-based frequency histogram (qualitative calculation) through release years of germplasms.

Planting and Agronomic Practices

Plants were grown near College Station, TX for summer nurseries and Weslaco, Texas for winter nurseries from 2016 to 2019. All nurseries were grown based on range and row design with two replications per HIF. Each row plot (6.10 m long) in each range contained two row plots of two different HIFs. Plot rows were 3.05 m long for each HIF, and 18 seed were planted per HIF row plots. During the advancement of HIFs from 2016 to 2018, SNP1 and SNP2 calls were primarily maintained by selecting heterozygotes (X:Y) to advance and increase. For traditional and UAS phenotyping in College Station 2019, entire plots of X:X, Y:Y, and X:Y for each HIF were planted on the 12th of April, 2019, in two replicates. These HIFs were grown in a total of 18 ranges with 16 row plots each as well as parental lines and red stalker inbreds (Supplementary Table S3). Row plots of red stalker inbreds were used as planting indicators to verify that the planting was correct via orthomosaic because of their red stem and leaf color. Experimental designs were applied as a split:split:split plot design where the main split was replicate, the second split was population/genetic background, and the third split was genotype. Unless noted, all reported hand measurements and unoccupied aerial vehicle (UAV) flights were conducted when HIFs were grown near College Station in 2019.

Phenotyping

Days to anthesis (DTA) and silking (DTS) were recorded on a plot basis when 50% of the plants were showing anthers and silks, respectively, checking plots daily. Three different terminal PHT measurements were taken using a ruler including TH, FH, EH July 2nd, 2019, about 2 to 3 weeks after flowering. In addition, UAV (aka drone)

PHT measurements were taken weekly from emergence to the end of the growth period. The flight dates were shown as day/month/year (dd/mm/yy). Grain yield was not taken as it has little value in the inbred lines screened which often are confounded by inconsistent pollination in the heat stress of Texas. UAV images of the field were taken using a DJI Phantom 4 Pro V2.0 (DJI, Shenzhen, China) at an above ground altitude of 25 m. The standard integrated camera resulted in images having a resolution of 72 DPI. DJI standard flight control software was used. Orthomosaics and point clouds were created with the images for each flight by using Agisoft Metashape V15.2 software (Agisoft LLC, Russia). The captured images were at 72 dpi with 90% overlap and were used to create an orthomosaic and point cloud for determining the PHT as a function of time during the growth period. Ground control points were used during the flights to assist the data processing and reduce effects due to aberrations and the resulting georeferenced mosaics. Previous work has shown that various methods to measure inbred maize plants from the ground using point clouds produced similar results (Anderson et al., 2019). Point clouds of each flight were processed using CloudCompare (version: 2.11. alpha). To set a canopy height model (CHM), first flight containing bare ground was used as a digital terrain model (DTM). Digital surface model (DSM) of each flight was subtracted from DTM to calculate CHM (Supplementary Figure S2). Each plot was drawn using the polygon function of CloudCompare.

Statistical Inference

Statistical models were developed according to the distribution of SNP1 and SNP2 combinations obtained from the HIFs. Spatial variation was partitioned as random

effects into ranges and rows. Each model was run using a restricted maximum likelihood method in JMP version 15.0.0 (SAS Institute Inc., Cary, NC, USA) to predict the best linear unbiased estimates (BLUEs) of SNPs. SNPs were fit as fixed effects to obtain BLUEs values for flights as well as for ruler measurements. Separate models with genotypes as random effects in an all random model were fit to obtain variance components. All components, except the SNPs and population, were always fit as random effects under the following mixed linear models in each model. First, each SNP was tested separately within each population (Equation 1). While one of two SNPs was segregating, the other one was fixed (not segregating as XX or YY) in respective populations to compare the BLUEs of SNP calls. This equation was used for hand measurement data on a plant basis for each population.

$$Y_{ijkl} = \mu + SNP_i + Range_j + Row_k + Rep_l + \varepsilon_{ijkl} \quad \text{Equation 1}$$

Within this base model, response variable (Y_{ijkl}) was one of the three hand measures of plant height data; (SNP_i) represented variance of one of SNPs to be tested on condition that other one is fixed XX and/or YY within each respective population. Other variance components, including range ($Range_j \sim N(0, \sigma^2_{Range})$, row ($Row_k \sim N(0, \sigma^2_{Row})$ and rep ($Rep_l \sim N(0, \sigma^2_{Rep})$, account for the spatial variation. $\varepsilon_{ijkl} \sim N(0, \sigma^2)$ is the pooled unexplained residual error.

Plant height and flowering time were also tested for SNP1 and SNP2 individually combining all data across populations 1, 2 and 3 (Equation 2). While one of the two SNPs segregated, the other one was fixed (not segregating as XX) in the model. In this equation, the population (Pop_i) effect was added compared to Equation 1. BLUEs and

BLUPs of SNPs and their interactions with populations respectively were obtained for each UAS flight and ruler measurement.

$$Y_{ijklm} = \mu + Pop_i + SNP_j + [Pop * SNP]_{ij} + Range_k + Row_l + Rep_m + \epsilon_{ijklm}$$

Equation 2

The interactions of both SNPs and populations using the full factorial function was tested for both flowering time and for plant height from the ruler measurement and UAS flights temporally across populations 1 and 2 (Equation 3).

$$Y_{ijklmn} = \mu + Pop_i + SNP1_j + SNP2_k + [Pop * SNP1]_{ij} + [Pop * SNP2]_{ik} + [SNP1 * SNP2]_{jk} + [Pop * SNP1 * SNP2]_{ijk} + Range_l + Row_m + Rep_n + \epsilon_{ijklmn}$$

Equation 3

Here, response variable (Y_{ijklmn}) is plant height data. $SNP1_j$, $SNP2_k$ and $Pop_i \sim N(0, \sigma^2_{Pop})$ represent the variance components of SNP1, SNP2 and population respectively while other variance components were the same as stated previously in Equation 1 and Equation 2. In this equation only population 1 and 2 were used due to sample size.

Orthogonal contrasts were applied to SNP_i and $[Pop * SNP]_{ij}$variance components in equation 2 as well as $[SNP1 * SNP2]_{jk}$ and $[Pop * SNP1 * SNP2]_{ijk}$ in Equation 3 to illustrate temporal statistically significance differences between BLUEs of loci calls. In equation 2, BLUEs of XX and YY calls of two SNPs were orthogonally contrasted for each SNP and each population while BLUEs of XX:XX (SNP1:SNP2) and other call combinations (XX:YY, YY:XX and YY:YY) were contrasted for SNP1 and SNP2 interactions as well as SNPs and population interactions in equation 3.

Statistically significance differences between calls for each time point were reported at the level of 0.01, 0.05 and 0.001 in Figure 18, 19, 20 and 21.

Repeatability (R) was calculated based on following formula with number of replication (r) for single environments (Equation 4).

$$Repeatability\ (R) = \frac{\sigma^2_{Pop}}{\sigma^2_{Pop} + \sigma^2_{\epsilon}/r} \qquad \text{Equation 4}$$

Additional data processing and visualizations were performed in R version 3.5.1 (R core team 2018).

Data Availability

UAV-point cloud data, tiff files and canopy height measurements (CHM) of all flight dates and ruler height measurement are publicly accessible at; https://figshare.com/articles/dataset/Flight_dates_tif_/13046306; https://figshare.com/articles/dataset/Data_set_2/13269953. Primer development and designs used in KASP genotyping are given in Table S1 and S2. Table S3 contains the number of row plots of HIFs with their population background and SNPs information. Tables S4 and S5 contain the results of explained percent variations estimated by Equations 2 and 3 respectively for ruler measurements. Figures S3 and S4 contain the BLUEs for SNPs and the interaction of SNPs with populations obtained by Equation 2 for ruler measurements. Figure S5 contains the BLUEs for flowering times estimated by Equation 3. Figures S6 and S7 contain the BLUEs for the interactions between both SNPs and combined interactions between SNPs and populations respectively for ruler measurements estimated by Equation 3. Figure S8 contains Pearson correlations between

UAS-PHT with ruler measured means and median. Figure S9 contains the linkage disequilibrium decay plots for each chromosome.

Results

The effects of cytosine/C for SNP1, adenine/A for SNP2 (e.g., XX) calls in both SNPs, contributed by both NC356 and LH82 parents (Supplementary Figure S1), increased all three ruler measures of PHTs (TH; from ground to tip of tassel, FH; from the ground to the flag leaf collar, EH; first ear height from the ground to first ear shank). Tassel height differences between XX and YY calls were statistically significant across all populations (Figure 17), varying from 2.0 cm to 8.9 cm (SNP1) and 3.0 cm to 11.9 cm (SNP2) depending on the populations genetic background (Figure 17). The favorable locus (XX) of SNP1 and SNP2 across populations increased TH ~ 4 cm and FH ~ 3 cm (Equation 2; Supplementary Figure S3). Interactions between SNP1*population and SNP2*population varied, with TH differences were observed up to 10 cm, followed by up to 7.0 cm for FH (Supplementary Figure S4). Flowering times (DTA and DTS) when used as response in Equation 2 demonstrated that the taller XX allele of SNP1 and SNP2 for PHTs also caused later flowering. XX allele of SNPs delayed flowering times between 1 day and 5 days depending on the genetic backgrounds of populations (Supplementary Figure S5). Result of orthogonal contrasts conducted between calls of each population showed this lateness was statistically significant (Supplementary Figure S5). In Equation 3, SNP1 and SNP2 interactions $[SNP1 * SNP2]_{jk}$ for TH and combined interaction with populations $[Pop * SNP1 * SNP2]_{ijk}$ were found to be significantly taller than shortest combination (YY-YY) when either SNP1, SNP2, or both were XX

favorable locus, resulting in that combined favorable SNP1 and SNP2 loci (XX-XX) was tallest in TH, which was 8.8 cm taller than the YY-YY combination (Supplementary Figure S6). This was 3.5 cm taller than expected from SNP1 or SNP2 alone and represents a synergistic effect between these two loci. There was also an epistatic effect of these loci with the XX-XX combination increasing height 8 cm in population 1 but 9.6 cm for population 2 which was consistent for other measurements of PHT (Supplementary Figure S7). The proportion of total experimental variance attributable to differences between populations (Var(Pop)) varied from 64% to 80% within Equation 2 and Equation 3 for PHT measurements by ruler. Population effects, spatial (range, row) partitioned large amounts of experimental variance, but repeatability was high at 89% to 95% (Supplementary Tables S4 and S5).

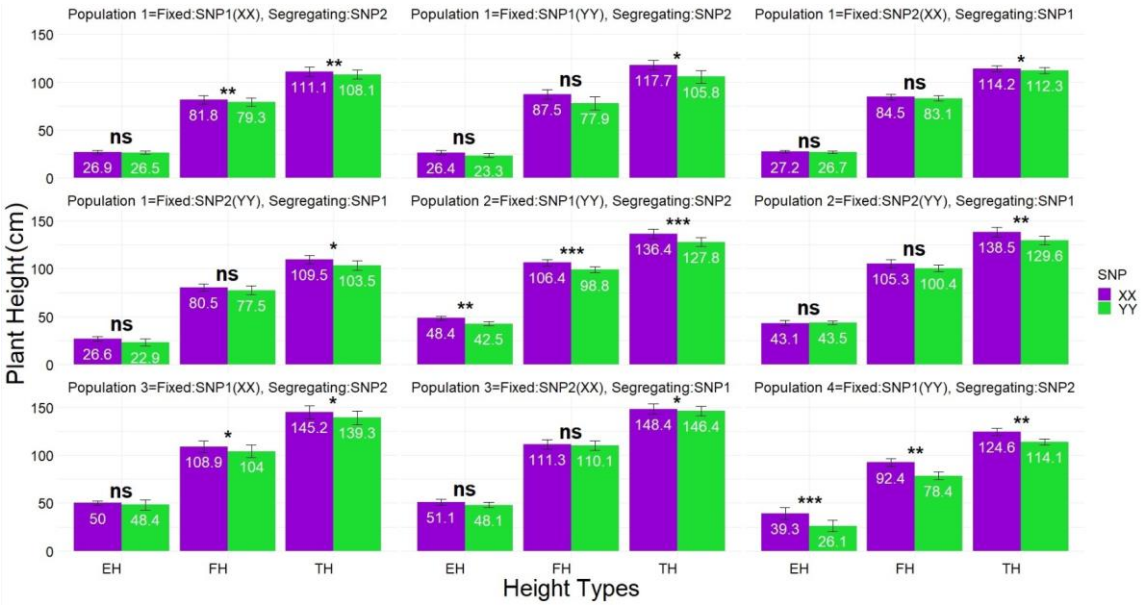

Figure 17 BLUEs of all three ruler measures of plant heights. This showed XX calls significantly increased all height measures in a consistent direction across populations. Population 1, 2, 3, and 4 are NILs of [LAMA (recurrent parent) LH82], [Ki3 NC356 (recurrent parent)], [Ki3 (recurrent parent) NC356], and [Tx740 (recurrent parents) NC356], respectively. BLUEs were calculated using Equation 1 (SNP_i term).

Differences of BLUEs between XX and YY calls were statistically significant across all populations for TH which changed between 2.0 cm and 8.9 cm for SNP1 and between 3.0 cm and 11.9 cm for SNP2. *, **, and *** indicate significance levels at 0.05, 0.01 and 0.001, respectively, while ns indicates not significant. Whiskers represent the standard error. TH, tip of tassel height; FH, flag leaf collar height; and EH, height of the first ear shank from ground on the x-axis. Reprinted from Adak, Conrad, et al., 2021.

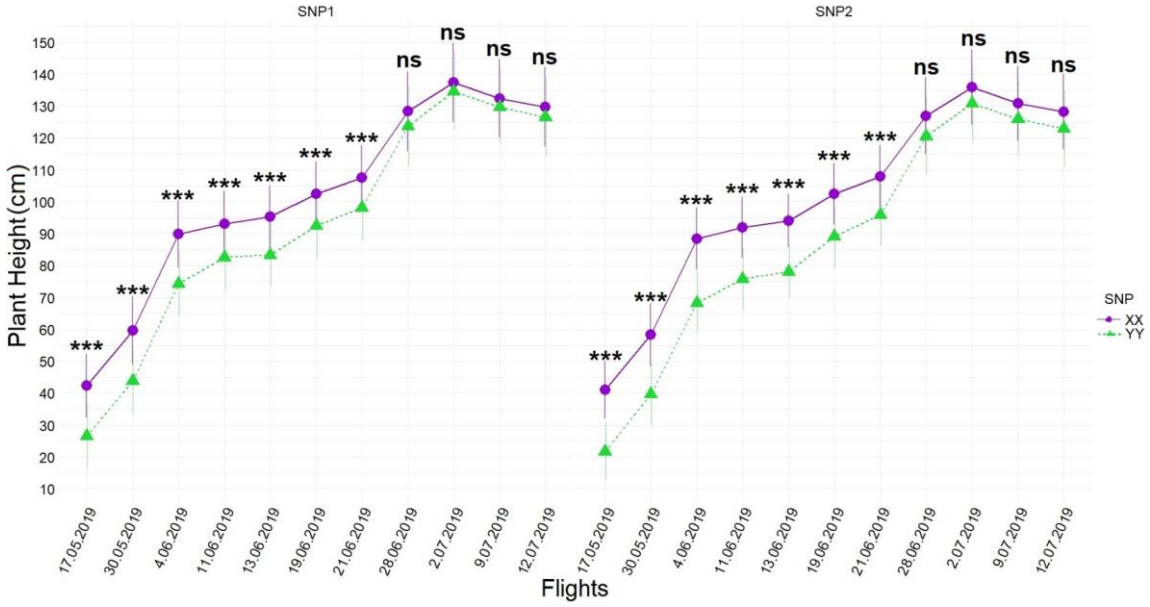

Figure 18 Temporal resolution of differences between SNP1 (left) and SNP2 (right) calls obtained by Equation 2 (SNP_j term) during UAS flights across all populations. Whiskers represent the standard error. BLUEs of calls (XX vs YY) were orthogonally contrasted for each SNP at each time point and statistically significant differences were placed above the effects. *** indicates significance level at 0.001, while ns indicates not significant. Reprinted from Adak, Conrad, et al., 2021.

Statistical Inferences of UAS PHT

Temporal resolution of each UAS flight captured that the highest PHT (Canopy Height Model; CHM) differences between favorable (XX) and unfavorable loci (YY) were 16–20 cm in early growing stages (34–54 days after sowing; first four flights) but narrowed 3– 5 cm by harvest time depending on when either SNP1 or SNP2 was tested

in Equation 2, respectively (Figure 18). The differences between favorable and unfavorable loci varied depending on the interaction between populations with SNP1 [Pop* SNP1]$_{ij}$ and populations with SNP2 [Pop*SNP2]$_{ik}$ by Equation 2. The differences between calls in either interaction had a descending pattern from early growing season to time of harvest, showing the highest differences between calls for populations were captured between 9 cm and 26 cm in early season and narrowed 1 cm to 10 cm by the time of harvest (Figure 19). In Equation 3, UAS captured that favorable loci combinations of XX-XX (SNP1: SNP2) were tallest in every flight followed by YY-XX, XX-YY, and YY-YY (Figure 20), resulting in height differences between favorable and unfavorable loci combined for population 1 and population 2 of 11–25 cm in the early growing stages and 7–10 cm by the time of harvest (Figure 21). Synergetic effects of the favorable loci combination on the unfavorable loci combination also decreased from 9 cm to 2 cm as the growing period progressed. Population variation (Var(Pop)) always explained the highest percentage of total variation in both Equation 2 and Equation 3, resulting in repeatability estimates which fluctuated between 84% and 97% (Tables 1 and 2) during growing periods for PHT. SNP1 (Var(SNP1)) and SNP2 (Var(SNP2)) in Equation 2 showed decreasing trends from ~20% to 30% of explained total variation to below 1% over the growing period (Table 2) as well as decreases from ~2% to 5% to below 1% in the interaction of SNPs in Equation 3 (Table 3).

Accuracy Assessment Between UAS-PHT and TH

For accuracy assessment, means and medians of each plot measured by ruler on July 2nd, 2019, were correlated with UAS-PHT captured on the same date, and a

correlation coefficient was found to be 0.83 for either the median or mean correlated with UAS-PHT (Supplementary Figure S8).

Candidate Genes Associated with The SNPs

LD decay distances calculated for each chromosome were found to be 1.5, 5.8, 4.5, 3.7, 4.5, 5.1, 4.5, 4.5, 4.9, and 5.7 kb for chromosomes 1 to 10, respectively (Supplementary Figure S9). Candidate genes were determined based on the LD decay around the surrounding regions of SNP1 (Chr2: 27,482,431 kb) and SNP2 (Chr7: 164,955,163 kb) as well as their physical positions using the Maize Refgen v2 coordinates (Supplementary Figure S2). SNP1 (Chr2: 27,482,431 kb) has a strong LD (R2:1, sig ¼ 0.00) with an adjacent locus (Chr2: 27,482,479 kb) which is 48 base pair away (upstream region) and both loci are in the genic region of GRMZM2G035688 (Chr2: from 27,478,703 to 27,483,682 kb) genes (Supplementary Figure S2). The region 5.8 kb upstream and downstream of SNP1 was also investigated, since the LD decay distance chromosome 2 was 5.8 kb. Only one other gene, GRMZM2G035637 (Chr2: from 27,478,035 to 27,479,631 kb), falls within the downstream region of SNP1 (1 kb away). SNP2 (Chr7: 164,955,163 kb) has strong LD (R2:0.86, sig = 0.95) with a locus (Chr7: 164,954,968 bp) that is located at 195 bp away downstream region of SNP2. SNP2 and the locus, which is located 195 bp away from SNP2 with high LD, are located in the genic region of GRMZM2G009320 (Chr7: from 164,954,304 to 164,956,841 kb). The region 4.5 kb upstream and downstream of SNP2 was scanned, since LD decay distance for chromosome 7 was 4.5 kb. There is only one other gene, GRMZM2G009538 (Chr7: from 164,948,659 to 164,953,684 kb), is located downstream

of SNP2 (within 1 kb away; Supplementary Figure S1). Physical locations of GRMZM2G035688 and GRMZM2G009320 were updated to reference genome version 5 (Supplementary Figure S1).

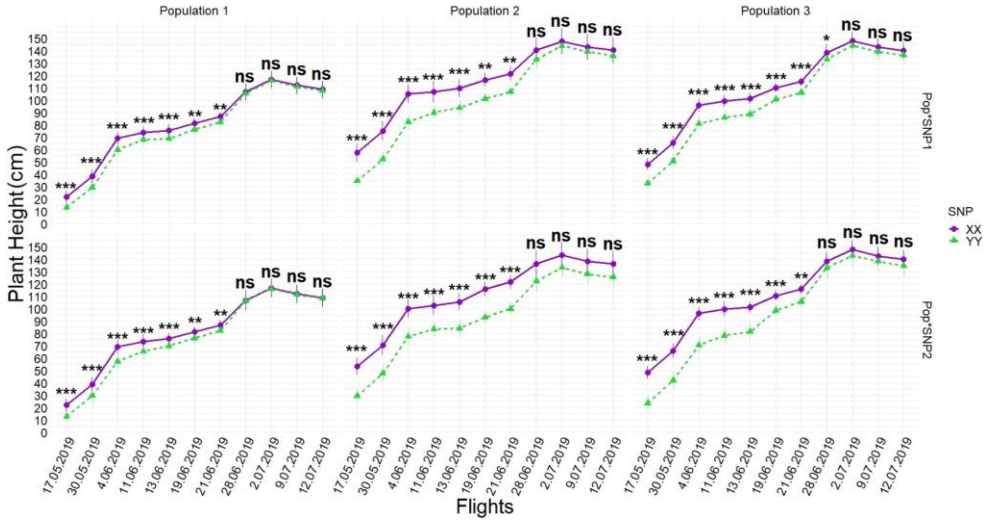

Figure 19 Temporal resolution of interactions of $[Pop*SNP]_{ij}$ obtained by Equation 2 during UAS flights. Modeling interactions showed that there were large differences between how the SNPs behaved on different genetic backgrounds. Whiskers represent the standard error. BLUEs of calls (XX vs YY) were orthogonally contrasted for each SNP in each population at each time point and statistically significant differences were placed above the effects for each time points. *, **, and *** indicate significance levels at 0.05, 0.01, and 0.001 respectively, while ns indicates not significant. Reprinted from Adak, Conrad, et al., 2021.

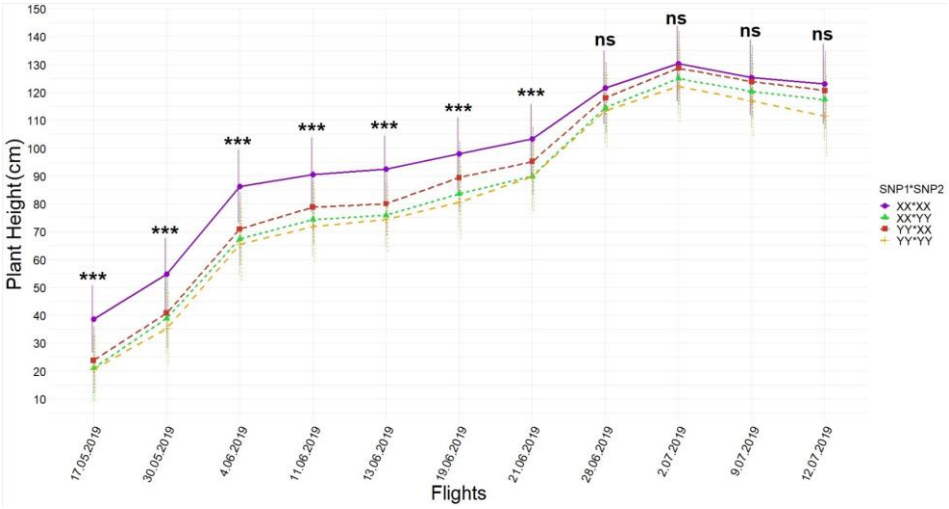

Figure 20 Temporal resolution of differences among SNP1-SNP2 interactions during UAS flights. The interaction $[SNP1*SNP2]_{jk}$ was obtained from Equation 3 and shows that the two loci had a synergistic effect on increasing height. Whiskers represent the standard error. BLUEs of XX:XX (SNP1:SNP2) and other call combinations (XX:YY, YY:XX, and YY:YY) were contrasted for SNP1 and SNP2 interactions at each time point and statistically significant differences were placed above the effects for each time points. and *** indicate significance levels at 0.05, 0.01, and 0.001 respectively, while ns indicates not significant. Reprinted from Adak, Conrad, et al., 2021.

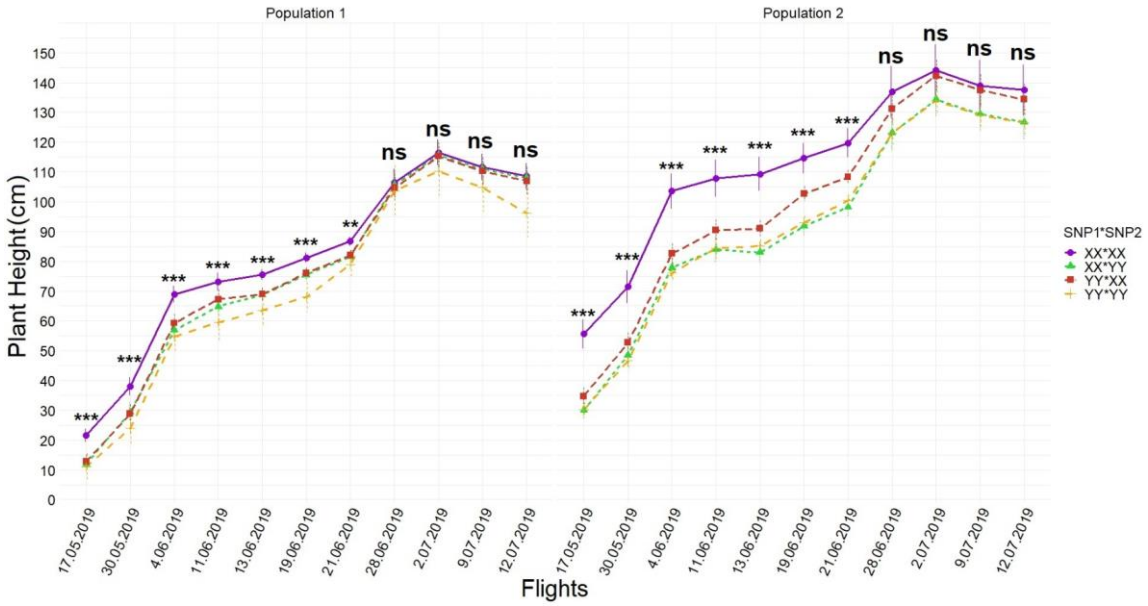

Figure 21 Temporal resolution of differences for two populations among SNP1-SNP2 interactions during UAS flights. Interactions $[Pop*SNP1*SNP2]_{ijk}$ obtained from Equation 3 showed the SNP combinations had different effects across different populations genetic backgrounds, especially early in the season. Whiskers represent the standard error. BLUEs of XX:XX (SNP1:SNP2) and other call combinations (XX:YY, YY:XX, and YY:YY) were contrasted for SNPs and population interactions at each time point and statistically significant differences were placed above the effects for each time points. and *** indicate significance levels at 0.05, 0.01, and 0.001 respectively, while ns indicates not significant. Reprinted from Adak, Conrad, et al., 2021.

Table 2 Percentages of total variance explained by each component in Equation 2 when SNP1 was tested (above) and SNP2 was tested (below) as well as the total variance in number and repeatability for each UAS flight *, **, and *** indicate significance levels at 0.05, 0.01, and 0.001 respectively. Reprinted from Adak, Conrad, et al., 2021.

Variance component (Random effect)	Percentage of variation explained by each variable component for each flight										
	17.05.19	30.05.19	4.06.19	11.06.19	13.06.19	19.06.19	21.06.19	28.06.19	2.07.19	9.07.19	12.07.19
Population	45.7	46.2	45.5	47.1	47.2	64.3	66.0	54.0	53.8	54.3	54.1
SNP1	20.4	18.1	18.9	9.1	13.9	8.1	7.6	0.7	0.3	0.3	0.4
Population*SNP1	2.6	1.8	1.7	1.7	1.8	1.1	1.3	0.0	0.0	0.0	0.0
Replication	8.0	9.4	8.5	7.4	7.8	4.9	4.7	14.7	14.5	14.2	14.0
Row	0.2	0.3	0.0	1.1	0.5	0.5	0.6	3.4	3.2	3.3	3.2
Range	11.7**	13.0**	13.8**	14.3**	15.9**	12.4***	10.9**	7.0*	7.5*	7.2*	7.7*
Residual	11.4	10.8	11.7	19.3	12.9	8.7	9.0	20.3	20.7	20.7	20.6
Total variation in number	449.4	490.1	476.7	474.9	412.5	395.4	371.8	547.8	551.3	550.1	559.3
Repeatability (R)	0.89	0.89	0.87	0.83	0.88	0.94	0.94	0.84	0.84	0.84	0.84
Variance component (Random effect)	Percentage of variation explained by each variable component for each flight										
	17.05.19	30.05.19	4.06.19	11.06.19	13.06.19	19.06.19	21.06.19	28.06.19	2.07.19	9.07.19	12.07.19
Population	30.9	32.3	32.8	34.7	32.2	50.9	88.2***	48.4***	50.5***	49.2***	82.0***
SNP2	32.4	27.6	30.8	21.9	24.2	16.6	0.1***	0.1***	0.2***	0.1***	0.1***
Population*SNP2	7.1	5.8	3.9	4.3	7.9	7.1	0.0	0.1***	0.1***	0.1***	0.1***
Replication	9.2	11.3	9.3	12.2	7.8	6.2	0.4	30.4	27.3	28.0	7.2
Row	0.1	0.1	0.1	0.1	0.2	0.8	0.7	0.8***	0.6***	0.4***	1.0***
Range	11.9**	14.3**	14.8**	17.2**	16.3**	11.8**	5.7***	7.4***	7.3***	7.3***	2.7***
Residual	8.4	8.6	8.2	9.7	11.3	6.6	4.9	12.9	14.0	14.9	6.8
Total variation in number	475.2	512.6	548.9	473.8	394.7	403.0	385.2	660.4	484.1	608.2	1379.2
Repeatability (R)	0.88	0.88	0.89	0.88	0.85	0.94	0.97	0.88	0.88	0.87	0.96

Table 3 Percentages of variance explained by each component in Equation 3 as well as total variance and repeatability for each UAS flights. The flight dates were shown as day/month/year (dd/mm/yy). Reprinted from Adak, Conrad, et al., 2021.

Variance component (Random effect)	Percentage of variation explained by each variable component for each flight										
	17.05.19	30.05.19	4.06.19	11.06.19	13.06.19	19.06.19	21.06.19	28.06.19	2.07.19	9.07.19	12.07.1
Population	81.4***	81.1***	74.6***	81.1***	79.3***	68.3	84.8***	70.8***	57.4***	57.3***	57.4**
SNP1	2.2***	2.7***	2.1***	1.5***	1.6***	1.4	0.1***	0.6***	0.7***	0.6***	0.3**
Population*SNP1	0.1***	0.1***	0.1***	0.1***	0.1***	0.1	0.1***	0.3***	0.5***	0.6***	0.6**
SNP2	5.5***	3.9	5.7	3.4	3.2	4.1	0.3***	2.0***	1.2***	1.0***	0.2**
Population*SNP2	0.1***	0.2***	0.2***	0.1***	1.6***	6.1	3.5***	1.4***	2.2***	2.6***	2.2**
SNP1*SNP2	0.7***	0.7***	1.2***	1.1***	1.8***	2.0	1.7***	0.2***	0.3***	0.3***	0.7**
Population*SNP1 *SNP2	0.7***	0.2***	0.1	0.1***	1.1***	0.1***	0.1***	0.1***	0.1***	0.1***	0.1**
Replication	0.7	1.4	1.3	1.3	0.0	0.0	0.0	7.4	5.1	4.8***	5
Row	0.2***	0.1***	0.1	0.1***	0.5***	1.1	0.9***	2.3***	2.9***	2.8***	2.8**
Range	3.3***	5.0***	7.2**	5.2***	3.7***	6.4*	2.4***	4.2***	11.2***	11.2***	11.5**
Residual	5.1	4.5	7.4	6.0	7.1	10.3	6.1	10.7	18.3	18.7***	19
Total variation in number	640.1	807.7	609.1	895.6	691.2	377.0	593.0	871.2	473.8	463.0	466
Repeatability (R)	0.97	0.97	0.95	0.96	0.95	0.93	0.96	0.93	0.86	0.86	0.8

Discussion

These results demonstrated in maize for the first time that quantitative height loci first discovered through GWAS testcrossed diversity panel studies also conferred effects across four very diverse genetic backgrounds. An uncommonly discussed advantage of GWAS over linkage mapping is the ability to detect alleles that function nonspecifically

across genetic backgrounds, maximizing discovery of context-independent alleles unaffected by genetic background epistasis that has hindered use of quantitative loci in the past. These alleles were first confirmed in linkage mapping populations (F3:4) developed from parental lines segregating for the two SNPs of interest (Y. Chen, 2016). However, (Y. Chen, 2016) estimated different absolute effect sizes for these loci compared to those estimated in the initial GWAS (Farfan et al., 2015).

Across many studies, thousands of maize loci have been associated with agronomic traits in maize (e.g., (Andersen, Schrag, Melchinger, Zein, & Lübberstedt, 2005; Anderson, Mahan, Murray, & Klein, 2018; Farfan et al., 2015; Larsson et al., 2013; H. Li et al., 2013; Peiffer et al., 2014; Thornsberry et al., 2001; Weng et al., 2011)). Although strong population structure and relatedness has been controlled in most GWASs to reduce false positive results (Lipka et al., 2015; Myles et al., 2009), we are cautioned by the cryptic population structure of dwarf8 (Larsson et al., 2013) and possibilities of overfitting GWAS models to identify noncausal loci. Independent genetic confirmation of loci from GWASs is therefore necessary to understand whether the alleles are robust and useful as well as if the effect sizes are consistent across genetic backgrounds. Therefore, it is critically valuable that the two loci used in this study were validated over HIFs from four linkage populations, as contributing to taller PHTs in both ruler measurements and UAS data.

Temporal Resolutions of Loci Effects on PHT

The first seven UAS flights, flown during vegetative growth (typically up to 70 days after planting), found the largest effect sizes of loci and interaction effects of

loci (Figures 18–22) as well as explained the most variation (Tables 1 and 2). This was unexpected since these SNPs were initially discovered in the GWAS panel through terminal height measurements using a ruler (Farfan et al., 2015). However, UAS phenotyping technologies were not available when Farfan et al. 2015 was conducted and temporal ruler measurements would have been infeasible. The last four UAS flights were flown in the reproductive stage (days 70–100 after sowing) after vegetative growth when internodes had stopped increasing and the effect size of loci and their interactions had become much smaller, in agreement with ruler measurement results taken July 2nd, 2019 (82nd day after sowing, between R5 and R6) (Tables 1 and 2; Supplementary Tables S4 and S5). In the reproductive growth phase, measuring plants individually with a ruler and plots by UAS, the differences between the main effects of loci could still be resolved (Supplementary Table S4 and S5). Maize yield has been most strongly correlated with PHT, in V6 (6-leaf), V10 (10-leaf), and V12 (12-leaf) growth stages, with V10 and V12 growing stages more important than other stages when earliness was desired (Yin, McClure, Jaja, Tyler, & Hayes, 2011). While no other studies have looked at maize yield relationships with height at intermediate growth time points, strong correlations have been reported between terminal PHT and grain yields in Texas maize (Anderson et al., 2019; Farfan et al., 2013). Context-dependency effects of loci under different genetic backgrounds were best able to be resolved in early UAS flights with larger effects sizes for populations 1 and 2 in the earliest flights (Figures 19 and 21). Population 3, developed as a reciprocal cross of population 2, was also observed to have had effect size differences (Figure 21).

Pleiotropy of Loci with Flowering Times

Both loci in this study were found to have pleiotropic effects on flowering (Supplementary Figure S5) not observed in the initial GWAS (Farfan et al., 2015). This was likely because heterosis in hybrid backgrounds tends to reduce or compress variation seen in inbred lines and because heterosis causes maize to flower earlier. Here the earliest flowering population had the smallest difference between alleles (population 1, <0.5 days) while the latest flowering population had and was able to discriminate the largest differences (population 3, >2 days) (Supplementary Figure S5).

Description of Candidate Genes

GRMZM2G035688, within 5.8 kb of SNP1, corresponding to aberrant phyllotaxy1 (also known as abph1) ,was first observed in maize mutant showing transformed phyllotaxy behavior (Jackson & Hake, 1999). Phyllotaxy is the geometric arrangement of leaves and flowers to control the plant formation by shoot apical meristem (SAM). Unlike auxin action in phyllotaxy regulation in Arabidopsis (Arabidopsis thaliana), cytokinin-inducible type A response regulator is encoded by abph1, indicating that cytokinins play a role on aberrant phyllotaxy in maize (B.-h. Lee et al., 2009). Auxin or its polar transport is necessity for abph1 expression due to fact that abph1 expression was dramatically lessened after treatment of a polar auxin transport inhibitor to maize shoots (B.-h. Lee et al., 2009). Taken together, GRMZM2G035688 encoding abph1 is essential for adequate maize PINFORMED (PIN1) expression, which is polar auxin transporter for leaf primordia expression in maize, and auxin localization in embryonic leaf primordia in SAM (B.-h. Lee et al.,

2009). Another gene, 1 kb away in the downstream region of SNP1, is GRMZM2G035637. This gene is the Mo25 like gene that involves the cell proliferation, asymmetric cell establishment, as well as expansion that is crucial for plant establishment (Bizotto, Ceratti, Braz, & Masuda, 2018). This gene has not been previously implicated in PHT. However, given the pattern observed by UAV of stronger differentiation in alleles at early growth stages, when cells are dividing rather than expanding, this candidate is just as logical as abph1.

GRMZM2G009320, within 4.5 kb of SNP2, encodes a GAPDH, which catalyzes the sixth step of glycolysis into energy as well as carbons in higher plants. Under stress conditions such as salt or oxidative stresses, the activity of enzyme increases to manipulate energy formation in plants (Bustos et al., 2008; X.-H. Zhang et al., 2011). Another gene 1 kb away in the downstream region of SNP2 is GRMZM2G009538. This gene is a member of the acidic leucine-rich nuclear phosphoprotein 32 (Anp32) family that involves in crucial biological process such as the regulation of cell signaling, transduction, and cell formation (Matilla & Radrizzani, 2005).

Recent Breeding Has Selected the Favorable Alleles at Both Loci

Previously, several genes important in post domestication adaptation were identified by comparing maize lines from different early and late eras to show the proof of directional selection (van Heerwaarden, Hufford, & Ross-Ibarra, 2012); the genes of importance here (GRMZM2G035688 and GRMZM2G009320) were not included. Recent publicly available genotyping of diverse public inbred lines and germplasm ((Romay et al., 2013); 989 subset containing 448 public inbred lines, 87 germplasm

enhancement of maize (GEM)-like lines, 215 GEM lines, 118 Ex-PVP lines, 121 CIMMYT germplasm) for SNP1 and SNP2 information was extracted and grouped into five categories (Figure 22) and qualitatively compared by year of development or release. The frequency of SNP favorable alleles (X:X; increased height yield and flowering) showed consistent increases over time within most groups (Figure 22). Ex-PVP lines developed and released by industry and US public lines showed the greatest shifts toward the favorable alleles, almost to fixation. A lower frequency but less dramatic shift in CIMMYT originated tropical germplasm lines suggests that these loci still segregate in elite tropical maize, perhaps because the effects are less dramatic in the tropics. These alleles show favorable allelic selection over time, especially in temperate areas, unsurprising given their large phenotypic effects. This is another piece of evidence that these loci are economically valuable for improved varieties.

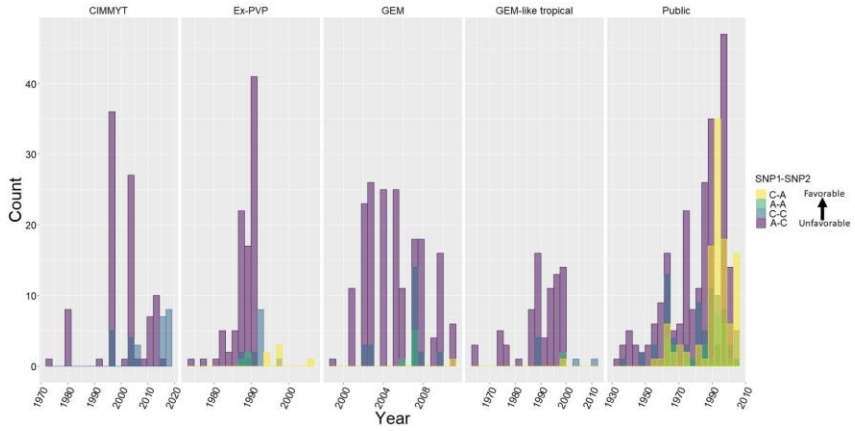

Figure 22 The allelic frequency combinations of SNP1 and SNP2 over years for five germplasm categories. The favorable C (SNP1) and A (SNP 2), referred to as XX, XX in this study, are both increasing in frequency in newer germplasm and are essentially fixed in US temperate Ex-PVP and public germplasm. The 989 subset of genotyped lines contained 448 public inbred lines, 87 GEM-like lines, 215 GEM lines, 118 Ex-PVP lines, and 121 CIMMYT germplasm lines. Reprinted from Adak, Conrad, et al., 2021.

In summary, a previous GWAS field study of hybrids under stress successfully nominated quantitative trait variants (QTVs) that work across genetic backgrounds, in inbred lines and throughout diverse environments, confirmed through this study. New UAS tools provided substantially more information and better screening for the effects of these alleles than the traditional terminal ruler height measurements in which they were discovered. To get a better understanding of QTV's affecting complex traits such as PHT and grain yield in maize, a combination of high-throughput phenotyping and genotyping studies must be evaluated together, which will be critical for managing the phenotypic plasticity of complex traits.

CHAPTER III

UNOCCUPIED AERIAL SYSTEMS (UAS) DISCOVERED OVERLOOKED LOCI CAPTURING THE VARIATION OF ENTIRE GROWING PERIOD IN MAIZE[2]

Quantitative variation of complex traits in maize (*Zea mays* L.) have been challenging to dissect since they show strong environmental interactions and are generally inconsistent between populations and different screening environments (Beavis, Grant, Albertsen & Fincher, 1991; Peiffer et al., 2014, Veldboom & Lee, 1996; Wang, Yao, Zhang & Zheng, 2006; Sari-Gorla, Krajewski, Di Fonzo, Villa & Frova, 1999; Koester, Sisco, & Stuber, 1993). Plant height, traditionally measured terminally at the end of the growing season with a ruler, is a prime example of a quantitative, complex trait; it is relatively easy to measure across many plots and it has high repeatability/heritability (Anderson, Mahan, Murray & Klein, 2018; Anderson et al., 2019; Mahan et al., 2018; Anderson et al., 2020; Peiffer et al., 2014; Veldboom & Lee, 1996; Rood & Major, 1981). Genetic mapping and theory suggest an omnigenic model supported by the genetically polygenic inheritances observed and the variable contributions of pedigree as a source of variation, consistent with a large number of loci with minor effects governing these traits (Boyle, Li & Pritchard, 2017; Wallace et al., 2016; Wang, Yao, Zhang & Zheng, 2006; Peiffer et al., 2014; Mackay, 2001). Recently,

---

Adak, A., Murray, S. C., Anderson, S. L., Popescu, S. C., Malambo, L., Romay, M. C., & de Leon, N. (2021). Unoccupied aerial systems discovered overlooked loci capturing the variation of entire growing period in maize. The Plant Genome, 14(2), e20102. https://doi.org/10.1002/tpg2.20102

emerging high throughput phenotyping tools have demonstrated that complicated phenotypically dynamic growth patterns are occurring (Anderson et al., 2020; Pauli et al., 2016; Wang et al., 2019; Wu & Lin, 2006; Miao, Xu, Liu, Schnable & Schnable, 2020) and that the importance of various loci change temporally throughout plant growth and development (Furbank & Tester, 2011).

Using ruler-based terminal plant height, a limited number of genes well-known to play a role in hormone synthesis and signaling pathways in maize have been found. These larger-effect plant height genes are involved in processes such as regulating gibberellin signaling and biosynthesis (Bensen et al., 1995; Lawit, Wych, Xu, Kundu & Tomes, 2010; Winkler & Helentjaris, 1995), hindering of polar movement of auxin transport (Multani et al., 2003) and brassinosteroid synthesis (Hartwig et al., 2011; Makarevitch, Thompson, Muehlbauer & Springer, 2012). Disruption of such hormone synthesis and signaling genes can cause significant reductions in plant heights. Although application to breeding have remained limited because of an antagonistic effect on yield (Bensen et al., 1995; Winkler & Helentjaris, 1995; Thornsberry et al., 2001), genetic variants at large effect hormone loci may have been fixed or found to not segregate widely as a consequence of directional selection over time (Peiffer et al., 2014). As a phenotype, terminal plant height can also be a strong predictor of yield in some environments, even in elite commercial hybrids (Farfan, Murray, Labar & Pietsch , 2013). It has been observed that early plant height measures (ie. in seedling, jointing and flowering growth stages; V0-VT) may provide novel insights into maize yield (Machado et al., 2002) and have the potential to predict yield at earlier time points (Yin, McClure,

Jaja, Tyler & Hayes, 2011; Zhang et al., 2017; Anderson et al., 2019; Miao et al., 2020). It is likely that many quantitative trait loci (QTLs) studies have been limited in explaining erratic plant height variation because they relied on end of season terminal height phenotyping data that did not monitor plant architecture and environmental stresses throughout plant growth (Su et al., 2019; Wang et al., 2010). Partitioning the genetic component from the total variation at each growth stage in a timely and repeated manner might further help to explain the hidden heritability issue in genetic dissection (Gibson, 2010).

Complex traits are orchestrated by the interplay of many genes, some constitutively expressed during all growth periods, while others are expressed at specific time periods (Tessmer, Jiao, Cruz, Kramer & Chen, 2013; Feldman et al., 2017; Bac-Molenaar, Vreugdenhil, Granier & Keurenties , 2015; Schmid et al., 2005; Sun & Wu, 2015; Li & Sillanpää, 2015). High throughput phenotyping (HTP) can measure the physical characteristics of plants in a temporal manner and has previously been used to discover temporal QTLs under field conditions for rice (Yang et al., 2014; Tanger et al., 2017), triticale (Würschum et al., 2014), cotton (Pauli et al., 2016), barley (Neumann et al., 2017) and wheat (Lyra et al., 2020). In order to capture temporal gene-trait associations in maize, two studies have used automated greenhouse based-HTP platforms (Junker at al. 2015) under environmentally controlled conditions (Zhang et al., 2017; Muraya et al., 2016) while two others used unoccupied aerials system (UASs) based-HTP platforms under field conditions (Anderson et al., 2020; Wang et al., 2019) but only for inbred lines and not hybrids, which are what farmers grow.

Repeated data collection of maize plant height by UASs has already shown dynamic correlations with yield at different time points in a segregating population of hybrid lines (Anderson et al., 2019). Within the scope of the Genomes to Fields (G2F) project, UAS HTP data captured the temporal variations of growth patterns in diverse hybrids as well as other agronomic traits (i.e. flowering times and yield) under three different environmental management conditions (optimal planting with irrigation, optimal planting without irrigation and late planting with irrigation) during 2017. In breeding programs, a predictive model that can quickly identify the highest yielding cultivars to advance before or without harvest yield data in larger nurseries would facilitate faster decisions, saving time and resources and possibly shortening the breeding cycle.

The objectives of this study were to (i) use temporal plant heights of the maize hybrids belonging to 22 flight dates (corresponding to 60 time points for three trials) as predictor variables in order to predict maize yield via a random forest algorithm; (ii) dissect the underlying temporal QTLs associated with the variation captured by each flight via a genome wide association (GWA) study; and (iii) estimate and compare the temporal genomic predictions for plant height of each flight for each trial.

Materials and Methods

Genetic Materials, Experimental Conditions and High Throughput Phenotyping

The G2F project is an umbrella initiative involving collaborators from a variety of disciplines aiming to perform high-throughput genotyping and phenotyping to understand gene-gene (GxG) and genotype-environment (GxE) interactions in maize (https://www.genomes2fields.org). Under this project, a HTP platform via UAS was

used to capture plant growth during various development stages over three management conditions per year in College Station, TX. In 2017, 280 hybrids were planted on March 3rd under optimal planting time with irrigation (G2FI), while 230 hybrids of the same set were planted on March 3rd under dryland conditions (G2FD; optimal planting time without irrigation) and on April 6th for increased heat stress (G2LA; delayed planting with irrigation) in College Station, Texas. To visualize the heat stress to which the G2LA has been exposed, cumulative growing degree days (°C) and photoperiod (hour) were illustrated for the first 150-days period following optimal (G2LE and G2FD) and delayed (G2LA) planting times (Supplemental Figure S1). Growing degree days (GDD) were calculated per day by subtracting the average of the daily maximum and minimum temperature from the base temperature (10 °C). If GDD was below zero for any given day, it was set to zero. All hybrids in each trial were grown based on a randomized complete block design with two replications. In each replication of each trial, all hybrids were grown as two adjacent row plots (7.62 m row plot length and 0.76 m row plot spacing between all rows) and grain yield (GY) was collected from two adjacent row plots per hybrid with a plot combine harvester. Days to anthesis (DTA) and silking (DTS) were recorded for each hybrid as the number of days from the time of planting until at least fifty percent of each hybrid showed anthesis and silking emergence in the two row plots. Agronomic field data and weather data is available for 2017 https://doi.org/10.25739/w560-2114 (McFarland et al., 2020).

Preliminary studies of image processing and plant height extraction from HTP platform for the three trials of 2017 were reported previously by Anderson et al., (2019).

First, point clouds were clipped based on the trial boundaries of G2FI, G2FD and G2LA. Then noise points, which are located at the far bottom and top of the point clouds were illustrated by using the lateral view function in CloudCompare v2.10 (Girardeau-Montaut, 2016). These noise points can cause big fluctuations in plant height data extraction, so they were manually selected using segment tool function of CloudCompare v2.10 and removed from point cloud data. Executable functions of LAStools (Isenburg, 2015; rapidlasso, 2017) and FUSION/LDV (McGaughey, 2016) software were transported in R. A custom batch script was developed with several steps to extract the plot-based plant height data. "R/UAStools" package was used to create the polygons (ESRI shapefile) for each two adjacent row plots in each trial using the unique plot IDs (Anderson and Murray et al., 2020); two adjacent row plots-based polygon construction was also illustrated in https://github.com/andersst91/UAStools/wiki/plotshpcreate.R. A brief overview of the plant height extraction steps of custom batch script from point cloud data in R was described as follows; (i) points of clipped point cloud data of each trial were first sorted using the function of "lasssort.exe" of LAStools software; (ii) the noisy points that were so close to the canopy structure of plants in row plots were removed using the function of lasnoise.exe of LAStools before constructing the digital surface model (DSM); (iii) ground points were identified using the hierarchical robust interpolation algorithm (HRI; Kraus and Pfeifer, 1998) using the function of "GroundFilter.exe" of FUSION software (iv) maximum points from the ground points were determined using the function of "lasthin.exe" of LAStools software; and finally (v) a digital terrain model (DTM) was

generated based on the maximum points from the previous steps using the function of "GridSurfaceCreate.exe" of FUSION software. Next, canopy surface models (CSM) generated from the DTM (output of step v) were extracted from the DSM (the output of step ii). Row plots in CSM then were clipped based on the previously generated ESRI shapefile using the function of "PolyClipData.exe" of FUSION software. As a final step, plant heights were extracted for each clipped cloud points of each row plot as a percentile metrics using the function of CloudMetrics.exe of FUSION software. This study only used 99 percentile based-plant heights (Malambo et al., 2018). All flight dates were converted into days after planting (DAP) and specified DAP in the text, figures and tables in this study.

The point cloud data (and all raw data) is available on Cyverse (Murray et al., 2019). In total, 21, 20 and 19 flights were used for G2FI, G2FD and G2LA trials, respectively. For plant height, obvious outliers (>3-meter-tall) were removed from the phenotypic data. Missing phenotypes (two hybrids at 36 and 39 DAP in G2LA) were imputed using "missForest" package in R.

Statistical Models and Random Forest Application to HTP Data

In order to calculate phenotypically estimated breeding values for each flight (UAS_{PEBVs}), a full random model was fit using standard least squares (restricted maximum likelihood method, REML) in JMP version 15 Pro (SAS Institute Inc., Cary, NC, USA). Best linear unbiased predictions (BLUPs) of hybrids along with all random effects of variance components were estimated based on (Equation 1):

$$y_{grij} = \mu + Genotype_g + Replation_r + Range_i + Row_j + \varepsilon_{grij}$$

Eq. 1

Where y is the response vector of plant heights belonging to each flight time, μ is grand mean, g is the vector of genetic effects of the hybrids ($g \sim NID(0, I\sigma_g^2)$), r, i and j are replication ($r \sim NID(0, I\sigma_r^2)$), field range ($i \sim NID(0, I\sigma_i^2)$) and field row ($j \sim NID(0, I\sigma_j^2)$) effects, respectively, accounting for spatial effects in the randomized complete block design; ε is the vector of error ($\varepsilon \sim NID(0, I\sigma_\varepsilon^2)$). $Genotype, replication, range$ and row are the incidence matrices of the variance components in the model.

Repeatability was estimated as follows (Equation 2):

$$R = \frac{\sigma_g^2}{\sigma_g^2 + \frac{\sigma_\varepsilon^2}{no.of\ reps}} \quad \text{Eq. 2}$$

Pearson correlation coefficients were also calculated using UAS_{PEBVs} belonging to each flight of each trial separately to show the correlations among plant heights of different time points.

UAS_{PEBVs} belonging to each flight of each trial were used as predictors to predict continuous yield. Linear (LM) and random forest regressions (RF) were applied to each trial separately. The training and test populations were set as 70% and 30%, respectively. The "*Caret*" package was used to implement two regression models in R by setting the method = "lm" for LM and “rf” for RF models. K-fold cross validation was implemented by using the "trainControl" function of "Caret" package for both models. To conduct the 10-fold with 3 replications cross validation, method, number, and repeats were set

"repeatedcv", 10 and 3 respectively. Root mean square error (RMSE), mean absolute error (MAE) and Rsquared were used to assess models for each trial. To tune the parameters of RF, "tunegrid" was used to find best number of predictors sampled for splitting at each node (m_{try}) and number of trees grown ($ntree$) based on lowest RMSE. To illustrate the importance of UAS_{PEBVs} belonging to each flight, "*varImp*" function was used after RF model where higher "*varImp*" scores indicate higher importance of the explanatory variable (flight dates) in prediction the yield. To show the relationships between each predictor (flight dates) and outcome (yield) in the RF, partial dependence plots were generated by using the "pdp" package in R (Friedman 2001).
To assess prediction skill of the LM and RF models, predict function of Caret "caret::predict()" was used to predict yield of test data set using 1000 bootstraps. Correlations between actual yield of test data and predicted yield of test data were calculated for LM (r_{lm}) and RF (r_{rf}) models at each bootstrap. The Wilcoxon signed rank test was then applied to each trial to compare correlation results of the LM and RF models.

SNP Discovery and Association Mapping

More than 1500 inbred lines with a total of 955,690 SNPs (GBS v2.7) were produced using Illumina Hi-seq 2000/2500 at the Institute for Genomic Diversity, Cornell University, Ithaca, NY, USA (Glaubitz et al., 2014). The imputed ZeaGBSv2.7 data is also available through CyVerse with AGPv4 physical coordinates (McFarland et al., 2020; www.panzea.org, Elshire et al., 2011). GBS data of 158, 118 and 118 hybrids from 2017 was synthesized from sequence information of the available parental inbreds

for the G2FI, G2FD and G2LA trials, respectively. Tassel 5 software was used to call polymorphic markers (Bradbury et al., 2007). First, markers were set as missing if the either or both inbreds of hybrids used in this study were heterozygous. Second, sequence information of each hybrid was generated using the "Create Hybrid Genotype" function in Tassel 5. Third, markers with missing data (more than 10%) and minor allele frequency (MAF) of less than 1% were filtered out. Missing markers were imputed using "SNP.impute=major" code in GAPIT (Genome Association and Prediction Integrated Tool) package in R (Lipka et al., 2012). Finally, 153,252 markers remained.

Plant heights of hybrids, using the BLUPs in Eq. 1, captured by each flight were associated with filtered GBS data in the three trials individually, implementing the fixed and random model circulating probability unification (FarmCPU) (Liu, Huang, Fan, Buckler & Zhang, 2016) with principal components (PCs) in GAPIT (Lipka et al., 2012). In GAPIT, the "Model.selection=TRUE" code was used to determine the optimal number of PCs based on Bayesian information criterion (BIC). The first three PCs were used in GWA study (Supplemental Figure S2). To calculate the explained variation by the SNPs with a higher score than conservative Bonferroni correction ($-log_{(10)}(p)$>6.5 ; 0.01/no. of markers), a "Random.model=TRUE" code was used in GAPIT function. In addition, a false positive discovery rate (FDR) was set ($-log_{(10)}(p)$>5) to determine the same SNP(s) (if any), which were discovered with Bonferonni correction in one flight, were important in any other different flight. MaizeGBD (http://www.maizegdb.org/) was used to look up SNPs positions for determining the candidate genes in those regions using AGPv4 physical coordinates of B73. The Gramene database

(http://www.gramene.org) was used to determine the functions of candidate genes. Linkage disequilibrium (LD) was examined for co-localized SNPs that were discovered in more than one flight or trial using R^2 (>0.8) in LD heatmap package in R (Shin, Blay, McNeney & Graham, 2006).

Genomic Prediction of Flights

Genome wide prediction was applied to each flight of each trial to calculate genetic estimated breeding values (UAS_{GEBVs}) using rrBLUP (ridge regression best linear unbiased prediction) package in R (Endelman, 2011). Training and test data sets were arranged at 70% and 30%, respectively. Equation 3 was used to estimate GEBVs:

$$y = 1\mu + Z\beta + \varepsilon \quad \text{Eq. 3}$$

Where y is the vector of observations as BLUPs of plant heights of flights, μ is the overall mean, Z is the marker matrix, β is the marker effects matrix and ε is the residual effects vector with the assumptions of $\beta \sim NID(0, I\sigma_\beta^2)$ and $\varepsilon \sim NID(0, I\sigma_\varepsilon^2)$. Prediction accuracies for genomic predictions (r_{gpa}) were obtained for each flight using correlations between UAS_{PEBVs} and UAS_{GEBVs} of test data set, which were calculated by using cross-validation with 500 iterations.

Results and Discussion

Variance Components, Repeatability and Breeding Value Estimations of Hybrids Using HTP Data

Using plot-based plant height extraction from the 2017 G2F project in College Station, TX, BLUPs of plant heights belonging to maize hybrids for each flight date (UAS_{PEBVs})

were estimated using [Eq. 1]. The UAS_{PEBVs} were categorized into two groups, low and high yielding hybrids using the average yield threshold of each trial. As expected from previous work, taller hybrids, especially at flights after flowering, were relatively higher yielding than hybrids that were shorter (Figure 23).

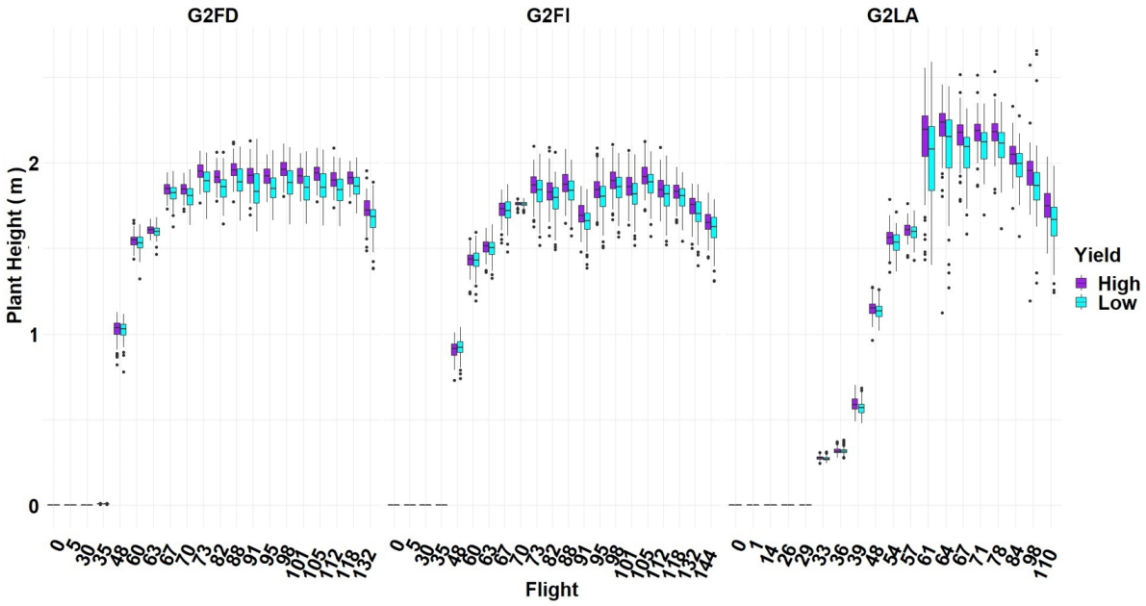

Figure 23 Illustrations of categorizing the plant heights of each flight of the hybrids grown in 2017 according to the high and the low yield values. G2FI, G2FD, and G2LA trial represent the optimal planting time with irrigation, optimal planting time without irrigation (dryland), and delayed planting time (late) with irrigation, respectively. *X* axes represents the flights as days after planting. *Y* axis represent the best linear unbiased predictions of plant heights (as meter unit) of both hybrids' categories; high yield and low yield hybrid categories were represented by purple and cyan color box plots, respectively, for each flight date. Every hybrid was categorized as low- or high-yielding hybrids if they had lower and higher yield value than average yield value of regarding trials. Reprinted from Adak, Murray, Anderson, et al., 2021.

Late plantings (G2LA) being taller is consistent with our normal observations in our breeding program over the years. Our best reason for this result is that hybrids were exposed to longer day length with higher heat accumulation (as illustrated in Supplementary Figure S1) when planted late (e.g. G2LA in this research). We do not

know the entire mechanism but speculate it has to do with a combination of photoperiod (our plantings in Texas have been the only G2F location where plants flower as the days are getting longer, the later planting flowers closer to the longest day of the year) and/or with temperature (more rapid accumulations of growing degree days). These environmental conditions caused by late planting may cause the maize hybrids to produce more photosynthetic activity resulting in taller plant height and biomass, however less yield.

The UAS_{PEBVs} variation explained by pedigree fluctuated between 5% to 80% of total variation explained by the model. Repeatability ranged from 12 to 93% across flights and trials (Figure 24). The hybrids with continuous taller plant heights across flights resulted in higher yield (Figure 23) even though repeatability results were not consistently estimated for plant heights through the flights. In addition, correlation coefficients among the plant heights (UAS_{PEBVs}) belonging to later flights (after flowering times) had higher and more consistent correlation coefficients than the correlation coefficients of the plant heights (UAS_{PEBVs}) belonging to earlier flights (before flowering times) (Supplemental Figure S3). It is likely that differences in repeatability for each flight were related to the image and stitching quality of each flight (Anderson et al., 2019; Malambo et al., 2018) as well as weed pressures especially in earliest flights (e.g. 35 DAS in G2FD).

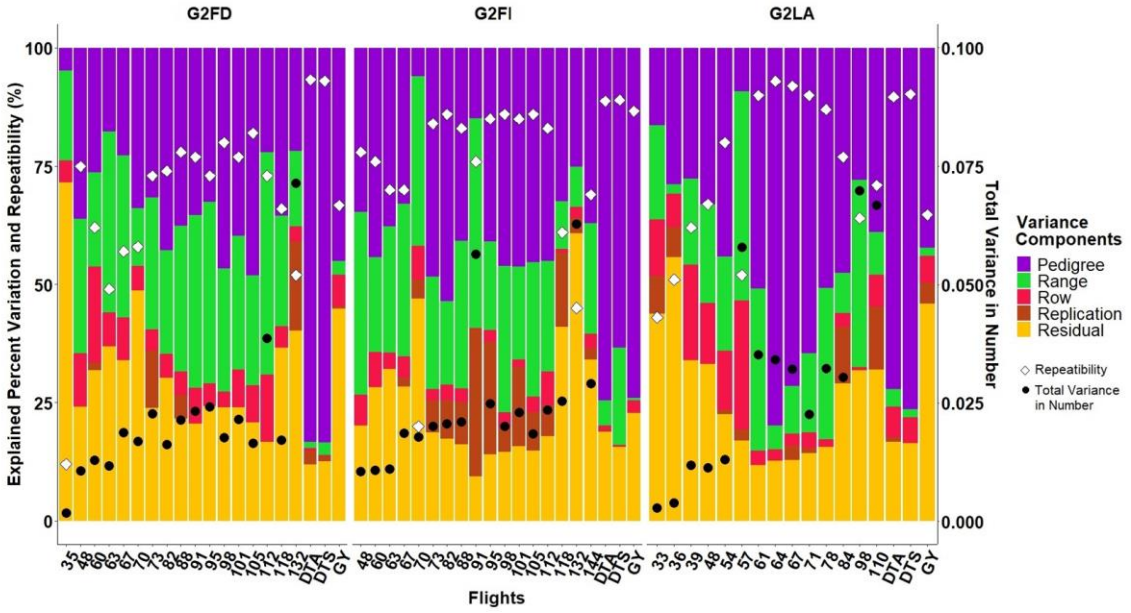

Figure 24 Stacked bar graph showed the explained percentage variations by each component calculated by Eq. 1 with repeatability and total variance (as number) for each trial. *X* axis is the flight as days after planting (DAP). Left *y* axis was scaled as percentage to show the repeatability values (white diamond) and percent variations by components. Right y axis was scaled as number to show the total variation explained as number (black round). DTA, DTS, and GY are the abbreviations of days to anthesis, silking (days), and plot-based grain yield (t ha^{-1}), respectively. Total variance of DTA, DTS, and GY in number are 5.67, 5.80, and 3.48 for G2FD; 4.22, 3.99, and 2.24 for G2FI; and 4.59, 4.32, and 1.49 for G2LA. G2FI, G2FD, and G2LA trials represent the optimal planting time with irrigation, optimal planting time without irrigation, and delayed planting time with irrigation respectively. Reprinted from Adak, Murray, Anderson, et al., 2021.

It is also likely that plant height at any point in time was impacted by the activity of many genes and interplays between genes in response to changing environmental conditions during various growth periods (Veldboom & Lee, 1996; Messmer et al., 2009; Sibov et al., 2003; Anderson et al., 2020; Dijak et al., 1999; Han et al., 2018). Since UAS allowed temporal variation of plant height to be estimated here, this variation can be used in dissecting underlying genetic mechanisms such as discovering time specific and co-localized genes in association mapping.

Random Forest Algorithm for Determining the Importance Ranks of Flights

Plant heights captured by various flights from the three different trials were used as predictors to predict grain yield using the LM and RF algorithm. The RF model was consistently found to perform better than the LM model in predicting yield in each trial based on Rsquared, RMSE and MAE (Figure 25). Prediction accuracies of the RF model (r_{rf}) were found to be greater than prediction accuracies of LM model (r_{lm}) in each trial (Figure 25), indicating that the RF model works slightly better in predicting grain yield using temporal plant heights. Variable importance scores (*varImp*) were used to determine variable (flight dates) importance (Figure 25). Results of *varImp* scores showed that different flight dates were most important across different trials; earlier flights (e.g. 48 DAP in G2FI and 52 DAP in G2LA) and later flights (e.g. 82 and 101 DAP in G2FD and 78 and 98 DAP in G2LA) had the highest scores (Figure 25). The partial dependence plots are a functional illustration for evaluating the relationship between each explanatory variable (flight dates) and the response variable (yield); the relationships might be linear, parabolic or something even more complex (Friedman, 2001). The partial dependence plot shows the changing predicted yield values based on the plant heights at a particular time point; illustrations of this change are critical to understand the relationships between plant heights at different flight dates and yield. Partial dependence plots of every flight date in each trial were illustrated (Figure 26). For instance, the most important variable (based on *varImp* scores) was found to be 101 DAP in G2FD, 48 DAP in G2FI and 57 DAP in G2LA (Figure 25). Plant height between 2.00 and 2.05 meters at 101 DAP in G2FD, plant height between 0.75 and 0.80 meters at

48 DAP in G2FI and plant height between 1.60 and 1.70 meters at 57 DAP in G2LA were found to be desired plant heights that attached to maize hybrids with higher yield values (Figure 26). There were additional plant height thresholds belonging to each flight times that can be used as selection criteria for higher yielding hybrids, considering the relationships between plant height at particular time points and yield (Figure 26). The majority of plant heights belonging to the flight dates were found to have nearly linear relationships with predicted yield values, except for first three flights in G2FD and first four flights in G2FI (Figure 26). However, it is noteworthy to mention that linear relationships between plant heights of majority flights in G2FI is more obvious than G2FD and G2LA, indicating that stress factors in G2FD and G2LA caused the trend of linear relationships between plant heights and higher grain yield to change. In addition, taller plant height in earlier flight dates (33, 36, 39 and 48 DAP in G2LA) were better indicators of higher yield in G2LA than G2FI and G2FD (Figure 26). Different contributions of plant heights belonging to different growth periods and environments in predicting grain yield suggests that discovering genes controlling the plant height variation at different growth periods will provide supportive genetic information to manipulate yield in maize.

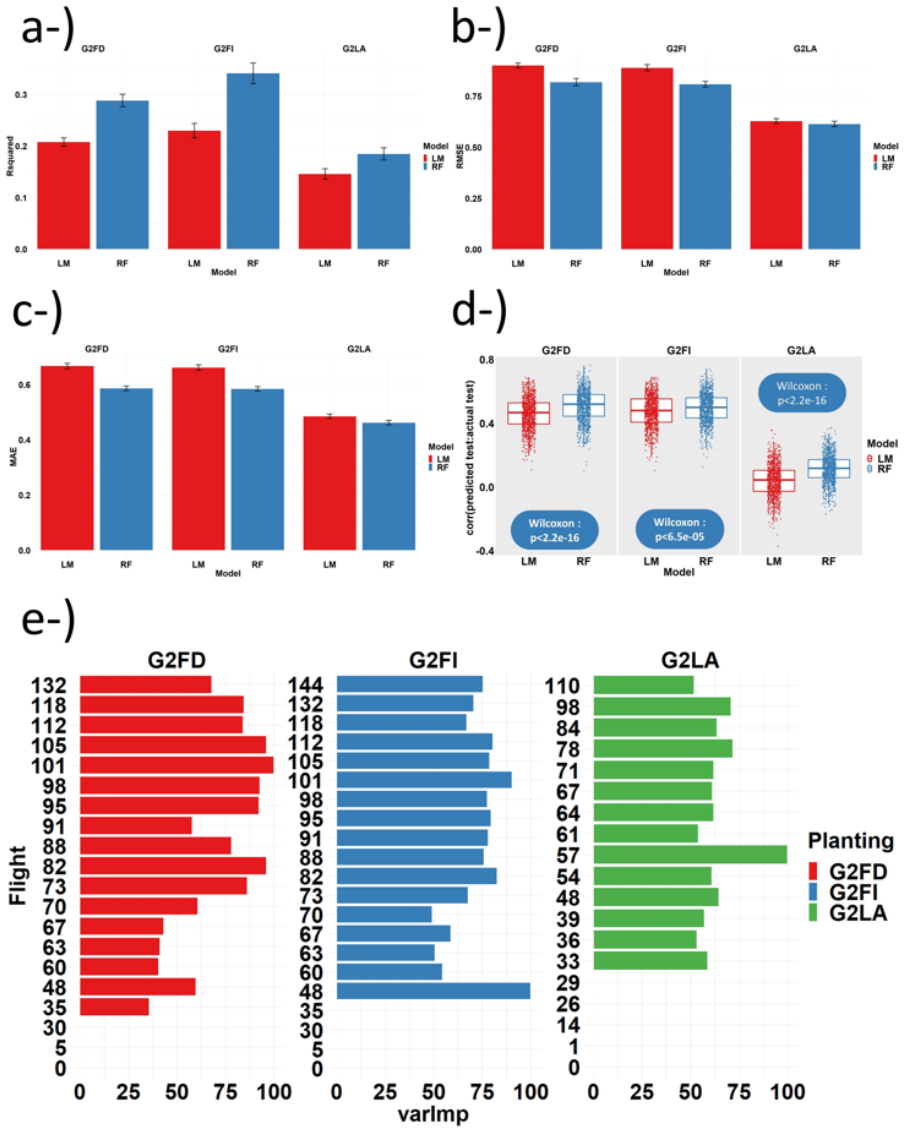

Figure 25 Model evaluations and variable importance scores. (a) The R^2 of linear (LM) and random forest (RF) model, higher is better. (b) Root mean square error (RMSE) of each model in each trial, lower is better. (c) Mean absolute error (MAE) of each model in each trial, lower is better. (d) Correlation results between predicted yield and actual yield of test data obtained by 1,000 bootstrap belonging to each model in each trial. Wilcoxon sign rank test results showed the comparison of correlations belonging to both analysis models in each trial. (e) Variable importance scores (varImp) show the variable importance scores of the predictors (flight dates) where higher varImp score indicates more importance variable in prediction the yield. G2FI, G2FD and G2LA trial represent the optimal planting time with irrigation, optimal planting time without irrigation, and delayed planting time with irrigation, respectively. Reprinted from Adak, Murray, Anderson, et al., 2021.

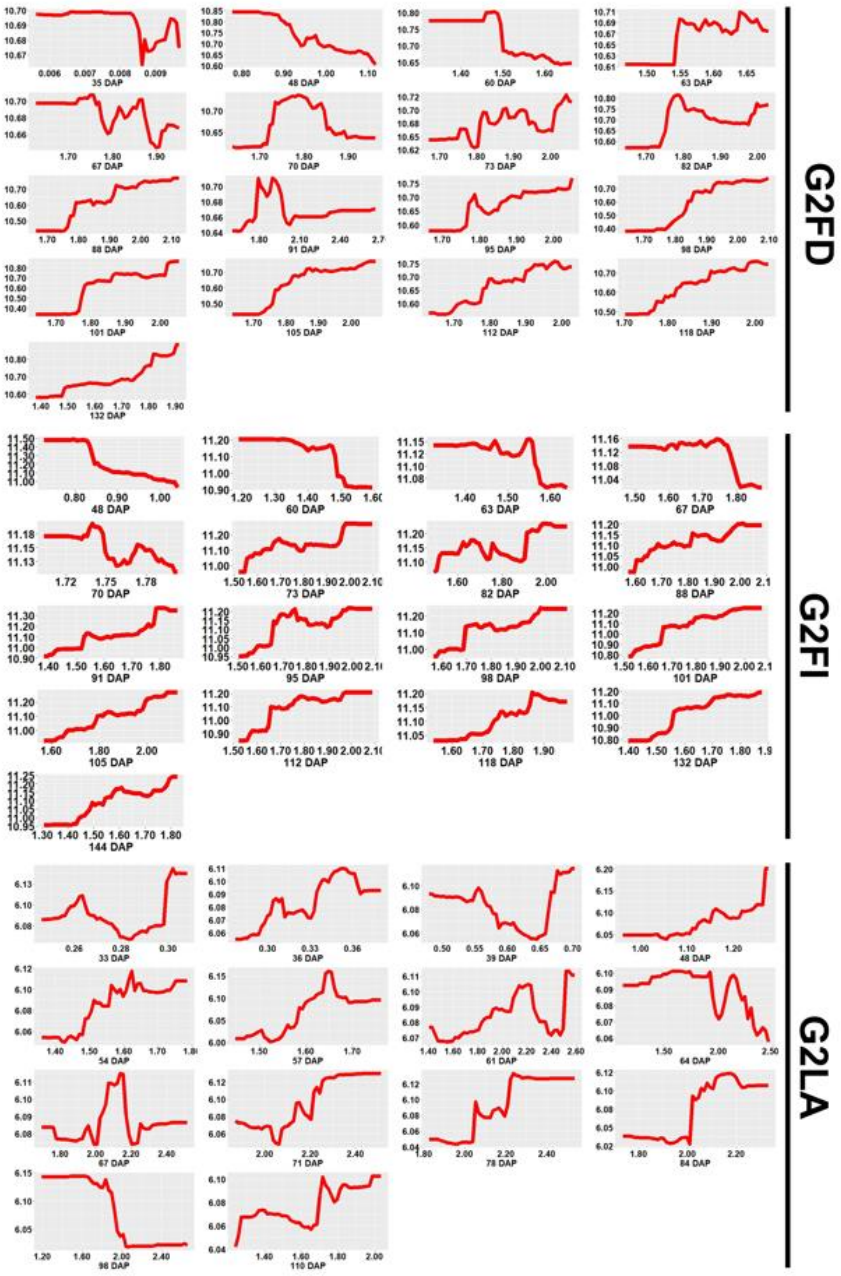

Figure 26 The partial dependence plots for each predictor (flight dates as days after planting; DAP) in each trial. *Y* axis of each plot shows the predicted continuous yield (t ha^{-1}), while *x* axes are the predictor values that are plant heights of each flight dates. Red lines show the relationships between each predictor and predicted yield values. G2FI, G2FD, and G2LA trial represent the optimal planting time with irrigation, optimal planting time without irrigation, and delayed planting time with irrigation, respectively. Reprinted from Adak, Murray, Anderson, et al., 2021.

In general, the slightly convex shape distribution in *varImp* scores of flight dates in G2FD and G2FI trial (Figure 25), showed that 82 to 112 DAP in G2FI, 73 to 88 DAP and 95 to 118 DAP in G2FD contributed to higher grain yield than other flight dates. The same flight dates varied in terms of *varImp* scores in G2FD and G2FI, especially later flight dates were found to have grater *varImp* scores in G2FD than G2FI. This is interesting because G2FI and G2FD trials were planted and flown at the same time, however they were managed differently for optimal and dryland conditions, respectively. This suggests that plant height belonging to different growth periods of these management conditions affected grain yield differently; while this has long been hypothesized (Haghighattalab et al., 2017; Sun et al., 2019) and shown for a few varieties, it has previously been impossible to observe this across large segregating populations in field situations. The late planting, G2LA, further differs from the other two trials but, also being a stress trial (Supplemental Figure S1), is unsurprisingly more similar to the dryland planting, and the late flight dates are more important predictors for grain yield than early flight dates (Figure 25).

SNPs-Flights Associations and Functions of Candidate Genes

Over the three trials, the 99 percentile plant heights over 60 UAS flights, as well as grain yield were genetically mapped using 153,252 SNP markers. Principal component analysis suggested that there were effectively three populations (Supplemental Figure S3). After accounting for population structure across all three trials, a total of 52 SNPs with p-values above the Bonferroni correction were detected

and annotated; seven were discovered to be common in more than one flight date, while 45 of these were flight time-specific (Figure 27, Supplemental Table S1).

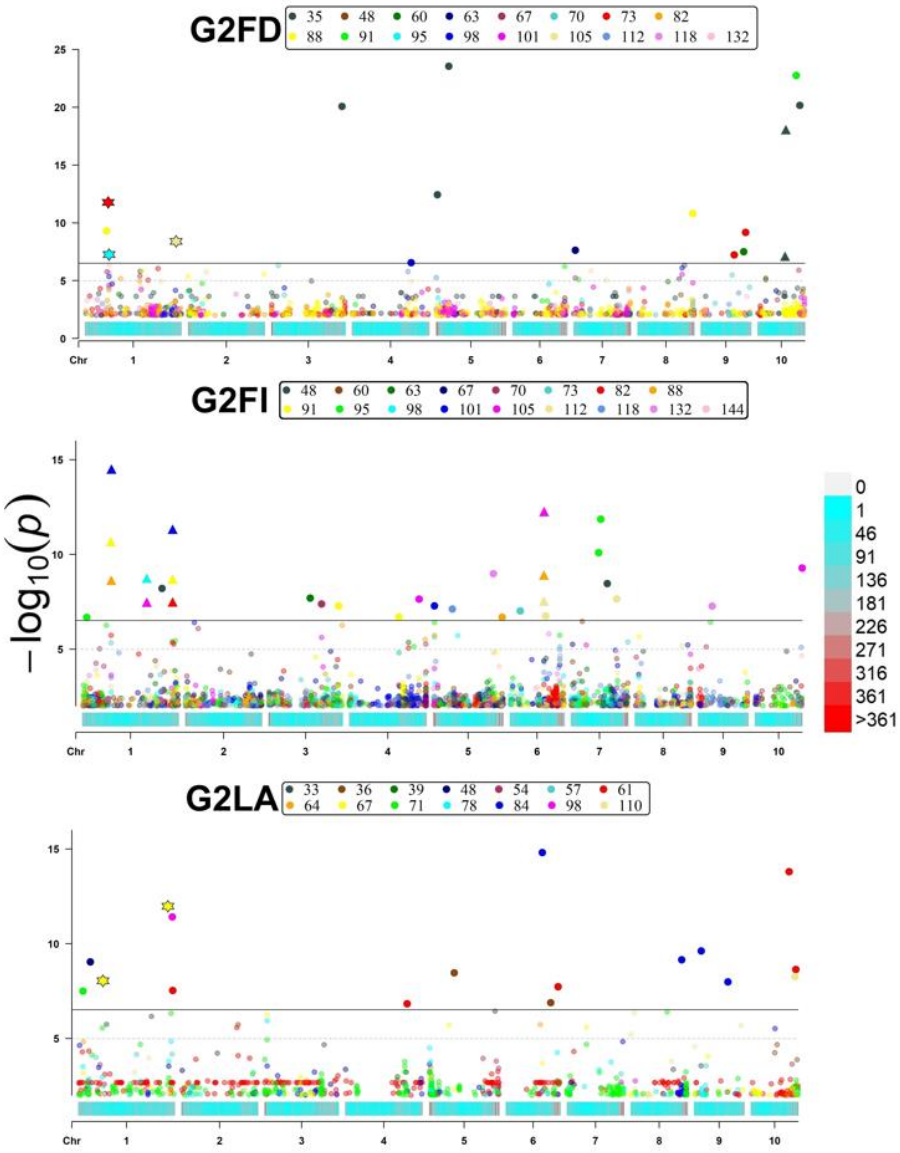

Figure 27 Combined Manhattan plots for plant heights of each flight using best linear unbiased predictions (BLUPs) of the mixed effects spatial model. The heat map at the bottom of each Manhattan plot shows the single nucleotide polymorphism (SNP) density (within 1 Mb window size) through the chromosomes. Scale of this heat map was given on the right side of Manhattan plot. Star shapes were used for colocalized SNPs detected in more than one trial. Triangle shapes were used for colocalized SNPs detected in more than one flight within any trial. Round shapes were used for unique SNPs. Each unique

color within each trial represents the association between SNPs and plant heights of each flight; color charts are given inside the rectangles at the top of each Manhattan plots. G2FI, G2FD, and G2LA trial represent the optimal planting time with irrigation, optimal planting time without irrigation, and delayed planting time with irrigation, respectively. Reprinted from Adak, Murray, Anderson, et al., 2021.

Of the seven SNPs that showed association with the trait in multiple flights and/or trials, three were located on chromosomes 1 and 10 and showed association in two flights, four were located on chromosomes 1 and 6 showed association across three flights (Supplemental Table S1). Additionally, two SNPs on chromosomes 1 showed association in two trials (Supplemental Table S1). Of the SNPs that showed association in two trials, none showed association in the same flight in different trials (Supplemental Table S1). In other words, the same SNPs were discovered in an earlier flight of the delayed planting trial (67 DAP in G2LA) but later flights in optimal planting (73 and 95 DAP in G2FD) (Supplemental Table S1); these were not the same calendar date flights. Discovering the common SNPs for plant heights belonging to different flights in more than one trial suggested that the same genetic cause of phenotypic variation in plant height can occur in different times under different management conditions such as delayed and optimal planting (Supplemental Table S1). This results in the discovery of the same loci at different time points of growth belonging to different management conditions.

The ranges in linkage disequilibrium (LD) observed in the regions surrounding the seven co-localized SNPs cannot exclude linked SNPs as causal (Figure 28). In chromosome 1, SNPs (76,153,074bp and 76,153,056bp) were found to be significant in flights of 73 and 95 DAP in G2FD and 67 DAP in G2LA, both high stress trials. While

these two SNPs discovered in G2FD 73 and 95 DAP flights with the highest LOD scores (>6.55), these SNPs were also nearly significant later in 98, 112, 118 and 132 DAP flights (LOD scores >5) in G2FD. LD regions surrounding these two SNPs extends to 131 kbp (Chr1:76.08 to 76.21) (Figure 27) and contains four candidate genes in the LD interval. One of the candidate genes in LD interval is GRMZM2G005630, located 26 kbp away from these SNPs. GRMZM2G005630 encodes the EID1-like F-box protein 2 that regulates ABA-dependent signaling that manages seed germination, root growth and transition to flowering time as well as the accumulation of anthocyanin under drought conditions in *Arabidopsis* (Koops et al., 2011). F box genes are one of the most diverse and largest gene families in higher plants; maize has around 359 F-box genes (Zhang et al., 2019, Jia et al., 2013). The F-box protein family regulates plant growth and development as well as biotic and abiotic stresses in maize (Jia et al., 2013).

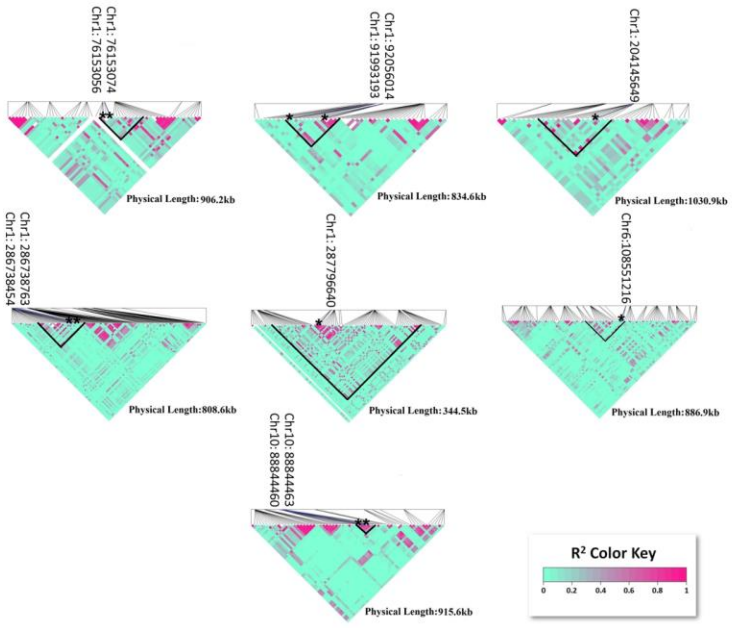

Figure 28 Linkage disequilibrium (LD) blocks of seven colocalized single nucleotide polymorphisms (SNPs) located in chromosomes 1, 6, and 10 associated with plant

height. Black lines indicated the pairwise LD regions of the SNPs with 0.8 or higher R^2 within the physical lengths. Black stars showed the locations (base pair; bp) of the above SNPs. Reprinted from Adak, Murray, Anderson, et al., 2021. Reprinted from Adak, Murray, Anderson, et al., 2021.

Two additional SNPs associations were found close to each other on Chromosome 1 (91,993,193bp and 92,056,014bp) and were significant at 88, 91 and 101 DAP in G2FI trials. The LD region is ~66 kbp (Chr:91.99 to 92.06) (Figure 28) and contains three candidate genes. One of the candidate genes in LD is GRMZM5G806839 that controls the AP2 transcription factor (also known as ereb44) in maize. GRMZM5G806839 mediates response to multiple abiotic and biotic stresses (Kizis, Lumbreras & Pagès, 2001) such as southern corn leaf blight response (*Bipolaris maydis*) in maize (Bian, Yang, Balint-Kurti, Wisser & Holland, 2014).

Another SNP association on chromosome 1 (204145649bp) was found at 98 and 105 DAP in G2FI. The surrounding LD region of this SNP is ~170 kbp (Chr1:203.98 to 204.15) and contains seven candidate genes in the interval, of which none have been previously identified. One of the candidate genes, GRMZM2G016210, contains this SNP in its genic region and includes the umc1122 simple sequence repeat (SSR) marker. The flanking region between umc1035 and umc1122 markers was previously found to control plant height at different growth stages with different effect sizes in maize (Yan et al., 2003). *Qph1*, which is a rare SNP in *Bractic2* gene, is one of the well-known QTL controlling plant height that has also been mapped near umc1122 (Xing et al., 2015). This QTL is congruent with the idea of a major QTL often described based on studies largely conducted in optimal environmental conditions of the Midwestern U.S. and Europe would only be detected in Texas under the most favorably managed trial.

Two Chromosome 1 SNP associations (286,738,454bp and 286,738,763bp) were found at 82, 91 and 101 DAP in G2FI. LD block around the SNPs is ~ 66 kbp (Chr1:286.73-286.79) (Figure 28) and it contains three candidate genes. GRMZM2G028286 is one of the candidate genes in the LD region and it is reported to control the cellulose biosynthesis pathway (Kianifariz, 2017). In a previous study, GRMZM2G028286 was found to be downregulated when the *NUT1* mutant gene is active; the *NUT1* mutant gene causes an erratic tassel phenotype (e.g. tassel browning and sterility) especially under drought stress because of a defect in water transport (Dong et al., 2020), as well as reduced plant height in maize (Dong et al., 2020). Another candidate gene in this LD region is GRMZM2G028151 (ereb184 - AP2-EREBP-transcription factor) that is an AP2-like ethylene responsive transcription factor and it was reported to be upregulated under heat stress (Casaretto et al., 2016).

The Chromosome 1 SNP association (287,796,640bp) was found at 67 and 105 DAP in G2LA and G2FD trials. LD region surrounding this SNP is ~253kbp (Chr1:287.66 to 287.92) and contains eleven candidate genes. One of the candidate genes within the LD interval is GRMZM2G122139, and this SNP is also found in its genic region. This candidate gene encodes Cytosolic purine 5-nucleotidase. This enzyme was purified from maize microsomes (Carter & Tipton, 1985) and wheat seedling leaves and potato (Polya, 1974, 1975) suggesting a relationship with a cyclic nucleotide regulatory system in higher plants. Another candidate gene, GRMZM2G072806, encodes the ubiquinone oxidoreductase enzyme; its activity plays a role on NAD(H)

biosynthesis by transporting a hydride ion (H-). This gene could disrupt regular enzymatic activities causing oxidative stress (Moller, 2001).

A SNP association on chromosome 6 (108,551,216bp) was found at 88, 105 and 112 DAP in the G2FI trial. The LD region around this SNP is ~ 180 kbp (Chr6:108.40 to 108.58) (Figure 28) and contains nine genes. One candidate gene in this interval is Zm00001d036994. This candidate gene has been reported to encode trichome birefringence-like (TBL) proteins that were localized in Golgi and transfers the acetyl groups to xylan resulting in the elongation of the xylan (Xiong, Cheng & Pauly, 2013). Two TBL related recessive mutants in rice were found to reduce the xylan monoacetylation in cell wall and cause the reduced plant height and susceptibility to leaf blight (Gao et al., 2017).

Chromosome 10 SNP associations (88,841,430 and 88,845,809) were found at 35 DAP in the G2FD trial. The LD region around these SNPs is ~6 kbp (Chr10: 88.84 to 88.85) (Figure 28) and contains two candidate genes. One of the candidate genes in this interval, GRMZM2G089484 (MAP kinase), was reported to be a possible candidate associated with northern corn leaf blight (NCLB) resistance caused by *Exserohilum turcicum* (Ding et al., 2015). Another candidate gene, GRMZM2G422090 (GTP-binding protein), is related to the control of cell elongation due to stimulation of the auxin hormone (Terryn, van Montagu & Inzé, 1993).

Five SNPs that are in the genic region of GRMZM2G010356, GRMZM2G455869, GRMZM2G051050, GRMZM2G058522 and GRMZM2G028014 were discovered for grain yield in G2FD and in G2FI (Figure 29). GRMZM2G010356, also known as tps17,

involves the terpene synthase biosynthesis that contributes the defense mechanisms against parasitoids and pathogens in maize (Block, Vaughan, Schmelz & Christensen, 2019; Liang et al., 2018). GRMZM2G455869, also known as MYB37, regulates the elongation of bundle sheath cells in maize (Chang et al., 2012). GRMZM2G051050, also known as Ypt/Rab domain of the gyp1p superfamily protein, was found to be related with yield under high infestation of Mediterranean corn borer (*Sesamia nonagrioides* Lefebvere) in maize (Jiménez-Galindo, Malvar, Butrón, Caicedo & Ordás, 2018). GRMZM2G058522, also known as superoxide dismutase, creates an initial defense response against reactive oxygen species (ROS) that stemmed from exposure of numerous environmental stresses such as drought, intense UV lights, air pollutants and chilling temperatures (Alscher, Erturk & Heath, 2002). GRMZM2G028014 is one of member in F-box protein family in maize that is responsible for regulation of protein degradation, signal perception and transduction pathways inside and often outside of cells regions in maize (Jia, Wu, Li, Huang & Zheng, 2013)

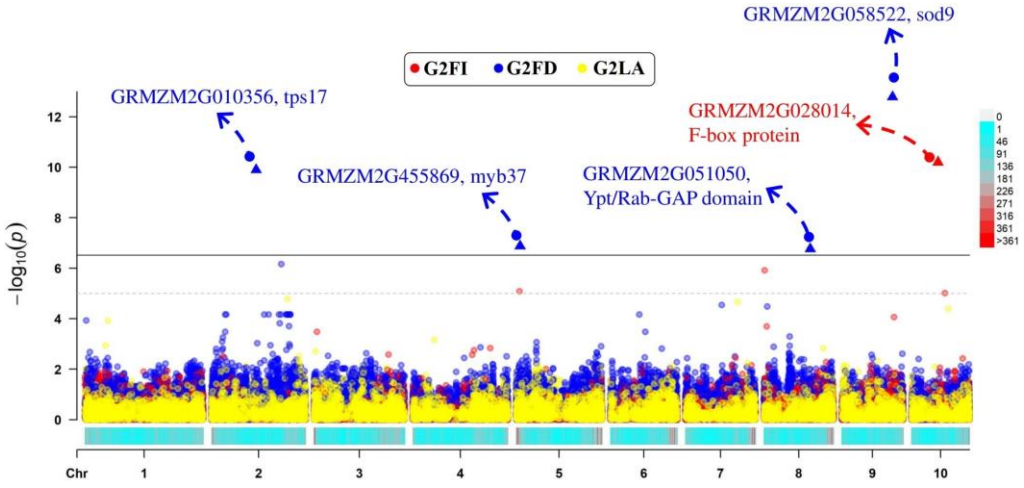

Figure 29 Single nucleotide polymorphisms (SNPs) associated with hybrid grain yield (t ha^{-1}) for G2FI, G2FD, and G2LA trials. G2FI, G2FD, and G2LA trial represent the

optimal planting time with irrigation, optimal planting time without irrigation (dryland), and delayed planting time with irrigation respectively. The heat map at the bottom of the Manhattan plot shows the SNP density (within 1 Mb window size) through the chromosomes. Scale of this heat map was given on the right side of Manhattan plot. Reprinted from Adak, Murray, Anderson, et al., 2021.

Contributions of UAS to Association Studies

High throughput phenotyping by UAS captured phenotypic variation arising from the response of diverse hybrids to various abiotic stresses across plant development stages. When this variation was combined with genomic information in an association mapping study, SNPs were detected and linked candidate genes were identified for plant heights of different flights and grain yield involved in coping with many environmental stress factors (Figure 27, Figure 29, Supplemental Table S1). The resulting candidate gene annotations for these SNPs showed that segregating loci controlling numerous biological functions orchestrate differences between hybrids temporally throughout plant development, yet there were substantial differences under the two abiotic stresses. Some of these loci conditioned variation across multiple time periods, while others appeared at a specific time point and under specific growing conditions. Plant height is a result of many environmental stress factors during the development periods, causing temporal modifications in plant height depending on different growth stages. The temporal variations in plant height can therefore be evaluated as a phenotypic consequence of the response of maize hybrids to environmental stresses during growth. When temporal phenotypic data collected by UAS are combined with genomic (e.g. GBS) data, phenotypic plasticity of plant height occurred within growth stages and underlying genes can be scrutinized with higher accuracy and resolution.

Cumulative SNP Effects

Genomic prediction and selection approaches rely on contributions of genome-wide genetic markers. However, the phenotypes used in these studies typically have been low-dimensional and low-throughput; obtained from limited time intervals (one or a few times) or small sample sizes. Therefore, different contributions of each locus at different time points for the same phenotype of interest will remain unobserved, with the exception of those effects that make substantial enough contribution to be detected during the terminal measurements. As we were able to only obtain genotypes of 158 hybrids of the over 270 hybrids studies, this limited these studies potential detection ability. In this study, cumulative SNP marker effects of each chromosome were found to differ depending on the flight date (Figure 30). However, like repeatability (Figure 24) the cumulative marker effects likely varied over time due to both unexplained error and different sources of phenotypic variation at different flights. For instance, there is a peak in cumulative marker effects at 64 DAP in the G2LA trial (Figure 30). 64 DAP also had the highest repeatability value in G2LA trial (Figure 24). This is a particular example where repeatability and total cumulative marker effects were highest in G2LA trial which may help explain that variation by pedigree at 64 DAP in G2LA trial has stemmed mostly from marker effects contributed by many regions across the genome (Figure 30). Furthermore, the different results we observed between the three management conditions demonstrated that genetic by environment (G by E) interplay, illustrated here by the interaction of hybrids and trials, had a cryptic influence on phenotypic variation (Gage et al., 2017). Plasticity is occurring even within an environment temporally as

demonstrated by fluctuating marker effects, repeatability values and explained variation by pedigree. The flights revealed this temporal within environmental variation, which was combined with G-by-E to better scrutinize phenotypic plasticity. This study was only carried out within one year, but additional years would likely further increase the amount of G-by-E effects found.

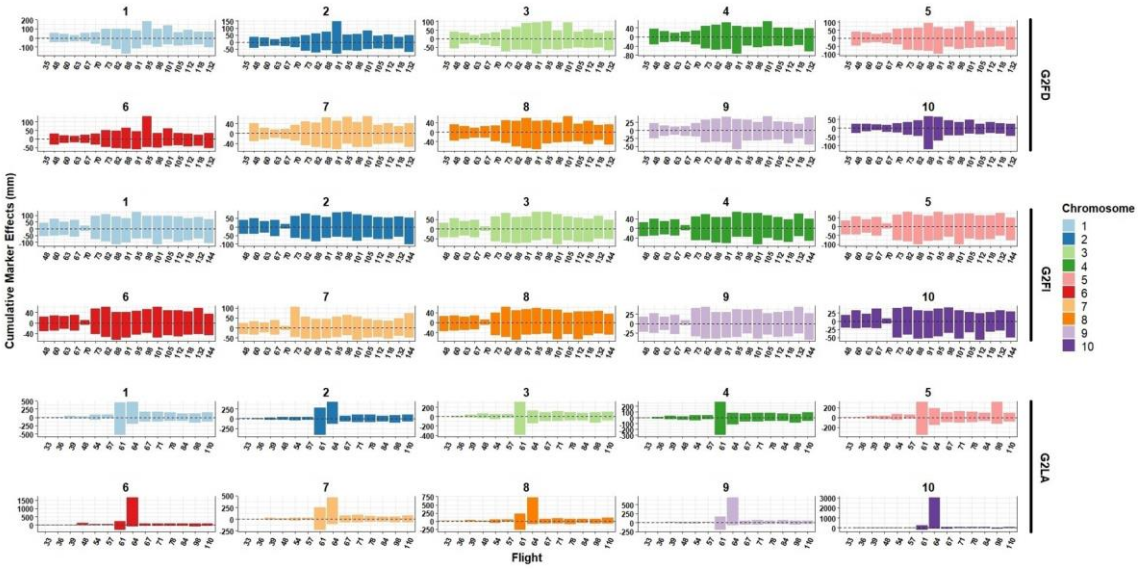

Figure 30 Temporal cumulative marker effects of each chromosome (negative and positive) for each flight of each trial. The cumulative effects of whole-genome-wide markers (*y* axis, mm) were dependent upon the flights (*x* axis, DAP). G2FI, G2FD, and G2LA trial represent the optimal planting time with irrigation, optimal planting time without irrigation, and delayed planting time with irrigation, respectively. Reprinted from Adak, Murray, Anderson, et al., 2021.

Temporal Genomic Predictions

Genomic prediction accuracies (r_{gpa}) for plant heights belonging to each flight in each trial were illustrated in figure 31. r_{gpa} for days to anthesis (DTA), silking (DTS) and grain yield (GY) were also calculated for each trial (Figure 31).

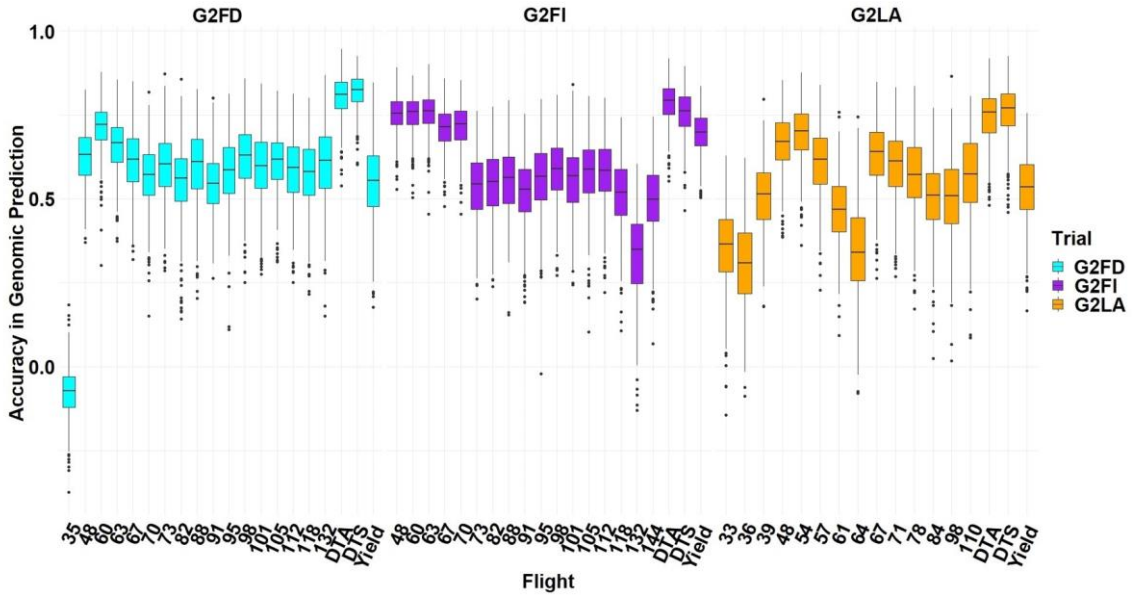

Figure 31 Genomic prediction accuracies (r_{gpa}) (*y* axes) for flights (*x* axis as days after planting [DAP]) as well as for days to anthesis (DTA), days to silking (DTS), and yield in three trials. G2FI, G2FD, and G2LA trial represent the optimal planting time with irrigation, optimal planting time without irrigation, and delayed planting time with irrigation respectively. Reprinted from Adak, Murray, Anderson, et al., 2021.

Our findings showed r_{gpa} for plant heights captured by flights fluctuated within G2FD (-0.06~0.73), G2FI (0.33~0.76) and G2LA (0.26~0.78) trials (Figure 30). r_{gpa} for 40 to 60 DAP flights (pre-flowering) were surprisingly higher than in later flights for each trial (Figure 31). Dynamic patterns of r_{gpa} tended to decrease towards later flights, especially in the G2FI optimal trial. In other words, flights before initiation of flowering times had higher r_{gpa} as opposed to later flights in each trial (Figure 31). In the findings of this study, the time-dependent alteration of genomic prediction results (Figure 31) and the genome wide marker effects (Figure 30) revealed that the same markers (loci) may have diverse effects on plant height depending on different growth periods in maize.

In conclusion, the estimations of breeding values for genetic materials using HTP combined in association with high throughput genotyping data (eg. GBS) has only begun

to be explored. This study was among the first evaluating a high number of hybrid maize plots with UAS in a genome wide association study to discover loci (and where LD permitted, candidate genes) and the prediction ability for the phenotype of interest. Within the scope of this study, early growth stages were found to have undiscovered phenotypic variation controlled by unique loci not found at later stages; this is important to increase our understanding of complex traits in crops. Major conclusions of this study were that (i) earlier plant height data had more importance for grain yield under optimal planting and irrigation, whereas later plant height data had more importance in terms of yield under stressed conditions; (ii) genomic prediction accuracies (r_{gpa}) varied for plant heights belonging to different growth stages; and (iii) a large number of plant height data captured by UAS can be used as predictors to predict yielding hybrids via random forest algorithm.

CHAPTER IV

TEMPORAL VEGETATION INDICES AND PLANT HEIGHT FROM REMOTELY SENSED IMAGERY CAN PREDICT GRAIN YIELD AND FLOWERING TIME BREEDING VALUE IN MAIZE VIA MACHINE LEARNING REGRESSION[3]

Estimating breeding values for genotypes (pedigrees) before harvest would be useful for speeding the breeding cycle while reducing combine measurement resources. Early season breeding values can be enabled by implementing temporal field-based high throughput phenotyping (HTP) (Krause et al., 2020a). Unoccupied aerial systems (UAS; i.e., drones with sensor payloads) can objectively capture the temporal variation of complex traits in crops with limited resources; providing a new tool to dissect complex traits in a time-series manner. UAS provides higher quality raw images with better resolutions than traditional remote sensing platforms such as Landsat-derived images (Shi et al., 2016). UAS raw images are processed (e.g., orthomosaic and point cloud densification) to generate geographically corrected mosaics over each time point throughout the growing period (Shi et al., 2016). To increase precision of data extracted from the processed images, novel plot-based data extraction pipelines have been developed for breeding nurseries (Anderson & II, 2020; Matias, Caraza-Harter, &

Adak, A., Murray, S. C., Božinović, S., Lindsey, R., Nakasagga, S., Chatterjee, S., ... & Wilde, S. (2021). Temporal vegetation indices and plant height from remotely sensed imagery can predict grain yield and flowering time breeding value in maize via machine learning regression. Remote Sensing, 13(11), 21-41. https://doi.org/10.3390/rs13112141

Endelman, 2020). When successfully performed, multiple plot-based temporal phenotypes can be generated that include various vegetation indices (VIs) (Bendig et al., 2015; Gitelson, Kaufman, Stark, & Rundquist, 2002; Hague, Tillett, & Wheeler, 2006; Hamuda, Glavin, & Jones, 2016; Hunt, Cavigelli, Daughtry, Mcmurtrey, & Walthall, 2005; Louhaichi, Borman, & Johnson, 2001; G. E. Meyer & Neto, 2008; Tucker, 1979; Woebbecke, Meyer, Von Bargen, & Mortensen, 1995) as well as canopy height measurements (CHMs) (Adak, Conrad, et al., 2021; Anderson et al., 2020; Anderson et al., 2019; Pugh et al., 2018; Tirado, Hirsch, & Springer, 2020). Temporal VIs and CHMs have been used for downstream analysis in prediction models (Adak, Conrad, et al., 2021; Aguate et al., 2017b; Anderson et al., 2020; Anderson et al., 2019; García-Martínez et al., 2020; Maresma, Ariza, Martínez, Lloveras, & Martínez-Casasnovas, 2016; Montesinos-López et al., 2017; Y. Peng & Gitelson, 2011; Shanahan et al., 2001; G. Wu, Miller, De Leon, Kaeppler, & Spalding, 2019b) demonstrating improvement in prediction modeling when utilizing UAS image-based phenotypes over conventional manual measurements. Temporal HTP platforms are enabling researchers to improve the understanding of environmental and growth stage specific interactions.

Genotype-by-environment (GxE) interaction is a special case in plant breeding used to dissect the phenotypic plasticity and reaction norm of complex traits occurring among discriminate environments (Gage et al., 2017; Xin Li et al., 2018; Rogers et al., 2021). GxE describes how differences in measured appearances between different genotypes are a result of interactions of each with their environments creating plasticity, which is nearly impossible to predict. However, the examination of temporal phenotypic

plasticity (TPP) for complex traits occurring beyond a single growth stage is typically unfeasible due to labor, time, and resource demands. Dissecting the TPP of complex traits at differential growth stages has lagged behind commonly collected terminal phenotypes (e.g., grain yield) resulting in understanding GxE interactions based on the accumulation of the entire growth season. As a result, it is difficult to determine if specific time points caused the significant GxE variation at the end of the season. HTP platforms, such as UAS, enable repeated phenotypic data collection, allowing evaluation of phenotypes at various time points throughout plant lifecycles with large numbers of genotypes at low cost (Araus & Cairns, 2014). Recently, UAS have demonstrated that quantitative trait loci (QTL) have varying effect sizes for the same trait (e.g., CHM) at different time points throughout growth periods of maize (Adak, Conrad, et al., 2021; Adak, Murray, Anderson, et al., 2021; Anderson et al., 2020). Similarly, both unique and common loci belonging to different time points have been discovered to have associations with vegetative indices and canopy height measurements in maize throughout growth (Adak, Conrad, et al., 2021; Adak, Murray, & Anderson, 2021). The uniqueness of temporal QTL has also been shown in cotton (Pauli, Andrade-Sanchez, et al., 2016), wheat (Singh et al., 2019), and sorghum (Miao et al., 2020). These findings underline new opportunities in dissecting complex traits using remotely sensed phenotypes belonging to multiple time points instead of one or a few terminal time points, as has been done traditionally.

Multicollinearity Challenges in Temporal Predictions

Multiple time point-derived temporal phenotypes have previously improved yield prediction accuracies beyond single time point-derived phenotypes, but come with new challenges (Adak, Murray, Anderson, et al., 2021; Aguate et al., 2017a; Anderson et al., 2019). For instance, when using phenotypic data from many VIs derived across time points as predictors, multicollinearity problems are often revealed in multiple linear regression analysis. Multicollinearity leads to the variance inflation factors (VIFs) among predictors that causes inflation of the variation of the estimated regression coefficients in the prediction model (James, Witten, Hastie, & Tibshirani, 2013). When multiple time point derived temporal phenotypes are used as predictors, the coefficients of the predictors need to be penalized to increase the prediction accuracy. The reasoning being: (i) the predictors included in a model may have relatively similar and large effects on the predicted variable, (ii) a small number of predictors may have significant and large effects on the predicted variables while others have smaller effects, or (iii) any conditions involving these two possibilities. The three conditions above are underlying phenomena that need to be controlled to accomplish better prediction accuracy in the prediction of complex quantitative terminal traits such as yield and flowering times. This study aimed to (i) predict the temporal breeding values of maize hybrids using fifteen VIs and CHMs derived from twelve UAS flights over the two trials; (ii) compare performances of linear regression and machine learning based regressions (ridge, lasso, and elastic net) in predicting grain yield and flowering times (days to anthesis; DTA and days to silking; DTS) from temporal breeding values of fifteen VIs and CHMs; and (iii) calculate the temporal variable importance scores of the predictors in the best

performing (i.e., least error with highest prediction accuracy) machine learning regression for yield and flowering times. Understanding these aims will help to better understand how to maximize and improve the results of phenomics-assisted breeding through remote sensing and identify new fundamentally important biological processes for further investigation in plant breeding and quantitative genetic researches.

Materials and Method

Experimental Conditions

The two trials, containing same 100 advanced maize breeding hybrids, were planted in College Station, Texas (30°32′46.3″ N 96°26′00.2″ W) on 21 March 2019 (OHOT trial; irrigated) and 12 April 2019 (DHOT trial; delayed planting) respectively. Each population was planted in a separate randomized completed block design with two replications. Experimental plots consisted of two-row adjacent plantings of the same genotype (0.76 m row spacing, 7 m plot length). Each randomized complete block trial consisted of 13 ranges (from front to back of field, perpendicular to the tractor rows), where each range contained 16 hybrids across tractor rows represented by two-row plots, 32 single rows in total. The last range in each trial had eight two-row plots of commercial check fill to form a rectangle, and commercial checks were planted around the trial as a border.

Field-Based High Throughput Phenotyping

A DJI Phantom 4 Pro V2.0 (DJI, Shenzhen, China) was flown 25 m above the ground to capturing RGB images at 72 DPI resolution from the standard integrated camera. The raw images were taken using 5472 × 3648 pixels with 90 percent forward

and sideward overlap. These images were processed using Agisoft Metashape V15.2 software (Agisoft LLC, Russia) to generate an orthomosaic and point cloud for each flight date (Figure 32). Ground control points (GCPs) were used to aid in data processing during the flights and mitigate aberrations in the resulting georeferenced mosaics. In total, 45 GCPs were used during the flights. A total of 25 UAS surveys were conducted throughout the growing season. Following qualitative QC/QA (Quality Control/Quality Assurance) of the orthomosaics and point clouds, twelve flights were identified to be free of artifacts and blunders (Table 4).

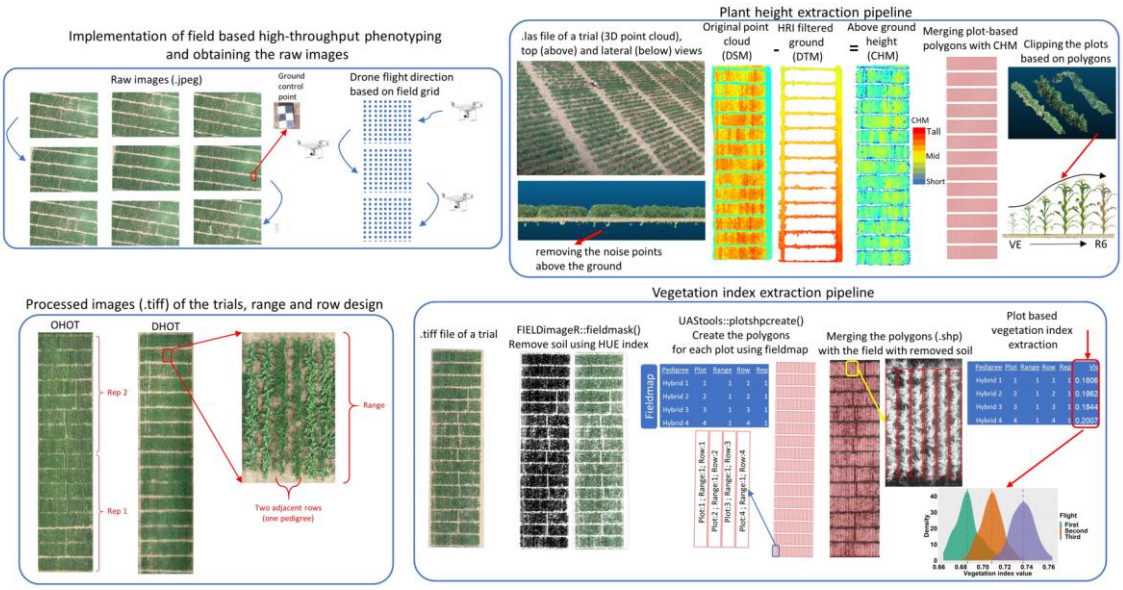

Figure 32 Shows the steps of high-throughput phenotyping pipeline including data collection, processing, and extraction from the RGB images. Reprinted from Adak, Murray, Božinović, et al., 2021.

Table 4. Summary table of UAS flights dates and corresponding days after planting (DAP) times for each trial. The optimal planting date trial (OHOT) and delayed planting date trial (DHOT) were sown on March 21st, 2019 and April 12nd, 2019, respectively. Reprinted from Adak, Murray, Božinović, et al., 2021.

Flight time (month)	April	May	June	July

Flight time (day)	20th	22nd	29th	6th	10th	23rd	4th	17th	25th	11th	16th	26th
Days after planting (DHOT trial)	8	10	17	24	28	41	53	66	74	90	95	105
Days after planting (OHOT trial)	30	32	39	46	50	63	75	88	96	112	117	127

The UAS was flown in moderate weather at midday during periods of clear skies and no wind, whenever possible. Consistent time periods were attempted between flights but to obtain more data not all flights could be made in ideal conditions. As the season progressed, issues due to windy conditions became more prevalent in the processing stream with plants swaying further when affected by the wind. Cloud coverage was addressed by a brightness correction measurement from an onboard solar radiance detector or by using images of calibrated reflectance targets in situ prior to and after flights. Large overlaps of images reduced water reflections. Importantly, because varieties were primarily being compared within flights, errors from many of these potential sources of variation are nested within each flight and rendered irrelevant compared to if comparisons are made between flights.

Extracting Temporal Traits from RGB Images and 3D Point Clouds

Fifteen VIs and temporal plant heights were extracted from the orthomosaic images (.tif file extensions) and three-dimensional (3D) point clouds (.las or .laz file extensions), respectively. First, ESRI (Environmental Systems Research Institute, Inc.) shape files (.shp file extensions) were created using R/UAStools::plotshpcreate function (Anderson & II, 2020; James et al., 2013) in R to create the polygons for each consecutive row plot (nrowplot = 2, multirowind = T) for each population based on their

respective field maps/experimental layouts. The buffer arguments were set to “rowbuf = 0.61” and “rangebuf = 3.1” to reduce adjacent plot overlap and uninformative data within the walking alleys data extractions. Two fit ESRI shape files were generated separately to extract plot information from each one of the consecutive two row plots in the images and point clouds. These shape files were then used in extracting VIs and plant heights for each time point (Figure 32).

To extract the plot-based VIs the FIELDImageR package (Matias et al., 2020) was used. Before extraction of VIs, the R/FIELDImageR::fieldMask function was implemented to remove the soil color from the RGB (Red-Green-Blue, also known as true color)images using HUE index corresponding to soil color (Escadafal, 1993). The fifteen VIs were extracted from RGB images using the R/FIELDImageR::fieldIndex function for each flight date. The VIs included: the blue green pigment index (BGI) (Zarco-Tejada et al., 2005), brightness index (BI) (Richardson & Wiegand, 1977), blue index, excessive green (EXG) (Woebbecke et al., 1995), excess green minus excess red index (EXGR) (G. E. Meyer & Neto, 2008), green leaf index (GLI) (Louhaichi et al., 2001), green index, modified green red VI (MGVRI) (Bendig et al., 2015), normalized difference index (NDI) (Hamuda et al., 2016), normalized green-blue difference index (NGBDI) (Hunt et al., 2005), normalized green red difference index (NGRDI) (Tucker, 1979), red index, red green blue VI (RGBVI) (Bendig et al., 2015), visible atmospherically resistant index (VARI) (Gitelson et al., 2002) and vegetativen (VEG) (Hague et al., 2006) (Table 5). BI, GLI, NGRDI, VARI and BGI are prebuilt VIs that

were used in the FIELDimageR package, but remaining VIs were added externally as an additional function into FIELDimageR using 'R/RIELDImageR::myIndex' function.

Table 5. Ratios of vegetation indices used in this study. Reprinted from Adak, Murray, Božinović, et al., 2021.

Vegetation index	Formula	References
Blue green pigment index (BGI)	$\frac{B}{G}$	(Zarco-Tejada et al., 2005)
Brightness index (BI)	$sqrt(\frac{R^2 + G^2 + B^2}{3})$	(Richardson & Wiegand, 1977)
Excessive green (EXG)	$(2 * G) - R - B$	(Woebbecke et al., 1995)
Excess green minus excess red index (EXGR)	$(3 * G) - (2.4 * R) - B$	(G. E. Meyer & Neto, 2008)
Green leaf index (GLI)	$\frac{2 * G - R - B}{2 * G + R + B}$	(Louhaichi et al., 2001)
Modified green red index (MGVRI)	$\frac{G^2 - R^2}{G^2 + R^2}$	(Bendig et al., 2015)
Normalized difference index (NDI)	$128 * (\left(\frac{G - R}{G + R}\right) + 1)$	(Hamuda et al., 2016)
Normalized green-blue difference index (NGBDI)	$\frac{G - B}{G + B}$	(Hunt et al., 2005)
Normalized green red difference index (NGRDI)	$\frac{G - R}{G + R}$	(Tucker, 1979)
Red green blue index (RGBVI)	$\frac{G^2 - R * B}{G^2 + R * B}$	(Bendig et al., 2015)
Visible atmospherically resistant index (VARI)	$\frac{G - R}{G + R - B}$	(Gitelson et al., 2002)
Vegetativen (VEG)	$\frac{G}{R^{0.667} * B^{0.334}}$	(Hague et al., 2006)

3D point clouds were used to extract the plot-based plant heights of each flight based on the pipeline described in (Anderson et al., 2019). First, areas of the two trials (OHOT and DHOT) were clipped, and extreme points above or below the bare ground were

removed from the point clouds in CloudCompare (version 2.12 alpha) (Girardeau-Montaut, 2016). After initial anomaly removal, executable functions of batch scripts of FUSION/LDV (McGaughey, 2016) and LAStools (Isenburg, 2015; Rapidlasso, 2017) software were transported into R to construct the plant height extraction pipeline for each flight. A brief outline of the pipeline contains (i) the sorting the points of clipped point cloud data (LAStools\lasssort.exe), (ii) removing the erratic points around the canopy structure of plants in row plots (LAStools\lasnoise.exe) to construct the digital surface model (DSM), (iii) identifying the ground points using a hierarchical robust interpolation (HRI) (Kraus & Pfeifer, 1998) ground filtering algorithm (HRI) (Kraus & Pfeifer, 1998) (FUSION\GroundFilter.exe), (iv) identifying the maximum points from the ground filter to outline digital terrain model (DTM) (LAStools\lasthin.exe), and (v) constructing the DTM model using the maximum points from the previous step (FUSION\GridSurfaceCreate.exe). Next, the DTM model was extracted from the previously constructed noise-filtered point cloud data (DSM model as an output of step ii) to canopy surface models (CSM). Each row of plots in CSM then were clipped (FUSION/PolyClipData.exe), and plot-based plant heights were estimated using the 99th percentile metrics (FUSION/CloudMetrics.exe) (Figure 32).

Plot-based yield was collected using a plot combine. Flowering time was recorded as the point in which 50% of the individuals within a plot were shedding pollen (DTA) or silks emerging (DTS). Days to anthesis/silk were calculated by subtracting the planting date from the recorded flowering date of the respective trait. All temporal

phenotypic data as well as R codes are publicly available (see the Data Availability Statement and Supplementary Materials sections).

Statistical Analysis for High Throughput Phenotyping Data

Statistical analysis of extracted temporal data (VIs and CHM) and visualizations were processed in R studio (version 1.3.959). In the analysis of high-throughput phenotyping data, a nested statistical design was fit. To predict the breeding values for each pedigree in both trials the row, range, (block) and replicates model terms were used to control for spatial variation. This tends to perform as well as other methods of spatial correction for furrow irrigated trials in our environment due to the patterns created by irrigation and tractor-applied fertilizer and cultivation in otherwise fairly uniform soils. A nested design was used to estimate the temporal breeding values in a time-series manner for fifteen VIs and CHMs. To do this, the statistical Equation (1) below was developed to implement the two trials separately using a mixed linear model in lme4 package in R (Bates et al., 2014) to estimate temporal best linear unbiased predictors (TBLUP) of the respective response variable (Y) for each pedigree (maize hybrids).

$$Y_{ijklm} = \mu + flight_i + [pedigree(flight)]_{ij} + [range(flight)]_{ik} + [row(flight)]_{il} + [replication(flight)]_{im} + error_{ijklm}$$

where, Y represents each individual observation of pedigree at each ith time point (flight dates as DAP unit); μ represents the grand mean; $flight$ represents the effect of ith flight date, $i \in (8, 10 \ldots 105; DHOT)\ and\ i \in (30, 32 \ldots 127; OHOT)$; $[\mathrm{pedigree}(flight)]_{ij}$ represents the effect of jth pedigree within ith flight date; $[\mathrm{range}(flight)]_{ik} \sim N(0, \sigma^2_{[\mathrm{range}(flight)]_{ik}})$ represents the effect of kth range within ith

flight date; $[\mathrm{row}(flight)]_{il} \sim N(0, \sigma^2_{[\mathrm{row}(flight)]_{il}})$ represents the effect of lth row within ith flight date $[\mathrm{replication}(flight)]_{im} \sim N(0, \sigma^2_{[\mathrm{replication}(flight)]_{im}})$ represents the effect of mth replication within ith flight date, and $error_{ijklm} \sim N(0, \sigma^2_{error})$ represents the pooled error comprising residuals of all experimental factors above. Temporal repeatability was calculated for each temporal trait based on the results of explained percent variation of $[pedigree(flight)]_{ij}$ ($\sigma^2_{pedigree(flight)}$) and $error_{ijklm}(\sigma^2_{error})$ with numbers of replication (b) (Equation (2)):

$$Temporal\ repeatability = \frac{\sigma^2_{pedigree(flight)}}{\sigma^2_{pedigree(flight)} + \frac{\sigma^2_{error}}{b}}$$

The previous model was adjusted to run without the $flight$ component to estimate the BLUP for pedigree (maize hybrids) for single time-measured traits that are yield, DTA and DTS (Equation (3)):

$$Y_{ijkl} = \mu + pedigree_i + range_j + row_k + replication_l + error_{ijkl}$$

where Y represents the each individual observation of pedigree; μ represents the grand mean; $pedigree_i$ represents the effect of ith pedigree; $range_j \sim N(0, \sigma^2_{range_j})$ represents the effect of jth range; $row_k \sim N(0, \sigma^2_{row_k})$ represents the effect of kth row; $replication_l \sim N(0, \sigma^2_{replication_l})$ represents the effect of lth replication, and $error_{ijkl} \sim N(0, \sigma^2_{error_{ijkl}})$ represents the pooled error comprising residuals of all experimental factors above. Repeatability was calculated for Yield, DTA and DTS from Equation (4):

$$Repeatability = \frac{\sigma^2_{pedigree}}{\sigma^2_{pedigree} + \frac{\sigma^2_{error}}{b}}$$

Statistical Equation (5) was developed by adding the $management$ and $[pedigree * management]$ components into Equation (1) as nested within $flight$. In Equation (5), the management effect contained the OHOT and DHOT trials, indicating optimal and delayed planting, respectively. Equation (5) aimed to contrast each trait value of flight date for each trial. To do that, $[management * flight]_{ik} \sim N(0, \sigma^2_{[management*flight]_{ik}})$ effect was included. Here, $management$ represents the effect of kth management, $k \in (DHOT\ and\ OHOT)$; $[management * pedigree(flight)]_{ijk} \sim N(0, \sigma^2_{[management*pedigree(flight)]_{ijk}})$ represents the interaction of jth pedigree with kth management within ith flight date. Spatial variation ($range$, row and rep) were treated nested within $management$ and $flight$ in Equation (5).

$$Y_{ijklmn} = \mu + flight_i + [pedigree(flight)]_{ij} + management_k + [pedigree * management(flight)]_{ijk} + [flight * management_{ik}] + [range(managment, flight)_{ikl}] + [row(managment, flight)_{ikm}] + [rep(managment, flight)_{ikn}] + error_{ijklmn}$$

Multi-management based repeatability was calculated by expanding Equation (2) to include the interaction term between $management$ and $pedigree$ nested within

$flight$ [$pedigree * management(flight)$] with the number of the management (a) and replication (b) (Equation (6)):

$$Repeatability = \frac{\sigma^2_{pedigree(flight)}}{\sigma^2_{pedigree(flight)} + \frac{\sigma^2_{pedigree * management(flight)}}{a} + \frac{\sigma^2_{error}}{a * b}}$$

Machine Learning Regression

All temporal breeding values (TBLUPs) of VIs and CHMs of pedigree were used to predict three predicted variables (Yield, DTA and DTS) for both populations. Linear, lasso, ridge, elastic net and partial least square regression (PLSR) were run to predict the predicted variables using the *caret* package in R. The data set was split into 60% training and 40% validation data. Cross validation was adjusted using the *R/caret::trainControl()* function, with ten resampling iterations (i.e. folds; numbers=10) and ten repeated k-fold cross validations (repeats=10). The adjusted cross validation was then used in each regression model. To run all regression models, *R/caret::train()* function was implemented using *method=lm* for linear regression and *method=glmnet* for ridge, lasso, and elastic net regressions and "*method=pls*" for PLSR. The *tuneGrid* argument was used to tune the "*lambda*" (for elastic net, lasso and ridge regressions) and "*alpha*" (for elastic net regression) using the *expand.grid()* function. Value of "*alpha*" was set as 0 for ridge regression and 1 for lasso regression, while sequential numbers between 0 and 1 by ten equal increment sequences were performed to find the best alpha for elastic net regression. Sequential "*lambda*" values between 0 and 1 by five equal increment sequences were empirically tested to find the best lambda values for lasso, ridge, and elastic net regressions. In PLSR, the *tuneLength* function was used to find the best

number of principal components with the lowest cross-validation error. In the prediction of yield in the DHOT trial, alpha and lambda values used were 1 and 0.25, 0 and 1, 0.1 and 0.50 for lasso, ridge and elastic net regressions, respectively, and numbers of principal component (*ncomp*) used was 8 for PLSR. In the prediction of DTA in the DHOT trial, *alpha* and *lambda* values used were 1 and 0.0001, 0 and 1, 0.1 and 0.0001 for lasso, ridge and elastic net regressions, respectively, and *ncomp* used was 10 for PLSR. In the prediction of DTS in the DHOT trial, alpha and lambda values used were 1 and 0.0001, 0 and 1, 0.1 and 0.0001 for lasso, ridge and elastic net regressions, respectively, and *ncomp* used was 7 for PLSR. In the prediction of yield in the OHOT trial, *alpha* and *lambda* values used were 1 and 0.25, 0 and 1, 0.1 and 1 for lasso, ridge and elastic net regressions, respectively, and *ncomp* used was 4 for PLSR. In the prediction of DTA in the OHOT trial, *alpha* and *lambda* values used were 1 and 0.25, 0 and 1, 0.1 and 0.50 for lasso, ridge and elastic net regressions, respectively, and *ncomp* used was 10 for PLSR. In the prediction of DTS in the OHOT trial, *alpha* and *lambda* values used were 1 and 0.25, 0 and 1, 0.1 and 0.25 for lasso, ridge and elastic net regressions, respectively, and *ncomp* used was 9 for PLSR. To compare the regression models, coefficient of determination (R^2), root mean square errors (*RMSE*), and mean absolute errors (*MAE*) were evaluated for each model. To evaluate the prediction accuracy of the linear, ridge, elastic net, lasso and PLSR models, *R/caret::predict()* was used to predict DTA, DTS, and yield of the test data set in each trial using 500 bootstraps iterations. The predicted results of the test data were correlated (Pearson pairwise correlation) with the actual values of test data set in each bootstrap. Finally, the

Tukey HSD (Honest Significant Difference) test was applied to compare the means of correlation results belonging to each model for DTA, DTS, and yield in both trials. Letters were assigned to each model indicating the comparison results of Tukey HSD test to indicate statistically significant differences. The *R/caret::varImp()* function was used to rank the predictors based on their importance (0-100 scale) for lasso, ridge, elastic net and PLSR regression. All R codes are available in Github repository (https://github.com/alperadak/Supplementary-File-1/blob/main/Supplementary%20file%201.txt).

Results

Explained Percent Variation of Flight and Repeatability

The variation explained by the flight component in (Equation (1)) was the greatest of the variance components and was statistically significant (>0.0001) for each UAS trait (fifteen different VIs and CHMs) in each trial. The flight component explained up to 97 - 98 % of variation in the CHM for DHOT and OHOT, respectively, while explaining the lowest for true bands (Blue, Red and Green) and BI (41 - 51 %; Figure 33). Similarly, the highest temporal repeatability values were also estimated for CHMs (0.76 in DHOT and 0.74 in OHOT; Equation (2)) and lower repeatability estimates were found for the VI's (<0.6 ; Figure 33).

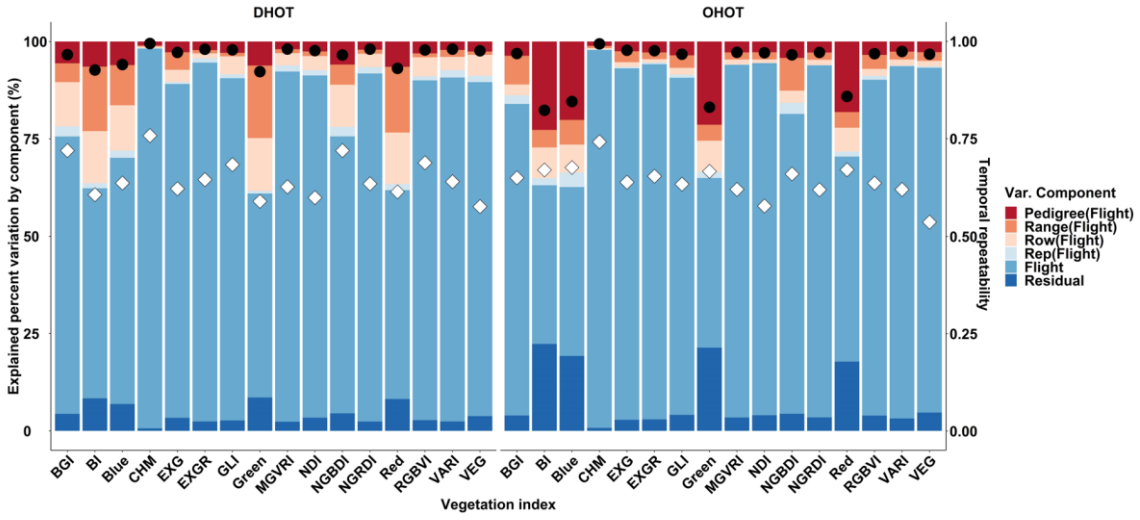

Figure 33. Variance component decomposition (Equation (1)) for each predictor trait (fifteen vegetative indices, VIs and canopy height measurement; CHM) for each trial (DHOT on the left and OHOT on the right). X axes, left Y axis, and right Y axes represent the traits, explained percent variation by each variance component, and temporal repeatability, respectively. Black circles and white diamonds represent the R^2 and repeatability values, respectively, for each trait according to the right Y axis scale. Temporal repeatability was calculated based on the Equation (2). Reprinted from Adak, Murray, Božinović, et al., 2021.

For predicted variables (yield, DTA and DTS) used in the regression models, the explained percent variations of the pedigree component in Equation (3) explained the greatest variation (53–83%). Repeatability values for predicted variables were calculated between 0.91 and 0.98 (Figure 34). Predicted values (Equation (3)) of maize hybrids for DTA, DTS, and yield in both trials were given in Figure 35. DHOT trial had shorter days after planting values in DTA and DTS than those of OHOT while grain yield (t/ha) was higher in OHOT than those of DHOT (Figure 35).

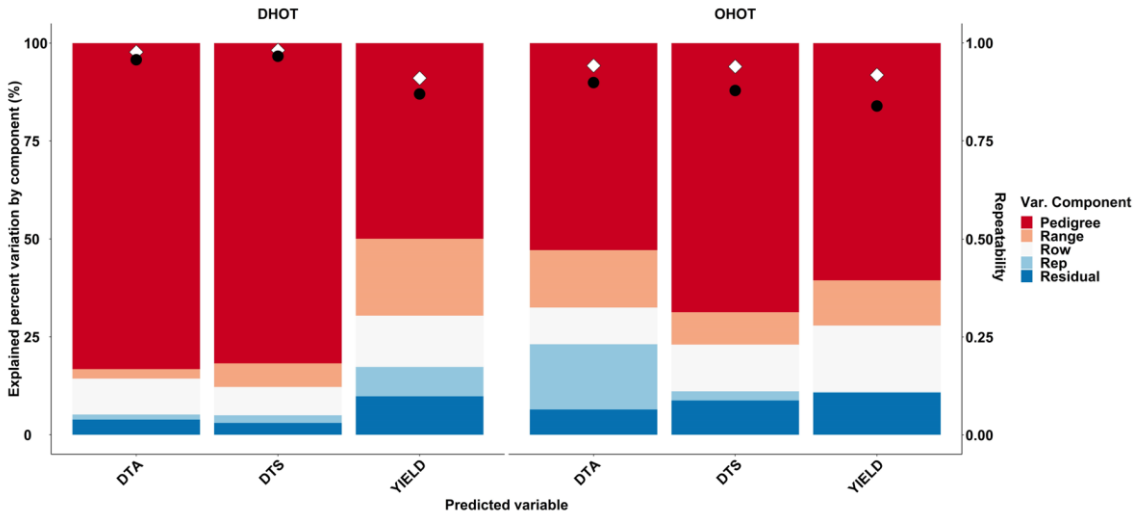

Figure 34 Explained percent variation of each component in Equation (3) for each predicted variable (days to anthesis (DTA), days to silking (DTS), and yield (t/ha)) for each trial (DHOT on the left and OHOT on the right). X axes, left Y, and right Y axes represent the traits, explained percent variation by each variance component, and repeatability, respectively. Black circles and white diamonds represent the R^2 and repeatability values, respectively. Reprinted from Adak, Murray, Božinović, et al., 2021.

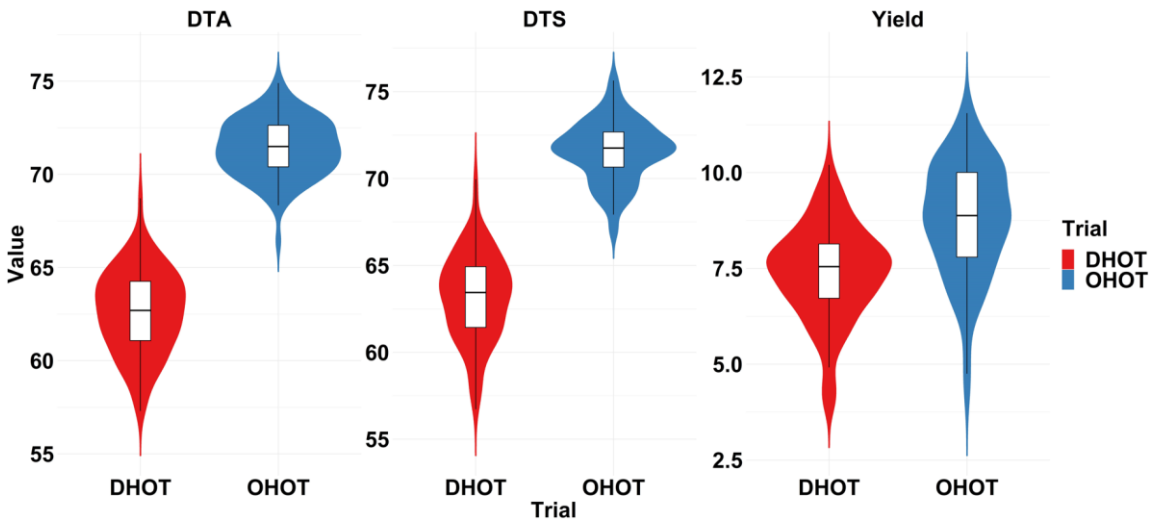

Figure 35 The best linear unbiased predictors (BLUPs) values of predicted variables [days to anthesis (DTA), days to silking (DTS), and yield (t/ha)]. Y axes shows to best linear unbiased predictors (BLUP) of hybrids for DTA, DTS and yield unique to each trait while X axes shows the trials. Reprinted from Adak, Murray, Božinović, et al., 2021.

Temporal Breeding Values

Effects of the pedigree(flight) (Equation (1)) were illustrated to display temporal breeding values (TBLUPs) of predictor traits (fifteen VIs and CHMs) of pedigrees for optimal planting (OHOT) and delayed planting (DHOT) trials separately (Figure 36 and Figure 37). In all, TBLUPs of 16 traits, which were derived from 12 flight time points, were displayed, corresponding to 192 predictors evaluated in regression models for each trial.

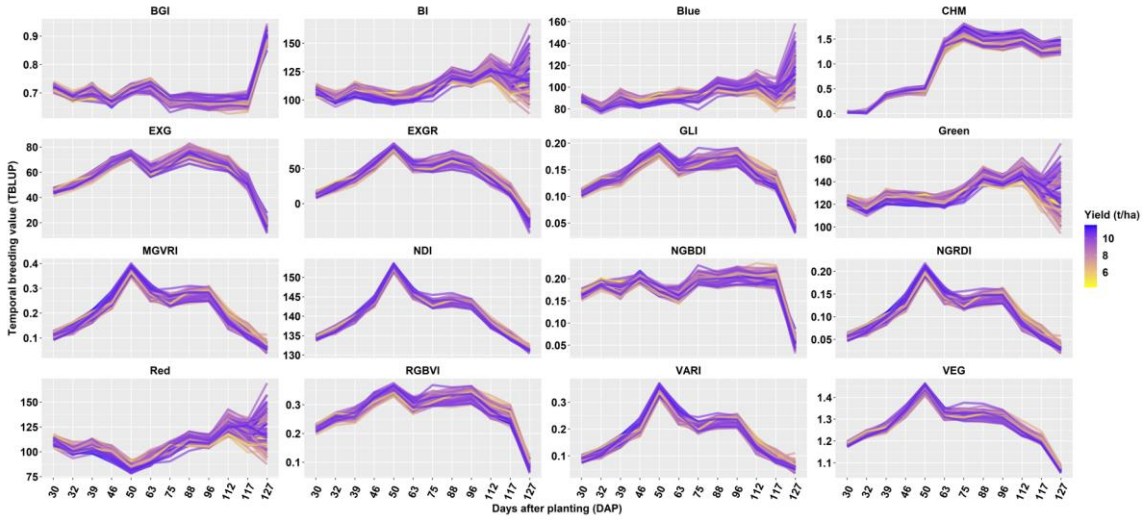

Figure 36 Temporal best linear unbiased predictions (TBLUPs) of the traits (fifteen vegetation indices, VIs and canopy height measurement; CHM) of the pedigrees in the OHOT (optimal planting trial) population estimated by Equation (1). Each Y axis shows the range of TBLUPs unique to each trait while each X axis shows the flight dates as days after planting (DAP) same to each trait. The heatmap scale was generated from the range of yield (t/ha) values in the OHOT trial, and then applied to each pedigree to show the TBLUPs of each trait through the flight dates along with yield values of pedigree. Blue, white, and red colors in the heatmap scale were used to indicate low, medium, and high yield values, respectively, specific to the OHOT trial. Reprinted from Adak, Murray, Božinović, et al., 2021.

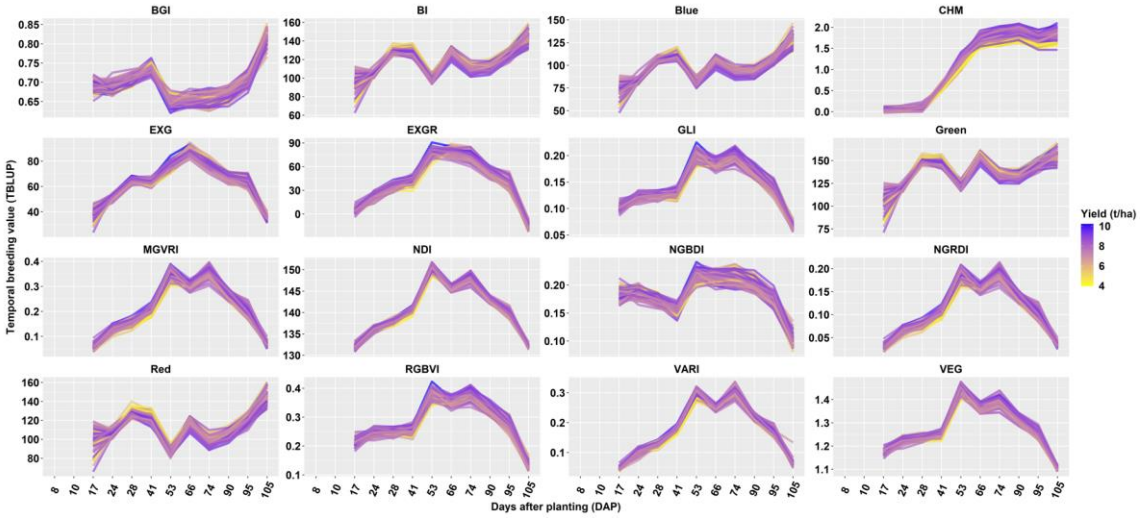

Figure 37 Temporal best linear unbiased predictions (TBLUPs) of the traits (fifteen vegetation indices, VIs and canopy height measurement; CHM) of the pedigrees in the DHOT (delayed planting trial) population estimated by Equation (1). Each Y axis shows the range of TBLUPs unique to each trait while each X axis shows the flight dates as days after planting (DAP) same to each trait. The heatmap scale was generated from the range of yield (t/ha) values in the DHOT trial, and then applied to each pedigree to show the TBLUPs of each trait through the flight dates along with yield values of pedigree. Blue, white, and red colors in the heatmap scale were used to indicate low, medium and high yield values, respectively, specific to the DHOT trial. Reprinted from Adak, Murray, Božinović, et al., 2021.

TPP of VIs and CHMs occurring among the flight dates ([pedigree(flight)] component of Equation (1)) were found to be statistically significant (<0.0001) in both trials. TPP patterns were also found to be unique for many traits across trials. In general, EXG, EXGR, GLI, MGVRI, NDI NGRDI, RGBVI, VARI, and VEG followed concave plasticity patterns while Red followed a slightly convex plasticity pattern (Figure 36 and Figure 37). BI, Blue, Green, and NGBDI slightly increased over time while BGI slightly decreased across the flight dates. CHM followed a sigmoidal plasticity pattern through the flight dates. However, each trial had different slopes, edges, and peaks of the TBLUPs of the traits depending on the flight times (Figure 36 and Figure 37).

Equation (5) was developed to compare the flight means of each trial for each trait by adding the management (DHOT and OHOT trials) effects within flight dates ([management(flight) effects in Equation (5)). The [management(flight)] component explained between 29 and 96% of total depending on VIs and 14 percent for CHM (Figure 38).

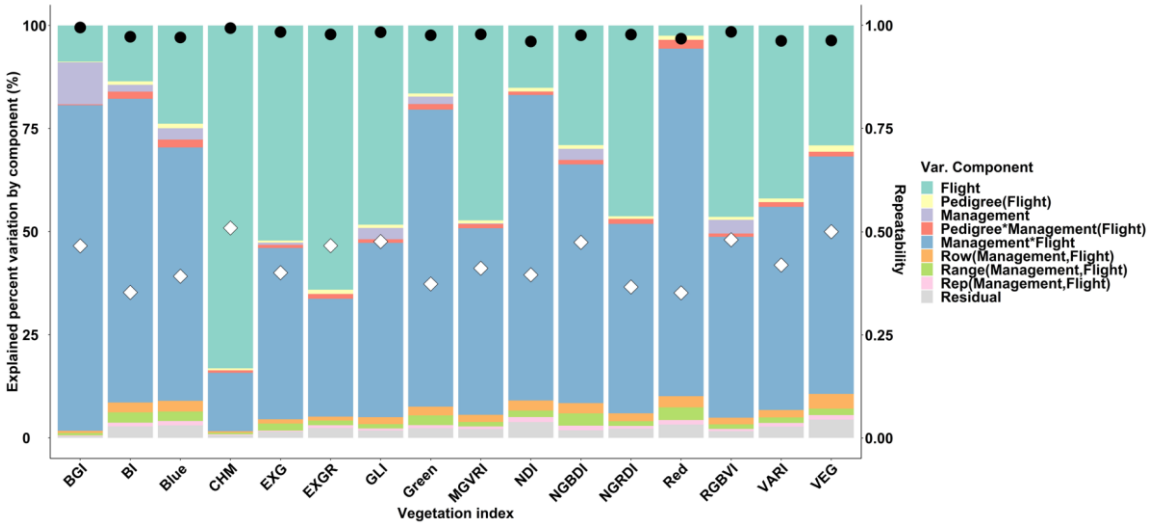

Figure 38 Explained percent variation of each component in Equation (5) for each predictor trait (fifteen vegetation indices, VIs and canopy height measurement; CHM). X axis, left and right Y axes represent the traits, explained percent variation by each variance component and R^2 respectively. Black circles and white diamonds represent the R2 and repeatability values, respectively, for each trait according to the right Y axis scale. Repeatability was calculated based on Equation (6). Reprinted from Adak, Murray, Božinović, et al., 2021.

The majority of the mean comparisons of each time point (flight dates) between the trials were found to be statistically significant (Figure 39). In addition, there were found to be cross over changes in comparisons of flight means varying between one to six times depending on different traits; meaning that the relative performance at one time point and trial could not predict the relative performance in a different time point.

However, where there were more cross overs, they were less likely to be significantly different.

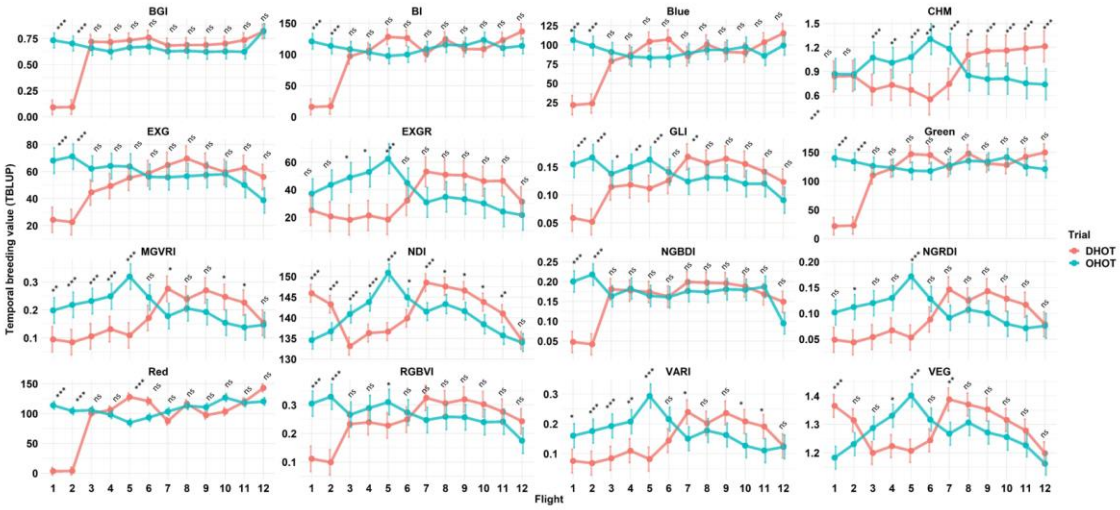

Figure 39 Temporal comparison results of each time point between each test. The joint analysis of temporal effects of the trials based on means of flight dates was derived from Management(flight) component in Equation (5). Each Y axis shows the range of flight means unique to each trait while each X axis shows the flight dates as successive order same to each trait. *, **, *** are significance levels at 0.05, 0.01 and 0.001; ns is not significant. Whiskers represent the conditional standard deviations for each time point of each trait. Reprinted from Adak, Murray, Božinović, et al., 2021.

Temporal Correlations between Predictors and Predicted Variables

Temporal correlation coefficients (Pearson correlation) were calculated between TBLUPS of the traits (predictors) and predicted variables (DTA, DTS, and yield) (Figure 40). To calculate the temporal correlations, BLUPs of pedigrees for each flight date were derived from [pedigree(flight)] in Equation (1) for each trait and trial. BLUPs of DTA, DTS, and yield were correlated with TBLUPs of predictor traits for each flight date. Temporal correlation results varied from −0.6 to 0.6 across the flight dates. The majority of predictor traits fluctuated in correlation temporally (Figure 40). The highest

and lowest temporal correlation with DTA, DTS, and yield were found more frequently in DHOT than in OHOT (Figure 40). All traits were found to have both negative and positive correlation coefficients in both trials through the flight dates, except for positive correlation coefficients between CHM and yield in both trials throughout the flight dates (Figure 40).

Figure 40 Each correlogram chart contains the pairwise correlation coefficients (r^2) belonging to time points of each trait with predicted traits [days to anthesis (DTA), days

to silking (DTS), and yield (t/ha)]. Correlogram charts above and below the horizontal black dashed line belong to DHOT (delayed planting trial) and OHOT (optimal planting trial) respectively. Time points (days after planting, DAP) were given diagonal and horizontal for each vegetation index and CHM in both trials along with DTA, DTS and yield in each correlogram chart. The correlation coefficient heatmap change from −1 to 0 from pink to white and from 0 to 1 from white to cyan. The cross signs (×) show statistically insignificant pairwise correlations at the 0.05 level. Reprinted from Adak, Murray, Božinović, et al., 2021.

Regression Model Comparisons

Temporal best linear unbiased predictors (TBLUPs) of pedigrees for each predictor trait (fifteen VIs and CHM) were estimated by the component of [pedigree(flight)] in Equation (1) for each trial separately. BLUPs of predicted variables (DTA, DTS, and yield) were estimated from the pedigree component in Equation (3). Predictor traits (fifteen VIs and CHM) were used in four different regressions to predict the predicted variables. TBLUPs, including the individual BLUPs of sixteen predictor traits on twelve flight dates (192 predictors for each trial), were estimated by Equation (1) separately and then used in regression models to predict the predicted variables (DTA, DTS and Yield) for each trial. Elastic net, lasso, ridge, PLSR and linear regressions were used to predict the predicted variables using all 192 predictors and models. Model fit was evaluated based on their root mean square errors (RMSE), mean absolute errors (MAE), and coefficient of determination (R2) as well as prediction accuracies of the models. Linear regression was found to perform the worst among regression models in predicting all three predicted variables in both trials, resulting in the highest RMSE, MAE, and lowest R2 values and lowest prediction accuracies followed by PLSR (Figure 41 and Figure 42). Slight differences were found among the results of machine learning regressions in terms of predicting predicted variables (Figure

41 and Figure 42). Accordingly, lasso and elastic net regressions were found to be best in predicting flowering times (DTA and DTS) with the prediction accuracy of between ~0.75 and ~0.80 in DHOT and OHOT trials (Figure 42). However, ridge regression was found to be best in predicting yield, with prediction accuracy of ~0.60 in DHOT and OHOT trials (Figure 42).

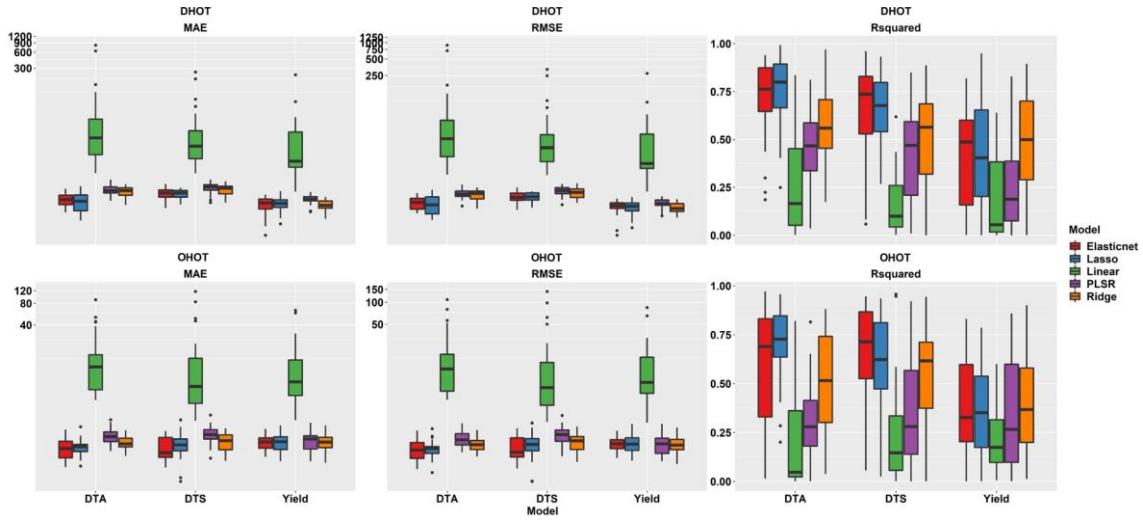

Figure 41 Box plots of root mean squares (RMSE), mean absolute errors (MAE), and coefficient of determination (R^2) values (from left to right) of linear, elastic net, lasso, and ridge regressions for DHOT (delayed planting trial; above) and OHOT (optimal planting trial; below). Each Y axis has the unique value ranges for RMSE, MAE and R^2 in each trial while each X axis shows the predicted variables used in each regression models [days to anthesis (DTA), days to silking (DTS), and yield (t/ha)] same to RMSE, MAE, and R^2 in each trial. Whiskers represent the standard errors. Y axes of RMSE and MAE were scaled based on the log2 to show the outliers belonging to the linear model. Reprinted from Adak, Murray, Božinović, et al., 2021.

Variable Importance

The relative importance of the TBLUPs were calculated to show the temporal importance of predictor traits in the prediction of the predicted variables (DTA, DTS, and yield) used in machine learning regressions.

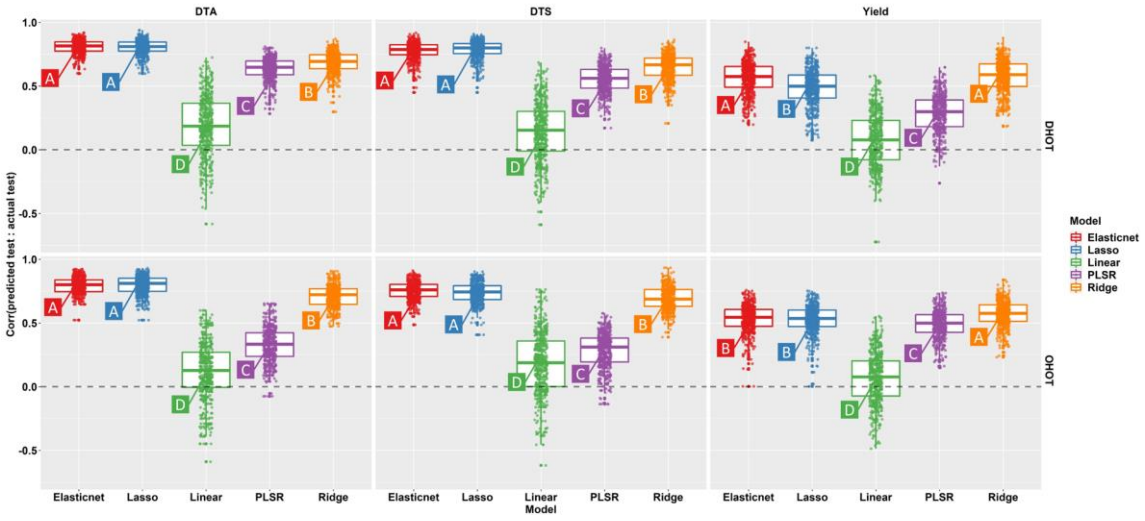

Figure 42 Prediction accuracy results of each model for days to anthesis (DTA), days to silking (DTS), and yield (t/ha), respectively. Y axes represents the correlation coefficients (r^2) between predicted value and actual value of days to anthesis (DTA), days to silking (DTS) and yield (t/ha) (from left to right) in DHOT (delayed planting trial) and OHOT (optimal planting trial) (From top to bottom). X axis shows the predictive models used in this study. Each box represents letters of Tukey HSD comparison results for each predicted trait in each trial. Reprinted from Adak, Murray, Božinović, et al., 2021.

Results showed that some of the VIs were found to contribute predictions of predicted variables throughout the flight dates, while others were found to contribute predictions at specific flight dates, depending on the predicted variables as well as the trials (Figure 43 and Figure 44). The best-performing predictors of yield nominated in ridge (in both trials) and elastic net (in DHOT only) regressions (Figure 42) were NGRDI, NGBDI VARI and GLI, traits with fluctuating variable importance scores across the flight dates in both trials (Figure 43 and Figure 44). Their variable importance scores were frequently higher before flowering than after flowering time (Figure 43 and Figure 44).

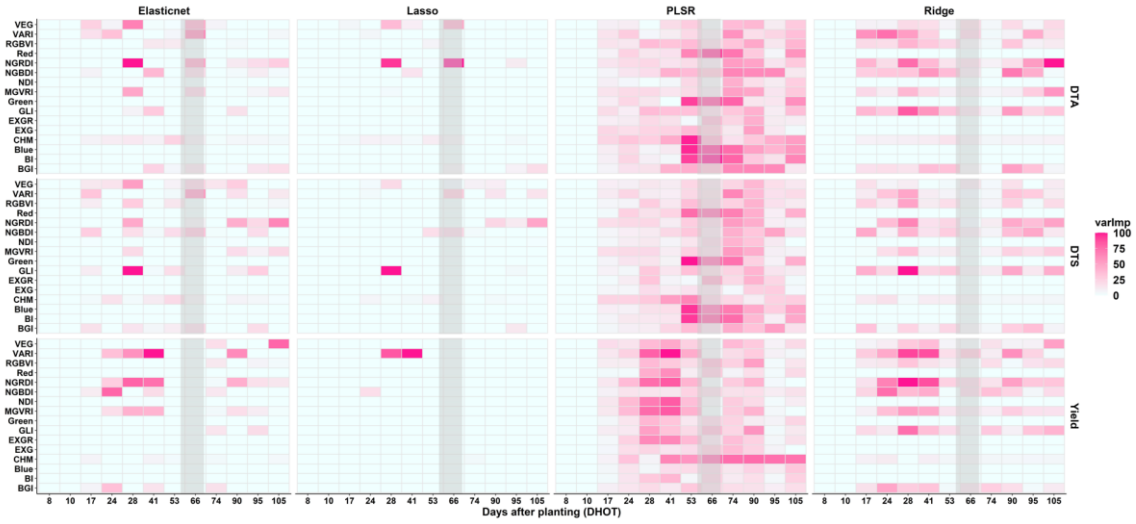

Figure 43 Heatmap temporal variable importance of predictor traits across the flight dates generated by the '*varImp*' function of each machine learning regression in the DHOT trial. X axes are identical and represent the flight dates of DHOT as days after planting (DAP). Left Y-axes are identical and represent the predictor traits for each regression model and predicted variables. The heatmap illustrations were divided into nine for the elastic net, lasso and ridge regressions top to bottom and DTA, DTS and Yield predicted variables from left to right. Heatmap scales show the variable importance scores as 0–100 scales calculated from the '*varImp*' functions of each machine learning regression. Flowering times varied from 57 to 69 for DTA and 57 to 70 for DTS (grey boxes) in DHOT. Reprinted from Adak, Murray, Božinović, et al., 2021.

Figure 44 Heatmap of temporal variable importance of predictor traits across the flight dates generated by the '*varImp*' function of each machine learning regression in the OHOT trial. X axes are identical and represent the flight dates of OHOT as days after planting (DAP). Left Y axes are identical and represent the predictor traits for each regression model and predicted variables. The heatmap illustrations were divided into nine for the elastic net, lasso and ridge regressions top to bottom and DTA, DTS and Yield predicted variables from left to right. Heatmap scales show the variables importance scores as 0–100 scales calculated from the '*varImp*' functions of each machine learning regression. Flowering times varied from 66 to 75 for DTA and 67 to 76 for DTS (grey boxes) in OHOT. Reprinted from Adak, Murray, Božinović, et al., 2021.

The remaining traits were found to have a lower importance score than NGRDI, NGBDI, VARI and GLI in the prediction of yield across both trials (Figure 143 and Figure 44); however, their importance sores were also higher before the plants flowered in both trials.

Lasso and elastic net regressions performed best in predicting the flowering times (DTA and DTS), in the both trials (Figure 42). The methods nominated fluctuating variable importance of the temporal traits across the flight dates (Figure 43 and Figure 44); many of the flight dates belong to the period before flowering. For instance, GLI and NGRDI on 28th DAP were important date/predictor combinations for flowering time in the DHOT trial (Figure 43). NGBDI and GLI on 46th, 50th, 63rd DAP for DTA, (Figure 44), and NGRDI, VARI, CHM, GLI and MGVRI on 30th DAP for DTS (Figure 44) were important date/predictor combinations in the OHOT trial.

Discussion

Implementing field-based high-throughput phenotyping (HTP) tools such as unoccupied aerial systems (UAS) in agriculture has been recognized to be an efficient way to monitor temporal variation of plant growth (Adak, Murray, Anderson, et al.,

2021; Anderson et al., 2019; Araus & Cairns, 2014; Shi et al., 2016). Temporal variations throughout growth are novel sources of variation that have not previously been measured and now can be used for plant breeding and genetics in prediction models. Estimating the degree of phenotypic variation controlled by the genetic variation of tested pedigrees for HTP-derived traits (e.g., measuring repeatability for VIs and CHMs) is a first fundamental step to determine how heritable or consistent trait measurements are before using VIs and CHMs in prediction models. The sixteen traits (fifteen VIs and CHM) used in this study had temporal repeatability values of 0.60 to 0.76 in delayed and optimal planting trials (DHOT and OHOT trials, respectively) (Figure 33), suggesting that estimating the breeding values from HTP-derived traits of tested pedigrees has potential in prediction models as well as in the decision making process for plant breeding. Temporal variation of each HTP-derived trait, estimated by Equation (1) for each trial separately, was the source of the biggest proportion of total experimental variation. This temporal resolution, derived from twelve time points, supported the existence of TPP across pedigrees for fifteen VIs and CHMs in both trials. Joint analysis of both trials, estimated by Equation (5), showed that different reaction norms to compare each time point (flight means) under different environmental conditions characterized the dissimilar TPP patterns of VIs and CHMs. Importantly, NGBDI and BGI were found to have the least TPP under two distinct environmental conditions and are proposed as the most robust VIs from this study. Moreover, NGBDI was found to be an important variable in yield prediction at 30 DAP in the OHOT trial, as well as for predicting flowering times at 28 DAP in both OHOT and DHOT; if this

can be further validated it would be valuable and exciting for early-season predictions of grain yield. The above, along with the high repeatability values (~0.7 in Figure 33) nominate NGBDI, NGRDI, and GLI as the most effective and robust predictors of yield and flowering times in this study. However, it remains worthwhile to estimate multiple VI's since the same collected data is needed and many indices had non-redundant information.

Physiological Basis of These Predictions

Vegetation indices (VIs) are biologically based remote sensing measurements that can assess the physiological processes of maize hybrids quantitively using the reflected wavelengths. More specifically, VIs are ratios that belong to the green apparatus of maize where photosynthetic activity occurs. The visible spectrum of solar radiation (400 nm to 700 nm) is absorbed by plants pigments, of which chlorophyll a and b absorb the blue-violet and red-blue regions of the visible spectrum to provide the light for photosynthetic activity and reflect far red wavelengths. Photoassimilate is produced by photosynthetic activity containing the light dependent reactions that are likely affected by different environmental conditions and contributed to yield differences. As a result of these processes, temporal correlations, and predictive ability of VIs with yield in maize likely depends on environmental variability (M. R. Smith, Rao, & Merchant, 2018); in agreement with our findings (Figure 40). Differences between the wavelengths belonging to different varieties tested in different environmental conditions relate to how the plants handle multiple stresses (Zaman-Allah et al., 2015).

Although this study showed the surprising predictive ability of VIs belonging to time points earlier than the reproductive (flowering) stage, for flowering times later time points were also important, likely relating to senescence after grain fill. Grain yield can be adversely affected because of heat stress or early senescence after flowering. VIs belonging to time points after flowering lose their ability to predict yield as senescence accelerates, which was found for both trials. Early leaf senescence, especially, shortens the grain-filling duration in maize, and would be expected to reduce measured grain yield. A leaf senescence index has been proposed to be well correlated with VIs, as well as yield in maize under low nitrogen stress (Zaman-Allah et al., 2015). Slow reduction in photosynthetic pigments throughout plant growth is associated with greater yield, as well as with the stay-green trait (E. A. Lee & Tollenaar, 2007). As such, using temporal breeding values of the VIs near the end of growth may quantitatively select maize hybrids where the higher yield is a result of slow reduction in the VIs across growth. This study used VIs calculated by wavelength of ranges of visible light, not affected by additional factors that affect near-infrared (NIR) reflectance such as soil brightness, moisture and color, canopy and cell structure, or cloud shadows [13]. As such, these VIs belonging to false positive color reflectance should result in greater precision in extraction of VIs, compared to NIR reflectance (Gitelson et al., 2002; X. Zhang et al., 2019). For example, normalized difference vegetation index (NDVI) which contains the NIR reflectance, was found to be very sensitive towards background brightness since NDVI increases accordingly if the background brightness increases (Xue & Su, 2017). It might be concluded that the VIs without NIR used here are more sensitive in detecting

high amounts of absorption of red referring to the presence of the chlorophyll and green vegetation, disregarding noisy reflectance.

The delayed planting trial (DHOT) had higher growing degree days as well as higher photo-thermal time accumulations than the optimal planting trial (OHOT) across plant growth stages in maize breeding nurseries in Texas. The temporal differences in weather station measurements between the two trials suggest a primary reason for the TPP of the pedigrees of several VIs likely stemmed from the rapid accumulation of growing units in DHOT, a combination of both higher photoperiod and increased heat. Taken together, despite the fact that VIs and CHMs were shown to be controlled by genetic variation to a certain extent, monitoring of TPP belonging to VIs and CHMs can be more appropriate to evaluate performance of maize hybrids under diverse environmental conditions including their different time points. Because correlations between VIs and yield, or CHMs and yield, are dynamic, and different time points had different correlation coefficients (Figure 40), this suggests that correlations in earlier time points could be considered to assess the performance of maize hybrids. In genomic selection, selections are accomplished through estimating the large and small marker effects on phenotype belonging to terminal growth stages. Now, with temporal phenotypes estimated by Equation (1), it is possible to include the genotypic variation occurring at early stages into phenomic selection (Rincent et al., 2018) and phenomic selection can contain temporal marker effects on VIs and CHMs that give rise to better prediction accuracy. Analyzing multiple time points of different management conditions can supply better confidence levels, as well as more statistical power in predicting

temporal breeding values; this will allow temporal breeding values to be later used in downstream analysis, such as, more accurate prediction modeling. In addition, using VIs with high repeatability values as predictive variables will lead to more effective estimates, especially under stress conditions, largely because the signal-to-noise ratio is higher (Montesinos-López et al., 2017; Weber et al., 2012).

Model Comparisons

Machine learning-based prediction models performed best in comparison with linear models for predicting flowering times and yield using the temporal data. The predictive ability of ridge regression in genomic prediction has been demonstrated (Endelman, 2011). Similarly, ridge regression excelled in predicting yield in phenomic prediction compared to other models in this study (Figure 42), signifying that prediction accuracy of ridge regression can be increased in selecting the high yielding maize hybrids when a greater number of phenotypic predictors are extracted from UAV images. Ridge regression models have previously been used in yield prediction using reflectance wavelengths (between 350 to 2500 nm) in wheat and performed best in prediction under drought (Hernandez et al., 2015). This result is in agreement with our finding that ridge regression performed best under the stress trial (DHOT) in yield prediction by using VIs. (Hernandez et al., 2015) wheat used only reflectance at anthesis and grain filling time periods; this study, however, discovered important effects of VIs at many earlier time points in maize, even before flowering and grain filling such as at 28 and 30 DAP in the DHOT and OHOT trial, respectively. If this can be validated in further work it is an exciting and important finding not only for speeding up breeding

decisions earlier in the season, and the associated physiological ramifications, but also for identifying important growth stages for precision agricultural management by farmers. Our findings also support the value of temporal VIs measurement for predicting yield; not only during specific time periods of growth, but that the entire growth period has value with different effect sizes at each time point. In this way these VI's may be better used like a genomic selection approach of incorporating and weighting all time points, than a genetic mapping approach of identifying and monitoring only the time point with the largest effect size; as supported in phenomic selection approaches, using laboratory near-infrared reflectance spectroscopy data of grain (Rincent et al., 2018). This study also revealed that flowering times (DTA and DTS) can be best predicted before flowering using the temporal VIs, which is critical where earliness traits for maize can be selected based on the values of certain VIs at specific early time points, such as NGRDI and VARI at 28 DAP in DHOT; NGRDI and GLI at 30 DAP in OHOT (Figure 43 and Figure 44).

Single time point-derived CHMs (Anderson et al., 2019) and reflectance bands (Aguate et al., 2017a) have previously been shown to perform worse than using fewer parameters estimated from modeling combined data derived across multiple time points. Our findings suggested that temporal variations of VIs and CHMs should be trained together in a predictive model using machine learning based regressions to predict grain yield with more accuracy, when the number of predictors are high, which otherwise may lead to overfitting and multicollinearity problems.

Given the long history of satellite remote sensing to predict yield (B. Peng, Guan, Pan, & Li, 2018; B. Peng et al., 2020), the results of the temporal and visible aspects of this study were surprising. However, it must be emphasized that to date there have been comparatively few studies using remote sensing predictors across segregating genetic populations to predict differences within species. These findings similarly suggest that unquantified genetic variation might exist that would affect satellite yield predictions. This also suggests new temporal measurements that farmers might be able to use to identify plant stress and intervene earlier than previously to predict yield loss. In summary, the strong predictive power of temporal VIs and CHMs for predicting yield was shown in this study which could serve as an alternative to genomic prediction methods in the near future.

In conclusion, field-based high-throughput phenotyping identified that the phenotypic variation occurring early in developmental stages of plants can be used as novel predictors to predict yield and flowering times in phenomic selection. This research extracted fifteen different vegetation indices and canopy height measurements from the aerial drone imageries belonging to twelve time points across the growth of tested maize hybrids. Our study demonstrated that (i) predicted temporal vegetation indices and plant heights for each pedigree (maize hybrid) have discrimination power of low-yielding and high-yielding maize hybrids and that these temporal vegetation indices and plant heights are heritable traits in maize; (ii) machine learning-based regressions have better prediction accuracy in prediction yield and flowering times than linear regression when temporal vegetation indices and plant heights are used as predictors in

phenomics selection in maize; and (iii) variable importance scores of vegetation indices are higher at earlier time points than later time points, indicating that variation in earlier in growth should be monitored to predict yield and flowering times with higher accuracy in maize.

Data Availability Statement

Data set containing predictors (temporal vegetation indices and canopy height measurements) and predicted traits (days to anthesis, silking and yield) belonging to OHOT (optimal planting trial) and DHOT (late planting trial) used in prediction models was given as supplementary data 1 set. The R code used in prediction models was given in Github repository(https://github.com/alperadak/Supplementary-File-1/blob/main/Supplementary%20file%201.txt, accessed on 28 May 2021).

CHAPTER V

PHENOMIC DATA-DRIVEN PREDICTION THROUGH FIELD-BASED HIGH THROUGHPUT PHENOTYPING, AND INTEGRATION WITH GENOMIC DATA IN MAIZE

Genetic gain is a goal for plant breeding programs relying on selection intensity, selection accuracy, genetic variance, and the interplay within breeding cycles over time (Heffner, Sorrells, & Jannink, 2009). All parameters have direct relationships with both the quality and quantity of phenotype data. Increasing selection intensity and selection accuracy requires growing large numbers of genetically diverse breeding materials and collecting phenotypic data from each genotype across breeding cycles. Traditional phenotyping approaches provide limited phenotype data that are resource intensive and poorly scale across time. This results in increased uncertainty and error-prone decision making in plant breeding programs with low accuracy in downstream statistical analysis (Araus, Kefauver, Zaman-Allah, Olsen, & Cairns, 2018; Desta & Ortiz, 2014; Furbank & Tester, 2011). Field based high-throughput phenotyping (FHTP) technology can supply phenomic data with high time-dimensional (multiple time points) and high organismal resolution despite requirements of high computational demands and processing. FHTP is more affordable per observation and less arduous compared to traditional phenotyping methodologies. Thanks to unoccupied aerial vehicles (UAVs, aka drones) equipped with high-tech sensors, plant nurseries and trials can be screened multiple times with high spatial (pixel), and temporal (days) resolution at different plant

growth stages. Reflectance bands can be captured to use as novel predictors and/or secondary traits in prediction of agronomically important traits e.g. yield and flowering times (Adak, Murray, Božinović, et al., 2021; Aguate et al., 2017a; Galán et al., 2020; Rutkoski et al., 2016; Sandhu, Mihalyov, Lewien, Pumphrey, & Carter, 2021; G. Wu et al., 2019b). Extracting reflectance band data from remotely sensed images over multiple time points reveals novel temporal pedigree values that provide key information for plant scientist to discover critical time/trait combinations. This allows early selection criteria to be proposed, before the collection of traditional end-of-season phenotypes have been collected e.g. grain yield by combine (Adak, Murray, Božinović, et al., 2021; Krause et al., 2020a; Sun et al., 2019), similar to genomic based approaches.

Marker assisted selection (MAS) enables selection of traits inherited by Mendelian and quantitative loci (QTLs) on the condition that segregation for these phenotypic traits of interest can be largely explained by the QTLs across breeding cycles. However, complex quantitative traits generally follow an omnigenic model, where thousands of small interacting loci contribute to the formation of the phenotype of complex traits (e.g., yield and flowering times) (Boyle et al., 2017). To better include the contributions of genome wide markers in selection, genome wide markers are being used as predictors for the phenotypic formation of complex traits as a measure of genetic merit; this method was first applied in maize as genomic prediction (GP) by (Bernardo, 1994),also known as genomic best linear unbiased prediction (GBLUP) today. Subsequently, ridge-regression BLUP (rrBLUP) was developed where effects of each marker (treated as random) on phenotype were estimated assuming that marker effects are distributed normally with a

common variance (Endelman, 2011; Whittaker, Thompson, & Denham, 2000). Bayesian GP methods were then developed to better predict phenotype where marker effects are not normally distributed and/or marker effects do not share a common variance (Meuwissen et al., 2001). Prediction results of these models across genome wide markers are now applied to the selection of candidate plants known as genomic selection (GS) (Bernardo & Yu, 2007). Genomic prediction has proved reliable for the selection of complex traits in various crops across plant breeding cycles (Jose Crossa et al., 2014; Heslot, Jannink, & Sorrells, 2015; Windhausen et al., 2012; Y. Zhao et al., 2012). However, GS requires significant effort in DNA extractions and genotyping to obtain useful genome wide markers from populations with GP models. The GS model must be trained for hundreds to thousands of candidate plants using their genomic and phenomic data then again in each growing period for selection and to update the models. To train accurate GS models, large phenotypic data sets must be collected; a bottleneck in predictive plant breeding. Reducing the resources needed and improving the throughput of data collection using FHTP technologies is a critical need to (i) associate phenotypic traits to genomic data to boost the potential of GS and (ii) use directly as novel predictors.

FHTP has revealed dynamic associations between genomic data and temporal phenotypes of complex traits never before possible in plants (Adak, Murray, & Anderson, 2021; Adak, Murray, Božinović, et al., 2021; Anderson et al., 2020; Bac-Molenaar, Vreugdenhil, Granier, & Keurentjes, 2015; Campbell et al., 2017; Feldman et al., 2017; Pauli, Chapman, et al., 2016; Ward et al., 2019). These same types of temporal

associations are difficult to be revealed when more limited phenotypic data collected via traditional phenotyping methods are used in GS. Phenomic data collected from multiple environments and/or multiple time points can be better predictors than genome-wide markers for the purpose of selection the desired plants in plant breeding (Bernardo, 2021). High throughput phenotyping data has untapped potential not only to enhance the prediction of the complex traits in plants, but also to supply complementary phenomic data sets for genomics to dissect these complex traits and their plasticity within high time dimension over the growth.

When combined with high-revisit temporal UAS phenotypic data, genome wide markers were found to have fluctuating phenotypic effects sizes when used in GWAS and QTL studies (Adak, Conrad, et al., 2021; Adak, Murray, & Anderson, 2021; Adak, Murray, Anderson, et al., 2021; Anderson et al., 2020; Jinyu Wang et al., 2021). This phenomenon demonstrates that the same markers could have different effects sizes in terms of the temporal fitness of phenotypes of both traits and genotypes. Much like using the genome wide markers as predictors, temporal phenotype data of different sensor-based traits (e.g. vegetation indices) can be used as predictors. The predictive ability can then be compared to the predictive ability of genomic wide markers (Adak, Murray, & Anderson, 2021; Rincent et al., 2018).

Genome wide markers are collected once, and different individuals are typically straightforward to compare at the same genetic location regardless of when the data is collected. In contrast, phenomic markers are temporally and environmentally dependent and it is not straightforward to compare phenomic features collected in different

environments, at different growth stages or on different days. This is a major barrier to using phenomic features in prediction

This study used recombinant inbred lines (RILs) from the three different bi-parental maize populations totaling 520 RILs, grown from 2016 to 2018. Multiple UAS surveys were conducted using the red-green-blue (RGB) and multispectral sensors in 2017 and 2018. 520 RILs were also genotyped using the Infinium genotyping assay. Days to anthesis and silking were collected from RILs across three years and predicted by phenomic and genomic data using the different regression methods and scenarios. Specifically, our objectives were to:

1) Predict the flowering times using temporal phenomic data derived from multispectral and RGB sensors and compare the phenomic prediction accuracies across irrigated and drought trials grown in 2018. As the same flights were used for both trials these can be achieved directly via existing methods.
2) Predict the flowering times using the temporal phenomic data derived from multispectral sensor across 2017 to 2018. We adopt principal component analysis (PCA) to overcome the challenge that data are not directly comparable between years.
3) Predict flowering times using the genomic data across years (2016 to 2018) and combined data containing genomic and phenomic data between trials in 2018.
4) Integrate temporal phenomic data with genomic data to conduct GWAS, temporal genomic prediction, validation of temporal effects of candidate gene as

well as temporal SNP effects for temporal traits derived from drone images belonging to multiple time points.

Materials and Methods

Developing Recombinant Inbred Lines and Experimental Design

Parental maize inbred lines used for constructing the three bi-parental linkage populations were developed from three parental crosses: Tx740xNC356, Ki3xNC356 and LH82xLAMA. From 2014 to 2018, population were advanced to the $F_{7:8}$ using single seed descent method across College Station (summer nursery) and Weslaco (winter nursery) in Texas. In total, 238, 178 and 104 RILs were derived from Ki3xNC356, LH82xLAMA and Tx740xNC356, respectively. LH82 is a temperate adapted line while Ki3 is tropical and NC356, LAMA and Tx740 are tropical but temperate selected lines. One LAMA line (pedigree: ((LAMA2002-12-1-B-B-B-B/LAMA2002-1-5-B-B-B-B)-3-2-B-1-B3-B]) parent was Tx740 (pedigree: (LAMA2002-12-1-B-B-B)) and would be expected to be 50% related (Kerry Mayfield et al., 2012). All plantings were made in the ranges (horizontal grids, 0.76 m between plots) and rows (lateral grids 3.81 m long per plot) accounting for randomized complete block design with two replications in 2018 and one replication in 2016 and 2017. In 2018, the RILs were grown under two different experimental conditions, with and without irrigation and referred to as irrigated (2018_I) and drought (2018_D) trials in this study. RILs were planted on the 8th of April in 2016, the 24th of March in 2017 and the 14th of March in 2018 (both 2018_I and 2018_D).

Field Based High Throughput Phenotyping Platforms and Image Processing

Two different UAS platforms were used in this study. A rotary wing type UAS where a rotary wing UAS (DJI Phantom 3 Professional) equipped with a RGB sensor (12-megapixel DJI FC300X camera) was flown at an altitude of 25 m resulting in ~1 cm per pixel resolution. Additionally, a fixed-wing Tuffwing UAS mapper equipped with a multispectral camera (MicaSense RedEdge-MX) was flown at an altitude of 120 m resulting in ~7.5 cm per pixel resolution. In both platforms, 80 percent side and forward overlap was used. The RGB platform was flown 16 times over both trials (2018_I and 2018_D) in 2018, while the multispectral platform was flown 8 times over both trials in 2018 and 10 times in 2017. Dates of the flights belonging to both platforms with corresponding days after planting times are in **Supplementary Figure 1**.

To obtain the orthomosaics for every flight, raw images belonging to each flight were processed in Pix4Dmapper (https://www.pix4d.com) for RGB and Agisoft PhotoScan (Agisoft, 2016) for multispectral platforms, respectively. Later each orthomosaic were subjected to plot-based data extraction.

Data Extraction from Orthomosaic

A shapefile was first created in QGIS containing the examined population field in each orthomosaic; each orthomosaic was clipped into population levels in QGIS (https://qgis.org/en/site) using the "Clip Raster by Mask Layer" function and further data extraction was conducted in R. UAStools (https://github.com/andersst91/UAStools, (Anderson & II, 2020)and FIELDimageR (https://github.com/OpenDroneMap/FIELDimageR, (Matias et al., 2020)) packages

were used in R to create the shape files and extract the vegetation indices (VIs), respectively. Briefly, (i) shape files for each plot were created using the field map (where range, row and plot info are stored) using UAStools::plotshpcreate(); (ii) high resolution orthomosaics (only in RGB FHTP platform) were reduced using the raster::aggregate(); (iii) FIELDimageR::fieldmask()was used to remove the soil from the vegetation, (iv) FIELDiamgeR::fieldindex() was used to define the VIs; (v) FIELDimageR::fieldInfo() was used to extract the defined VIs for each plot according to the shapefile created in step one. More complete descriptions of these steps can be found in previous literature (Adak et al., 2021). VIs used in this study are presented in Supplementary Table 1.

Statistical Analysis of Phenomic Data

A nested design was implemented to examine genotypic variation of RILs for each VI extracted from orthomosaics at all flight times of RGB FHTP platform in 2018 and multispectral FHTP platform in 2017 and 2018. The main idea of the nested design was to treat the RILs nested within flight times to predict the temporal best linear unbiased predictors (TBLUP) (Adak, Murray, & Anderson, 2021; Adak, Murray, Božinović, et al., 2021). The nested design was run using restricted maximum likelihood method (REML) mixed models for each VI where all components in equation 1 (*Eq. 1*) were attributed as random effects.

$$Y_{ijklm} = \mu + F_i + G_{i(j)} + Range_{i(k)} + Row_{i(l)} + Rep_{i(m)} + \varepsilon_{ijklm} \; (Equation\ 1; Eq.1)$$

where, Y_{ijklm} is the value of each vegetation index of each row plot at all flight times; μ = overall mean; F_i = the random effect of ith flight time (as days after planting time;

DAP) with $F_i \overset{iid}{\sim} N(0, \sigma^2_{F_i})$, $i \in$ [31, 39, 49, 52, 67, 84, 91, 97, 111, 123; Tuffwing with multispectral camera FHTP platform in 2017], $i \in$ [66, 68, 86, 91, 96, 100, 105, 117; Tuffwing with multispectral camera FHTP platform in 2018], and $i \in$ [27, 34, 42, 56, 61, 64, 68, 71, 75, 78, 82, 84, 90, 99, 110, 127; rotary-wing with RGB camera FHTP platform in 2018 including irrigated and drought trials]; $G_{i(j)}$= the random effect of jth RIL within the ith flight time with $G_{i(j)} \overset{iid}{\sim} N\left(0, \sigma^2_{G_{i(j)}}\right)$, $j \in \{1, \dots, 520\}$; $Range_{i(k)}$ = the random effect of kth range within the ith flight time with $Range_{i(k)} \overset{iid}{\sim} N\left(0, \sigma^2_{Range_{i(k)}}\right)$, $k \in \{1, \dots, 32; in\ 2017\ and\ 2018\}$; $Row_{i(l)}$= the random effect of lth row within the ith flight time with $Row_{i(l)} \overset{iid}{\sim} N\left(0, \sigma^2_{Row_{i(l)}}\right)$, $l \in \{1, \dots, 34\}$; $\theta_{i(m)}$= the random effect of mth replication within the ith flight time with $Rep_{i(m)} \overset{iid}{\sim} N\left(0, \sigma^2_{\theta_{i(m)}}\right)$, $m \in \{1; in\ 2017\}$, $m \in \{1, 2; in\ 2018\}$; ε_{ijklm} is pooled error with $\varepsilon_{ijklm} \overset{iid}{\sim} N\left(0, \sigma^2_{\varepsilon_{ijklm}}\right)$. Results of the $G_{i(j)}$ component of each VI in *Eq. 1* was then combined to create the TBLUP phenomic data used as predictors in the regression models. Thus 560 predictors in RGB FHTP platform in 2018, 728 predictors in multispectral FHTP platform in 2018 and, 910 predictors in multispectral FHTP platform in 2017 were extracted to predict DTA and DTS. Temporal repeatability for each VIs was calculated based on the below *Eq. 2*:

$$Temporal\ repeatability = \frac{\sigma^2_{G_{i(j)}}}{\sigma^2_{G_{i(j)}} + \frac{\sigma^2_{\varepsilon_{ijklm}}}{no\ of\ rep}} \quad (Equation\ 2; Eq. 2)$$

Dependent phenotypic traits DTA and DTS were predicted to obtain the actual breeding values (ABVs) for each RIL using *Eq. 1* where the flight component was removed, and then DTA and DTS were merged with the phenomic data to be predicted in regression models.

A genotype by environment model was run to dissect the plasticity of the manually collected flowering times across three years (2016 to 2018) based on *Eq. 3* using REML in mixed model as follows:

$$Y_{ijkl} = \mu + G_i + E_j + (GE)_{i*j} + Range_k + Row_l + \varepsilon_{ijkl} \; (Equation\ 3; Eq. 3)$$

Where, μ = overall mean; G_i= the random effect of ith RIL with $G_i \overset{iid}{\sim} N(0, \sigma^2_{G_i})$, $i \in \{1, \dots, 520\}$; E_j= the random effect of jth environment with $E_j \overset{iid}{\sim} N\left(0, \sigma^2_{E_j}\right)$, $j \in \{2016, 2017,\ 2018\_I\ and\ 2018\_D\}$; $(GE)_{i*j}$ = the random effect of interaction of the ith RIL at jth environment; $Range_k$ = the random effect of kth range with $Range_k \overset{iid}{\sim} N(0, \sigma^2_{Range_k})$, $k \in \{1, \dots, 32; in\ 2016, 2017,\ 2018_I and\ 2018_D\}$; $Row_{i(l)}$= the random effect of lth row with $Row_l \overset{iid}{\sim} N(0, \sigma^2_{Row_i})$, $l \in \{1, \dots, 34\}$; ε_{ijkl} is pooled error with $\varepsilon_{ijkl} \overset{iid}{\sim} N\left(0, \sigma^2_{\varepsilon_{ijkl}}\right)$.

Repeatability for the DTA and DTS across trials in 2016 to 2018 was calculated based on the below *Eq. 4*:

$$Repeatability$$

$$= \frac{\sigma^2_{G\,i}}{\left(\sigma^2_{G\,i} + \frac{\sigma^2_{(GE)_{i*j}}}{no\ of\ environment} + \frac{\sigma^2_{\varepsilon_{ijkl}}}{no\ of\ environment * no\ of\ rep}\right)} \quad (Equation\ 4; Eq.\ 4)$$

To analyze the genotype by environment interaction of flowering time, weighted average of the absolute scores (WAASB) and which-won-where biplot view illustration by Genotype and Genotype-vs-Environment interaction (GGE) model were run using DTA scores of each RIL belonging to 2016, 2017, 2018_I and 2018_D trials using the "*metan*" package in R (Olivoto & Lúcio, 2020). WAASB scores were used as values of stability analysis for each RIL across four environments, and which-won-where biplot view was used to identify the diverse environments including DTA performance of the RILs.

DNA Extraction, Genotyping and Filtering

These procedures were previously documented in (Chen, 2016) but are briefly described here. Genomic DNA samples were extracted according to a CTAB protocol (Chen and Ronald, 1999) where eight seedlings were bulked for each RIL and used in DNA extraction. Genomic DNA for each of the 520 genotypes was collected using an Infinium whole-genome genotyping assay in AgReliant Genetics LLC, resulting in 17,444 genome wide single nucleotide polymorphisms (SNPs). B73 RefGEN_v3 was used to determine the physical location of the genome wide SNPs. Tassel 5 software (Bradbury et al., 2007) was used to filter and impute the genomic data as follows; (i) heterozygote calls set as missing, (ii) markers filtered if allele frequency was lower than 0.05 and missing values were higher than ten percent across RILs, finally (iii) genomic

data were imputed based on LD-kNNi (Money et al., 2015). As a result, 11,334 SNPs were retained to be used in genome wide association analysis (GWAS) and genomic prediction.

Phenomic Prediction

Eight regression methods were implemented in the Caret package in R (Kuhn, 2008) to predict the DTA and DTS using two phenomic derived data sets from RGB and multispectral FHTP platforms. The data was split into a training set (70%) and a test set (30%) randomly in each bootstrap, and 10-fold cross validation with 3 replications were applied to all regression methods. 500 bootstraps were applied in all prediction models to assess the phenomic prediction accuracy; phenomic prediction accuracy was calculated based on correlation coefficients between actual breeding value (ABV) and phenotypically estimated breeding value (PEBV) for each regression method and predicted variable (DTA and DTS). Assessment of the prediction accuracy of each regression method are given in "Prediction accuracy assessment of phenomic prediction models: scenario 1 and -2".

In the caret::train(), the regression method was set as "lm" for linear regression, "glmnet" for ridge, lasso and elastic net regressions, "rf" for random forest regression, "svmLinear" for support vector machine regression with linear kernel, "pcr" for partial least square regression, and "knn" for k-nearest neighbors regression. For each regression model, respective tunning parameters are chosen to minimize root mean square error (RMSE). The functional parameter alpha value was set to 0 for ridge regression, 1 for lasso while optimal alpha value was searched between 0 and 1 with the

5 increments for elastic net using the expand.grid (). Lambda value for ridge, lasso and elastic net regressions were also explored between 0.0001 and 1 with the 5 increments using expand.grid(). Mtry (variables randomly sampled at each split) was explored between 30 to 50 with 5 increments and ntree was set as 1000 for random forest regression. The Cost was explored between 0 to 2 with 20 increments for support vector machine regression with linear kernel. TuneLength was set as 100 to find an optimal number of principal components minimizing RMSE in the partial least square regression. TuneLength was set as 100 to specify the number of k minimizing RMSE in k-nearest neighbors regression.

Genomic Prediction

DTA and DTS were predicted using genomic data (11,334 SNPs) in the rrBLUP package in R (Endelman, 2011). "rrBLUP::A.mat()" was used to impute the missing calls in genomic data using the expectation maximization algorithm (impute.method =EM) (Poland & Rife, 2012). Data was split into a traninig set (70%) and a test data set (30%) respectively, and 500 bootstraps were applied to the genomic prediction model. Prediction accuracy of the genomic predictions were calculated based on the correlation coefficients between actual breeding value (ABV) and genotypically estimated breeding value (GEBV) of DTA and DTS in each bootstrap. Assessment of the genomic prediction model was given in "Prediction accuracy assessment of genomic prediction models: scenario 3 and -4".

Prediction Accuracy Assessment of Phenomic Prediction Models: Scenario 1

In the scenario 1, RGB and multispectral phenomic data were each used individually to predict DTA and DTS in 2018 to assess the prediction accuracy of each phenomic prediction model. 2018_I and 2018_D trials were used as tested (training) and untested (validation) environments respectively, and 70 and 30 percent split data were used as tested and untested genotypes respectively. Phenomic prediction models were trained using the 70 percent of data in 2018_I (see phenomic prediction) and four type of phenomic prediction accuracies were calculated between ABV and PEBV (i) of tested genotypes in tested environment (2018_I), (ii) untested genotypes in tested environment, (iii) tested genotypes in untested environment (2018_D) and (iv) untested genotypes in untested environment.

Prediction Accuracy Assessment of Phenomic Prediction Models: Scenario 2

In scenario 2, multispectral phenomic data were used to predict DTA and DTS between 2017 and 2018 since multispectral FHTP platform was conducted in 2017 and 2018. 2018_I and 2017 trials were used as tested and untested environments respectively. The reason the later year (2018) was selected to build the calibration was because it had both RGB and multispec, and the overall quality was improved; the important point was that these were different years for phenomic prediction. It is important to note that flight times of the multispectral FHTP platform did not match between 2017 and 2018, which is a current unsolved challenge in the use of phenomic tools. To address this principal component scores (PCs) of each VI were calculated and used for each RIL using “prcomp” function in R. The first five PCs of each VI were used in 2017 and 2018 multispectral phenomic data. Thus, predictors were able to be matched

using the PCs in multispectral phenomic data in 2017 and 2018. Here, the time interval of the VIs were chosen as close as possible; phenotype data of VI belonging to 52, 67, 84, 91, 97, 111, 123 DAPs were chosen in 2017 and, 66, 68, 86, 91, 96, 100, 105, 117 DAPs were chosen in 2018_I trial. Model training and phenomic prediction accuracy were the same as scenario 1.

Prediction Accuracy Assessment of Genomic Prediction Model: Scenario 3

In the scenario 3, genomic data was used to predict the DTA and DTS using the "rrBLUP" package. The 2018_I trial was used as a tested environment while 2018_D, 2017 and 2016 trials were used as untested environments respectively, and 70 and 30 percent split data was used as tested and untested genotypes, respectively. The genomic prediction model was trained using 70 percent of data in 2018_I (see genomic prediction) and eight types of genomic prediction accuracies were calculated between ABV and GEBV: (i) tested genotypes in tested environment, (ii) untested genotypes in tested environment, (iii) tested genotypes in untested environment (2018_D trial), (iv) untested genotypes in untested environment (2018_D trial), (v) tested genotypes in untested environment (2017 trial), (vi) untested genotypes in untested environment (2017 trial), (vii) tested genotypes in untested environment (2016), and (viii) untested genotypes in untested environment (2016).

Prediction Accuracy Assessment of Genomic Prediction Model: Scenario 4

In the scenario 4, genomic data was merged with the RGB phenomic data to predict the DTA and DTS using the "rrBLUP" package in 2018. 2018_I and 2018_D

trials were used as tested and untested environments respectively. Model training and calculations of four type of prediction accuracies were the same as scenario 1.

Prediction Accuracy Assessment of Phenomic and Genomic Prediction Model for Stability: Scenario 5

In the scenario 5, WAASB stability scores that were calculated for days to anthesis (DTA) of RILs were predicted by RGB phenomic data belonging to drought and irrigated trials in 2018 [RGB (2018_D); RGB(208_I)], RGB plus multispectral phenomic data belonging to drought and irrigated trials in 2018 [RGB(2018_D) + Multi(2018_D); RGB(2018_I) + Multi(2018_I)], RGB phenomic data belonging to drought and irrigated trials in 2018 plus multispectral phenomic data belonging to 2017 [RGB(2018_D) + Multi(2017); RGB(2018_I) + Multi(2017)] and genome wide markers (11,334 SNPS) to assess the predictive ability of six different phenomic and genomic data in the prediction of WAASB stability scores. 70 and 30 percent split data was used as tested and untested genotypes, respectively for each data set. To be consistent, ridge regression in caret and rrBLUP packages were used for phenomic and genomic prediction respectively. Models were trained using the 70 percent of each data set (see phenomic and genomic prediction) and two type of prediction accuracies were calculated (i) of tested genotypes (CV1), (ii) untested genotypes (CV2).

Genome Wide Association Study of Temporal Traits and Flowering Times

Beyond prediction, it is valuable to understand the underlying biological function of phenomic features that predict the flowering time traits of interest. The fixed and random model circulating probability unification (FarmCPU) method was conducted in

GAPIT (version 3) in genome wide association studies (GWAS) in R using 11,334 filtered SNPs (Liu et al., 2016; Wang and Zhang, 2021). Flowering times (DTA and DTS) belonging to 2016, 2017, 2018_D and 2018_I, and temporal traits of all vegetation indices in RBG phenomic data belonging to 2018_D and 2018_I and multispectral phenomic data belonging to 2017, 2018_D and 2018_I were used as phenotype data in GWAS. To control for population structure, genomic data was used to calculate a kindship matrix based on the centered_IBS method (Endelman & Jannink, 2012), and principal component analysis (PCA) in Tassel 5 software (Bradbury et al., 2007). Three PCs (explaining 26.4%, 8.3% and 2.2% among the first three PCs) were used along with kindship matrix in GWAS studies. Population structure, PC scores, and SNP distribution across each chromosome are shown in Figure 45. A false positive discovery (FDR) rate was applied as [p <= 10^(-5)] to consider the significant SNPs in the GWAS study. Candidate genes within 100 kb of discovered SNPs, as well as within the linkage disequilibrium (LD) block where the minimum R2 value was 0.8. LD was calculated and visualized using the LDheatmap package in R (Shin, Blay, McNeney, & Graham, 2006). LD blocks of ten chromosome are presented in Figure 46.

Environment Modelling of The Trials

Thirteen environmental parameters were collected at 10-minute increments and obtained from the Texas A&M Research Farm Mesonet. Wind speed [WS (m s-1)], gust [Gust (m s-1)] temperature [Temp (°C)], relative humidity [RH (%)], barometric pressure [BP (mBar)], solar radiation [SR [W (m2)-1], photoperiod [photoperiod [hr]), growing degree days; [GDD [(T_max+T_min)/2-T_base (10°C)], photothermal time

[PTT; (GDD*photoperiod)], photo thermal ratio [PTR; (GDD/photoperiod)], diurnal temperature range [DTR; (T_max-T_min)], minimum temperature (Min, T_min), and maximum temperature (Max, T_max) were used as environmental parameters. The environmental parameters were used as predictors to classify the trials grown in 2016, 2017 and 2018. To do so, environmental parameters were merged from planting times of each trial to average of the days to anthesis times of each trial. Average values of DTA were predicted by Eq. 4 resulting in 68, 70 and 76 DTA for each trial grown in 2016, 2017 and 2018 respectively. Predicted variables were years treated as categorical variables. This classification was intended to dissect the underlying environmental paraments of flowering time plasticity occurring across years with different planting times for the RILs in this study. A random forest algorithm was used to classify the years based on the environmental variables using the 10-fold with three repeat cross validation in caret package in R. Variable importance scores (*varImp*) were calculated to identify the most important environmental parameters, and a partial dependence plot was used to visualize the probability of occurrence of the trials grown in different years based on the values of each environmental predictor using edarf package in R. Environmental parameters and their values from planting time to the mean of days to anthesis times for each trial grown in 2016, 2017 and 2018 were illustrated in Supplementary Figure 46. Correlations among the environmental variables for each trial grown in 2016, 2017 and 2018 were given in Supplementary Figure 47.

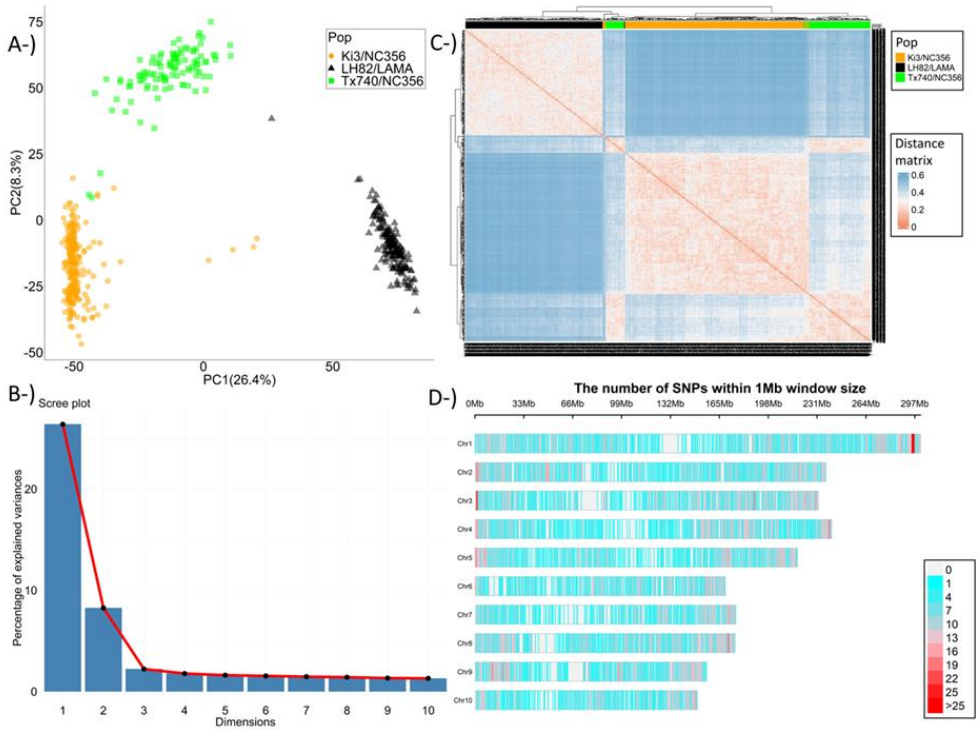

Figure 45 A-) the biplot illustration including first two principal component showing separation of 520 recombinant inbred lines (RILs), B-) Scree plot showing the explained percent variation by each principal component, C-) distance matrix showing the population structure of 520 RILs, and D-) distribution of 11,334 filtered single nucleotide polymorphisms across ten chromosomes.

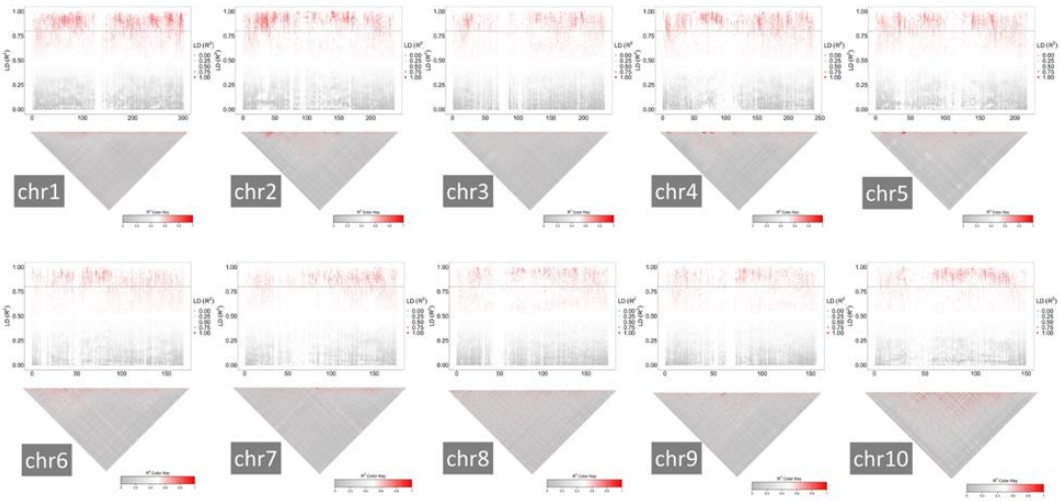

Figure 46 the linkage disequilibrium (LD) blocks of each chromosome were illustrated based on R^2. X axis shows the genomic positions in (mega basepair) and points shows the R^2 value of pairwise LD value of among SNPs. Vertical dashed line indicates the 0.8 LD threshold in each chromosome.

Results

Nested Design Results: Temporal Repeatability, Variance Components, Temporal Breeding Values and Correlation

Temporal repeatability values of VIs in multispectral phenomic data varied between ~0.10 and 0.60 in 2017, ~0.16 and 0.61 in 2018_D, ~0.19 and 0.69 in 2018_I whereas temporal repeatability values of VIs in RGB phenomic data varied between ~0.50 and 0.71 in 2018_D, ~0.54 and 0.81 in 2018_I (Supplementary Data 1). The RGB platform had higher resolution (~1 cm per pixel) than the multispectral platform (~7.5 cm per pixel) thanks to flight surveys along with a lower flight altitude (25 m) than those of multispectral HTP platform, resulting in overall higher temporal repeatability values in the RGB phenomic data. The flight component in the nested design (*Eq. 1*) explained the highest amount of total variation for a majority of VIs in the phenomic data set (Supplementary Data 1). The genetic variance components, in which genetic materials (RILs) were considered nested within flights, were used to predict temporal breeding values of RILs for each VI in RGB and multispectral phenomic data. Temporal breeding values were found to have different temporal trajectories throughout plant growth (Supplementary Data 2). Correlations were calculated (i) within five phenomic data and genomic data, and (ii) between phenomic data and flowering times (DTA and DTS). Correlation between phenomic data and flowering times were found to be temporally changing between -0.4 and +0.4 depending on the flight dates. Temporal VIs in RGB

phenomic data in 2018 (drought and irrigated) had the correlations that were mostly inverted in flowering times from positive to negative or vice versa, these correlation inversions were more obvious between flowering times and RGB phenomic data belonging to 2018 drought trial than RGB phenomic data belonging to 2018 irrigated trial (Figure 47). In the 2017 multispectral phenomic data, it was calculated that rather than the inversion of the correlations, the correlations approached zero from the planting time to the flowering time and continued in this way (Figure 47). However, there was no obvious inversion in multispectral phenomic data belonging to 2018 (drought and irrigated), because there were no flight date belonging to earlier time point of growth (Figure 47).

Correlation of phenomic data showed that temporal VI phenotypes belonging to the same growth stages were usually correlated in a positive way, whereas temporal phenotype of VIs belonging to different growth stages often negatively correlated or had no correlation (Figure 48). High temporal dimension (time points) of VI inhibited the multicollinearity problem in phenomic data set.

Plasticity of the Flowering Times

The genotype by environment model (Eq. 3) revealed the existence of plasticity in flowering times. The year variance component explained the highest percentage of the total variation (59.6% for DTA and 51.2% for DTS); interaction variance components between pedigree (RILs) and years explained 3.5% and 4.6% variation of total variation for DTA and DTS, respectively (Figure 49). Weighted average of the absolute scores (WAASB) were calculated as a unit of stability index for each RIL.

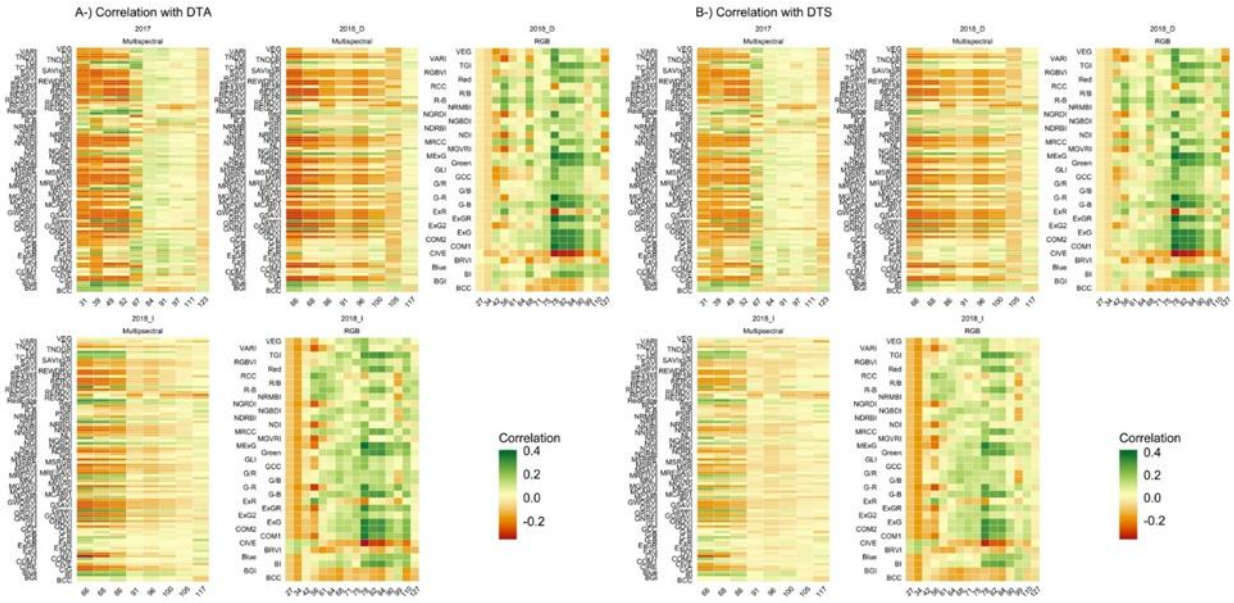

Figure 47 shows the correlations as heatmap illustration between each vegetation index (on the Y axis) belonging to each time point (on the X axis as days after planting unit) in each phenomic data and flowering times (DTA and DTS). A and B shows the correlations between each phenomic data with DTA and DTS respectively. Phenomic data was defined at the top of each heatmap where top line represents the year and bottom line shows the type of phenotyping platform (multispectral or RGB).

This showed that as environmental means in flowering times increased from 2016 to 2018, stability of the RILs weakened. Which-won-where view of GGE biplot illustration also revealed that DTA performance of RILs were found to be affected by different planting times of the different trials from 2016 to 2018 (Figure 49). Under the existence of plasticity, flowering times across years with different planting times along with the interplays of the environmental parameters, phenomic, genomic and phenomic plus genomic data were used to predict flowering times across trials in different years and managements to assess their predictive ability by applying four different cross validation schemes.

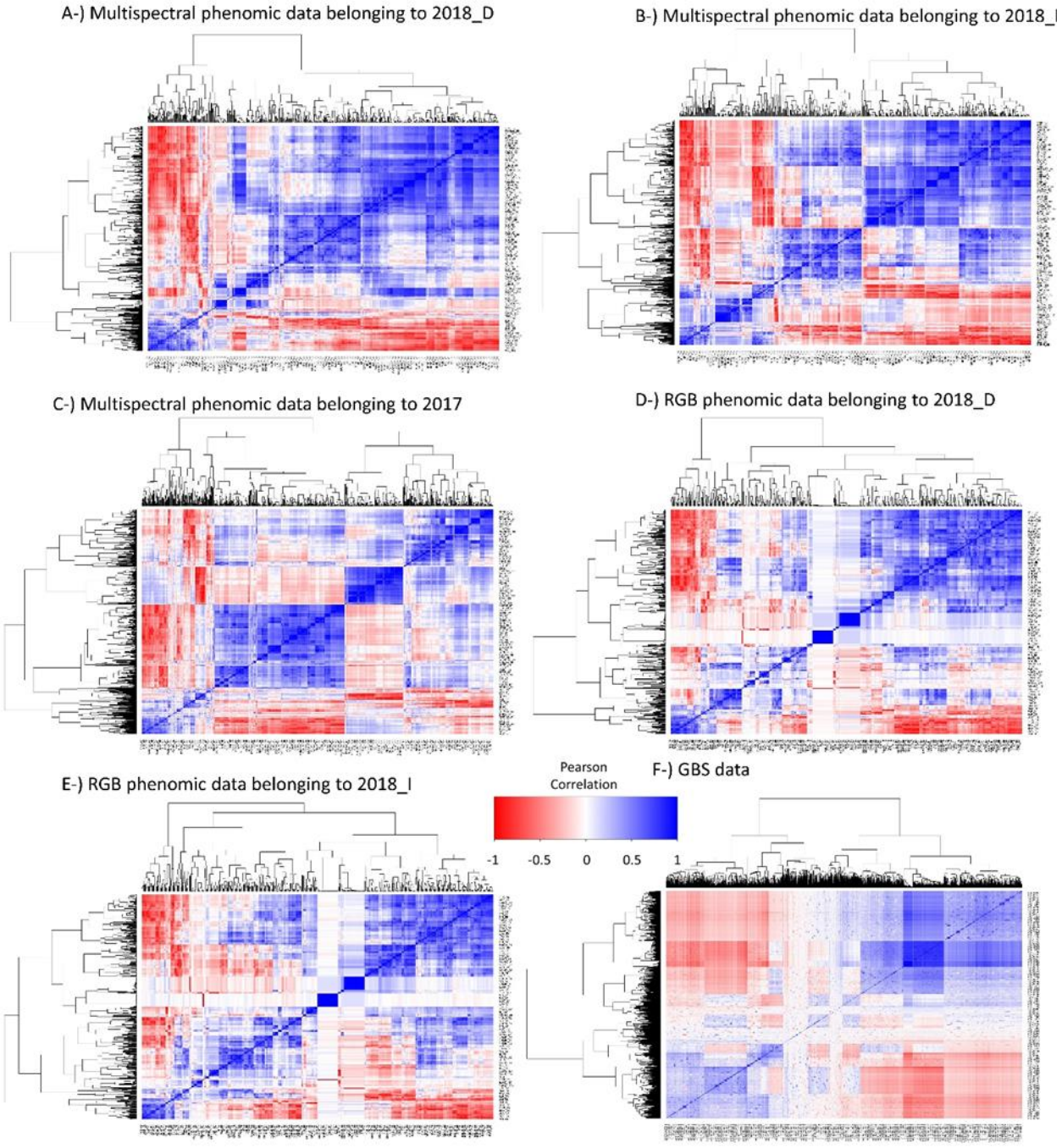

Figure 48 the correlation of temporal VIs in (A) the multispectral phenomic data in 2018_D, (B) in 2018_I, (C) in 2017 and RGB phenomic data in (D) 2018_D, (E) 2018_I and (F) GBS data.

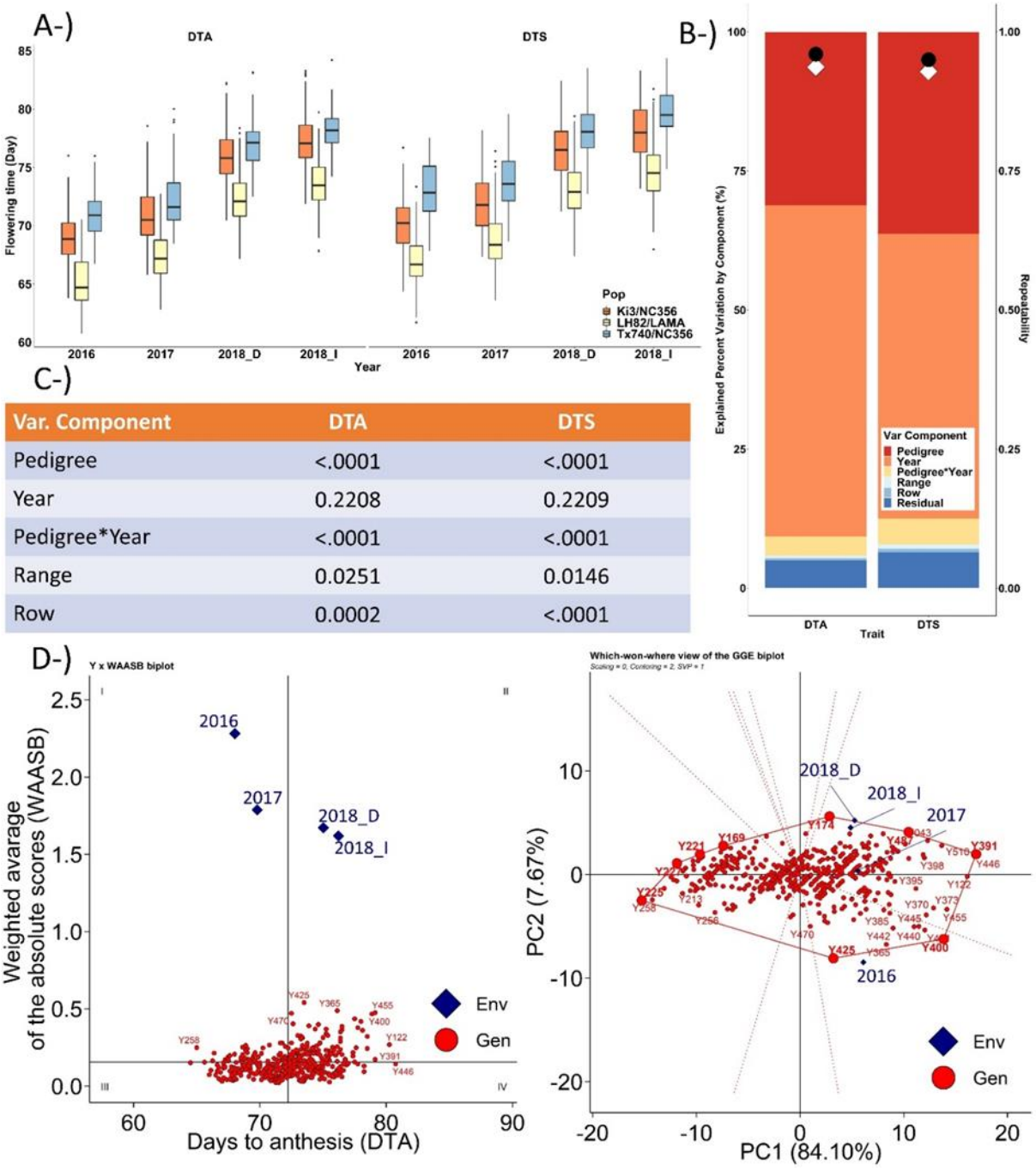

Var. Component	DTA	DTS
Pedigree	<.0001	<.0001
Year	0.2208	0.2209
Pedigree*Year	<.0001	<.0001
Range	0.0251	0.0146
Row	0.0002	<.0001

Figure 49 Results of the variance component of genotype by environment model (equation 3, Eq. 3). A-) box plots of the predicted flowering time values of recombinant inbred lines belonging to their sub-populations across trials and years as a result of the genotype by environment interaction component in *Eq. 3*. B-) explained percent

variation by each component in Eq. 3. C-) statistically significance information of each component in *Eq. 3*. D-) Weighted average of the absolute scores (WAASB)-based stability values of each RIL across 2016, 2017, 2018_D and 2018_I (left), and which-won-where biplot illustration by Genotype plus Genotype-vs-Environment interaction (GGE) analysis showing diverse environments (trials in different years: 2016, 2017, 2018_I and 2018_D) and different performances of RILs in terms of days to anthesis (DTA) across environments (left).

Results of Scenario 1

Prediction accuracies were obtained from eight different machine learning regression model algorithms using the multispectral and RGB phenomic data in scenario 1. The most challenging cross-validations (CVs), prediction of tested and untested RILs in the untested environment (CV3 and CV4), demonstrated that ridge regression was the best performing model for predicting flowering time in this data set using both RGB and multispectral phenomic data (Figure 50). Ridge regression prediction accuracy was ~0.36 for DTA and ~0.27 for DTS for CV3; and ~0.35 for DTA and ~0.25 for DTS in CV4 when multispectral phenomic data was used. Ridge regression prediction accuracy was ~0.54 for DTA and ~0.52 for DTS in CV3, ~0.52 for DTA and ~0.48 for DTS in CV4 when RGB phenomic data was used (Figure 50). The linear model was found to be the worst performing model. Using this methodology of scenario 1, management conditions with the same flight dates can be tested but this approach is impossible across environments or years where flight dates differ and may not be valid where rates of crop development differ. For this reason, an approach using principal component analysis (PCA) was developed and tested in scenario 2.

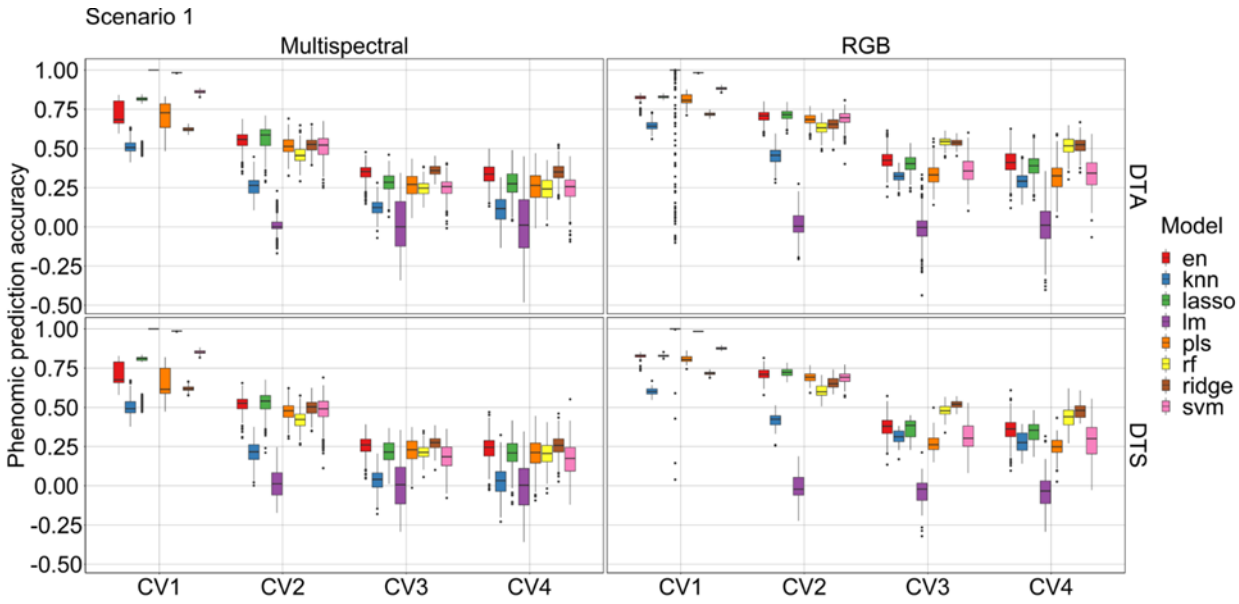

Figure 50 Phenomic prediction accuracies (y-axis) of eight machine learning regression models (x-axis) for days to anthesis (DTA) and silking (DTS) using multispectral and RGB phenomic data in scenario 1. En: elastic-net regression, lasso: lasso regression, pls: partial least square regression, ridge: ridge regression, knn: k-nearest neighbor regression, lm: linear regression, rf: random forest regression, svm: support vector machine regression. Cross validation 1 (CV1): tested RILs in tested environment (2018_I trial), CV2: untested RILs in tested environment (2018_I trial), CV3: tested RILs in untested environment (2018_D trial), CV4: untested RILs in untested environment (2018_D trial).

Results of Scenario 2

This prediction scenario addressed the subject of prediction of the flowering times between years using multispectral phenomic data across two years whose flight times did not match. To address different flight times, principal component scores (PCs) were used to align predictors in multispectral phenomic data across two years 2018 (both irrigated and drought trials) and 2017 to conduct the prediction of the flowering times across years (RGB was not available in 2017). Among the eight machine learning regression models, ridge regression was found to be the best performing model, though

not significantly different from others, and predicted flowering times across years with accuracies of ~0.15 for DTA and ~0.16 for DTS in CV3 and CV4 (Figure 51).

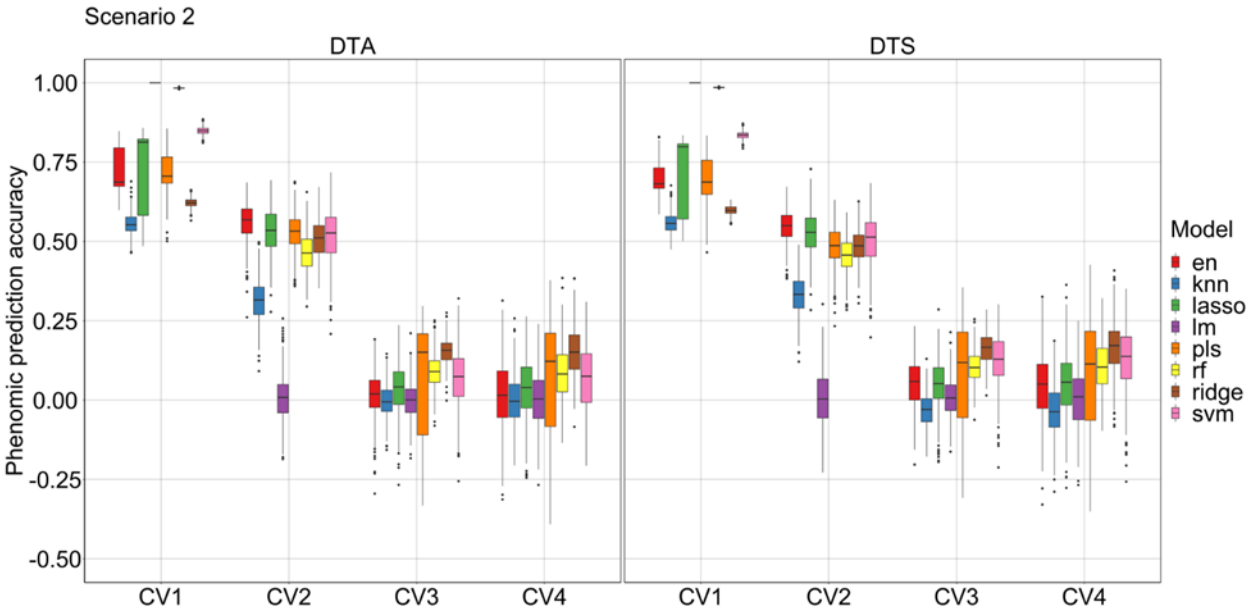

Figure 51 phenomic prediction accuracies (y-axis) of eight machine learning regression models (x-axis) for days to anthesis (DTA) and silking (DTS) using multispectral and RGB phenomic data in scenario 2. En: elastic-net regression, lasso: lasso regression, pls: partial least square regression, ridge: ridge regression, knn: k-nearest neighbor regression, lm: linear regression, rf: random forest regression, svm: support vector machine regression. Cross validation 1 (CV1): tested RILs in tested environment (2018_I trial), CV2: untested RILs in tested environment (2018_I trial), CV3: tested RILs in untested environment (2017 trial), CV4: untested RILs in untested environment (2017 trial).

Results of Scenario 3

Genome wide markers were used as predictors in *rrBLUP* algorithm to predict the flowering times across trials and years in scenario 3; genomic prediction model (GP) was trained in 2018_I (to compare with other scenarios), and trained GP model was used to predict the flowering times in three different untested environments (2018_D, 2017, and 2016). Genomic prediction accuracies of untested RILs were ~0.67 for DTA and

~0.65 for DTS in 2018_D (CV4:), ~0.33 for DTA and DTS in 2017 (CV6), and 0.56 for DTA and 0.49 for DTS in 2016 (CV8) trial (**Figure 52**).

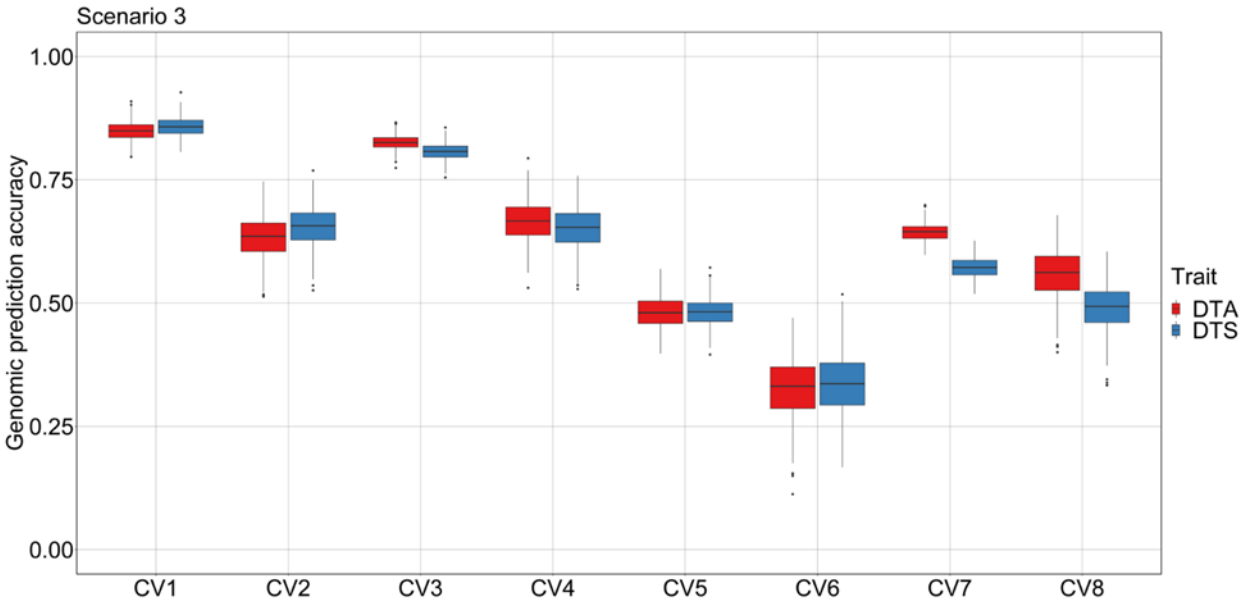

Figure 52 Genomic prediction accuracies (y-axis) of different cross validation schemes (x-axis) for days to anthesis (DTA) and silking (DTS) using genome wide markers in *rrBLUP* in scenario 3 with all trained on 2018_I. Cross validation 1 (CV1): tested RILs in tested environment (2018_I trial), CV2: untested RILs in tested environment (2018_I trial), CV3: tested RILs in untested environment (2018_D trial), CV4: untested RILs in untested environment (2018_D trial). CV5: tested RILs in untested environment (2017 trial), CV6: untested RILs in untested environment (2017 trial). CV7: tested RILs in untested environment (2016 trial), CV8: untested RILs in untested environment (2016 trial).

Results of Scenario 4

Genome wide markers were merged with RGB phenomic data to predict the flowering times in scenario 4; model was trained in 2018_I and used to predict the flowering times in 2018_D untested environment. Prediction accuracy of untested RILs were 0.77 and 0.75 for DTA and DTS in 2018_D, respectively (Figure 53). These

accuracies were higher than that of phonemic or genomic data independently as predictors of flowering time.

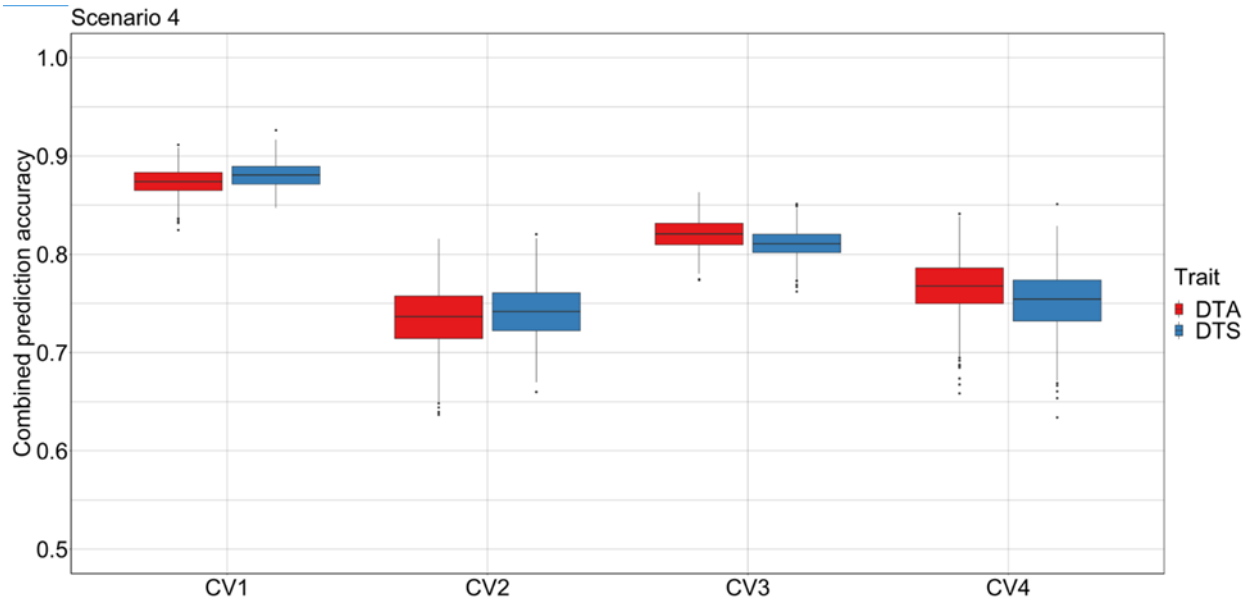

Figure 53 Combined prediction accuracies (y-axis) of different cross validation schemes (x-axis) for days to anthesis (DTA) and silking (DTS) using genome wide markers and RGB phenomic data as combined predictors in *rrBLUP* in scenario 4. Cross validation 1 (CV1): tested RILs in tested environment (2018_I trial), CV2: untested RILs in tested environment (2018_I trial), CV3: tested RILs in untested environment (2018_D trial), CV4: untested RILs in untested environment (2018_D trial).

Results of Scenario 5

Genome wide markers (GP), RGB phenomic data belonging to drought and irrigated trials in 2018 [RGB (2018_D); RGB(208_I)], RGB plus multispectral phenomic data belonging to drought and irrigated trials in 2018 [RGB(2018_D) + Multi(2018_D); RGB(2018_I) + Multi(2018_I)], RGB phenomic data belonging to drought and irrigated trials in 2018 plus multispectral phenomic data belonging to 2017 [RGB(2018_D) + Multi(2017); RGB(2018_I) + Multi(2017)] were used as predictors to

predict the stability of RILs (WAASB scores) for DTA calculated across three years. Stability was predicted using the phenomic and genomic data due to the fact that all the phenomic and genomic data provided positive prediction accuracy (0.18 - 0.35). The best prediction accuracy for CV2 in scenario 5 was provided by genome wide markers (0.35) followed by combined phenomic data containing RGB phenomic data belonging to 2018 and multispectral phenomic data belonging to 2017 (~0.25) (Figure 54).

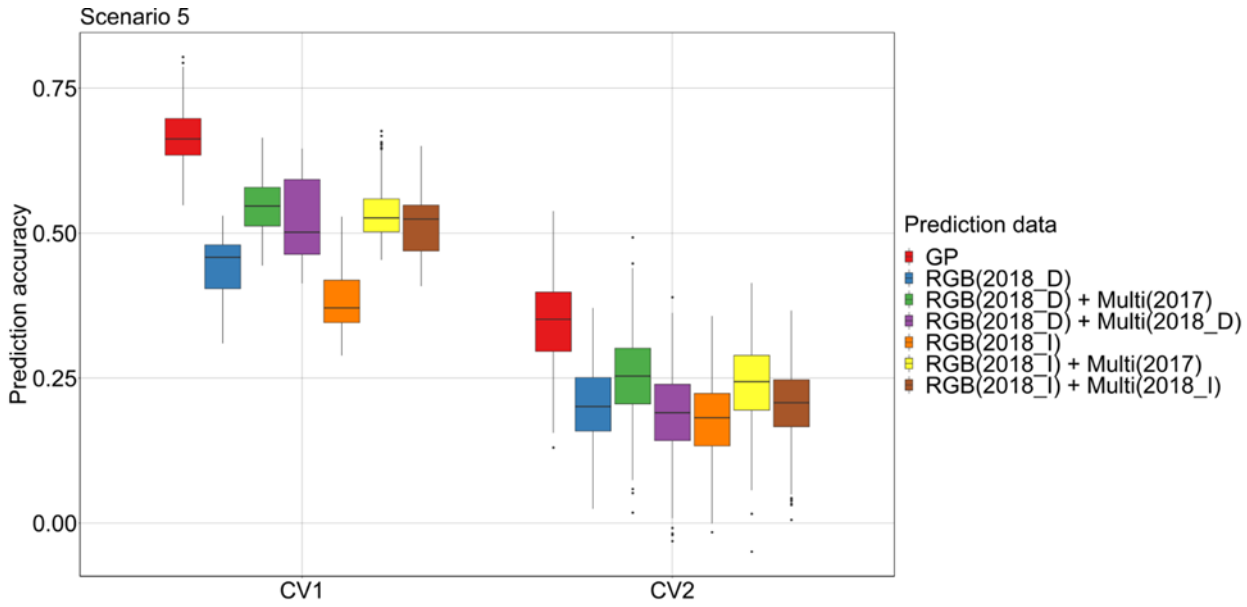

Figure 54 prediction accuracy for days to anthesis (DTA) stability index (WAASB) of RILs by RGB phenomic data belonging to drought and irrigated trials in 2018 [RGB (2018_D); RGB(208_I)], RGB plus multispectral phenomic data belonging to drought and irrigated trials in 2018 [RGB(2018_D) + Multi(2018_D); RGB(2018_I) + Multi(2018_I)], RGB phenomic data belonging to drought and irrigated trials in 2018 plus multispectral phenomic data belonging to 2017 [RGB(2018_D) + Multi(2017); RGB(2018_I) + Multi(2017)].

Important Predictor/Time Combination

Variable importance scores (*varImp*) were derived from the output of ridge regression because it was nominated as the best model in the prediction of the flowering times in the most challenging phenomic prediction scenarios (eg. CV3 and CV4 in

scenario 1 and 2). RGB phenomic data of 2018_I nominated RCC as one of the most informative VIs across multiple time points, followed by NGRDI, VARI, GCC and ExR. Multispectral phenomic data of 2018_I nominated NLI and MNLI as the most informative VIs across multiple time points in both prediction flowering times (**Figure 55**).

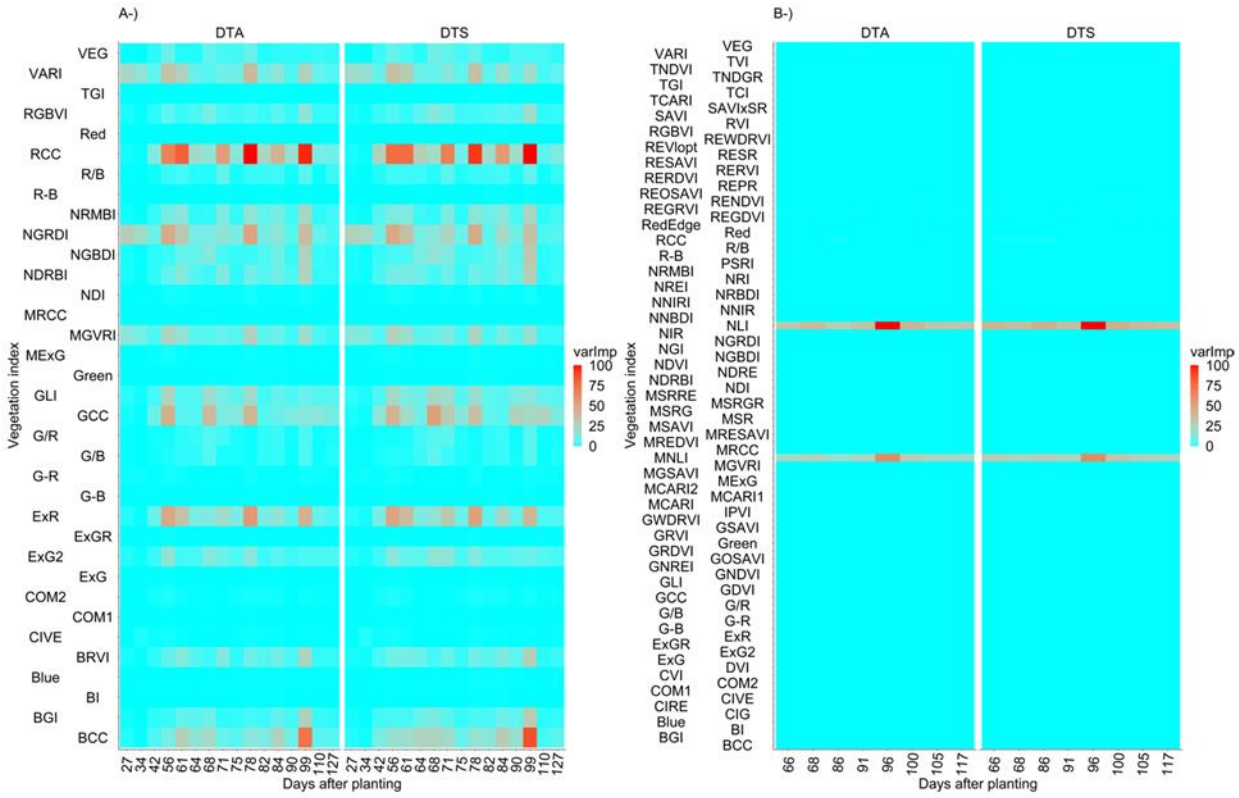

Figure 55 variable importance scores (*varImp*) derived from the ridge regression showing the variable importance scores of each vegetation index (y axis) belonging to each time point (x axis). A-) *varImp* belonging to the RGB phenomic data in scenario 1. B-) *varImp* belonging to multispectral phenomic prediction in scenario 1.

Partial Dependence Plot

Partial dependence plots were used to visualize the relationships between time points of most important variables (based on *varImp*) and predicted trait (DTA) from the

ridge and random forest regressions. RCC and NLI were identified by the RGB and multispectral phenomic data, respectively, and temporal relationships between RCC, NLI and DTA were visually identified. Direction of temporal relationships were found vary in positive or negative ways depending on values of RCC and NLI belonging to different time points (Figure 56). For example, the RCC value belonging to 56, 61, 78 and 99 DAPs were nominated among the most important VI/time points combination based on the *varImp* scores. Flowering occurred 68-83 days after planting (DAP), RCC values belonging to 56 and 61 DAPs (corresponding to before flowering times) had a positive relation with DTA whereas RCC values belonging to 78 and 99 had the negative relationships with DTA (Figure 56). Similarly, NLI values belonging to 96 DAP was nominated as an important VI/time point combination and was found to have negative relationship with DTA (Figure 56). Partial dependence plots of other important VIs in RGB and multispectral phenomic data were given in supplementary data 3.

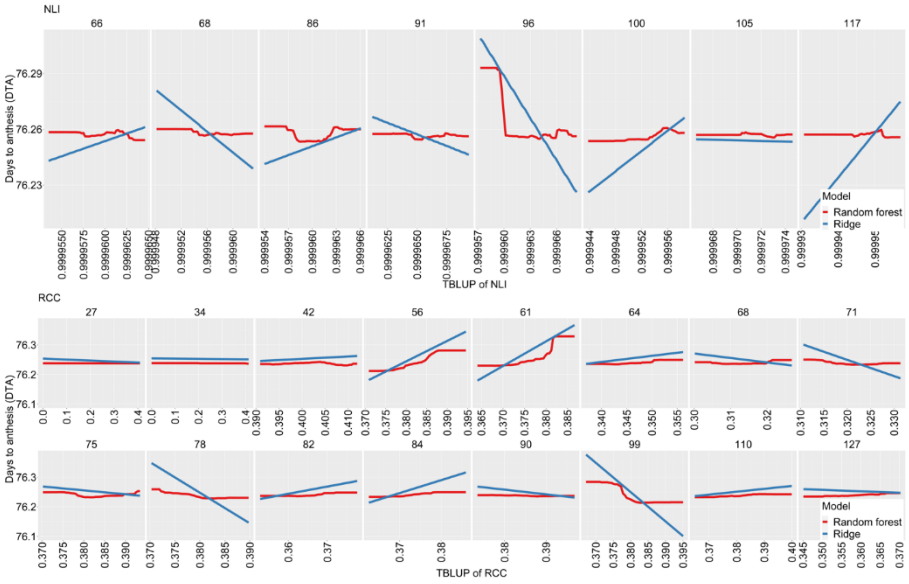

Figure 56 Partial dependence plots between temporal phenotype of NLI and RCC, which were nominated most important variable in RGB and multispectral phenomic data based on *varImp*, respectively, and predicted days to anthesis (DTA). Each flight time was separated as consecutive facet for NLI and RCC, showing the positive, negative and linear relationship depending on the time points.

Genome Wide Association Studies Discovered Plant Development Related Genes Using Temporal Phenotype

Temporal phenotype data of VIs in multispectral data and RGB phenomic data were used as phenotype data in a genome wide association study (GWAS) analysis. Combining all phenotypic data across environments, 728 phenotypes in 2018_I, 728 phenotypes in 2018_D and 910 phenotypes in 2017 belonging to multispectral data; 560 phenotypes in 2018_D and 560 phenotypes in 2018_I belonging to RGB data resulted in 3468 unique phenomic temporal x VI predictors. These 3468 phenomic measures were used in association mapping analysis, resulting in discovery of 6151 SNPs, of which 1599 were unique SNPs (Figure 59, Supplementary data 4).

A GWAS was conducted using all 2016, 2017 and 2018 DTA and DTS and the 11,334 SNPs collected. A total of 9 segregating loci were discovered for DTA and 13 SNPs for DTS using a FDR significance threshold [-log10(p) > 5]. Five of these loci corresponded to well-known candidate genes involved in various steps of floral transition pathways. These genes were identified based on strong LD blocks ($R2 \geq 0.8$) in the proximal regions of significant SNPs discovered for DTA and DTS (Figure 57). Of those, two phytochrome related genes, GRMZM2G057935 (phyC1) and GRMZM2G092174 (phyB2), transduce daylight into endogenous circadian clock pathway to initiate the floral transition (Dong et al., 2012). One of the 24 phosphatidylethanolamine-binding

(*PEBP*) genes in maize, GRMZM2G440005 (pebp24), corresponds to FLOWERING LOCUS T (*FT*) in Arabidopsis and regulates the floral transition in maize (Danilevskaya, Meng, Hou, et al., 2008). The small ubiquitin-related modifier (SUMO) related gene in maize, *GRMZM2G010505* (*esdl4*), is related to the SUMO-specific protease *ESD4* (*At4g15880*) in Arabidopsis causing early flowering in maize (Murtas et al., 2003). One of the photoperiod responsive genes in maize, *GRMZM2G381691* (*cct1*), encodes a CCT domain, it was expressed high in tropical maize germplasm under longer day circumstances (Hung et al., 2012) and contributes the maize adaptation towards to higher latitudes (C. Huang et al., 2018). Genomic positions of the SNPs discovered for the VIs and close to the genomic positions of the candidate flowering genes are illustrated in Figure 58 with nearby strong LD blocks illustration.

The five candidate genes, discovered using DTA and DTS, were also discovered using the temporal phenotype of certain VIs in GWAS analysis, considering the strong proximal LD regions ($R2 \geq 0.8$) containing the genomic positions of five candidate flowering genes (*phyC1, esdl4, pebp24, phyB2, cct1*) and the SNPs that were discovered for the VIs (Figure 58, supplementary data 4). For instance, SNPs, which were discovered for 17 different VIs belonging to various DAPs in multispectral phenomic data, were also discovered within the proximal genomic regions of the *GRMZM2G381691* (*cct1*) (Figure 58, supplementary data 4). The temporal phenotype data of the 17 VIs in multispectral phenomic data belonged to times ranging from 52 to 105 DAPs depending on 2017, 2018_I and 2018_D trials.

The temporal phenotype data of certain VIs also discovered flowering-related candidate genes different from the candidate genes discovered using the phenotype data of flowering times in the GWAS study. *GRMZM2G414779* (*EXPA11*) was discovered by multispectral phenomic data belonging to 2018_I, and was previously discovered for flowering times in maize (Jinyu Wang et al., 2021). *GRMZM2G011357* (indeterminate; ID1) was discovered by RGB phenomic data belonging to 2018_D, and was one of the flowering-time genes reported by (Wong & Colasanti, 2007) which has been shown to be upregulated under drought conditions (Kim, Song, Park, Kim, & Lee, 2021). *GRMZM2G017087* (*KNOTT1*; *kn1*) is the ortholog of GIBBERELLIC ACID INSENSITIVE (GAI) gene in Arabidopsis, and it is related to the GA pathway of flowering times in maize identified to impede the accumulation of the gibberellins regulating the GA2ox1 gene (Bolduc & Hake, 2009). *GRMZM2G106613* (LUMINIDEPENDENS, *ldp1*) was discovered by multispectral and RGB phenomic data belonging to 2017 and 2018_D, it is the ortholog of LUMINIDEPENDENS in Arabidopsis that regulates the flowering time (I. Lee et al., 1994). *GRMZM2G110153* (*zmm16*) was discovered by multispectral and RGB phenomic data belonging to 2017, 2018_D and 2018_I, it belongs to MADs-domain transcription factor that control the floral organ development in maize (Setter et al., 2011), and was found to have an expression peak in mature anthers (S. Qi et al., 2021). *GRMZM2G045275* (*pco135758*, ELF3-like) and *GRMZM2G106903* were discovered by RGB and multispectral phenomic data belonging to 2018_D and 2018_I; it controls the early flowering and flowering time related protein in maize respectively, their homologs correspond to

heading date, flowering time, and plant height in rice (S.-Y. Chen, Wang, & Cai, 2007; Fu et al., 2009). Another early flowering related gene, *GRMZM5G877647* (ELF4-like3) and *GRMZM2G359322*, discovered by RGB phenomic data belonging to 2018_I, encodes DUF1313 related protein that is highly preserved domain in plants and related to photoperiod sensitivity in maize (J. Li et al., 2016). *GRMZM2G141756* (*pebp7*, *ZCN7*) was discovered by multispectral phenomic data belonging to 2017, and is one of the phosphatidylethanolamine-binding (PEBP) genes that involves the floral transition in maize (Danilevskaya, Meng, Hou, et al., 2008); this is the paralog of ZCN8 encoding florigen hormone in maize (Mascheretti et al., 2015). Another phosphatidylethanolamine-binding (*PEBP*) genes, *GRMZM2G373928* (*pepb14*; *ZCN14*) and *GRMZM2G338454* (*pebp3*; *ZCN3*), discovered by multispectral and RGB phenomic data belonging to 2017, 2018_D (Danilevskaya, Meng, Hou, et al., 2008). AC233870.1_FG003 (pza01875) was discovered by multispectral and RGB phenomic data belonging to 2017 and 2018_I, and it is ELF3-like gene involving the regulation of photoperiodic related flowering (Kim et al., 2021). *GRMZM2G067921* (*dlf1*) was discovered by multispectral phenomic data belonging to 2017 and 2018_I, and it is homolog FLOWERING LOCUS D (FD) in Arabidopsis encoding the bZIP protein domain to initiate the floral signal in shoot apical meristem in maize (Muszynski et al., 2006). *GRMZM2G179264* (*pebp8*; *ZCN8*) was discovered by RGB and multispectral phenomic data belonging to 2018_D and 2018_I, it is a member of PEBP gene family promoting the transition from vegetative to generative phase encoding the florigen hormone in maize (X. Meng et al., 2011). *GRMZM2G004483* (*cct2*) was discovered by

multispectral phenomic data belonging to 2018_I and 2017, it encodes CCT domain that regulates flowering under long days in maize as well as maize adaptation to higher latitudes (C. Huang et al., 2018). GRMZM2G076602 (AP2; APETALA2-like TF) was discovered by multispectral and RGB phenomic data; it is floral development related gene and down regulated under drought stress causing the delayed flowering (Danilevskaya et al., 2019). Temporal values of VIs belonging to different growth stages of RILs enabled discovery of flowering related candidate genes in GWAS including early- and mid-vegetative stages as well as early reproductive stages depending on trials in different years that were given in supplementary data 4 and Figure 58.

Various plant development and plant defense related genes were also discovered using the temporal phenotype of VIs belonging to multispectral and RGB phenomic data in GWAS analysis (Supplemental data 4). While these are unlikely to have affected flowering time, it is likely that they are segregating in these population and responsible for some of the phenomic variation observed across growth. These genes are briefly mentioned. *GRMZM2G044481* (*an2*) involves kauralexin synthesis in maize that suppress the fungal attack (e.g. Fusarium) (Harris et al., 2005), and deficiency in kauralexin synthesis increased drought sensitivity in maize (Vaughan et al., 2015). *GRMZM2G077197* (*ZmNPR1*) is responsible for encoding the salicylic acid contributing immune system and initiate the plant defense in maize (Y. Wu et al., 2012). *GRMZM2G163015* (*acs1*) syntheses the ethylene and upregulated under the drought condition in maize (H. Zheng et al., 2020). *GRMZM2G083810* (*hsp18f*) encodes the heat shock protein that are responsible for heat stress in maize (J. Li et al., 2019).

GRMZM2G449033 (*na1*) is one of the well-known genes regulating the brassinosteroids biosynthesis, causing the dwarf mutants with deficiency in brassinosteroids biosynthesis in maize (Hartwig et al., 2011). *GRMZM2G373522* (dhn3) encodes dehydrin related protein that was upregulated under the drought and heat stress in maize (Blein-Nicolas et al., 2020; P. Li et al., 2017). *GRMZM2G081310* (*cdpk7*) differentially expressed under the Aspergillus flavus infection in maize (Parish, Williams, Windham, & Shan, 2019). *GRMZM2G025867* (*pco093706*) controls the drought stress by regulating the osmatic pressure based on proline synthesis in maize (L. Cao et al., 2018). *GRMZM2G118737* (*invan2*) regulates the nitrogen remobilization (X. Gong et al., 2020). *GRMZM2G414660* (*PsbZ*) encodes the photosystem II PsbZ protein that was upregulated under drought stress to contribute the efficiency of the photosynthesis (B. Wang et al., 2018). *GRMZM2G076987* differentially expressed for the phosphate deficiency in maize (Gupta, Kumari, Kumar, & Varadwaj, 2017). *GRMZM2G058451* (*bhlh164*) involves various maize development related traits such as cell wall associated pathways (Ramsay & Glover, 2005), root development (Z. Li et al., 2011) and photosynthetic related traits in maize (X. Zhao et al., 2019). *GRMZM2G072280* (*Ihca2*) involves chlorophyll fluorescence pathways by regulating the light absorption and transport; down regulation of this gene caused the low photosynthetic rate (X. Mu, Chen, Chen, Yuan, & Mi, 2017). *GRMZM2G056075* (*mus1*) is responsible for the DNA repair and replication mechanism in maize (Youssef et al., 2019). *GRMZM2G384528* (*ca3p4*) contributes drought stress tolerance (B. Wang et al., 2018). *GRMZM2G120401* (*ereb194*) regulates the early embryogenesis in monocot including maize (P. Zhao,

Begcy, Dresselhaus, & Sun, 2017). *GRMZM2G060824* is the phosphate homeostasis and deprivation related gene in maize (Calderón-Vázquez, Sawers, & Herrera-Estrella, 2011; Schlüter et al., 2012). *GRMZM2G335720* (*phd10*) encodes methyl-lysine related involving cellular processes and cell cycle development (Qiu, Sawada, Zhang, & Cheng, 2002). *GRMZM2G146885* was upregulated under drought for peroxisome that leads the ROS in maize (H. Zheng et al., 2020). *GRMZM2G020216* (*mpk2*) is responsible for the map kinases synthesis being associated to senescence (Lindsey, 2015). *GRMZM2G161905* (*gst25*) is a glutathione S-transferase gene that are associated with multiple pathogen resistances in maize such as southern and northern leaf blight and gray leaf spot (Wisser et al., 2011). *AC197146.3_FG002* (*myb69*) involves the cuticular wax pathway, showing co-expression with glossy genes in maize (J. Zheng et al., 2019). *GRMZM2G095725* (*incw5*) involves raffinose metabolism related genes, raffinose is key oligosaccharide to response harsh environmental factors such as drought and heat stresses in maize (M.-L. Zhou et al., 2012), it also contributes the maize kernel development involving grain filling and kernel size (J. Liu et al., 2017).

Temporal phenotypic data of VIs at time points including flowering times and time points close to flowering times (before and after) in high-resolution RGB phenomic data enabled discovery of a greater number of significant SNPs in GWAS than those of multispectral phenomic data (Figure 60). Conversely, temporal phenotypes of VIs at the time points including early growth vegetative stages and reproductive stages in multispectral phenomic data belonging to 2017 and 2018 (both 2018_I and 2018_D) trials enabled discovery of a greater number of significant SNPs in GWAS than those of

RGB phenomic data (Figure 60). Certain VIs and their temporal phenotype data belonging to different time points, annotated candidate genes, explained percent variations and effect sizes of discovered 6151 SNPs were given in supplementary data 4 as a tabular format; genomic position of the discovered 6151 SNPs across chromosomes were shown in Figure 59. Number of SNPs discovered by different VIs were also given in Figure 61.

NGRBI resulted in the highest number SNPs in GWAS belonging to 2018_I and 2018_D trials (Figure 61). The cumulative SNP effects of each chromosome calculated for NGRBI in GWAS was illustrated and contrasted for every DAPs of drought (2018_D) and irrigated (2018_I) trials, and cumulative SNP effects of each chromosome belonging to drought and irrigated trials in 2018 were found to be varying in terms of statistically significance depending on the DAPs (Figure 63). Different chromosomes were found to have different cumulative temporal SNP effects which were occasionally statistically significant between drought and irrigated trials in 2018 (Figure 63).

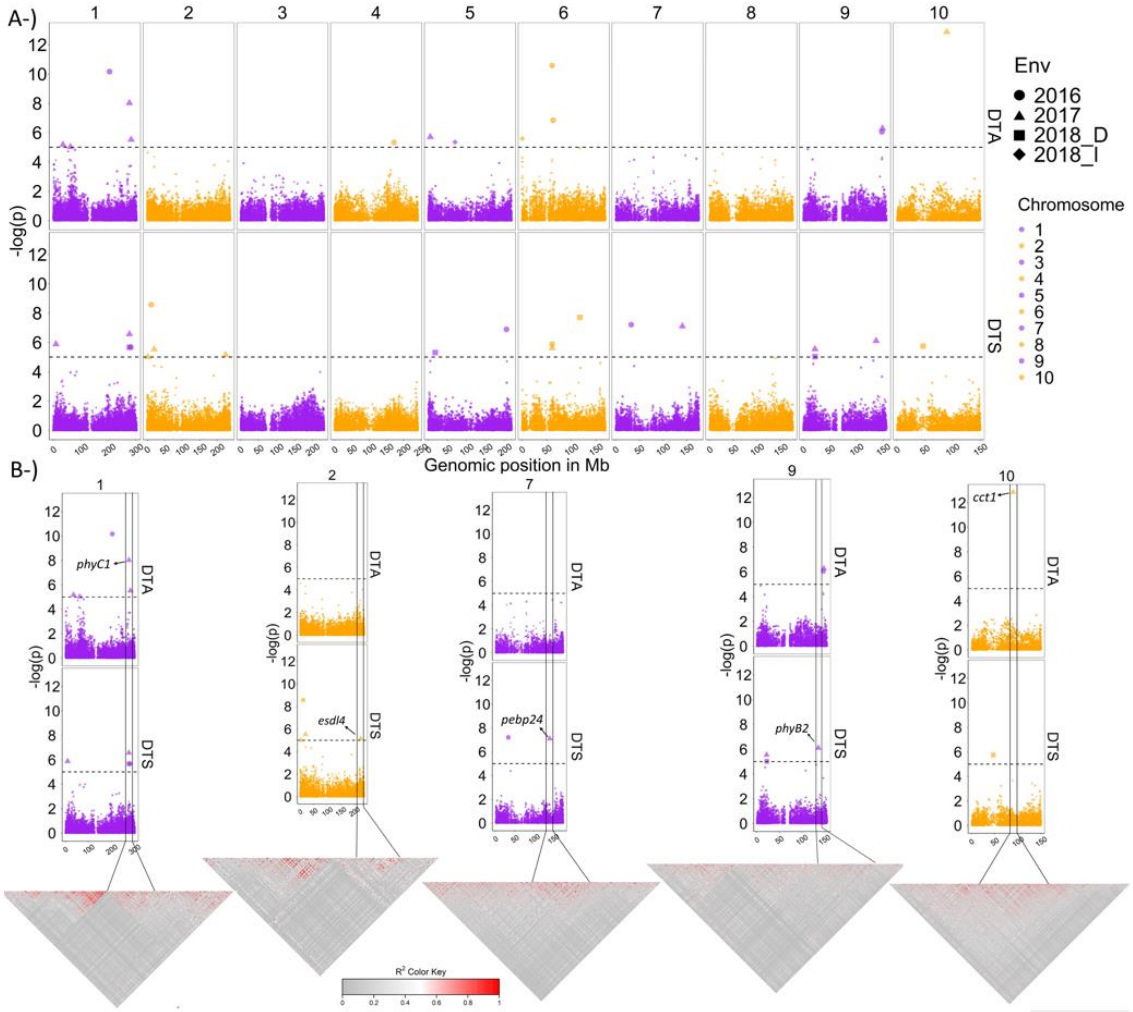

Figure 57 A-) Manhattan plot of days to anthesis (DTA) and silking (DTS) belonging to four environments (2016, 2017, 2018_D, 2018_I) by GWAS discovered well known genes controlling the flowering time in maize. B-) Five flowering related candidate genes with their linkage disequilibrium blocks.

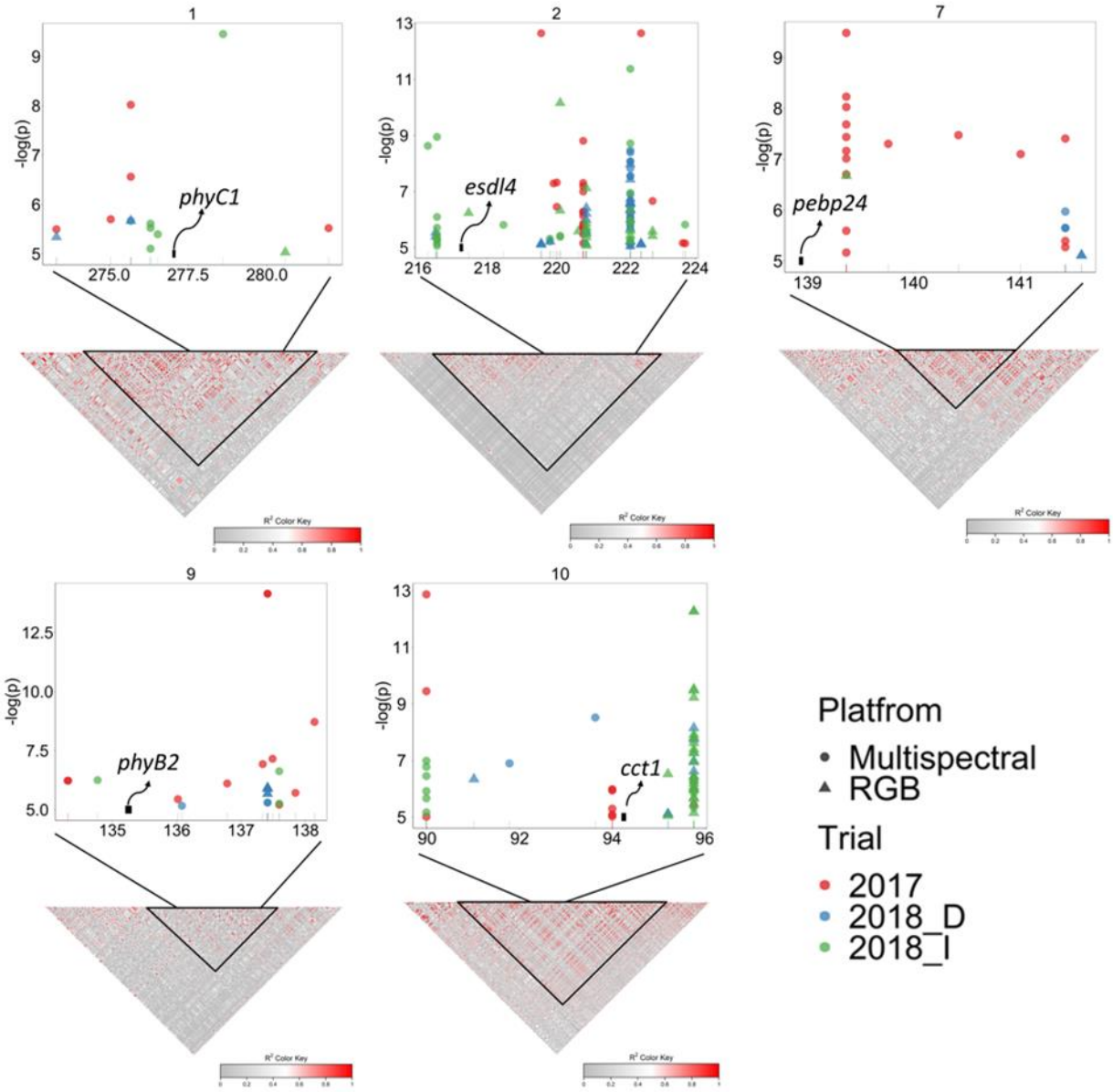

Figure 58 Five candidate flowering genes, discovered in GWAS using flowering phenotype belonging to 2016, 2017, 2018_I and 2018_D trials, were illustrated thick black lines with the with its name texts along with the nearby discovered SNPs for the certain temporal VIs belonging to multispectral (round shape) and RGB phenomic data (triangle shape) belonging to 2017 (red), 2018_D (blue) and 2018_I (green) trials. X axis shows the genomic positions of candidate flowering genes and their proximal regions in mega base pairs with the LD regions where high LD regions were drawn with black triangles; Y axis shows the negative logarithm of the p-values of discovered SNPs with ≥5.

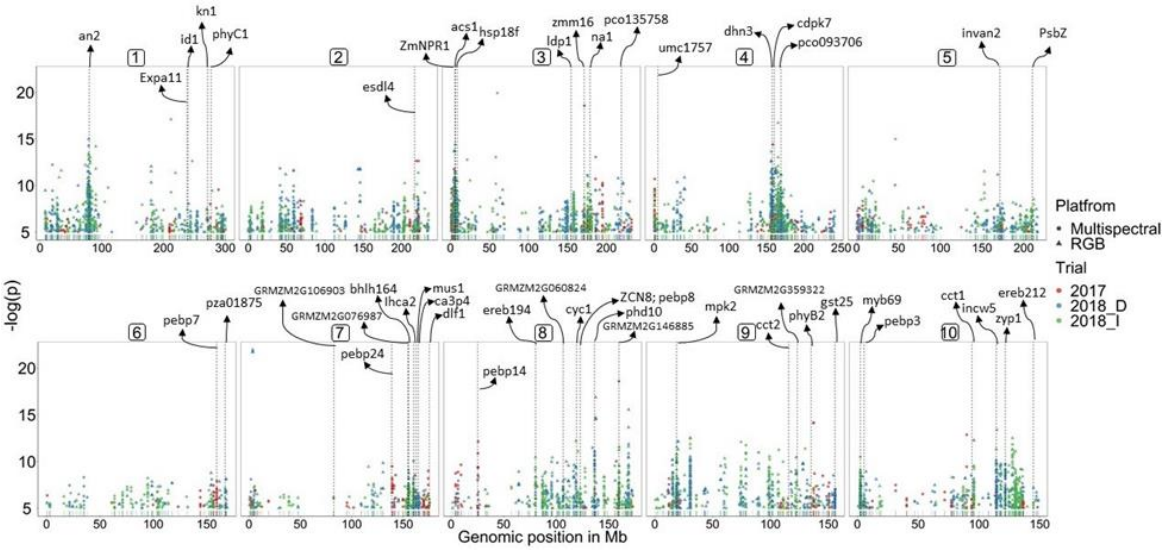

Figure 59 the Manhattan plot of 6151 SNPs with 5 -log(p) values (Y axis) using the RGB and multispectral phenomic data belonging to 2017, 2018_D and 2018_I trials.

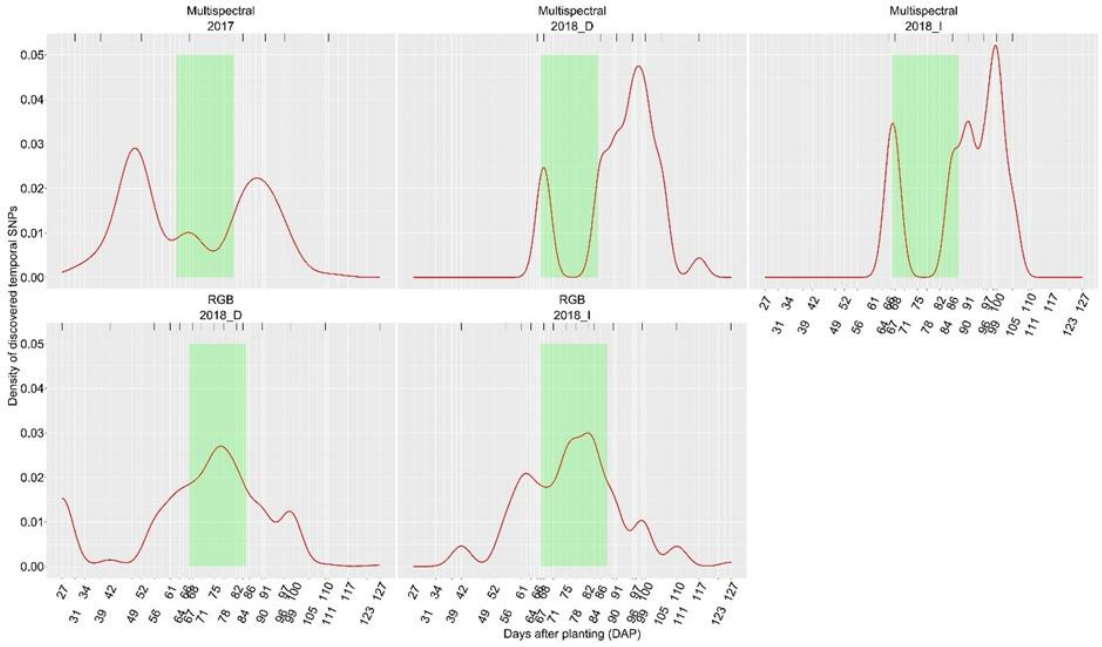

Figure 60 Density plot of significant temporal SNPs (6151 SNPs) across flight times (as DAP on X axis) belonging to RGB and multispectral phenomic data. Green region shows the scale of flowing times (DTA; days to anthesis) unique to each trial in different years, red line shows the density of the discovered SNPs based on Y axis.

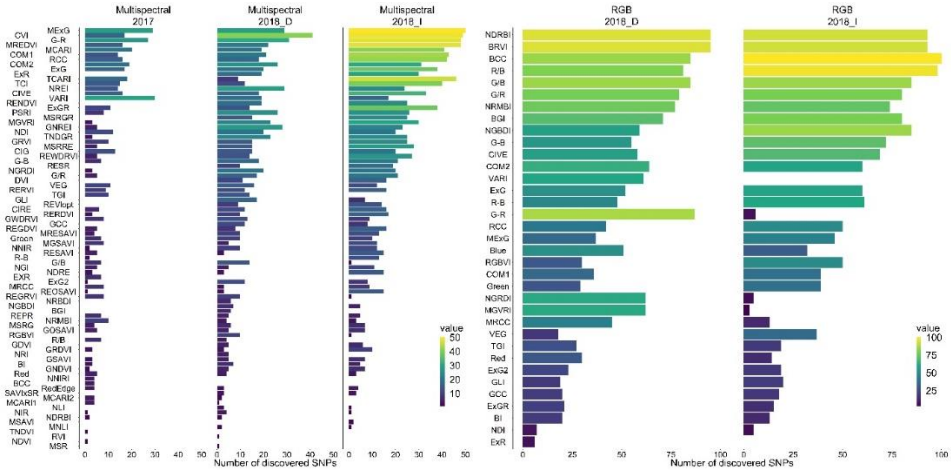

Figure 61 the number of SNPs discovered by using the temporal VIs belonging to phenomic data in different years.

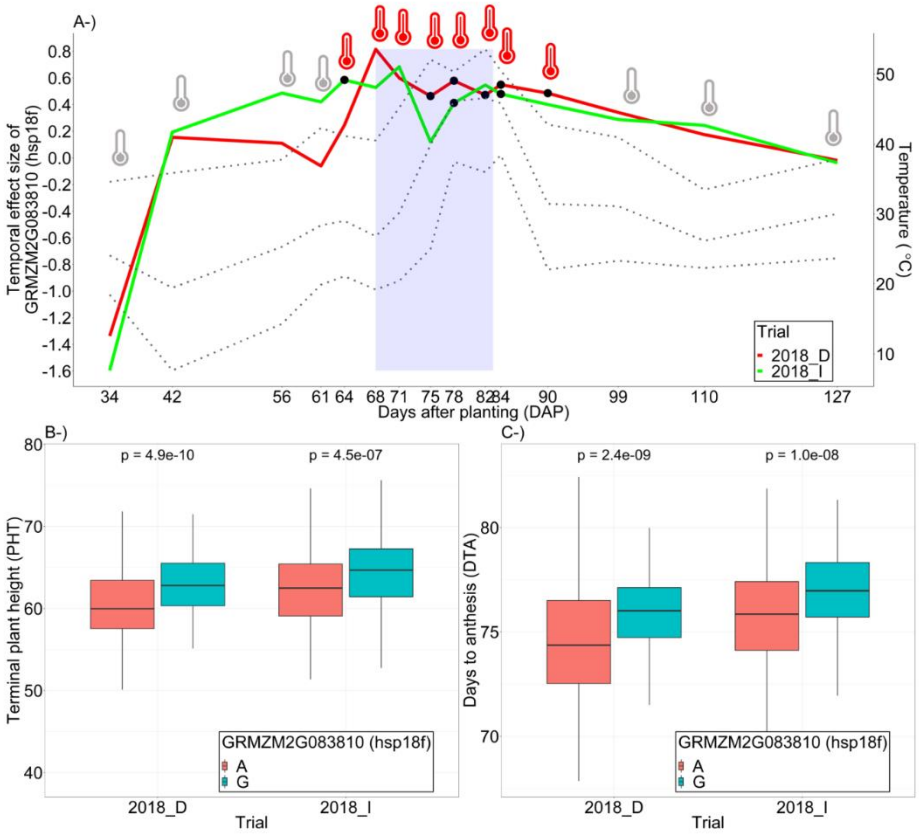

Figure 62 A-) Right Y axis shows temporal effect size of the GRMZM2G083810 (hsp18f) in 2018_D and 2018_I trials. GRMZM2G083810 (hsp18f) was discovered in GWAS using the blue index belonging to 64, 78 and 84 DAPs in 2018_I, and 75,78, 84 and 90 DAPs in 2018_D, these times were indicated by black points. Left y axis shows the temperatures (°C) of three dashed lines showing the highest, average and lowest (from above to below) temperature belonging to each DAP on x axis. Thermometers symbols show DAPs when temperatures reach the highest values and purple box corresponds to population days to anthesis. Allelic segregation (Adenine: A and Guanine: G) belonging to GRMZM2G083810 (hsp18f) differentiated the haplotypes with A versus G in terms of plant height (B) and days to anthesis (C). Haplotype groups were compared using Wilcoxon test, and p-values were located on the boxplots.

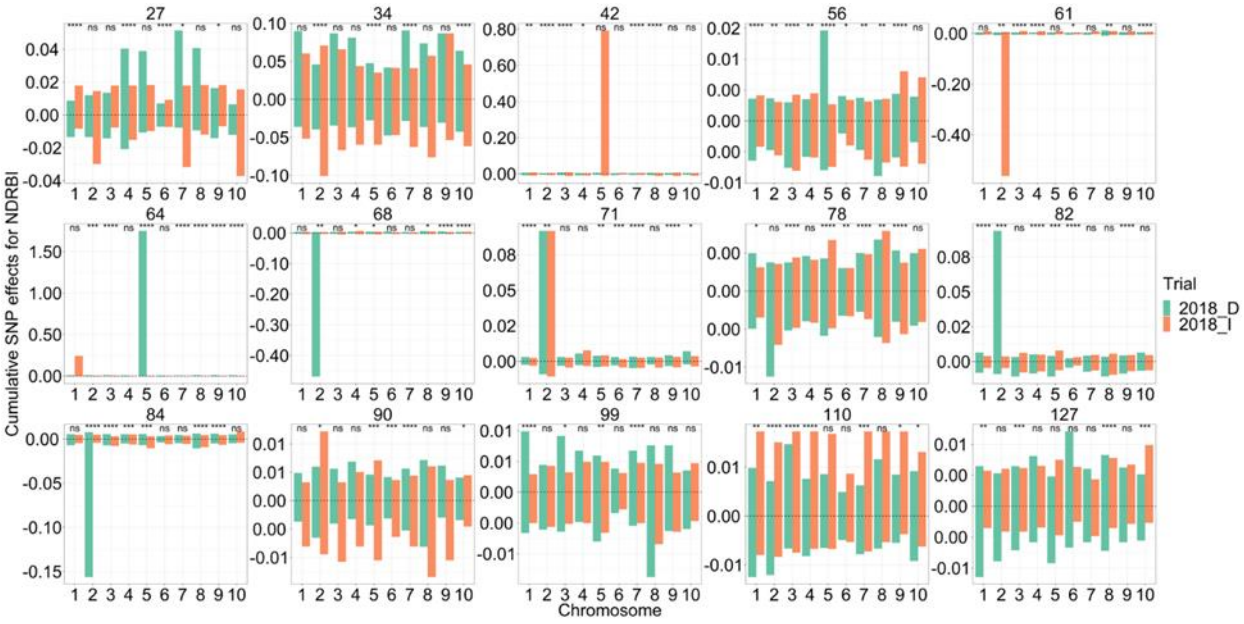

Figure 63 cumulative marker effects of each chromosome in each day after planting time (DAP) belonging to NDRBI vegetation index in 2018_I and 2018_D trials. Cumulative SNP effects of each chromosome belonging to two different trials were contrasted based on Wilcoxon test, and p-values were located on the bar plots; this comparison was applied to each DAP. *, **, ***, **** are significant at 0.05, 0.01, 0.001 and 0.0001; ns is not significant.

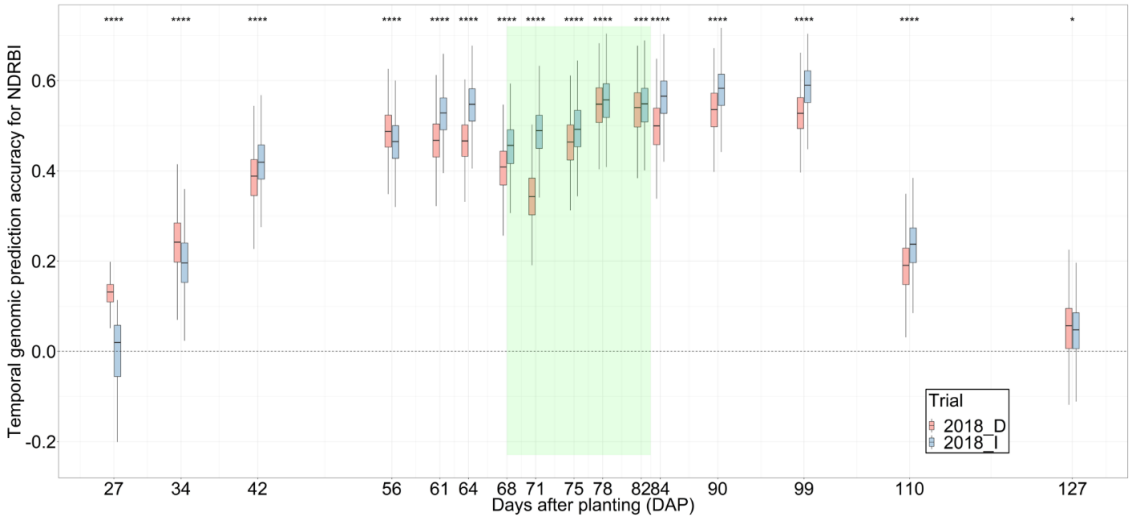

Figure 64 Temporal genomic prediction results for NDRBI vegetation index belonging to drought (2018_D) and irrigated (2018_I) trials in 2018. Temporal genomic prediction accuracies were found to be different between irrigated and drought trials at multiple time points. *, **, ***, **** are significant at 0.05, 0.01, 0.001 and 0.0001; ns is not significant.

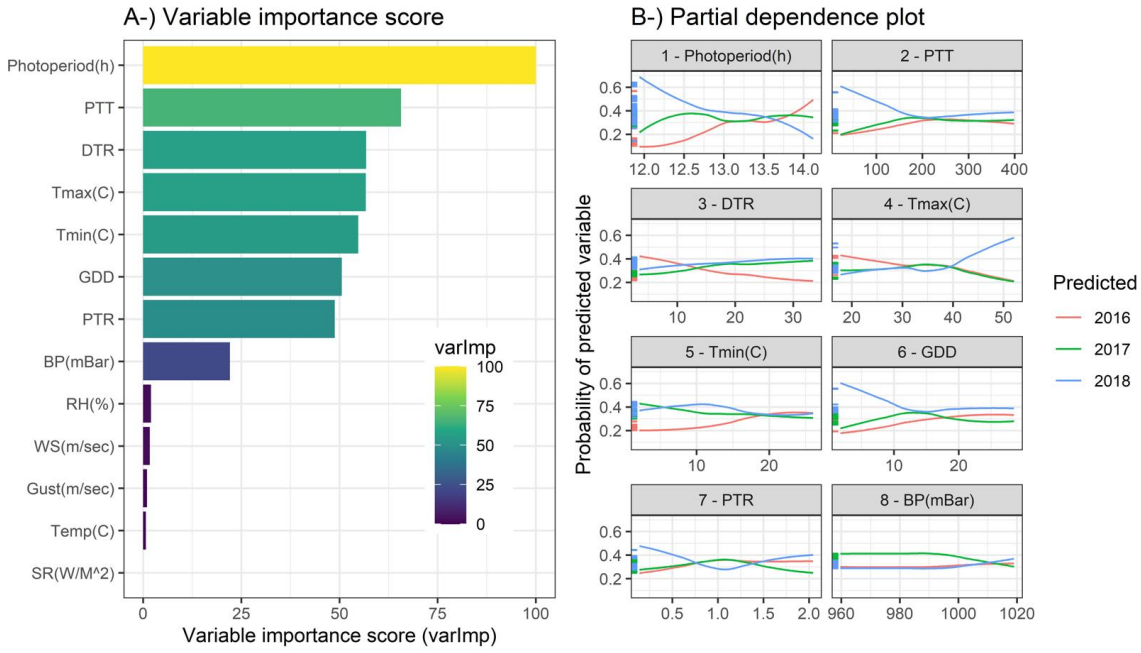

Figure 65 Random forest algorithm was used to classify the trails grown in 2016, 2017 and 2018 (irrigated and drought) trials, using their thirteen environmental parameters belonging to from planting times to means of days to anthesis of each trial grown in 2016, 2017 and 2018. A -) variable importance plot (scaled to 100 on X axis) nominated first three most important environmental parameters as photoperiod(h), photo thermal time (PTT) and diurnal temperature (DTR) respectively. B-) partial dependence plot shows the probability of the 2016, 2017 and 2018 (predicted categorical variables) on Y axis based on the values of environmental parameter related predictors (numbered based on their importance scores values from left to right and above to below) on the x axis.

Discussion

Days to silking and anthesis are well-known plastic traits with omnigenic inheritance in maize (Boyle et al., 2017; Buckler et al., 2009; Chardon et al., 2004; J. Li et al., 2016; Salvi et al., 2009; J. Xu et al., 2012). Both flowering traits have heritabilities relatively higher than other complex traits even under different latitude and altitude conditions (Buckler et al., 2009; Navarro et al., 2017). A major component of maize domestication and migration stemmed from modification of flowering response to photoperiod associated changes in latitudes. Towards this, related genes (CCT domain) enabled the migration of the maize post domestication, resulting in maize that has a wider range of adaptation and can be grown from temperate to tropical regions (Coles, McMullen, Balint-Kurti, Pratt, & Holland, 2010; Hung et al., 2012; Navarro et al., 2017; Swarts et al., 2021; Jinyu Wang et al., 2021). The underlying genetic mechanism of flowering time in maize to date contain circadian clock, photoperiod, autonomous, aging and gibberellin pathways and pathway integrators (Dong et al., 2012). Differing environmental conditions played a major role in discovering genes controlling the flowering in these pathways; effect sizes of those genes on flowering times as well as their expression levels were observed differently because of the reaction norm driven by

diverse environmental factors (Fournier-Level et al., 2011; Xin Li et al., 2018; Stratton, 1998). Our findings support those different environmental parameters, in part caused by different plantings times from 2016 to 2018 led flowering time plasticity (Figure 49D). In this study, the random forest algorithm nominated the photoperiod, photo thermal time (PTT) and diurnal temperature (DTR) as important environmental parameters that manipulated the days to flowering of RILs across years (Figure 65A); however, it is challenging to separate that photoperiod from the temperature. (Teixeira et al., 2015) showed that adaptation of tropical germplasm towards temperate regions requires selecting tropical germplasm with early flowering in temperate environments due to shorter day length conditions. In this study, RILs were exposed to longest day lengths in 2016 and shortest in 2018 from planting to flowering, resulting in 2018 having the latest flowering as well as weakest stability (Figure 45, Supplementary Figure 2, Figure 65B). This study considered photoperiod, temperature as well as their interplays (e.g., PTT and DTR) across growth to dissect plasticity in days to flowering in maize. The weakest stability observed in 2018 (Figure 49D) was triggered by the combination of shortest day length, lowest PTT environmental parameters (Figure 65). However, the difference in day length alone between 2016 and 2017 did not cause a weak stability as much as the weak stability observed in 2018, because the temperature and photoperiod related environmental parameters in 2016 and 2017 often followed more closely to each other than either between 2016 and 2018 or between 2017 and 2018. This resulted in prediction probabilities of 2016 and 2017 being close to each other at most values of temperature related environmental parameters as it seen in the partial dependence plots

(Figure 65B). However, prediction probabilities of 2018 were found to differ as compared to 2016 and 2017 at most temperature related environmental parameters as well as photoperiod (Figure 65B), leading to plasticity in flowering time as well as less stability of RILs (Figure 49D).

This study primarily intended to predict and understand the flowering times using high throughput phenomic data collected by multiple UAS surveys with different sensors within and between years, despite plasticity in flowering times. Temporal phenomic data and genomic data were subjected to correlation calculation to assess the multicollinearity problem, in that correlation pattern within both phenomic and genomic data reveal to be same changing the -1 to 1. It is important to note that high temporal dimension (multiple flight times) in the phenomic data inhibited the multicollinearity to great extent that enables to conduct phenomic prediction (Figure 48). Moreover, correlation between phenomic data and flowering times was correlated between each other that is a promising sign of better predictability (Figure 47).

Temporal phenomic data collected from drone images (multispectral and RGB sensors) were used as predictors in phenomic prediction, and promising prediction accuracies were obtained between diverse trials grown within and between years. When predicting yield in a single year, phenomic tools appeared to be as good or better than genomic tools (Adak, Murray, & Anderson, 2021; Rincent et al., 2018). However, combined data (phenomic plus genomic data) yielded greater than either genomic or phenomic data in prediction the flowering times in maize. This suggests that temporal phenomic data proposes promising complementary prediction for flowering time and

other complex traits in maize. Both phenomic and genomic prediction provide the opportunity to predict and select flowering performance of untested genotypes in untested environments; in addition to that, phenomic data can predict the stability scores of flowering times of RILs driven by environmental conditions across years.

Temporal Phenomic Prediction Can Predict the Complex Traits

In previous studies agronomic complex traits (e.g., flowering times and yield) were predicted using raw reflectance bands from one or limited number of vegetation indices belonging to one or limited number of time points and in one environment. For example, BNDVI (normalized difference between the blue and near infrared wavelength bands) has been used as predictor to predict the yield and flowering times in maize using the PLS regression; the prediction accuracies (0.54 to 0.79) varied depending on the temporal resolution (number of flights) used in different years (G. Wu, Miller, De Leon, Kaeppler, & Spalding, 2019a). However, prediction accuracies for flowering times, as well as, yield were shown to increase in diverse managements when a higher number of VIs (>0.80) over multiple time points were used in different machine learning algorithms in maize (Adak, Murray, & Anderson, 2021; Adak, Murray, Božinović, et al., 2021). These studies used a 25 m flight elevation which provided promising prediction for flowering time, as well as, grain yield in maize. (Aguate et al., 2017a) evaluated the prediction performance of the 62 hyperspectral reflectance bands between 392 and 850 nm obtained at 300 m of flight elevation in prediction of maize yield across diverse scenarios (populations, small plots, a farmers field, etc.) and over five time points; however single time points derived reflectance bands predicted yield around ~10 to 20%

lower than using all five time points derived from reflectance bands, and their highest prediction accuracies reached up to ~0.49 thanks to multiple time point derived reflectance bands. However, previously lower flight elevation providing higher pixel resolution (~1 cm per pixel) along with higher number of flights proved that prediction of yield in maize can result in higher prediction accuracies (>0.5) (Adak, Conrad, et al., 2021; Adak, Murray, Božinović, et al., 2021), although differences in populations and environments cannot be ruled out. Considering resources needed, this study similarly supported that high resolution images derived from low flight altitude with RGB camera belonging to high number of time points can provide better prediction than those derived from high flight altitude with more spectral bands belonging to fewer time points (results of scenario 1: Figure 50).

Genomic Prediction

Results of scenario 3 underlines that predictive ability of genome wide makers decreases when it comes to predicting unknown genotypes in unknown environments across years (results of scenario 3: Figure 52). This is likely in part because plasticity in flowering times driven by environmental variation cannot easily be taken into consideration from genome wide markers, since genomic variation is fixed across all environments. So, it is logical that the results of scenario 4 showed that prediction of flowering times of unknown genotypes in unknown environment (2018_D) was predicted with higher prediction accuracy when phenomic data was added to genomic data (~0.77) than either only genomic (~0.67) or phenomic data (~0.52) alone (results of scenario 4: Figure 53). This demonstrated the concept that combining high throughput

phenomic and genomic data in prediction better incorporates the genomic and environmental variation together. This resulted in a better prediction accuracy for complex traits in the most challenging scenario, the prediction the performance of untested genotype in untested environments.

Temporal Phenomic and Genomic Data Complemented Each Other

Vegetation indices were found to boost predictions when combined with genomic data, and higher resulting prediction accuracy has also been shown for yield in wheat and rye (Crain, Mondal, Rutkoski, Singh, & Poland, 2018; Galán et al., 2020; Rutkoski et al., 2016; Sun et al., 2019). Findings of the present study similarly supported that combining high throughput phenomics and genomic data outperformed the prediction of flowering time in maize as compared using either phonemic or genomic data as predictors individually. Specifically, combining genomic and phenomic data as predictors outperformed the prediction of untested genotype in untested environments (results of scenario 2 and 4: Figure 51 and 53), which has not previously been shown. Likely this will be trait, population and environmentally specific.

There is also a similarity between phenomic and genomic prediction with how ridge regression in general performs superior in genomic prediction and selection by including the contributions of minor effects of whole genome markers (Endelman, 2011). Our results also support that instead of using single preselected VIs (as is common) or limited reflectance bands, using higher number of VIs may provide greater prediction accuracy, that is similar transition trend from MAS to GWAS to genomic prediction through time in prediction using whole genome markers.

Combining Disparate Phenomic Data Across Years for Prediction

Among the most potentially important contribution of this study is an approach allowing data to be combined across years where flight date and development stages differ. In both scenario 1 and 2, multispectral phenomic data with low resolution (~120 meter) and time dimension (belonging to from initiation of flowering times to end of reproductive stages) was used between years (2017 and 2018). Principal component scores for each VI in multispectral phenomic data in both years were calculated to be used as predictors that resulted in positive but small (~0.15-0.16) prediction accuracies by ridge regression (Figure 51). This approach allows phenomics data to predict the unknown genotypes in unknown environments across different locations or years via principal component scores of phonemic data when flight times were different.

Ability To Predict Stability

In scenario 5, stability scores calculated for DTA were also predicted using genome wide markers (~0.35) and six different phenomic data (up to 0.25) with the positive prediction accuracy for untested genotypes (Figure 54). Results suggested that stability of flowering times of RILs can be predicted using genome wide marker as well as phenomic data. When phenomic data belonging to single year [RGB (2018_D); RGB(2018_I), RGB(2018_D) + Multi(2018_D) or RGB(2018_I) + Multi(2018_I)], was used to predict WAASB stability, prediction accuracy changed between 0.18 to 0.20. However, when phenomic data belonging to two years was used to predict to predict WAASB stability, prediction accuracy increased up to ~0.25. Flowering stability index of untested genotypes can be predicted with genomic and phenomic data up 0.35 and

0.25 respectively. Phenomic data belonging to multiple environments can predict the flowering time stability scores of untested genotypes more accurately than using the phenomic data belonging to single environment. When phenomic data belonging to two years were used as predictors, prediction accuracy was increased from ~0.18 to ~0.25. Since we observed the increase in prediction accuracy when combined phenomic data (2017 plus 2018) used to predict stability score, and we did not have a phenomic data belonging to 2016 trial, we could hypothesis that phenomic data likely has potential to predict the stability of complex trait as much as or better than genome wide markers when enough number of temporal data belonging to multiple environments and years were provided in phenomic data.

Integration of High Throughput Phenomic Data with Association Mapping and Genomic Prediction

Temporal plant height (aka, canopy height measurement; CHM) captured by UAS has been used as phenotype data in association mapping in maize hybrids (Adak, Murray, & Anderson, 2021; Adak, Murray, Anderson, et al., 2021) and inbreds (Anderson et al., 2020; Xiaqing Wang et al., 2019), resulting in discovery of numerous temporal loci. Temporal loci explain phenotypic variation of plant height differently depending on the growth stage measured, which allows better biological understanding of the loci segregating for control of growth. Similar findings have been shown in soybean using UAS based phenotyping (Xavier, Hall, Hearst, Cherkauer, & Rainey, 2017), in cotton using a ground-based vehicle phenotyping (Pauli, Chapman, et al., 2016), in wheat, rice and triticale using tractor-based phenotyping (Lyra et al., 2020;

Tanger et al., 2017; Würschum et al., 2014), as well as in maize and barley using automated-based phenotyping under greenhouse conditions (Muraya et al., 2017; Neumann et al., 2017; X. Zhang et al., 2017). Temporal NDVI (normalized difference vegetation index) captured by UAS have also been used in association studies in cotton (Pauli, Chapman, et al., 2016) and maize (Jinyu Wang et al., 2021). However, the present study showed that NDVI discovered among the lowest number of SNPs in association mapping (Figure 61), indicating that using only one or a few temporal phenotypes of VIs or CHM will not be sufficient to discover segregating temporal loci controlling plant growth. Various vegetation indices were previously found to have different capability to classify grain yield when their area under curve (AUC) values were used (Adak, Murray, & Anderson, 2021), and only temporal plant height predicted yield weakly (Adak, Murray, Anderson, et al., 2021; Anderson et al., 2019). However, usage of multiple temporal VIs belonging to multiple time points increased the prediction ability of yield in maize dramatically in this study and previous studies (Adak, Murray, & Anderson, 2021; Adak, Murray, Božinović, et al., 2021). These results highlight an incomplete understanding of segregating factors in plant growth when one or a few indices were used in either phenomic prediction or temporal association mapping. Our findings support the previous statement that temporal phenotypes of different VIs enabled the discovery of 1599 unique SNPs in multispectral and RGB platform out of total 6151 SNPs in this study (Figure 61, Supplementary data 4), and density of discovered SNPs varied depending on the measurement time (Figure 60). High resolution RGB images discovered more loci during the mid-growth, around

flowering, than other growth periods while low resolution multispectral images discovered more loci before and after the mid-growth stages (Figure 60). These results showed that temporal phenotypes captured by multiple drone surveys can discover previously unrevealed time dependent associations between temporal traits and genome wide polymorphisms. This enables dissection of temporal plant growth better than usage of low time dimensional phenotype data in association mapping studies.

Validation of Candidate Gene Using Temporal Phenotype Data

This study discovered a heat stress related candidate gene, *GRMZM2G083810* (*hsp18f*), using temporal blue index phenotype belonging to around only flowering times in both drought and irrigated trials in 2018. Flowering times are one of the most sensitive periods to heat and drought stress (Barnabás, Jäger, & Fehér, 2008) where heat stress led the discovery of *GRMZM2G083810* (*hsp18f*) with different effect sizes during flowering times in both drought and irrigated trials in this study (Figure 62). This finding is a proof of the concept that temporal phenotype value of VIs enables discovering opportunistic QTLs (oQTLs) (R. Wu, Wang, Zhao, & Cheverud, 2004) since high resolution drone images can capture the specific interplays between plant growth and biotic stresses belonging to certain growth period. In addition, the *GRMZM2G083810* (*hsp18f*) candidate gene caused the RIL haplotypes to have statistically different terminal plant height as well as flowering times in both drought and irrigated trials in 2018 consistently (Figure 62A). This indicates that the allelic variation associated with stress related genes discovered in early plant growth stages can impact on the terminal phenotype such as terminal plant height and flowering times (Figure 62B and 62C).

Drone images belonging to flowering times, which were most sensitive growth stages to heat stress in maize, provided a time specific genetic variation occurred in RILs and led the discovery of the heat stress related genes along with its impact on the terminal traits (e.g. terminal plant height and flowering time). This is a proof of concept that UASs can provide time specific temporal phenotype data belonging to when plants are exposed to abiotic stress factors at specific time points across growth (e.g. heat stress in flowering times in this study). Thus, the relationships between abiotic stresses belonging and plants along with related candidate genes with these stresses can be better dissected with temporal data captured by UASs. We proposed that we could discover the heat related genes using the temporal phenotype of VI belonging to specific time points (e.g. flowering times) in GWAS that enables us to select resistance candidate maize lines against to heat.

Temporal NDRBI values belonging to majority time points in irrigated trial were predicted greater than those in drought trial by genome wide markers (Figure 64). This finding underlies that genome wide makers do not perform stably in the prediction of temporal phenotype data of a trait across different management conditions as well as chromosomes (Figure 63). Repetitive UAS surveys can monitor the temporal prediction ability of genome wide markets for specific time points and managements. This approach advises to select the desired plants thanks to temporal genomic prediction results that can provide better precision in selection than using one time based genomic prediction.

In conclusion, field based high throughput phenotyping propose novel technologies and applications such drones and new tech sensors to better screen the breeding nurseries with higher precision, accuracy and high time dimension; that allows us to dissect the novel interaction between environment, plant and underlying genomic mechanisms. First, temporal phenomic data containing reflectance bands belonging to multiple time points thanks to repetitive UAS surveys predicted the complex traits (e.g. flowering times in this study) across different managements and years as well as the stability scores of flowering times in maize. Second, temporal phenotype data was found to be required to dissect the time-dependent associations between plant and abiotic stresses; reflectance bands belonging to flowering times led the discovery of heat-related candidate gene when heat stress reached peaked at flowering times. Overall, temporal phenomic prediction and dissecting time-dependent association between temporal phenotype, genomic and environmental data were demonstrated in this study. Integration of high throughput phenomic data into plant breeding and plant genomic will allow to select the complex traits and dissect the plant-environment interaction across plant development.

CHAPTER VI

TEMPORAL PHENOMIC PREDICTIONS FROM UNOCCUPIED AERIAL SYSTEMS CAN OUTPERFORM GENOMIC PREDICTIONS[4]

To improve genetic gain, plant breeders must phenotype more plants repeatedly during growth allowing higher selection intensity, accuracy, and increased statistical power(Araus et al., 2018; Shi et al., 2016). High quality and quantity phenomic data is essential to develop widely applicable prediction models (e.g., phenomic predictions) to predict yield across growing environments and conditions in the near future (Bernardo, 2021). To date, few phenomic data sets, approaches and applications have been reported, especially those applied in a breeding context.

Organismal fitness, such as terminal grain yield in crops, is a cumulative response of genetics (G), the environment (E), management (M) and integrated GxExM interactions temporally throughout growth. To predict cumulative fitness of an individual organism without direct measurement of that individual's fitness, proxies such as genetic markers are used, to link measurements of relatives and predict fitness with breeding values. Traditional best linear unbiased prediction (BLUP) derived breeding values (Henderson, 1975) were modified by (Bernardo, 1994) where genotypic marker

---

data of parental inbreds was combined with the yield data of the related single cross hybrids to predict yield performance of the single cross hybrids, known as genomic BLUP (GBLUP). However, prediction accuracies dropped dramatically when yield of unknown (previously untested) parental lines derived hybrids was predicted (Bernardo, 1996a, 1996b). Various genomic based statistical models have been developed after the traditional GBLUP approach with advent of genomic technology (Endelman, 2011; Meuwissen et al., 2001; Whittaker et al., 2000). These methods have been applied extensively as genome wide marker facilitated selection also known as genomic selection in plants (Bernardo & Yu, 2007). Predicting the performance of previously untested genotypes in both tested and untested environments remains the central problem in plant breeding selections, and new approaches to addressing this challenge are needed. Genomic selection to estimate genotype fitness, as measured by terminal grain yield, relies on manually collected phenotype data which is resource intensive to collect. Phenotypic characteristics of cumulative complex traits are often not accurately predicted in GS because of (i) the different interplays of genes on phenotype throughout different growth stages, (ii) different effect sizes of the same genetic markers on phenotype of complex traits at different growth stages and (iii) different sources of phenotypic variation of the complex traits at different growth stages (Adak, Conrad, et al., 2021; Adak, Murray, Anderson, et al., 2021; Adak, Murray, Božinović, et al., 2021; Anderson et al., 2019; Bac-Molenaar et al., 2015; Campbell et al., 2017; Feldman et al., 2017; Ward et al., 2019; R. Wu et al., 2004). Tools that can inexpensively evaluate individuals throughout growth, as they interact with their environment, would therefore

be a valuable addition to predicting an organism's fitness. Unoccupied aerial systems (UAS) are now able to provide these insights, frequently evaluating individuals temporally throughout growth. However, to date, fitness predictions from UAS alone have not been compared to the standard method of genomic prediction.

To evaluate fitness prediction of UAS based phenomics tools, the breeding value of each hybrid must be produced, these can be estimated from temporal VIs and structural measurements (canopy height) collected temporally throughout growth. Correlations between temporal VIs with yield and flowering times, as well as machine learning models can investigate predictive abilities for fitness traits (yield and flowering times). Phenomic predictions made from temporal vegetation indices and canopy height can be compared with traditional genomic predictions. Ultimately, major causal loci underlying phenomic predictions success for complex traits can be useful to understand underlying biology of organismal fitness over growth. Here we report phenomic data-driven selection for complex traits in maize breeding. We conducted UAS surveys with multispectral and RGB sensors to collect image-based temporal predictors throughout maize growth stages. We compared phenomic based prediction accuracy to that of genomic prediction, explored temporal shifts in image-based phenotypic variation explained by genome wide markers, and conducted association mapping utilizing temporal image-based phenotypes to identify biologically important loci.

Materials And Methods

Using the Genome to Fields initiative's 2017 germplasm, 280 unique maize hybrids were grown under optimal management (OM) and 230 were grown under stressed management (SM, no irrigation, low fertilizer) near College Station, Texas. Two replications were used in a randomized complete block design with each hybrid grown as two consecutive row plots.

UAS Surveys and Image Processing

A Phantom 3 Professional rotary-wing UAS, equipped with a 12-megapixel red-green-blue (RGB) DJI FC300X camera, flown 25 meters above the ground (TPP_RGB). Additionally, a Tuffwing UAS equipped with a MicaSense RedEdge-MX multispectral camera was flown 120 meters above the ground (TPP_Multi). Images were collected with 80% forward and side overlap in both surveys. Raw images were processed in Agisoft Metaphase Professional software (https://www.agisoft.com/) to generate the 3D point clouds and orthomosaics (***SI appendix*, Table S1)** (S. Murray et al., 2019).

Phenomic Data Extraction Pipeline

Environmental Systems Research Institute, Inc. (ESRI) shape file were constructed using R/UAStools::plotshpcreate function (Anderson & II, 2020) and applied to each survey's respective orthomosaic (.tif files) and 3D point clouds (.las or .laz files) to extract plot level image based phenotypes. Vegetation indices (***SI appendix*, Table S2)** for each flight date were extracted using the *FIELDImageR* package (Matias et al., 2020) for each UAS survey (***SI appendix, SI Materials and Methods*).** Plot based 99th percentile temporal plant heights (canopy height measurement; CHM) were

extracted from 3D point clouds following the methods of (Anderson et al., 2019) (***SI appendix, SI Materials and Methods*).**

Experimental Design and Nested Model for Phenomic Data

To analyze the temporal VIs and CHM, a custom nested design was applied to raw data of each VI and CHM belonging to each row plot in OM and SM, where experimental design and maize hybrids were treated as nested within drone flight times (SI appendix, SI Materials and Methods). Hybrids nested within pedigree results were used to predict GY, DTA, DTS, and PHT within and between the trials.

Machine Learning Based Phenomic Prediction Models

Manually collect phenotypes (GY, DTA, DTS and PHT) were predicted using linear, elastic net, ridge, lasso, and random forest regressions using the TPP_RGB and TPP_Multi image-based phenotypes (**Dataset S1**). Prediction models were trained using a random sampling of 70% of the common maize hybrids (tested genotypes) across the two management environments. The remaining 30% were used as the validation dataset (untested genotypes). Models were trained using OM trial (tested environment) while the SM trial served as the untested environment. Four cross validation schemes (CVs) were conducted as follows: (i) tested genotypes in tested environment (CV1), (ii) untested genotypes in tested environment (CV2), (iii) tested genotypes in untested environment (CV3), and (iv) untested genotypes in untested environment (CV4) (Xin Li et al., 2018). Phenomic prediction models and prediction steps are available in the ***SI appendix, SI Materials and Methods.***

Association Mapping for Phenomic Data

The image-based vegetation indices and Weibull_CHM were converted to cumulative area under curve (AUC) values and used as trait data in a genome wide association study (GWAS) **(*SI appendix, SI Materials and Methods*).** Association mapping was conducted using 158 maize hybrids and 101,100 genotyping by sequencing (GBS) SNP markers, implementing three multiple loci test methods; (i) fixed and random model circulating probability unification (FarmCPU) (X. Liu et al., 2016), (ii) multiple loci mixed model (MLMM) (Segura et al., 2012), and (iii) bayesian-information and linkage-disequilibrium iteratively nested keyway (BLINK) (M. Huang, Liu, Zhou, Summers, & Zhang, 2019) (***SI appendix, SI Materials and Methods*).** Linkage disequilibrium (LD) estimates were used to identify candidate genes within LD blocks ($R^2 \geq 0.8$) of colocalized SNPs (***SI appendix,* Fig. S1**).

Genomic Prediction for Phenomic Data

Genome-wide prediction was applied to 540 image-based phenotypes (35 VIs and CHM belonging to 16 flight times) of the 158 maize hybrids in TPP_RGB of OM using 153,252 SNPs, temporal genomic prediction model was explained in SI appendix, SI Materials and Methods.

Phenomic Prediction Versus Genomic Prediction

GBS marker data (GP) and two sets of phenomic data (TPP_RGB and TPP_Multi) were used to conduct genomic prediction and phenomic prediction for maize grain yield (GY). A total of 118 G2F maize hybrids were used to compare the predictive ability between the genomic and phenomic data sets. Four cross validation

schemes were applied as explained in “Machine learning based phenomic prediction models” section. Additional details regarding phenomic prediction versus genomic prediction are available within the SI appendix, SI Materials and Methods.

Results

Variance Decomposition and Repeatability Estimates Demonstrate UAS Sensor-Based Phenotypes were Genetically Stable

Variance component decomposition of the 83 sensor-based VIs (35 RGB and 54 multispectral) demonstrated UAS sensor-based data was statistically repeatable and biologically meaningful with a genetic basis. The rotary-wing equipped with an RGB (3 band, 12 MP) sensor flown at 25 m resulted in ~1 cm pix-1 image resolution and had higher repeatability than the Tuffwing platform equipped with a multispectral (5 band, 3.8 MP) sensor flown at 120 m (~8 cm pix-1). The main source of phenotypic variation for both platforms was explained by the temporal flight component (β_i component in Eq.1) of the nested design (31-96%) showing a temporal plasticity of maize spectral reflectance signatures throughout the plants growth cycle (SI appendix, Figs. S2 and S3). Genetic variance ($\Omega_{i(j)}$ component in Eq.1) was slightly greater for the higher resolution-low altitude RGB (1.5 - 5.2%; TR: 0.46 - 0.77) phenotypes compared to the lower resolution-high altitude RGB (1.1 - 4.5%; TR: 0.26 - 0.66) and lower resolution-high altitude multispectral (0.5 - 3.4%; TR: 0.28 - 0.62) phenotypes (SI appendix, Figs. S2 and S3). The repeatability estimates over the 35 RBG phenotypes were highly correlated (r=0.71) between the two sensor systems, although repeatability was improved by 0.08 on average, when implementing the higher resolution-low altitude

RGB platform. Noticeable improvements in repeatability estimates (>0.1) were achieved for 13 RGB VIs and 6 VIs repeatability were reduced (<0.06) when implementing the higher resolution-low altitude RGB platform (SI appendix, Figs. S2 and S3). Overall, significant genetic variation was attributed to all VIs on both platforms, useful in predictive modeling of important agronomic traits such as grain yield, flowering times, and plant height (SI appendix, Fig. S4).

Temporal Correlation

Temporal correlation between UAS survey dates of the VIs derived from the higher-resolution-low altitude RGB demonstrated that 14 of 35 RGB-derived VIs achieved a correlation above 0.50 (up to 0.61) to GY (SI appendix, Fig. S5). However, the 14 RGB- and 40 multispectral-derived VIs from the lower resolution-high altitude multispectral achieved correlations above 0.50 (up to 0.70) to GY (SI appendix, Fig. S6). Sensor-based VIs correlations with GY varied depending on the flight times. High correlations were found for VIs belonging to certain time points in both TP_RGB and TPP_Multi demonstrating that temporal VIs tend to synchronize with GY in maize hybrids indicating potential source for predicting yield.

Phenomic Prediction Using High Dimensional UAS Data

Temporal breeding values of each pedigree at each timepoint in TPP_RGB and TPP_Multi followed unique trajectories (SI appendix, Figs. S7 and S8) visually discriminating low, mid, and high yielding maize hybrids. Phenotype data of VIs at different time points had different discriminative ability for yield. This led us to test the predictive ability of two phenomic data derived from different sensors and resolutions

utilizing the different prediction models. To assess the multicollinearity of each phenomic data, correlation coefficients were calcauted. Correlation results of each phenomic data showed that correlations were fluctuating between -1 and 1, and VI's were found to be less correlated at different time points (SI appendix, Figs. S9). The three machine learning models improved prediction accuracy (>90%) for all four agronomic traits (GY, DTA, DTS, and PHT) compared to the linear model when temporal phenotypes in TPP_RGB and TPP_Multi phenomic data were used as predictors (Fig. 66). The linear models had the highest prediction errors (RMSE and MAE) and lowest R2 (SI appendix, Fig. S10). Ridge regression was the highest performing model for predicting GY regardless of the phenomic data sets; resulting in the best prediction performances for untested genotypes in tested environment (CV2), tested genotypes in untested environment (CV3), and untested genotypes in untested environment (CV4) (Fig. 66). Ridge regression best predicted GY for CV2 using the low-resolution multispectral sensor (TPP_Multi), while ridge regression also best predicted GY for tested and untested genotypes in untested environment cross validations (CV3 and CV4) using the high resolution RGB sensor (TPP_RGB; Fig. 66). Furthermore, ridge regression achieved the greatest prediction accuracy for the flowering times and plant heights utilizing the high resolution RGB UAS (Fig. 66). Prediction accuracies were higher in the most challenging CVs (CV3 and CV4) when TPP_RGB was used to predict GY, DTA, DTS, and PHT. These results demonstrate that the reduction in resolution, increased spectral bands, and increased sensor cost of incorporating the multispectral bands did not significantly improve model performance.

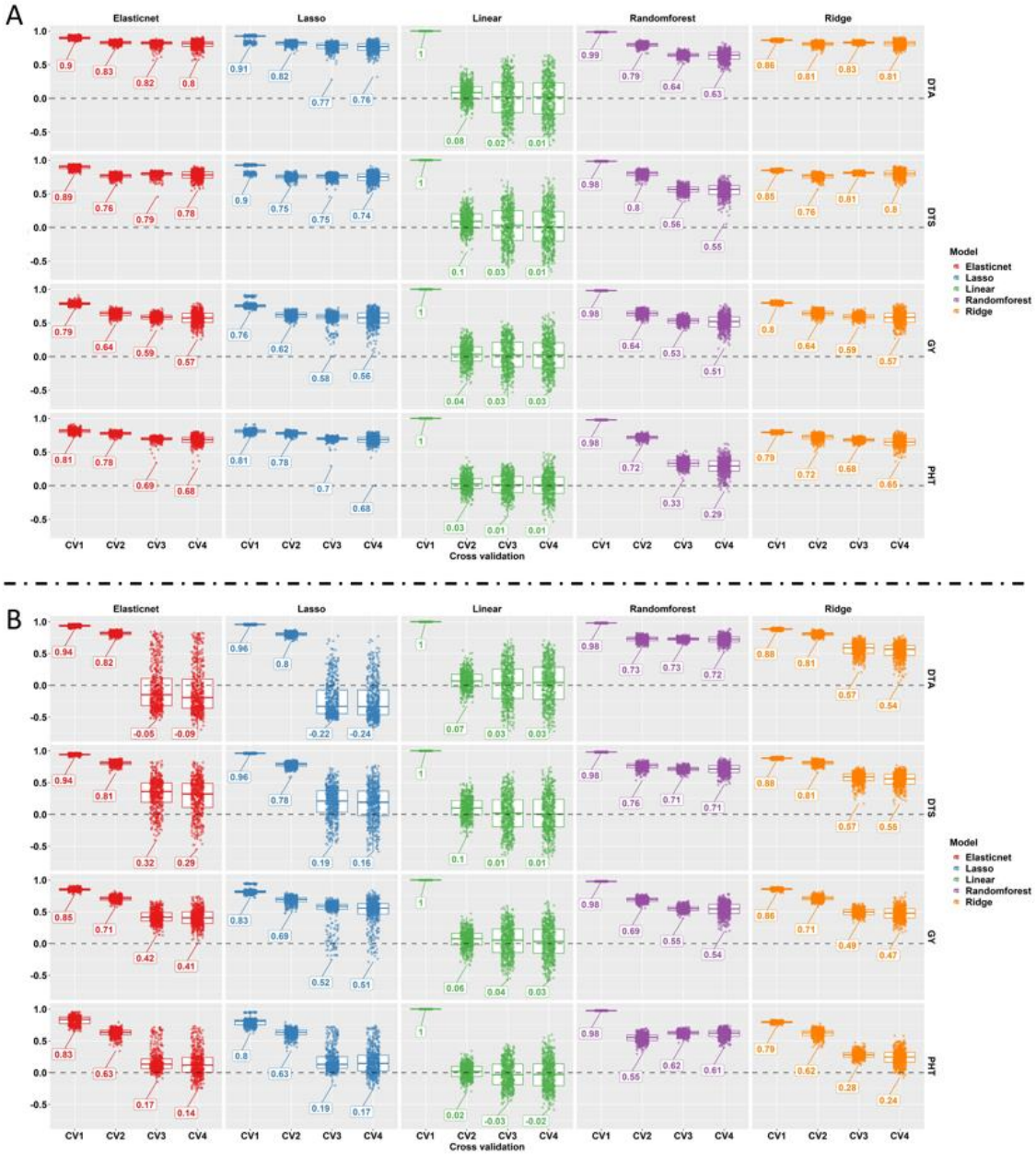

Fig. 66 Shows the prediction accuracy (on the y axis) of the phenomic prediction obtained by each model for four cross validation schemes (on the x axis) belonging to each predicted variable (from left to right) in phenomic prediction: (A) the prediction performance of TPP_RGB phenomic data derived from HTP platform including 25-meters elevation with RGB sensor. (B) the prediction performance of TPP_Multi phenomic data derived from HTP platform including 120-meters elevation with multispectral sensor. Ridge regression performed best overall for the most challenging cross-validation schemes, CV3 and CV4, compared to other prediction models when

TPP_RGB was used. Whereas, Randomforest performed best overall for the most challenging cross-validation schemes, CV3 and CV4, compared to other prediction models when TPP_Multi was used. Reprinted from Adak, Murray, & Anderson, 2021.

Variable Importance Scores of the Machine Learning Models

To understand potential biological causes behind the most accurate predictions, variable importance scores were derived from the prediction models to identify critical predictor/time point combinations for TPP_RGB and TPP_Multi phenomic data sets (SI appendix, Figs. S11 and S12). Different contributions of VIs and Weibull_CHM at multiple time points were important among both phenomic datasets in the prediction of GY, DTA, DTS and PHT (SI appendix, Figs. S11 and S12). For instance, the TPP_RGB red chromatic coordinate index (RCC) and TPP_Multi modified nonlinear index values (MNLI) belonging to various time points, either before or after flowering times, for all predicted variables were identified by all machine learning models consistently and are therefore critical VI/timepoints combinations for all predicted variables (SI appendix, Figs. S11 and S12). This demonstrates the ability of machine learning models to identify important image-based phenotypes for future UAS surveying efforts and provides foundational insight towards understanding the biological importance of images-based phenotypes within a plant's growth cycle.

Genome Wide Association Mapping Results

To gain further insight into biological significance of successful predictions, GWAS peaks were identified using area under curve values (***SI appendix*, Figs. S13 and S14)** of each high resolution VI and Weibull_CHM in the TPP_RGB phenomic data set (***SI appendix*, Figs. S13 and S14).** A total of 241 GWAS peaks were identified across

the 36-temporal image-based phenotypes in TPP_RGB. Five genomic regions had significant loci for VIs and candidate genes of relevant interest **(*SI appendix, SI Results*).** Two genomic regions were identified as hotspots (fourth bin in chr2 and eighth bin in chr4) having GWAS peaks belonging to 24 VIs discovered across the three GWAS models (***SI appendix*, Fig. S15 and Dataset S2**). A 15 kb genomic distance around the GWAS peaks was scanned to determine candidate genes based on the calculated LD decay (***SI appendix*, Fig. S1**). LD patterns of both hotspots were visualized along with six candidate genes with functions described in ***SI appendix*, Fig. S15**.

A hotspot was identified at 36,828,844 bp on chromosome 2 (*chr2_1*), identified by the excessive red, modified green red, normalized difference, Normalized green red difference, and visible atmospherically resistant indices by the three GWAS models consistently explaining 8-13% phenotypic variation (**Dataset S2**). The *chr2_1* peak is inside *GRMZM2G023204* (chr2:36827859..36,829,876; B73 RefGen_v4), a putative protein kinase domain that catalyzes the function of protein kinases. Another candidate gene (~4kb away from *chr2_1*) is *GRMZM2G021560* (*pebp25;* chr2:36,779,809..36,782,444; B73 RefGen_v4) a member of phosphatidylethanolamine-binding proteins (PEBPs) that regulate floral transitions (Danilevskaya, Meng, Hou, et al., 2008) as well as that *GRMZM2G021560* found to be expressed at the early vegetative stage (eg. third leaf stage) (SONG et al., 2019). Integrating GWAS with temporal phenotypes (TPP RGB), loci controlling the temporal VIs explained the

phenotypic variations of multiple VIs revealing the pleiotropic effects of the loci. Additional candidate genes for other hotspots are discussed in ***SI appendix.***

Genomic Prediction Results of Temporal Phenomic Data

Genomic prediction results of temporal VI's identified specific time points for each of the high-resolution VIs in TPP_RGB had varying ability to be predicted in cross validation (Fig. 67). Prediction accuracy showed flowering was the most (and in a few cases least) predictable by genomic markers for many VI's likely because of differential emergence of tassels (Fig. 67). It was surprising that time points prior to flowering in some cases had relatively similar or higher prediction accuracy than those at flowering time (Fig. 67). Overall, sensor-based VIs were predictable at different time points using whole genome markers but estimated different phenotypic effect sizes (Fig. 67). This demonstrates that genetic makers estimated changing effects sizes revealing the plasticity of temporal VIs that are more explanatory to monitor the interactions between genetic background of plants and their growing environments across plant growth.

Genomic Prediction vs Phenomic Prediction

Grain yield (GY) prediction ability of phenomic and genomic approaches were compared between both phenomic data sets (TPP_RGB and TPP_Multi) and genomic data (genomic prediction, GP). Comparing model prediction accuracies for untested genotypes in tested environment (CV2), low resolution multispectral (TPP_Multi) outperformed ($\bar{r}$ = 0.80) both genomic prediction ($\bar{r}$ = 0.71) and high resolution RGB (TPP_RGB; $\bar{r}$ = 0.72) (Fig. 68). Comparing model prediction accuracies for untested genotypes in untested environment (CV4), genomic prediction and RGB high resolution

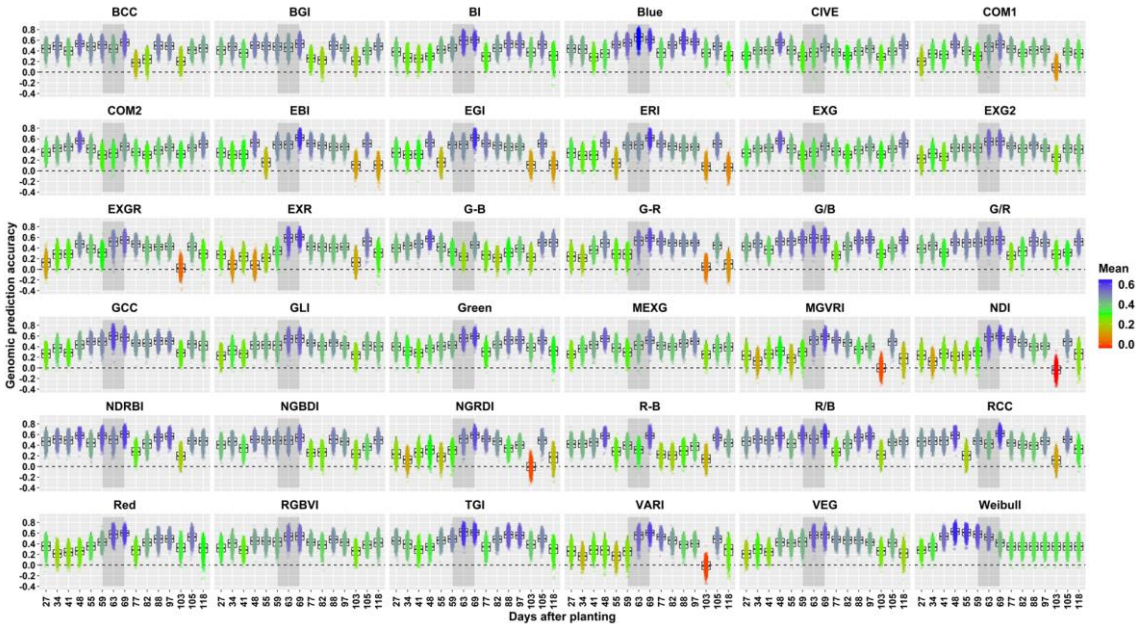

Fig. 67. Each box plot shows the genomic prediction accuracy results belonging to each time points of each temporal trait in TPP_RGB, each contains 500-prediction accuracies. Y axis shows the prediction accuracy and x axis shows the flight date as days after planting time. Each box plot was colored based on their mean. Heatmap color scale was given in the figure legend changing between 0 to 0.6. Gray shading in each represents flowering time. Different time points of temporal traits were found to have different response to genetic markers across growth stages of plant development. Reprinted from Adak, Murray, & Anderson, 2021.

phenomic selection supplied similar prediction accuracies ($\bar{r}$: 0.53-0.55), while low resolution with multispectral sensor based HTP supplied a lower prediction accuracy (Fig. 68). Overall, the phenomic prediction platforms used in this study were largely able to predict better (CV2), or equivalent to, genomic prediction (CV1 and CV3) depending on which of the four cross validation schemes is evaluated (Fig. 68). However, genomic prediction outperformed phenomic prediction when predicting known genotypes in unknown environments (CV3). Combining both UAS measures (TPP_RGB and

TPP_Multi) using ridge regression did not further improve prediction accuracies (data not shown).

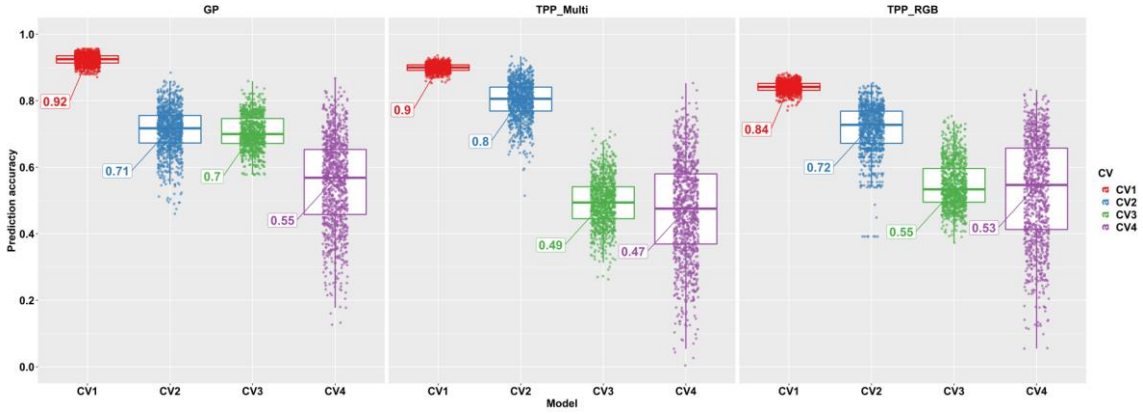

Fig. 68 shows the prediction accuracy results of yield belonging to the three models. GP represents the prediction accuracy of genomic prediction, TPP_Multi represents the prediction accuracy of phenomic prediction using the VIs derived from the multispectral images with low resolution, TPP_RGB represents the prediction accuracy of phenomic prediction using the VIs derived from the RGB images with high resolution. Four cross validation schemes were used: predicting tested genotypes in tested environments (CV1), predicting untested genotypes in tested environments (CV2), tested genotypes in untested environments (CV3), and untested genotypes in untested environments (CV4). Phenomic prediction predicted the grain yield (GY) of maize hybrids better in CV2 than genomic prediction. Prediction accuracies were close to each other in CV3 and CV4. Reprinted from Adak, Murray, & Anderson, 2021.

Discussion

Field-based high-throughput phenotyping technologies, such as drones, are able to provide phenome-wide measurements of plants in much the same way that high-throughput sequencers have provided genome-wide data. Uniquely, phenotyping technologies can screen high numbers of plots repeatedly through the growing period resulting in not only high spatial resolution but also high temporal resolution, helping dissect how different genotypes respond to their environments to maximize fitness in

near real-time (SI appendix, Figs. S7 and S8). Correlations were variable between overall VIs in the phenomic data (SI appendix, Fig. S9). First, there were low to moderate correlations between VIs. Second, temporal values of the same VIs had low correlations across different time points. These results indicates that both using different VIs and their temporal values belonging to multiple time points provide unique and additional information, thus importance of including different VIs and high temporal dimension in constructing the phenomic data was emphasized.

As new temporal phenomic markers are difficult to independently measure and validate, one of the first approaches to evaluate phenomic marker utility is to look at heritability/repeatability values over different replicates and environments. This approach is not needed for genomic markers which do not vary over replicates and environments and theoretically have a repeatability near 1, but are also unable to capture environmental interaction in real time. Temporal repeatability (Eq. 3) of VIs were moderate, above ~0.5 for TPP_RGB (SI appendix, Fig. S2) and between 0.26 and 0.66 for TPP_Multi (SI appendix, Fig. S3). Temporal repeatability relied on variation across plant development, biologically more meaningful than using genotypic variation which is static at every time point. Temporal variation captured by drones assesses temporal genotypic variation jointly over time via nested design (Eq. 2). Previously, repeatability has only been calculated between different vegetation indices/CHM and yield at a single time point (Aguate et al., 2017b; Anderson et al., 2019; Galán et al., 2021; Krause et al., 2020b; Montesinos-López et al., 2017; Rutkoski et al., 2016; Sun et al., 2019; G. Wu et al., 2019a); disregarding the temporal genotypic variation occurring across plant growth.

Furthermore, previous studies used either one or a limited number of time points and analyzed each time point separately.

High dimensional and temporal resolution phenomic data used in predictive plant breeding integrated with high throughput genotyping data discovered underlying genetic causes for many important temporal VI features. For instance, pleiotropy discovered via GWAS identified specific loci controlling more than one VIs (SI appendix, Figs. S14 and S15, Dataset S2). In addition, genomic prediction of temporal VI phenotypes proved that estimated effects of each marker varied through time, causing different prediction accuracy results for temporal phenotypes of the same VIs (Fig. 67). Therefore, instead of depending on discrete genome wide markers as predictors for yield, temporal phenotype data formed by estimated temporal marker effects could better predict certain scenarios (e.g., untested genotypes in tested environment). Predicting grain yield of untested genotypes in a tested environment is an important scenario for public breeding programs because lines developed in public breeding programs are mostly targeted for specific environments. So that figure 68 proved that TPP predicted the grain yield better than GP in CV2 indicating that TPP can be better solution for the public breeding programs for genetic gain. In addition, the predictive ability of TPP in untested genotype untested environments (CV4) was in the same range as that of GS (Fig. 68). This is also an important proof of concept that TPP can be used as widely as GP. Genomic prediction methods have been developed over more than a decade and phenomic prediction methods can likewise be improved. Further optimization and improvement of this

approach will likely benefit from the integration of novel crop growth models as genomic prediction has (Messina et al., 2018).

Phenomic Data Can Predict Yield and Flowering Times Via Machine Learning Regressions

Shrinkage factors previously shown as the best performing prediction models when using different hyper parameters have been adapted for predicting both yield (Adak, Murray, Božinović, et al., 2021; Aguate et al., 2017b; Kismiantini, Montesinos-López, Crossa, Setiawan, & Wutsqa, 2021) and flowering times (Adak, Murray, Božinović, et al., 2021) when different reflection bands were used as predictors. Machine learning models with different regularization parameter settings to predict yield and flowering times (**Fig. 66**) were more accurate than linear-based prediction models (Adak, Murray, Božinović, et al., 2021; Montesinos-López et al., 2017). This suggests that temporal variation in VIs do not have a linear relationship to predicted variables. This is because linear models tend to overfit when there are increasing numbers of predictors and with fluctuating collinearity between predictors, such as in phenomic data. Linear models are not capable to explain non-linear relationships between predictors and predicted variables.

Tuning regularization parameters of the ridge, lasso and elastic net-based prediction models is a good approach to deal with model overfitting when high dimensional phenomics data are used in prediction. Tuned regularization parameters in ridge, lasso and elastic net models can lessen coefficients, and predict test data more reliably than linear models. For example, pedigree within flight combination ($\Omega_{i(j)}$ component in *Eq.*

2) were found to be statistically significant for all VI and CHM (*SI appendix*, Fig. S2) indicating a temporal interaction among the pedigree across flight times because of fluctuating temporal phenotype values of VIs (*SI appendix*, Figs. S7 and S8). Nevertheless, a general trend demonstrated that high- and low- yielding pedigrees segregate according to temporal phenotypes of VIs. This reverse correlation of temporal breeding values of the pedigree through time supports the existence of nonlinear relationships, problematic for a linear model to capture. Because of multiple decision tree learning, the random forest model accounts for non-linearity, limiting overfitting.

Phenomic prediction reached up to ~0.80 for grain yield and flowering time prediction (Fig. 66) higher than previously reported prediction accuracies (Aguate et al., 2017b; Galán et al., 2021; Krause et al., 2020b; Rutkoski et al., 2016; Sun et al., 2019; G. Wu et al., 2019a). (Aguate et al., 2017b) showed use of raw reflected bands instead of ratios (e.g. vegetation indices) performed better in prediction models. (Montesinos-López et al., 2017) further reported using all bands simultaneously increased prediction accuracy instead of VIs alone. However, reflected bands used in past studies derived from five to nine time points, lower time dimension data than what we generated in our study. This suggests that predictors derived from additional time points could play an important role on increasing the prediction ability of the models; more so than using the predictors as either raw reflectance bands or vegetation indices.

Genomic Prediction for Temporal Traits Can Vary Depending On The Time Points Of Growth

TPP_RGB phenomic data tested using genomic prediction to identify temporal marker effects and their prediction accuracies for each VI and Weibull_CHM throughout time (Fig. 67) demonstrated that genomic markers could predict an individual's VI or Weibull_CHM value through cross validation using other individuals at the same stage. This demonstrated that certain stages and VIs have more genetic determination and are more heritable.

Temporally varying marker effects on the phenotype of VIs resulted in phenotypes at different timepoints of VIs and Weibull_CHM having different correlations with yield (*SI appendix*, Figs. S5 and S6) as well as different prediction abilities for dependent variables (Fig. 67). A dynamic pattern of marker effects as shown here has so far been overlooked in genomic prediction/selection of yield. (Bernardo, 2021) underlined that predicting the candidate genotype using the phenotype information collected from across multiple environments may be more accurate than using the genetic markers in the prediction model. Similarly, instead of predicting grain yield fitness by whole genome marker effect approaches such as RR-BLUP and GBLUP, including the temporal phenotypic variation occurring across growth into prediction models can result in more accurate fitness prediction as phenomic data already contain temporal marker effects. This study also showed that specific loci can explain different phenotypic variance across more than one derived VI (*SI appendix*, Figs. S14 and S15, Dataset S2) signifying pleiotropic effects of certain markers for the VIs. These pleiotropic effects have various associations with developing young tissues, inflorescence, and yield.

Phenomic Prediction Can Perform Similarly to or Outperform Genomic Prediction

Phenomic data (TPP_Multi and TPP_RGB) predicted grain yield as well as genomic data using ridge regression (Fig. 68) but different results were observed depending on the cross validation scheme. TPP_RGB contained 35 VIs derived from only RGB bands and Weibull_ CHM belonging to fifteen time points (525 phenomic features) resulting in an accuracy of 0.71; this accuracy was same as the accuracy of 0.71 belonging to GP containing the 153,252 segregating whole genome markers. However, when TPP_Multi, which contains the 89 VIs derived from the multispectral bands and Weibull_CHM belonging to twelve time points (1068 phenomic features), were used in the prediction the yield, prediction accuracy reached up to 0.80; substantially higher than both GP and TPP_RGB supplied for the untested genotype in tested environments schemes (CV2) (Fig. 68). Moreover, in the most challenging cross-validation scheme, untested genotypes in untested environment (CV4), GP, TPP_RGB and TPP_Multi performed approximately equally as their prediction accuracies were around 0.50 ± 0.05 (Fig. 68). These empirical findings suggest, for the first time, that increasing temporal as well as spectral information can be used to predict fitness substantially better than genomic prediction. This also suggests that temporal and continuous phenomic data can be better predictors than discrete genomic data in prediction and selection of high yielding genotypes. In the only two previous phenomic prediction studies reported to date, (Holly M Lane & Murray) used 3,076 NIRS bands at a single timepoint, while (Rincent et al., 2018) used 1,050 NIRS bands on grain samples. (Rincent et al., 2018) then showed these NIRS bands outperformed genomic selection which used 84,259 SNP

markers in wheat. Overall, phenomic selection is an emerging approach that may remove the cost of genotyping each year that is required by genomic prediction/selection. Adding a temporal component into phenomic prediction has innumerable known and yet to be discovered advantages.

In summary, this study demonstrated the predictive capability of phenomic data for complex traits in maize, yielding as much as genomic markers frequently applied in plant selection over the past 20 years. UAS surveys over the experimental field plots supplied temporal traits as predictors to facilitate the selection of untested genotypes in untested environments. Growing more plants and measuring them accurately are critical steps to drive effectiveness of selection intensity and accuracy resulting in higher genetic gain over time. This study exemplified that screening more plants and measuring them thanks to repetitive UAV flights across plant growth may results in greater genetic gain than genomic selection when phenomic prediction/selection is applied routinely.

In conclusion, genetic prediction methods, primarily genomic selection, became instrumental over the last decade to drive genetic gain for crop improvement. Such prediction methods leverage information shared between relatives to predict an individual's fitness but remain prohibitively resource intensive and unable to dissect responses to a changing environment. Unoccupied aerial systems (UAS; i.e., drones with sensors) have demonstrated high-throughput, low-resource approaches to temporally evaluate fitness of large and genetically diverse populations. For the first time, this study demonstrates that temporal phenomic predictions (TPP) made from UAS have capacity to perform equal to or better than genomic selection and require fewer resources. TPP

success opens new lines of inquiry for understanding organism reactions to their environment and for our understanding of genetic relationships.

Data availability

Dataset S1 contains the four phenomic data that belongs to RGB HTP platform in optimal management (TPP_RGB_OM), RGB HTP platform in stress management (TPP_RGB_SM), multispectral HTP platform in optimal management (TPP_Multi_OM) and multispectral HTP platform in stress management (TPP_Multi_SM). Dataset S2 contains the discovered SNPs in GWAS for the AUC phenotype values of each VI along with their chromosome, chromosome positions, p-values, minor allele frequencies, effects, explained percent variation, VIs and GWAS models. Dataset S1 and S2 are big files and available upon request by Texas A&M University Quantitative Genetic and Maize Breeding Program.

CHAPTER VII

PEDIGREE-MANAGEMENT-FLIGHT INTERACTION FOR TEMPORAL PHENOTYPE ANALYSIS AND TEMPORAL PHENOMIC PREDICTION

High throughput phenotyping (HTP) platforms are allowing researchers to examine phenotypes of complex traits in plants at high temporal resolution. Unoccupied aerial systems (UAS) HTP systems are used in field-based research where a large number of plants (such as in plant breeding nursery) can be phenotyped at high resolution with minimal labor, cost, and high functional (Shi et al., 2016). Importantly, repetitive UAS surveys over plant breeding nurseries enable examination of temporal phenotypic variation occurring across plant growth, impractical and overlooked in traditional phenotyping so far (Araus & Cairns, 2014).

One important phenotype estimated from UAS images (e.g. orthomosaics and 3D point cloud data) is plant height (aka, canopy height measurements; CHM) with other important measures being spectral reflectance. Temporal phenotypic information of plant height and reflectance bands revealed that various loci govern the temporal phenotypes of plant height and reflectance bands at different time points in genome wide association studies (Adak, Murray, & Anderson, 2021; Adak, Murray, Anderson, et al., 2021; Anderson et al., 2020; Pauli et al., 2016; J. Wang et al., 2021; Xavier, Hall, Hearst, Cherkauer, & Rainey, 2017). Thus, genome wide markers predicted temporal plant height and reflectance bands with varying prediction abilities (Adak, Murray, & Anderson, 2021; Adak, Murray, Anderson, et al., 2021; Adak, Murray, Božinović, et al., 2021). Different heritability values of temporal plant height and reflectance bands have

been calculated previously and range from X to Y showing they are repeatable (Adak, Conrad, et al., 2021; Adak, Murray, Anderson, et al., 2021; Anderson et al., 2019; Krause et al., 2019; Montesinos-López et al., 2017). The heritable nature of UAS derived measures were considered as novel predictors to predict yield in plant breeding programs; temporal phenotypes were used either alone (Adak, Murray, & Anderson, 2021; Adak, Murray, Anderson, et al., 2021; Adak, Murray, Božinović, et al., 2021; Krause et al., 2019) or combined with genomic data (Galán et al., 2021; Rincent et al., 2018; Sun et al., 2019) to predict yield.

The majority of current literature pertaining to UAS derived PHT and reflectance bands estimates has focused on the extraction of breeding values (i.e. genetic means or best linear unbiased predictors/estimates [BLUP/BLUE]) per individual flight dates in maize (Zea mays L.) hybrids (Anderson et al., 2020; Anderson et al., 2019; Pugh et al., 2018; Tirado, Hirsch, & Springer, 2020). Several optimization related studies regarding the implementation of field based HTP platforms were proposed in agricultural field-based research plots (Anderson et al., 2019; Chu, Starek, Brewer, Murray, & Pruter, 2018; Geipel, Link, & Claupein, 2014; Han et al., 2019; Han et al., 2018; Malambo et al., 2018; Pugh et al., 2018; Shi et al., 2016; Tirado et al., 2020). In addition, plot-based data extraction pipelines from the outputs of UAS flights (e.g. 3D point clouds and geographically corrected images) were proposed (Anderson & Murray, 2020; Matias, Caraza-Harter, & Endelman, 2020; Morales et al., 2020), which are important for plant breeding nurseries and trials to estimate the breeding values of tested genetic materials (e.g. hybrids or inbreds) from their temporal reactions under different environmental

conditions and managements (Araus & Cairns, 2014; Sankaran et al., 2015; Shi et al., 2016; Tirado et al., 2020).

Genotype-by-environment (GxE) interaction is special case study in crop science to understand plasticity of complex traits such as plant height in maize (Peiffer et al., 2014; Wallace et al., 2016b). However, understanding of the underlying causes of plasticity for measures like plant height and spectral reflectance remains limited, in part due to only having terminal measures (yield, terminal plant height); monitoring genotypes throughout growth stages, especially early growth, is needed. Single time point analysis of UAS flights disregards the hierarchy of biological variations in temporal plant height of tested genetic materials through the growth periods, which disregards the retrospective systematic effects leading plasticity during growth periods. Previous studies have identified unique quantitative trait loci (QTLs) associated with temporal plant height belonging to different time points. Additionally, the same QTL change effect sizes, demonstrating sources of variation in early growth periods in terms of temporal plant heights and reflectance bands (Adak, Murray, & Anderson, 2021; Adak, Murray, Anderson, et al., 2021; Anderson et al., 2020; J. Wang et al., 2021; X. Wang et al., 2019). This is important where temporal plant height and reflectance bands data should be analyzed jointly to better scrutinize their plasticity within growth stages. Previous field based HTP studies have evaluated temporal plant heights or reflectance bands by individual flight dates to predicting the breeding values for each flight date independently. Here we propose analyzing UAS derived temporal plant height data as an interaction based statistical design, where the genetic model term has interaction of

pedigrees and flight dates to obtain the temporal breeding values to dissect the plasticity along with different levels of management conditions (e.g. late and optimal planting) and populations (e.g. diverse hybrids population in maize). To test this interaction model, 228 and 100 maize hybrids were grown in 2017 and 2019 as both optimal and late plantings, and seven and five drone surveys were conducted over 2017 and 2019 trials respectively, where drone flights were same across plantings in each year.

The objectives of this study were to (i) conduct the interaction based statistical design to predict the temporal breeding values of CHM and a vegetation index (NGRDI; Normalized green-red difference index) of maize hybrids across flight dates and managements, and (ii) predict the grain yield using temporal phenotypes of CHM and NGRDI in each year, in which optimal planting and late planning were used as tested and untested environments to test the predictive ability of temporal phenotype data for grain yield in each year. Weather data were also combined with temporal phenotype data to test the second objective.

Material and Methods

Genetic Materials and Management Conditions

Two different populations were used in this study. The 2017 trial was a subset of the genome to field (G2F; https://www.genomes2fields.org/) project containing 228 hybrids. The 2017 trial was grown under two different management conditions, defined as optimal planting with irrigation (OI) and late planting with irrigation (LP). The LP trial was expected to expeiance increased heat stress. Optimal and late plantings of 2017 trials were planted on March 3, 2017 and April 6, 2017 respectively. The 2019 trial

contained 100 advanced maize hybrids developed by the Texas A&M maize breeding program. 2019 trials were grown under two different management conditions that were optimal planting with irrigation (OI) and late planting with irrigation (LP). Optimal and late plantings of 2019 trial were planted on March 20, 2019 and April 12, 2019, respectively.

Field Based High Throughput Phenotyping and Data Extraction

An unoccupied aerial vehicle (UAV, DJI Phantom 4 Pro V2.0 (DJI, Shenzhen, China) was flown over 2017 and 2019 trials to collect temporal plant heights and NGRDI. Seven and five UAV surveys were conducted for both managements (Table 6). A height of 25 meters was set for UAV flight elevation in each year. Resolution of the UAV images was 72 DPI obtained by the standard integrated camera of the DJI Phantom 4 Pro V2.0. Raw images were collected with the integrated 20-megapixel RGB camera with one-inch square CMOS (complementary metal oxide semiconductor). Image overlap was set to 90 percent side and forward overlap. All raw images were processed within Agisoft Metashape V15.2 software (Agisoft LLC, Russia) to generate orthomosaics, point clouds, and digital surface models (DSM). 99th percentile plant heights were estimated from the densified point cloud following the procedures set forth by (Anderson et al., 2019) using hierarchical robust interpolation approached. The R/UAStools::plotshpcreate (Anderson & Murray, 2020) function was used to create the polygons shapefiles (.shp) for each row plot. Resulting shapefiles were used within the R/FIELDimageR (Anderson & Murray, 2020) to extract the normalized green-red difference index (NGRDI) (Tucker, 1979) for each row plot of both populations.

Grain yield (t/ha) was collected using a research plot combine. Flowering times were collected as the number days after sowing at which approximately 50% of each plot expressed extruded silks [days till silking (DTS)] and 50% expressed tassels extruded anthers [days to anthesis (DTA)]. Three types of terminal plant heights were measured at the end of reproductive stage one time manually with a ruler. These were plant height (from ground to tip of tassel; PHT), flag leaf height (from ground to flag leaf; FHT) and ear height (from ground to closest ear to ground; EHT). Two consecutive row plots were used for each hybrid in flowering times, manually measured plant heights and yield data collections for each management in both years.

Table 6 The flights as days after plantings (DAP) and their corresponding days in optimal and late plantings in 2017 and 2019 were given.

Flight	2017	
(DAP)	Optimal planting	Late planting
48	20/4/2017	22/7/2017
63	5/5/2017	6/8/2017
70	12/5/2017	13/8/2017
73	15/5/2017	16/8/2017
82	24/5/2017	25/8/2017
98	9/6/2017	10/9/2017
112	23/6/2017	24/9/2017
Flight	2019	
(DAP)	Optimal planting	Late planting
39	28/4/2019	21/5/2019
63	22/5/2019	14/6/2019
75	3/6/2019	26/6/2019
88	16/6/2019	9/7/2019
96	24/6/2019	17/7/2019

Experimental Design and Statistical Analysis

Each trial was grown as a randomized complete block design with spatial variation partitioned into ranges and rows with two replications (Eq. 1). Each plot consisted of two consecutive row plots in each replication. Each row was ~7.62 m, and row spacing was 0.76 m. Variance components and yield (t/ha) of maize hybrids were estimated in each year using the Eq. 1 below :

$$Y_{ijklm} = \mu + pedigree_i + management_j + (pedigree * management)_{ij} + range_k + row_l + rep[management]_{m[j]} + error_{ijklm} \quad \text{Eq. 1}$$

Where, $Y_{ijklm}$is the yield value (t/ha) of the ith two row planted maize hybrid belonging to jth management, kth range , lth row and mth replication; μ = grand mean; $pedigree_i$ is the random effect of ith maize hybrid with $pedigree_i \overset{iid}{\sim} N(0, \sigma^2_{pedigree_i})$; $management_j$ is the random effect of jth management with $management_j \overset{iid}{\sim} N(0, \sigma^2_{management_j})$; $pedigree * management_{i*j}$ is the random effect of interaction between ith maize hybrid and jth management with $(pedigree * management)_{ij} \overset{iid}{\sim} N(0, \sigma^2_{(pedigree*management)_{ij}})$; $range_k$, and row_l are the random effects of kth range, lth row with $range_k \overset{iid}{\sim} N(0, \sigma^2_{range_k})$, $row_l \overset{iid}{\sim} N(0, \sigma^2_{row_l})$ which do not need nesting as unique locations in the field, rep_m is the random effect of mth replication nested within jth management with $rep[management]_{m[j]} \overset{iid}{\sim} N(0, \sigma^2_{rep[management]_{m[j]}})$. $error_{ijklm}$ is the residual error containing unexplained variation by any components in Eq. 1.

Repeatability of yield was calculated in each year with the below formula (Eq. 2).

$$Repeatability = \frac{\sigma^2_{pedigree}}{\sigma^2_{pedigree} + \left(\frac{\sigma^2_{(pedigree*management)}}{a}\right) + \frac{\sigma^2_{error}}{a \times c}}$$

Eq. 2

Where, a is the number of managements (late and optimal plantings) and c is the number of replications (two reps) in each year.

To predict the temporal phenotype data (CHM and NGRDI) of maize hybrids we here propose a three-way interaction design (Eq. 2) across flight dates and managements for each year as follows:

$$\begin{aligned} Y_{ijklmn} = \mu + pedigree_i + flight_j + management_k + (pedigree * flight)_{ij} \\ + (pedigree * management)_{ik} + (flight * management)_{jk} \\ + (pedigree * flight * management)_{ijk} + range_l + row_m \\ + rep[management]_{n[k]} + error_{ijklmn} \end{aligned}$$

Eq.3

Where, Y_{ijklm} is the CHM or NGRDI values of two rowss of the ith maize hybrid belonging to jth flight date, kth management, lth range, mth row and nth replication nested within kth management; μ = grand mean; $pedigree_i$ is the random effect of ith maize hybrid with $pedigree_i \overset{iid}{\sim} N(0, \sigma^2_{pedigree_i})$; $flight_j$ is the random effect of jth maize hybrid with $flight_j \overset{iid}{\sim} N(0, \sigma^2_{flight_j})$; $management_k$ is the random effect of

kth management with $management_k \overset{iid}{\sim} N(0, \sigma^2_{management_k})$; $(pedigree * flight)_{ij}$ is the random effect of interaction between ith maize hybrid and jth flight date with $(pedigree * flight)_{ij} \overset{iid}{\sim} N(0, \sigma^2_{(pedigree*flight)_{ij}})$; $(pedigree * management)_{ik}$ is the random effect of interaction between ith maize hybrid and kth management with $(pedigree * management)_{ik} \overset{iid}{\sim} N(0, \sigma^2_{(pedigree*management)_{ik}})$; $(flight * management)_{jk}$ is the random effect of interaction between jth flight and kth management with $(flight * management)_{jk} \overset{iid}{\sim} N(0, \sigma^2_{(flight*management)_{jk}})$; $(pedigree * flight * management)_{ijk}$ is the random effect of interaction between ith pedigree, jth flight and kth management with $(pedigree * flight * management)_{ijk} \overset{iid}{\sim} N(0, \sigma^2_{(flight*management)_{ijk}})$; $range_l$, and row_m are the random effects of lth range, mth row with $range_l \overset{iid}{\sim} N(0, \sigma^2_{range_l})$, $row_m \overset{iid}{\sim} N(0, \sigma^2_{row_m})$ and $rep[management]_{n[k]}$ is the random effect of nth replication nested within kth management with $rep[management]_{n[k]} \overset{iid}{\sim} N(0, \sigma^2_{rep[management]_{n[k]}})$. $error_{ijklmn}$ is the residual error containing unexplained variation after fitting components in Eq. 3.

Temporal repeatability (Eq. 4) for each temporal phenotype was proposed as follows:

$$Temporal\ repeatability = \frac{\sigma^2_{pedigree}}{\sigma^2_{pedigree} + \left(\frac{\sigma^2_{pedigree*management}}{a}\right) + \left(\frac{\sigma^2_{pedigree*flight}}{b}\right) + \left(\frac{\sigma^2_{pedigree*flight*managementent}}{a \times b}\right) + \frac{\sigma^2_{error}}{a \times b \times c}}$$

Eq. 4

Where, $a, b,$ and c are the numbers of managements (late and optimal plantings), flight times (seven in 2017 and five in 2019) and replications (two reps) in 2017 and 2019 trials. All equations were run using the lme4 package in R with restricted maximum likelihood (REML) approach

Prediction model

Grain yield breeding values (predicted by Eq.1) were used as predicted traits in machine learning based regression models by using temporal breeding values of CHM and NGRDI (predicted by Eq. 3) to assess the predictive ability of temporal phenomic data. To do so, results of (pedigree*flight*management) interaction components in Eq. 3 were combined and used as predictors. Prediction was conducted between managements of each year. Optimal planting trials (OI) were used for training as tested environments while late plantings (LP) were used as untested (validation) environments in each year. The R/caret package was used to construct the prediction models with 1000 bootstraps; each bootstrap contained the random data split where 60 percent of maize hybrids were used as tested genotypes while theremaining hold-out 40 percent were used as untested genotypes. Five-fold cross validation with three repeats was used in each bootstrap. One bootstrap of the prediction models is briefly explained here. First, a random data split was conducted as 60:40 percent ratio as training and test data set respectively by R/caret::createDataPartition(). Second ridge, and lasso regressions were trained using training data set (60 percent split data) by R/caret::train(), where model was set “glmnet” for both ridge and lasso regressions, alpha level was set as “0” and “1” for ridge and lasso regressions respectively, “lambda” values were also searched between 0 and 1

based on then equal increments numbers to tune the ridge and lasso regressions. Third, these trainings were applied to: tested genotypes in tested environment (Cross validation 1 (CV1): 60 percent maize hybrids in OI), untested genotypes in tested environment (CV2: 40 percent maize hybrids in OI), tested genotypes in untested environment (CV3: 60 percent maize hybrids in LP), untested genotypes in untested environment (CV4: 40 percent maize hybrids in LP) were predicted by trained ridge and lasso regressions. Finally, correlation between predicted grain yield values and actual grain yield breeding values were calcauted for four scenarios (given in the third step) and calculated as four types of prediction abilities.

Weather data were also merged with temporal phenomic data of 2017 and 2019 trials to predict yield following the same prediction procedures explained above. Daily weather data were obtained from the National Oceanic and Atmospheric Administration National Centers for Environmental Information (https://www.ncdc.noaa.gov/), and environmental parameters from planting to 100 days after planting times were used in prediction models. Specifically included were temperature (minimum, average and maximum; °C), dew point (minimum, average and maximum; °C), humidity (minimum, average and maximum, %), wind speed (minimum, average and maximum; mph), atmospheric pressure (minimum, average and maximum; Hg), precipitation (cm), photoperiod (day light as hours), diurnal temperature range ($Temp_{max} - Temp_{min}$), growing degree days ($\frac{Temp_{max}+Temp_{min}}{2} - T_{base}; T_{base}\ is$ 10°C), and photothermal time ($GDD * photoperiod$). These environmental parameters from planting to 100 days after

planting were illustrated for optimal and late planning trials in 2017 and 2019 in supplementary figure 69.

Results

Results of Interaction Design and Temporal Repeatability

Temporal phenomic data of CHM and NGRDI was predicted by an interaction design (Eq. 3) containing three-way interactions of maize hybrids (pedigree), drone flights (flights), and managements (optimal and late plantings). Overall, the $Flight$ variance component explained the highest percent variation of total variation for CHM and NGRDI (Figure 69). Interaction based design for temporal phenotype enables to calculate the temporal repeatability of CHM and NGRDI by equation 4 (Eq. 4). Temporal repeatability was 0.87 and 0.55 for CHM in 2017 and 2019, and 0.56 and 0.68 for NGRDI in 2017 and 2019 respectively (Figure 69).

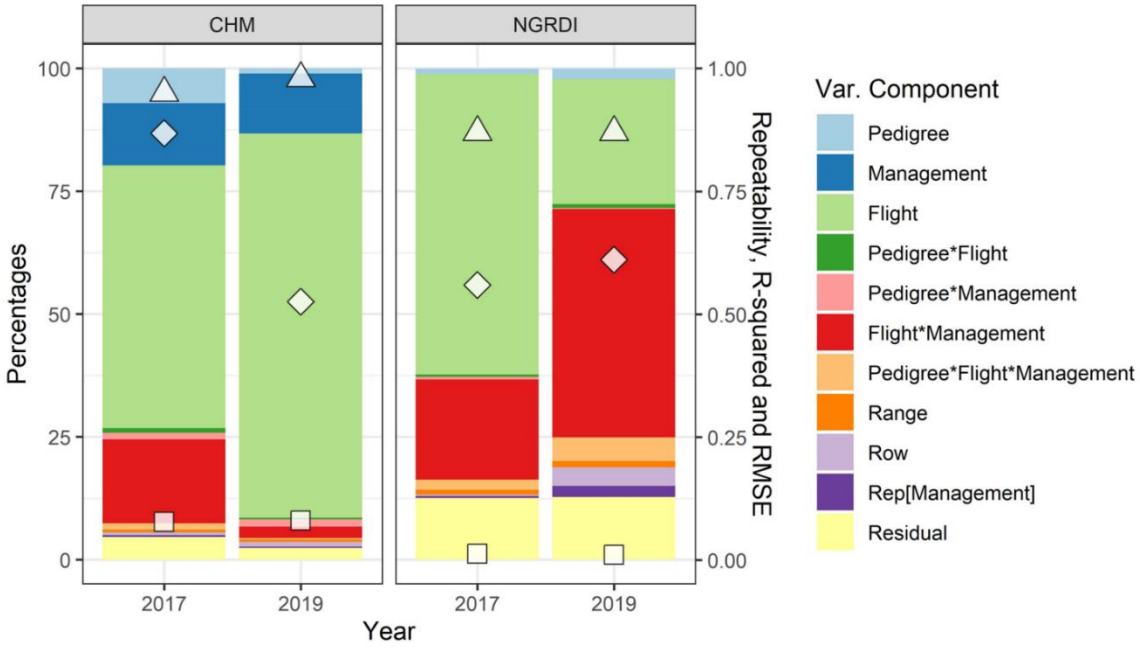

Figure 69 Explained percent variation by each variance component of Equation 3 (Eq. 3) for temporal plant height (canopy height measurement; CHM) and normalized green-red difference index (NGRDI). Left axis shows the percentages explained by the variance components; right axis shows the temporal repeatability values of the temporal traits (white diamond), R-squared (white triangle) and root mean square error (RMSE, white square) of the models. The flight effect and interactions explained the highest proportion of total variation.

The $Flight$ variance component explained the highest amount of variation. The temporal variation of the maize hybrids was scrutinized across management by demonstrating the $(Pedigree * Flight * Management)$ and $(Flight * Management)$ interactions for CHM (Figure 70) and NGRDI (Figure 71).

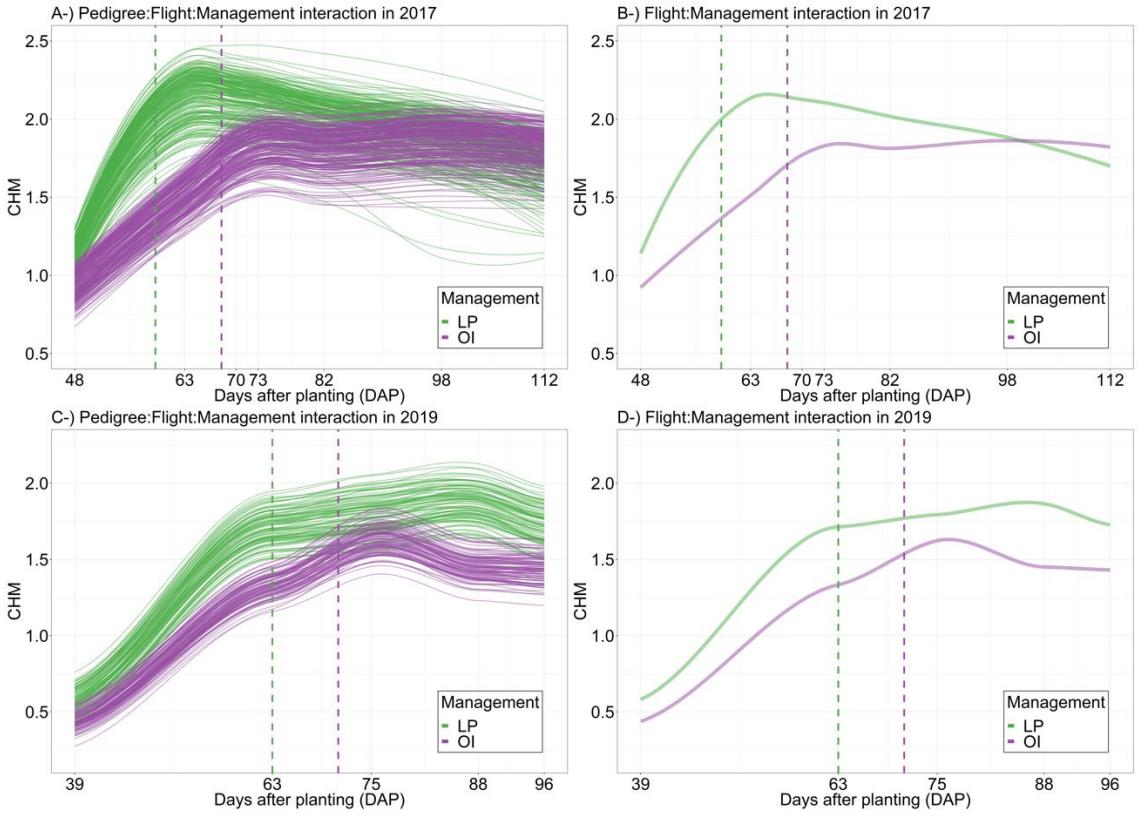

Figure 70 A and C show the (Pedigree*Flight*Management) and B and D show the (Flight*Management) interactions for the temporal plant height (canopy height measurement; CHM). A and B are the results of 2017 while B and D are the results of

2019. LP and OI are the late and optimal planting managements respectively. Temporal variation of CHM showed that late planting had taller plant heights than those of optimal planting for 2019 and most of 2017. Vertical dashed lines show the means of flowering time (days to anthesis; DTA) of each management in 2017 and 2019.

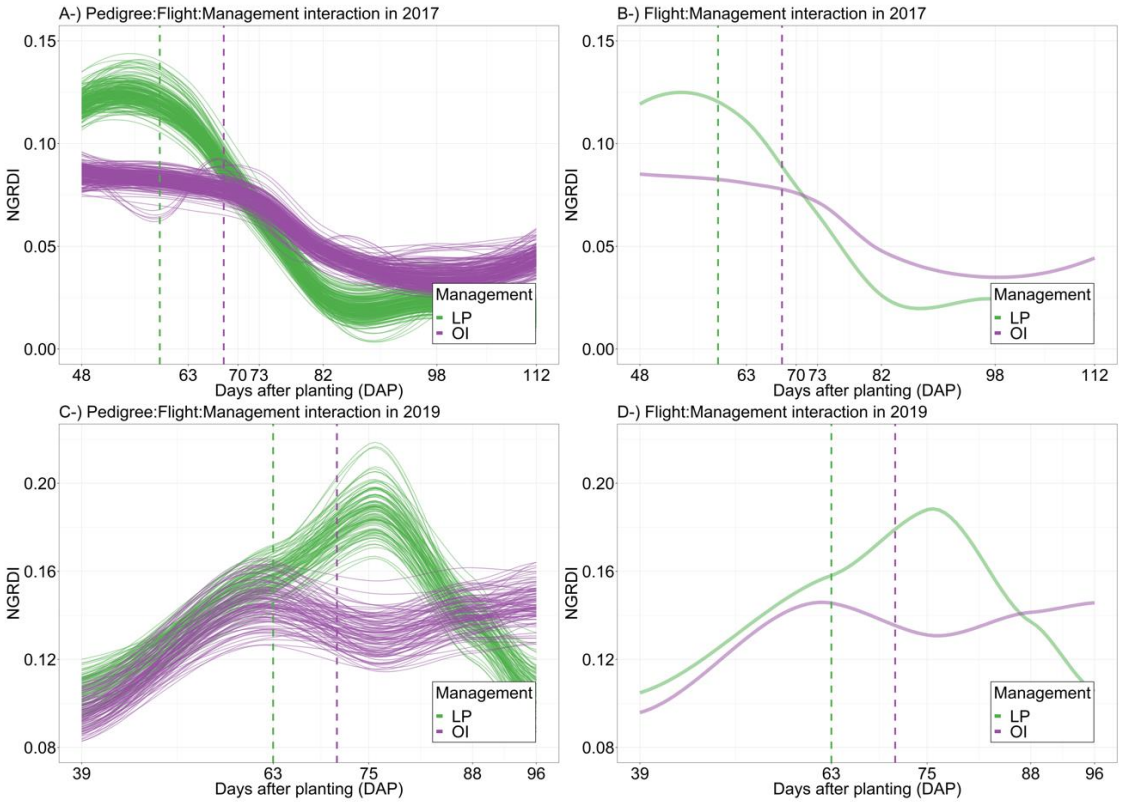

Figure 71 shows the results of (Pedigree*Flight*Management) and (Flight*Management) interactions for the normalized green-red difference index (NGRDI). A and C are the results of (Pedigree*Flight*Management) for 2017 and 2019 trials respectively; A and D are the results of (Flight*Management) interaction for the 2017 and 2019 trials respectively. Temporal variation of NGRDI showed that late plating had high there was a interaction after flowering times in both year consistently. Vertical dashed lines show the means of flowering time (days to anthesis; DTA) of each management in 2017 and 2019. LP and OI are the late and optimal planting managements respectively.

Temporal plant heights (CHM) were taller in late planting than optimal planting across flight dates in both years consistently, except during later growth in 2017 (Figure

70). This was in agreement with manually measured plant heights (PHT, FHT and EHT) (Figure 72). Maize hybrids flowered earlier in late planting, when measured in days after planting, than in optimal plantings in both years consistently (Figure 72). Normalized green-red difference index (NGRDI)always scored higher in late planting than optimal planting up to end of flowering times in both years consistently, however this was shifted where NGRDI scores were lower in late planting than optimal planting after flowering times in both years consistently, showing the earlier senescence of this planting (Figure 71). Grain yield was lower in late plantings than in the optimal plantings as typically observed(Figure 72). Comparing genotypes, correlations between NGRDI and grain yield were always positive belonging to early flight dates in both years consistently and reached up to ~0.5 in 2019 and ~0.6 in 2017; however, the correlations become weaker and sometimes turned non-significant during late flights in both years (Figure 73). Correlations between CHM and grain yield were more stable than correlations between NGRDI and grain yield, and reached up to ~ 0.5 in both years (Figure 73).

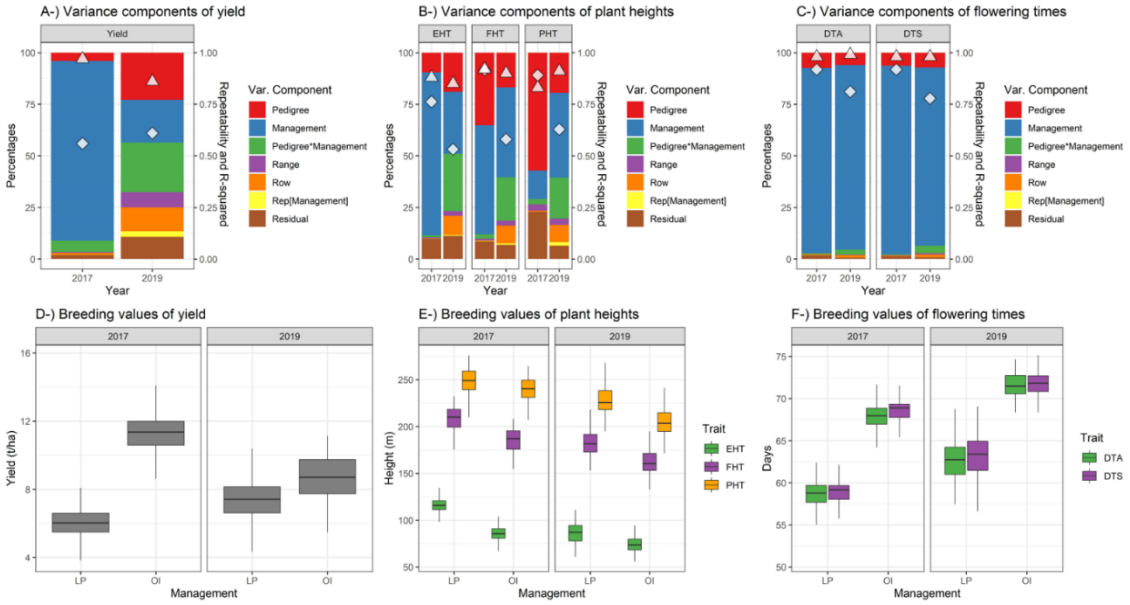

Figure 72 the explained percent variation by each variance component of equation 1 (Eq. 1) for grain yield, plant heights and flowering times. A, B and C show the explained percent variances by each component for grain yield, three types of manually measured plant heights and flowering times respectively. White diamonds are the repeatability values (calculated by equation 2) of yield, plant heights and flowering times; white rectangles are the R-squared of the models. EHT, FHT and PHT are manually measured plant heights from ground to first ear, to flag leaf and to tip of tassel respectively; DTA and DTS are days to anthesis and silking respectively. D, E and F are the breeding values of maize hybrids for grain yield, three types of manually measured plant heights and flowering times respectively; breeding values were obtained from (pedigree*management) component in each year.

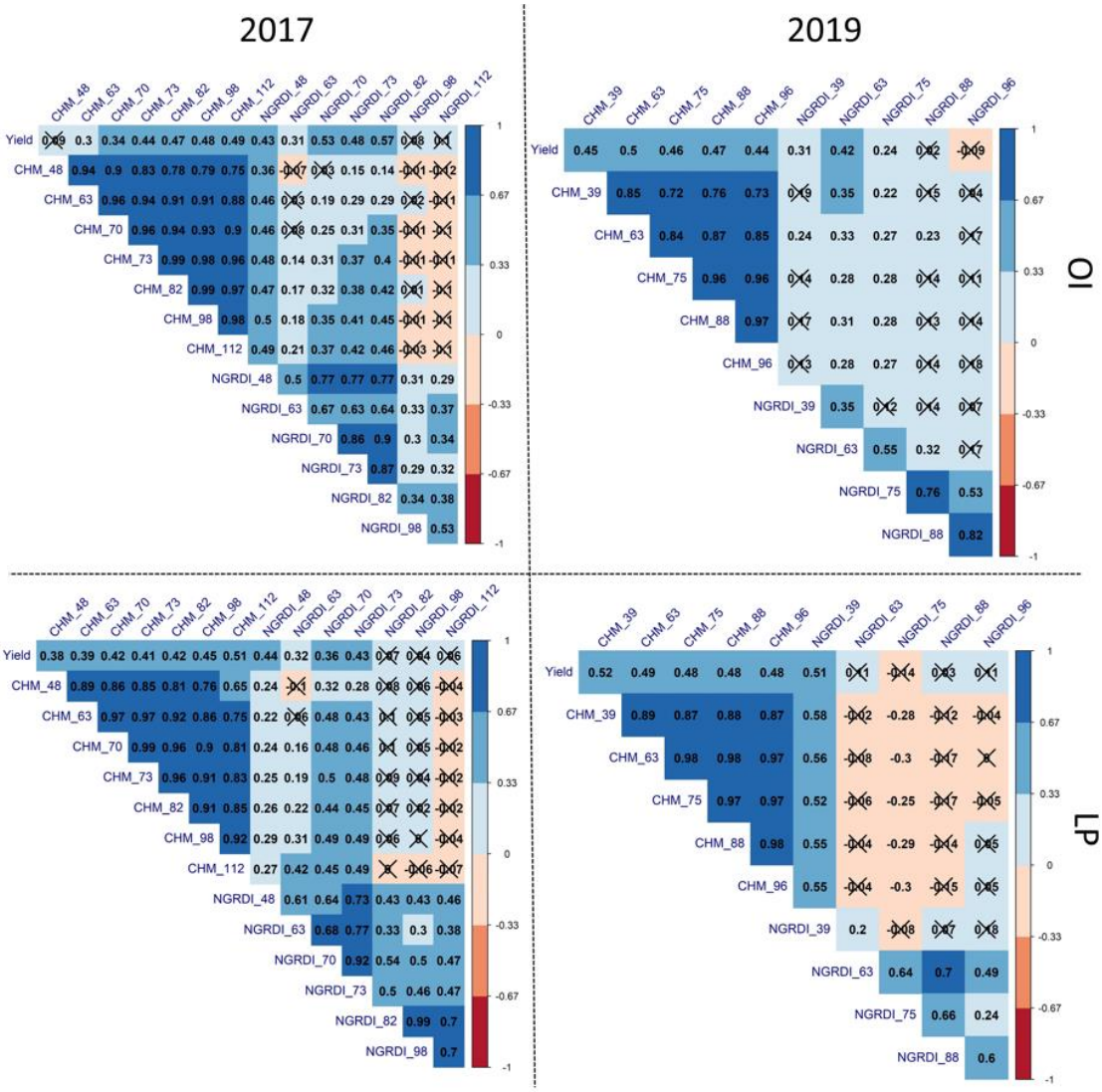

Figure 73 correlation coefficients of temporal phenomic data belonging to 2017 (left) and 2019 (right) and yield. LP and OI indicate late and optimal planting management respectively in both years.

Prediction Model

The predictions of grain yield were conducted based on four different prediction abilities (see the prediction model in M&M). Ridge regression performed better than lasso in prediction the grain yield in untested environments (CV3 and CV4) in 2017 and

2019 trial consistently (Figure 74). Phenomic data predicted the grain yield with the prediction ability of 0.23 in CV3 and CV4 of 2017 trial by lasso regression; however, prediction abilities were higher (0.34 in CV3 and CV4) by ridge regression (Figure 74). Similar results were observed in 2019; lasso predicted grain yield with the prediction ability of 0.5 in CV3 and 0.48 in CV4, which were less than the prediction ability of ridge regression (0.51 in CV3 and 0.49 in CV4) (Figure 74). Remarkably, combined data (phenomic data plus weather data) predicted grain yield greater than phenomic data in both years by ridge regression (Figure 74). Combined data predicted the grain yield in 2017 trial with the prediction accuracy of 0.49 in CV3 and CV4 by ridge regression, which were significantly / substantially higher than prediction accuracies (0.34 in CV3 and CV4) obtained when only phenomic data was used (Figure 74). Similarly, combined data predicted grain yield in the 2019 trial with the prediction accuracy of 0.53 in CV3 and 0.51 in CV4 by ridge regression, higher but not significantly different than the prediction accuracies (0.51 in CV3 and 0.49 in CV4) obtained when only phenomic data was used (Figure 74). Overall, prediction ability of the grain yield was improved in untested environments in both years when combined data (weather plus phenomic data) was used (Figure 74).

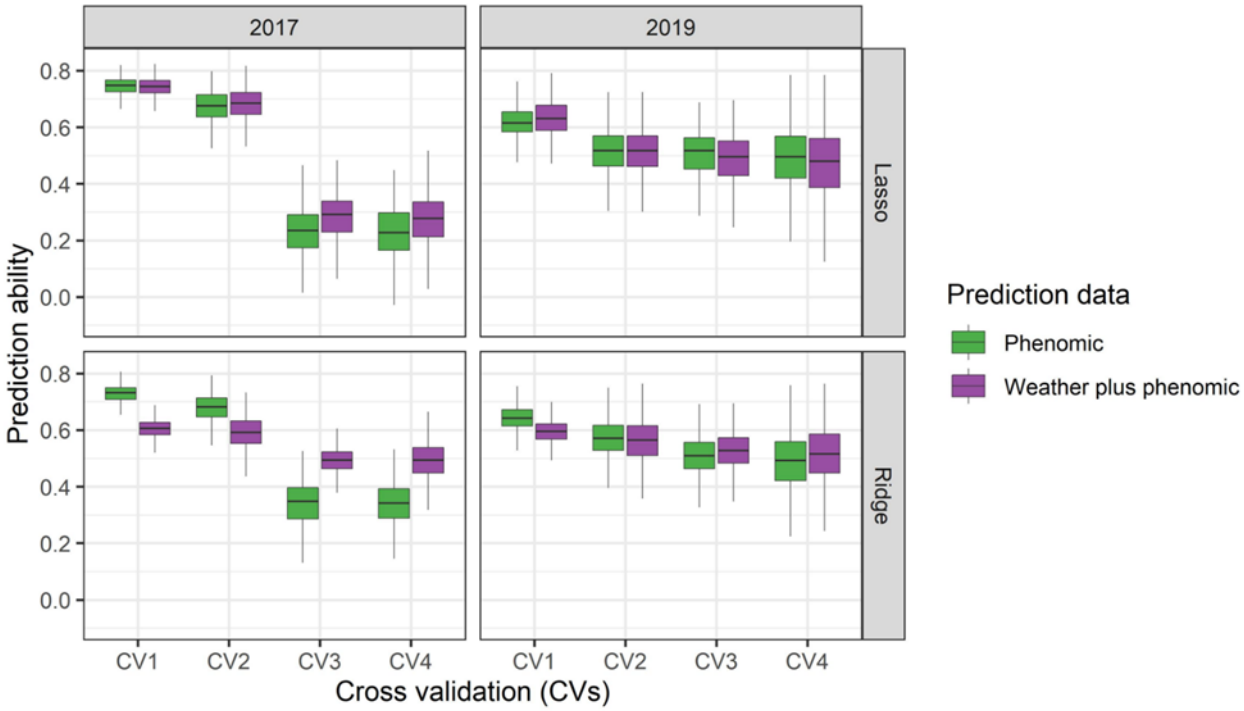

Figure 74 Prediction abilities calculated for grain yield using temporal phenomic data and combined data (phenomic and weather data) using ridge and lasso regressions in 2017 and 2019. Ridge regression predicted the grain yield of maize hybrids in untested environments. Combined data also boosted the prediction accuracies in prediction of grain yield of maize hybrids in untested environments. CV1 (cross validation 1) is the prediction accuracy of tested genotypes (60 percent maize hybrids) in tested environment (optimal planting, OI); CV2 is the prediction accuracy of tested genotypes (60 percent maize hybrids) in untested environment (late planting, LP); CV3 is the prediction accuracy of untested genotypes (40 percent maize hybrids) in tested environment (optimal planting, OI) and CV4 is the prediction accuracy of untested genotypes (40 percent maize hybrids) in untested environment (late planting, LP) in both years.

Discussion

The Importance of Interaction Designs in Temporal Data Analysis

In crop science, statistical model selection is an important step in evaluating the temporal traits that are collected from various time points of crop growth. UAS high throughput phenotyping application have been providing a vast amount of temporal data for complex traits. A need for statistical and biologically meaningful data assessment to

predict genetic performance has emerged as a major concern. This study proposed an interaction design containing three-way interaction of pedigree (maize hybrids), drone surveys (flight) and managements (optimal and late plantings). Thus, temporal breeding values of maize hybrids temporal traits (e.g. CHM and NGRDI) can be estimated and visualized through flight times as a result of three-way interaction components in the mixed model (equation 1; Eq.1). Using visualization of the temporal breeding values, phenotypic plasticity of traits was dissected within growth stages (Figure 74). Since segregation of temporal plant heights, and NGRDI during maize growth are orchestrated by unique loci as well as same loci with different effect sizes depending on the time points (Adak, Murray, & Anderson, 2021; Adak, Murray, Anderson, et al., 2021; Anderson et al., 2020; J. Wang et al., 2021; X. Wang et al., 2019), a natural biological variation in plant height are emerged as a result of the manipulation that create hierarchical layers belonging to different time points of crop growth (Bac-Molenaar, Vreugdenhil, Granier, & Keurentjes, 2015). Utilizing the interaction component (pedigree*flight*management component in Equation 1), the biological hierarchy in plant heights that occurs at any time of growth can be evaluated in that time level of the interaction factor. The interaction design is more powerful in regard to explaining the biology of the temporal trait genetic variation of maize hybrids (e.g. CHM and NGRDI) across flight times and management. With the interaction design approach for temporal traits, temporal variation of each plot can be considered within crop growth, potentially more meaningful in biological interpretation of plasticity in any of CHM and NGRDI across maize growth. The interaction design also is convenient model for dissecting

sources of phenotypic plasticity of complex traits in the hierarchy of the multiple time points that are captured by drones.

Prediction of Grain Yield

Temporal changes in the CHM and NGRDI had unique trajectories for late and optimal plantings in both years (Figure 70 and 71); these trajectories resulted in low and high grain yield in late and optimal planting managements in both years (Figure 72). In other words, these temporal trajectories of CHM and NGRDI were early predictors of grain yield, across diverse management (optimal vs late plantings); weather data merged with temporal phenotype data improved the predictions of grain yield. Weather parameters previously have been incorporated with genomic markers to predict the grain yield of maize hybrids (Rogers & Holland, 2021), these weather effects boosted the grain yield prediction ability. However, prediction ability was also found to have a dependence of similarity in levels between tested and untested environments. Similarity between training (optimal planning; OI) and test environments (late plating; LP) was less in 2017 than those in 2019 (Supplementary Figure 2). Therefore, it is notable that weather data boosted the prediction ability to be greater in 2017 than in 2019 (Figure 74). Temporal phenotype data captured by UAS is the response to changing environmental parameters occurring across growth. Temporal variation of UAS derived traits can therefore improve the link between training and test environments. Because temporal phenotype data are manipulated by multiple loci; some certain loci control the temporal traits at multiple time points with changing phenotypic effect sizes while other certain loci control the temporal phenotypes at single time points with the unique effect

sizes across time points of growth and environments (Adak, Murray, Anderson, et al., 2021; Li, Guo, Mu, Li, & Yu, 2018; Mu, Guo, Li, & Yu, 2021; Scheres & Van Der Putten, 2017). In other words, temporal phenotype data from UAS along with weather data can result in better predictors of grain yield across tested environments than genomic markers can; because genomic markers are not capable to capture temporal variation of pedigrees driven by various environmental parameters across growth in training and testing environments.

Previous prediction studies considering the genomic and environmental data together have shown that prediction accuracies were increased thanks to genotype by environment interaction effects.; However, prediction models were found to be most successful when similarity is high between training and test environments (Bandeira e Sousa et al., 2017; Cuevas et al., 2018; Monteverde et al., 2018). Our results indicate that temporal phenotype data along with environmental data predicted grain yield better when similarity between training and test environment was lower (Figure 74; 2017 trials). Using weather data and temporal phenomic data, is and extension of temporal phenomic prediction (Adak, Murray, & Anderson, 2021) that might provide greater ability to predict grain yield between unrelated environments.

In conclusion, with the advent of field based high throughput phenotyping, temporal data extraction from multiple time points via multiple UAS surveys provide novel temporal measurements for use in predictive plant breeding. This study also demonstrated an efficient interaction based mixed model to evaluate temporal data, with drone flights added as new variance component. Thus, pedigrees monitored across

multiple time points and environments dissected temporal plasticity occurred across growth.

Temporal phenomic prediction was previously introduced where drone derived temporal phenotypic data was used to predict yield across diverse managements in maze that yielded equal to or better than genomic prediction (Adak, Murray, & Anderson, 2021). This study extended temporal phenomic prediction by using different genotypes and environments and leveraging weather data to train machine learning based prediction models. With this approach, the prediction model performed better in predicting grain yields across hybrids in unknown environments because temporal phenotype data provide a link between training and unknown environments by taking advantages of capturing the temporal variation unique to training and unknown environments that has been disregarded so far by genomic markers.

REFERENCES

Adak, A., Conrad, C., Chen, Y., Wilde, S. C., Murray, S. C., Anderson, S., & Subramanian, N. K. (2021). Validation of Functional Polymorphisms Affecting Maize Plant Height by Unoccupied Aerial Systems (UAS) Discovers Novel Temporal Phenotypes. *G3 Genes| Genomes| Genetics*.

Adak, A., Murray, S. C., & Anderson, S. L. (2021). Temporal phenomic predictions from unoccupied aerial systems can outperform genomic predictions. *bioRxiv*.

Adak, A., Murray, S. C., Anderson, S. L., Popescu, S. C., Malambo, L., Romay, M. C., & de Leon, N. (2021). Unoccupied aerial systems discovered overlooked loci capturing the variation of entire growing period in maize. *The Plant Genome*, e20102.

Adak, A., Murray, S. C., Božinović, S., Lindsey, R., Nakasagga, S., Chatterjee, S., . . . Wilde, S. (2021). Temporal Vegetation Indices and Plant Height from Remotely Sensed Imagery Can Predict Grain Yield and Flowering Time Breeding Value in Maize via Machine Learning Regression. *Remote Sensing, 13*(11), 2141.

AgiSoft. 2016. *PhotoScan Professional. Version 1.2.6*. AgiSoft, St. Petersburg, Russia.

Aguate, F. M., Trachsel, S., González-Pérez, L., Burgueño, J., Crossa, J., Balzarini, M., . . . De los Campos, G. (2017). Use of hyperspectral image data outperforms vegetation indices in prediction of maize yield. *Crop science, 57*(5), 2517–2524

Andersen, J. R., Schrag, T., Melchinger, A. E., Zein, I., & Lübberstedt, T. (2005). Validation of Dwarf8 polymorphisms associated with flowering time in elite European inbred lines of maize (Zea mays L.). *Theoretical and Applied Genetics, 111*(2), 206-217.

Anderson, S. L., & II, S. C. M. (2020). R/UAStools:: plotshpcreate: Create multi-polygon shapefiles for extraction of research plot scale agriculture remote sensing data. *Frontiers in plant science, 11*.

Anderson, S. L., Mahan, A. L., Murray, S. C., & Klein, P. E. (2018). Four parent maize (FPM) population: Effects of mating designs on linkage disequilibrium and mapping quantitative traits. *The plant genome, 11*(2), 170102.

Anderson, S. L., Murray, S. C., Chen, Y., Malambo, L., Chang, A., Popescu, S., . . . Jung, J. (2020). Unoccupied aerial system enabled functional modeling of maize height reveals dynamic expression of loci. *Plant direct, 4*(5), e00223.

Anderson, S. L., Murray, S. C., Malambo, L., Ratcliff, C., Popescu, S., Cope, D., . . . Thomasson, J. A. (2019). Prediction of maize grain yield before maturity using improved temporal height estimates of unmanned aerial systems. *The Plant Phenome Journal, 2*(1), 1-15.

Araus, J. L., & Cairns, J. E. (2014). Field high-throughput phenotyping: the new crop breeding frontier. *Trends in plant science, 19*(1), 52-61.

Araus, J. L., Kefauver, S. C., Zaman-Allah, M., Olsen, M. S., & Cairns, J. E. (2018). Translating high-throughput phenotyping into genetic gain. *Trends in plant science, 23*(5), 451-466.

Aukerman, M. J., & Sakai, H. (2003). Regulation of flowering time and floral organ identity by a microRNA and its APETALA2-like target genes. *The Plant Cell, 15*(11), 2730-2741.

Bac-Molenaar, J. A., Vreugdenhil, D., Granier, C., & Keurentjes, J. J. (2015). Genome-wide association mapping of growth dynamics detects time-specific and general quantitative trait loci. *Journal of experimental botany, 66*(18), 5567-5580.

Bandeira e Sousa, M., Cuevas, J., de Oliveira Couto, E. G., Pérez-Rodríguez, P., Jarquín, D., Fritsche-Neto, R., . . . Crossa, J. (2017). Genomic-enabled prediction in maize using kernel models with genotype× environment interaction. *G3: Genes, Genomes, Genetics, 7*(6), 1995-2014.

Barnabás, B., Jäger, K., & Fehér, A. (2008). The effect of drought and heat stress on reproductive processes in cereals. *Plant, cell & environment, 31*(1), 11-38.

Barnes, E., Clarke, T., Richards, S., Colaizzi, P., Haberland, J., Kostrzewski, M., . . . Thompson, T. (2000). *Coincident detection of crop water stress, nitrogen status and canopy density using ground based multispectral data.* Paper presented at the Proceedings of the Fifth International Conference on Precision Agriculture, Bloomington, MN, USA.

Bates, D., Mächler, M., Bolker, B., & Walker, S. (2014). Fitting linear mixed-effects models using lme4. *arXiv preprint arXiv:1406.5823*.

Beavis, W. D. (2019). 10 QTL Analyses: Power, Precision, and Accuracy. *Molecular dissection of complex traits*.

Bendig, J., Yu, K., Aasen, H., Bolten, A., Bennertz, S., Broscheit, J., . . . Bareth, G. (2015). Combining UAV-based plant height from crop surface models, visible, and near infrared vegetation indices for biomass monitoring in barley. *International Journal of Applied Earth Observation and Geoinformation, 39*, 79-87.

Bernardo, R. (1994). Prediction of maize single-cross performance using RFLPs and information from related hybrids. *Crop science, 34*(1), 20-25.

Bernardo, R. (1996a). Best linear unbiased prediction of maize single-cross performance. *Crop Science, 36*(1), 50-56.

Bernardo, R. (1996b). Best linear unbiased prediction of the performance of crosses between untested maize inbreds. *Crop Science, 36*(4), 872-876.

Bernardo, R. (2021). Predictive breeding in maize during the last 90 years. *Crop science*.

Bernardo, R., & Yu, J. (2007). Prospects for genomewide selection for quantitative traits in maize. *Crop science, 47*(3), 1082-1090.

Betrán, F., Bockholt, A., Fojt III, F., Mayfield, K., & Pietsch, D. (2004). Registration of Tx714 maize germplasm line. *Crop science, 44*(3), 1028-1029.

Betrán, F. J., Bhatnagar, S., Isakeit, T., Odvody, G., & Mayfield, K. (2006). Aflatoxin accumulation and associated traits in QPM maize inbreds and their testcrosses. *Euphytica, 152*(2), 247-257.

Bizotto, F. M., Ceratti, R. S., Braz, A. S., & Masuda, H. P. (2018). Evolutionary history of Mo25 gene in plants, a component of RAM/MOR signaling network. *Mechanisms of Development, 153*, 64-73.

Blein-Nicolas, M., Negro, S. S., Balliau, T., Welcker, C., Cabrera-Bosquet, L., Nicolas, S. D., . . . Zivy, M. (2020). A systems genetics approach reveals environment-dependent associations between SNPs, protein coexpression, and drought-related traits in maize. *Genome research, 30*(11), 1593-1604.

Bolduc, N., & Hake, S. (2009). The maize transcription factor KNOTTED1 directly regulates the gibberellin catabolism gene ga2ox1. *The Plant Cell, 21*(6), 1647-1658.

Bomblies, K., & Doebley, J. F. (2006). Pleiotropic effects of the duplicate maize FLORICAULA/LEAFY genes zfl1 and zfl2 on traits under selection during maize domestication. *Genetics, 172*(1), 519-531.

Bomblies, K., Wang, R.-L., Ambrose, B. A., Schmidt, R. J., Meeley, R. B., & Doebley, J. (2003). Duplicate FLORICAULA/LEAFY homologs zfl1 and zfl2 control inflorescence architecture and flower patterning in maize.

Boyle, E. A., Li, Y. I., & Pritchard, J. K. (2017). An expanded view of complex traits: from polygenic to omnigenic. *Cell, 169*(7), 1177-1186.

Bradbury, P. J., Zhang, Z., Kroon, D. E., Casstevens, T. M., Ramdoss, Y., & Buckler, E. S. (2007). TASSEL: software for association mapping of complex traits in diverse samples. *Bioinformatics, 23*(19), 2633-2635.

Briggs, W. H., McMullen, M. D., Gaut, B. S., & Doebley, J. (2007). Linkage mapping of domestication loci in a large maize–teosinte backcross resource. *Genetics, 177*(3), 1915-1928.

Broge, N. H., & Leblanc, E. (2001). Comparing prediction power and stability of broadband and hyperspectral vegetation indices for estimation of green leaf area index and canopy chlorophyll density. *Remote Sensing of Environment, 76*(2), 156-172.

Bruggeman, Q., Prunier, F., Mazubert, C., De Bont, L., Garmier, M., Lugan, R., . . . Delarue, M. (2015). Involvement of Arabidopsis hexokinase1 in cell death mediated by myo-inositol accumulation. *The Plant Cell, 27*(6), 1801-1814.

Buckler, E. S., Holland, J. B., Bradbury, P. J., Acharya, C. B., Brown, P. J., Browne, C., . . . Glaubitz, J. C. (2009). The genetic architecture of maize flowering time. *Science, 325*(5941), 714-718.

Burgos-Artizzu, X. P., Ribeiro, A., Guijarro, M., & Pajares, G. (2011). Real-time image processing for crop/weed discrimination in maize fields. *Computers and Electronics in Agriculture, 75*(2), 337-346.

Buschmann, C., & Nagel, E. (1993). In vivo spectroscopy and internal optics of leaves as basis for remote sensing of vegetation. *International Journal of Remote Sensing, 14*(4), 711-722.

Bustos, D. M., Bustamante, C. A., & Iglesias, A. A. (2008). Involvement of non-phosphorylating glyceraldehyde-3-phosphate dehydrogenase in response to oxidative stress. *Journal of plant physiology, 165*(4), 456-461.

Calderón-Vázquez, C., Sawers, R. J., & Herrera-Estrella, L. (2011). Phosphate deprivation in maize: genetics and genomics. *Plant physiology, 156*(3), 1067-1077.

Campbell, M. T., Du, Q., Liu, K., Brien, C. J., Berger, B., Zhang, C., & Walia, H. (2017). A comprehensive image-based phenomic analysis reveals the complex genetic architecture of shoot growth dynamics in rice (Oryza sativa).

Cao, L., Lu, X., Zhang, P., Ku, L., Wang, G., Yuan, Z., . . . Liu, Y. (2018). Regulatory networks of gene expression in maize (Zea mays) under drought stress and re-watering. *bioRxiv*, 361964.

Cao, Q., Miao, Y., Wang, H., Huang, S., Cheng, S., Khosla, R., & Jiang, R. (2013). Non-destructive estimation of rice plant nitrogen status with Crop Circle multispectral active canopy sensor. *Field Crops Research, 154*, 133-144.

Chardon, F., Virlon, B., Moreau, L., Falque, M., Joets, J., Decousset, L., . . . Charcosset, A. (2004). Genetic architecture of flowering time in maize as inferred from quantitative trait loci meta-analysis and synteny conservation with the rice genome. *Genetics, 168*(4), 2169-2185.

Chen, D.-H., & Ronald, P. (1999). A rapid DNA minipreparation method suitable for AFLP and other PCR applications. *Plant Molecular Biology Reporter, 17*(1), 53-57.

Chen, J. M. (1996). Evaluation of vegetation indices and a modified simple ratio for boreal applications. *Canadian Journal of Remote Sensing, 22*(3), 229-242.

Chen, S.-Y., Wang, Z.-Y., & Cai, X.-L. (2007). OsRRM, a Spen-like rice gene expressed specifically in the endosperm. *Cell research, 17*(8), 713-721.

Chen, Y. (2016). *High-density linkage map construction, mapping of agronomic traits in tropical maize (Zea Mays L.) and validating SNPs controlling maize grain yield and plant height in southern hybrid testcrosses.*

Chu, T., Starek, M. J., Brewer, M. J., Murray, S. C., & Pruter, L. S. (2018). Characterizing canopy height with UAS structure-from-motion photogrammetry—results analysis of a maize field trial with respect to multiple factors. *Remote Sensing Letters, 9*(8), 753-762.

Colasanti, J., Yuan, Z., & Sundaresan, V. (1998). The indeterminate gene encodes a zinc finger protein and regulates a leaf-generated signal required for the transition to flowering in maize. *Cell, 93*(4), 593-603.

Coles, N. D., McMullen, M. D., Balint-Kurti, P. J., Pratt, R. C., & Holland, J. B. (2010). Genetic control of photoperiod sensitivity in maize revealed by joint multiple population analysis. *Genetics, 184*(3), 799-812.

Coneva, V., Zhu, T., & Colasanti, J. (2007). Expression differences between normal and indeterminate1 maize suggest downstream targets of ID1, a floral transition regulator in maize. *Journal of Experimental Botany, 58*(13), 3679-3693.

Crain, J., Mondal, S., Rutkoski, J., Singh, R. P., & Poland, J. (2018). Combining high-throughput phenotyping and genomic information to increase prediction and selection accuracy in wheat breeding. *Plant genome, 11*, 1-14.

Crippen, R. E. (1990). Calculating the vegetation index faster. *Remote sensing of Environment, 34*(1), 71-73.

Crossa, J., Pérez-Rodríguez, P., Cuevas, J., Montesinos-López, O., Jarquín, D., De Los Campos, G., . . . Beyene, Y. (2017). Genomic selection in plant breeding: methods, models, and perspectives. *Trends in plant science, 22*(11), 961-975.

Crossa, J., Perez, P., Hickey, J., Burgueno, J., Ornella, L., Cerón-Rojas, J., . . . Li, Y. (2014). Genomic prediction in CIMMYT maize and wheat breeding programs. *Heredity, 112*(1), 48-60.

Cuevas, J., Granato, I., Fritsche-Neto, R., Montesinos-Lopez, O. A., Burgueño, J., Bandeira e Sousa, M., & Crossa, J. (2018). Genomic-enabled prediction kernel models with random intercepts for multi-environment trials. *G3: Genes, Genomes, Genetics, 8*(4), 1347-1365.

Danilevskaya, O. N., Meng, X., Hou, Z., Ananiev, E. V., & Simmons, C. R. (2008). A genomic and expression compendium of the expanded PEBP gene family from maize. *Plant Physiology, 146*(1), 250-264.

Danilevskaya, O. N., Meng, X., Selinger, D. A., Deschamps, S., Hermon, P., Vansant, G., . . . Muszynski, M. G. (2008). Involvement of the MADS-box gene ZMM4 in floral induction and inflorescence development in maize. *Plant physiology, 147*(4), 2054-2069.

Danilevskaya, O. N., Yu, G., Meng, X., Xu, J., Stephenson, E., Estrada, S., . . . Thatcher, S. (2019). Developmental and transcriptional responses of maize to drought stress under field conditions. *Plant Direct, 3*(5), e00129.

Dash, J., & Curran, P. (2004). The MERIS terrestrial chlorophyll index.

Datt, B. (1999). Visible/near infrared reflectance and chlorophyll content in Eucalyptus leaves. *International Journal of Remote Sensing, 20*(14), 2741-2759.

Daughtry, C. S., Walthall, C., Kim, M., De Colstoun, E. B., & McMurtrey Iii, J. (2000). Estimating corn leaf chlorophyll concentration from leaf and canopy reflectance. *Remote sensing of Environment, 74*(2), 229-239.

Desta, Z. A., & Ortiz, R. (2014). Genomic selection: genome-wide prediction in plant improvement. *Trends in plant science, 19*(9), 592-601.

Doebley, J. (2004). The genetics of maize evolution. *Annu. Rev. Genet., 38*, 37-59.

Dong, Z., Danilevskaya, O., Abadie, T., Messina, C., Coles, N., & Cooper, M. (2012). A gene regulatory network model for floral transition of the shoot apex in maize and its dynamic modeling.

El-Soda, M., Malosetti, M., Zwaan, B. J., Koornneef, M., & Aarts, M. G. (2014). Genotype× environment interaction QTL mapping in plants: lessons from Arabidopsis. *Trends in plant science, 19*(6), 390-398.

Ellis, R., Summerfield, R., Edmeades, G., & Roberts, E. (1992). Photoperiod, temperature, and the interval from sowing to tassel initiation in diverse cultivars of maize. *Crop Science, 32*(5), 1225-1232.

Elsayed, S., Rischbeck, P., & Schmidhalter, U. (2015). Comparing the performance of active and passive reflectance sensors to assess the normalized relative canopy temperature and grain yield of drought-stressed barley cultivars. *Field Crops Research, 177*, 148-160.

Elshire, R. J., Glaubitz, J. C., Sun, Q., Poland, J. A., Kawamoto, K., Buckler, E. S., & Mitchell, S. E. (2011). A robust, simple genotyping-by-sequencing (GBS) approach for high diversity species. *PloS one, 6*(5), e19379.

Endelman, J. B. (2011). Ridge regression and other kernels for genomic selection with R package rrBLUP. *The plant genome, 4*(3).

Endelman, J. B., & Jannink, J.-L. (2012). Shrinkage estimation of the realized relationship matrix. *G3: Genes| genomes| genetics, 2*(11), 1405-1413.

Erdle, K., Mistele, B., & Schmidhalter, U. (2011). Comparison of active and passive spectral sensors in discriminating biomass parameters and nitrogen status in wheat cultivars. *Field Crops Research, 124*(1), 74-84.

Escadafal, R. (1993). Remote sensing of soil color: principles and applications. *Remote Sensing Reviews, 7*(3-4), 261-279.

Farfan, I. D. B., De La Fuente, G. N., Murray, S. C., Isakeit, T., Huang, P.-C., Warburton, M., . . . Kolomiets, M. (2015). Genome wide association study for drought, aflatoxin resistance, and important agronomic traits of maize hybrids in the sub-tropics. *PloS one, 10*(2), e0117737.

Farfan, I. D. B., Murray, S. C., Labar, S., & Pietsch, D. (2013). A multi-environment trial analysis shows slight grain yield improvement in Texas commercial maize. *Field crops research, 149*, 167-176.

Feldman, M. J., Paul, R. E., Banan, D., Barrett, J. F., Sebastian, J., Yee, M.-C., . . . Dinneny, J. R. (2017). Time dependent genetic analysis links field and controlled

environment phenotypes in the model C4 grass Setaria. *PLoS genetics, 13*(6), e1006841.

Ferrari, S., Vairo, D., Ausubel, F. M., Cervone, F., & De Lorenzo, G. (2003). Tandemly duplicated Arabidopsis genes that encode polygalacturonase-inhibiting proteins are regulated coordinately by different signal transduction pathways in response to fungal infection. *The Plant Cell, 15*(1), 93-106.

Fournier-Level, A., Korte, A., Cooper, M. D., Nordborg, M., Schmitt, J., & Wilczek, A. M. (2011). A map of local adaptation in Arabidopsis thaliana. *Science, 334*(6052), 86-89.

Fu, C., Yang, X., Chen, X., Chen, W., Ma, Y., Hu, J., & Li, S. (2009). OsEF3, a homologous gene of Arabidopsis ELF3, has pleiotropic effects in rice. *Plant Biology, 11*(5), 751-757.

Furbank, R. T., & Tester, M. (2011). Phenomics–technologies to relieve the phenotyping bottleneck. *Trends in plant science, 16*(12), 635-644.

Gage, J. L., Jarquin, D., Romay, C., Lorenz, A., Buckler, E. S., Kaeppler, S., . . . Edwards, J. (2017). The effect of artificial selection on phenotypic plasticity in maize. *Nature communications, 8*(1), 1-11.

Galán, R. J., Bernal-Vasquez, A.-M., Jebsen, C., Piepho, H.-P., Thorwarth, P., Steffan, P., . . . Miedaner, T. (2020). Integration of genotypic, hyperspectral, and phenotypic data to improve biomass yield prediction in hybrid rye. *Theoretical and Applied Genetics, 133*(11), 3001-3015.

Galán, R. J., Bernal-Vasquez, A.-M., Jebsen, C., Piepho, H.-P., Thorwarth, P., Steffan, P., . . . Miedaner, T. (2021). Early prediction of biomass in hybrid rye based on hyperspectral data surpasses genomic predictability in less-related breeding material. *Theoretical and Applied Genetics, 134*(5), 1409-1422.

Galli, G., Alves, F. C., Morosini, J. S., & Fritsche-Neto, R. (2020). On the usefulness of parental lines GWAS for predicting low heritability traits in tropical maize hybrids. *PloS one, 15*(2), e0228724.

García-Martínez, H., Flores-Magdaleno, H., Ascencio-Hernández, R., Khalil-Gardezi, A., Tijerina-Chávez, L., Mancilla-Villa, O. R., & Vázquez-Peña, M. A. (2020). Corn grain yield estimation from vegetation indices, canopy cover, plant density, and a neural network using multispectral and RGB images acquired with unmanned aerial vehicles. *Agriculture, 10*(7), 277.

Geipel, J., Link, J., & Claupein, W. (2014). Combined spectral and spatial modeling of corn yield based on aerial images and crop surface models acquired with an unmanned aircraft system. *Remote Sensing, 6*(11), 10335-10355.

Gitelson, A. A. (2004). Wide dynamic range vegetation index for remote quantification of biophysical characteristics of vegetation. *Journal of plant physiology, 161*(2), 165-173.

Gitelson, A. A., Kaufman, Y. J., & Merzlyak, M. N. (1996). Use of a green channel in remote sensing of global vegetation from EOS-MODIS. *Remote Sensing of Environment, 58*(3), 289-298.

Gitelson, A. A., Kaufman, Y. J., Stark, R., & Rundquist, D. (2002). Novel algorithms for remote estimation of vegetation fraction. *Remote sensing of Environment, 80*(1), 76-87.

Gitelson, A. A., Vina, A., Ciganda, V., Rundquist, D. C., & Arkebauer, T. J. (2005). Remote estimation of canopy chlorophyll content in crops. *Geophysical Research Letters, 32*(8).

Glaubitz, J. C., Casstevens, T. M., Lu, F., Harriman, J., Elshire, R. J., Sun, Q., & Buckler, E. S. (2014). TASSEL-GBS: a high capacity genotyping by sequencing analysis pipeline. *PloS one, 9*(2), e90346.

Goel, N. S., & Qin, W. (1994). Influences of canopy architecture on relationships between various vegetation indices and LAI and FPAR: A computer simulation. *Remote Sensing Reviews, 10*(4), 309-347.

Golzarian, M. R., & Frick, R. A. (2011). Classification of images of wheat, ryegrass and brome grass species at early growth stages using principal component analysis. *Plant Methods, 7*(1), 1-11.

Gong, P., Pu, R., Biging, G. S., & Larrieu, M. R. (2003). Estimation of forest leaf area index using vegetation indices derived from Hyperion hyperspectral data. *IEEE transactions on geoscience and remote sensing, 41*(6), 1355-1362.

Gong, X., Liu, X., Pan, Q., Mi, G., Chen, F., & Yuan, L. (2020). Combined physiological, transcriptome, and genetic analysis reveals a molecular network of nitrogen remobilization in maize. *Journal of experimental botany, 71*(16), 5061-5073.

Goodman, M. M. (1999). Broadening the genetic diversity in maize breeding by use of exotic germplasm. *Genetics and exploitation of heterosis in crops*, 139-148.

Gouesnard, B., Rebourg, C., Welcker, C., & Charcosset, A. (2002). Analysis of photoperiod sensitivity within a collection of tropical maize populations. *Genetic Resources and Crop Evolution, 49*(5), 471-481.

Guerrero, J. M., Pajares, G., Montalvo, M., Romeo, J., & Guijarro, M. (2012). Support vector machines for crop/weeds identification in maize fields. *Expert Systems with Applications, 39*(12), 11149-11155.

Guijarro, M., Pajares, G., Riomoros, I., Herrera, P., Burgos-Artizzu, X., & Ribeiro, A. (2011). Automatic segmentation of relevant textures in agricultural images. *Computers and Electronics in Agriculture, 75*(1), 75-83.

Gupta, S., Kumari, M., Kumar, H., & Varadwaj, P. K. (2017). Genome-wide analysis of miRNAs and Tasi-RNAs in Zea mays in response to phosphate deficiency. *Functional & integrative genomics, 17*(2-3), 335-351.

Haboudane, D., Miller, J. R., Pattey, E., Zarco-Tejada, P. J., & Strachan, I. B. (2004). Hyperspectral vegetation indices and novel algorithms for predicting green LAI of crop canopies: Modeling and validation in the context of precision agriculture. *Remote sensing of environment, 90*(3), 337-352.

Haboudane, D., Miller, J. R., Tremblay, N., Zarco-Tejada, P. J., & Dextraze, L. (2002). Integrated narrow-band vegetation indices for prediction of crop chlorophyll content for application to precision agriculture. *Remote sensing of environment, 81*(2-3), 416-426.

Haboudane, D., Tremblay, N., Miller, J. R., & Vigneault, P. (2008). Remote estimation of crop chlorophyll content using spectral indices derived from hyperspectral data. *IEEE transactions on geoscience and remote sensing, 46*(2), 423-437.

Hague, T., Tillett, N., & Wheeler, H. (2006). Automated crop and weed monitoring in widely spaced cereals. *Precision Agriculture, 7*(1), 21-32.

Hamuda, E., Glavin, M., & Jones, E. (2016). A survey of image processing techniques for plant extraction and segmentation in the field. *Computers and electronics in agriculture, 125*, 184-199.

Han, L., Yang, G., Dai, H., Xu, B., Yang, H., Feng, H., . . . Yang, X. (2019). Modeling maize above-ground biomass based on machine learning approaches using UAV remote-sensing data. *Plant methods, 15*(1), 1-19.

Han, L., Yang, G., Yang, H., Xu, B., Li, Z., & Yang, X. (2018). Clustering field-based maize phenotyping of plant-height growth and canopy spectral dynamics using a UAV remote-sensing approach. *Frontiers in plant science, 9*, 1638.

Harris, L., Saparno, A., Johnston, A., Prisic, S., Xu, M., Allard, S., . . . Peters, R. (2005). The maize An2 gene is induced by Fusarium attack and encodes an ent-copalyl diphosphate synthase. *Plant molecular biology, 59*(6), 881-894.

Hartwig, T., Chuck, G. S., Fujioka, S., Klempien, A., Weizbauer, R., Potluri, D. P. V., . . . Schulz, B. (2011). Brassinosteroid control of sex determination in maize. *Proceedings of the National Academy of Sciences, 108*(49), 19814-19819.

Hattan, J., Kanamoto, H., Takemura, M., Yokota, A., & Kohchi, T. (2004). Molecular characterization of the cytoplasmic interacting protein of the receptor kinase IRK expressed in the inflorescence and root apices of Arabidopsis. *Bioscience, biotechnology, and biochemistry, 68*(12), 2598-2606.

He, C., Du, Y., Fu, J., Zeng, E., Park, S., White, F., . . . Liu, S. (2020). Early drought-responsive genes are variable and relevant to drought tolerance. *G3: Genes, Genomes, Genetics, 10*(5), 1657-1670.

Heffner, E. L., Lorenz, A. J., Jannink, J. L., & Sorrells, M. E. (2010). Plant breeding with genomic selection: gain per unit time and cost. *Crop science, 50*(5), 1681-1690.

Heffner, E. L., Sorrells, M. E., & Jannink, J.-L. (2009). Genomic selection for crop improvement. *Crop science, 49*, 1-12.

Henderson, C. R. (1975). Best linear unbiased estimation and prediction under a selection model. *Biometrics*, 423-447.

Hernandez, J., Lobos, G. A., Matus, I., Del Pozo, A., Silva, P., & Galleguillos, M. (2015). Using ridge regression models to estimate grain yield from field spectral data in bread wheat (Triticum aestivum L.) grown under three water regimes. *Remote Sensing, 7*(2), 2109-2126.

Heslot, N., Jannink, J. L., & Sorrells, M. E. (2015). Perspectives for genomic selection applications and research in plants. *Crop science, 55*(1), 1-12.

Hu, G., Richter, T. E., Hulbert, S. H., & Pryor, T. (1996). Disease lesion mimicry caused by mutations in the rust resistance gene rp1. *The Plant Cell, 8*(8), 1367-1376.

Huang, C., Sun, H., Xu, D., Chen, Q., Liang, Y., Wang, X., . . . Li, D. (2018). ZmCCT9 enhances maize adaptation to higher latitudes. *Proceedings of the National Academy of Sciences, 115*(2), E334-E341.

Huang, M., Liu, X., Zhou, Y., Summers, R. M., & Zhang, Z. (2019). BLINK: a package for the next level of genome-wide association studies with both individuals and markers in the millions. *GigaScience, 8*(2), giy154.

Huete, A., Didan, K., Miura, T., Rodriguez, E. P., Gao, X., & Ferreira, L. G. (2002). Overview of the radiometric and biophysical performance of the MODIS vegetation indices. *Remote Sensing of Environment, 83*(1-2), 195-213.

Huete, A. R. (1988). A soil-adjusted vegetation index (SAVI). *Remote Sensing of Environment, 25*(3), 295-309.

Hufford, M. B., Xu, X., Van Heerwaarden, J., Pyhäjärvi, T., Chia, J.-M., Cartwright, R. A., . . . Kaeppler, S. M. (2012). Comparative population genomics of maize domestication and improvement. *Nature genetics, 44*(7), 808-811.

Hung, H.-Y., Shannon, L. M., Tian, F., Bradbury, P. J., Chen, C., Flint-Garcia, S. A., . . . Doebley, J. F. (2012). ZmCCT and the genetic basis of day-length adaptation underlying the postdomestication spread of maize. *Proceedings of the National Academy of Sciences, 109*(28), E1913-E1921.

Hunt, E. R., Cavigelli, M., Daughtry, C. S., Mcmurtrey, J. E., & Walthall, C. L. (2005). Evaluation of digital photography from model aircraft for remote sensing of crop biomass and nitrogen status. *Precision Agriculture, 6*(4), 359-378.

Hunt, E. R., Daughtry, C., Eitel, J. U., & Long, D. S. (2011). Remote sensing leaf chlorophyll content using a visible band index.

Jackson, D., & Hake, S. (1999). Control of phyllotaxy in maize by the abphyl1 gene. *Development, 126*(2), 315-323.

James, G., Witten, D., Hastie, T., & Tibshirani, R. (2013). *An introduction to statistical learning* (Vol. 112): Springer.

Jasper, J., Reusch, S., & Link, A. (2009). Active sensing of the N status of wheat using optimized wavelength combination: impact of seed rate, variety and growth stage. *Precision Agriculture, 9*, 23-30.

Johal, G. S., Hulbert, S. H., & Briggs, S. P. (1995). Disease lesion mimics of maize: a model for cell death in plants. *Bioessays, 17*(8), 685-692.

Johnson, C. D. (2019). *AgSeq workflow.* Paper presented at the Plant and Animal Genome XXVII Conference (January 12-16, 2019).

Jordan, C. F. (1969). Derivation of leaf-area index from quality of light on the forest floor. *Ecology, 50*(4), 663-666.

Kataoka, T., Kaneko, T., Okamoto, H., & Hata, S. (2003). *Crop growth estimation system using machine vision.* Paper presented at the Proceedings 2003 IEEE/ASME International Conference on Advanced Intelligent Mechatronics (AIM 2003).

Khush, G. S. (2001). Green revolution: the way forward. *Nature reviews genetics, 2*(10), 815-822.

Kim, K.-H., Song, K., Park, J.-M., Kim, J.-Y., & Lee, B.-M. (2021). RNA-Seq Analysis of Gene Expression Changes Related to Delay of Flowering Time under Drought Stress in Tropical Maize. *Applied Sciences, 11*(9), 4273.

Kiniry, J., Ritchie, J., & Musser, R. (1983). Dynamic Nature of the Photoperiod Response in Maize 1. *Agronomy Journal, 75*(4), 700-703.

Kismiantini, K., Montesinos-López, O. A., Crossa, J., Setiawan, E. P., & Wutsqa, D. U. (2021). Prediction of count phenotypes using high-resolution images and genomic data. *G3 Genes| Genomes| Genetics*.

Klein, R., Miller, F., Bean, S., & Klein, P. (2016). Registration of 40 converted germplasm sources from the reinstated sorghum conversion program. *Journal of Plant Registrations, 10*(1), 57-61.

Krause, M. R., González-Pérez, L., Crossa, J., Pérez-Rodríguez, P., Montesinos-López, O., Singh, R. P., . . . Mondal, S. (2019). Hyperspectral Reflectance-Derived Relationship Matrices for Genomic Prediction of Grain Yield in Wheat. *G3 Genes|Genomes|Genetics, 9*(4), 1231-1247. doi:10.1534/g3.118.200856

Krause, M. R., Mondal, S., Crossa, J., Singh, R. P., Pinto, F., Haghighattalab, A., . . . Sorrells, M. E. (2020a). Aerial high-throughput phenotyping enabling indirect selection for grain yield at the early-generation seed-limited stages in breeding programs. *bioRxiv*.

Krause, M. R., Mondal, S., Crossa, J., Singh, R. P., Pinto, F., Haghighattalab, A., . . . Sorrells, M. E. (2020b). Aerial high-throughput phenotyping enabling indirect selection for grain yield at the early-generation seed-limited stages in breeding programs. *Crop Science*(60), 3096–3114.

Kuhn, M. (2008). Building predictive models in R using the caret package. *Journal of statistical software, 28*(1), 1-26.

Kump, K. L., Bradbury, P. J., Wisser, R. J., Buckler, E. S., Belcher, A. R., Oropeza-Rosas, M. A., . . . Ware, D. (2011). Genome-wide association study of quantitative resistance to southern leaf blight in the maize nested association mapping population. *Nature genetics, 43*(2), 163-168.

Kusmec, A., Srinivasan, S., Nettleton, D., & Schnable, P. S. (2017). Distinct genetic architectures for phenotype means and plasticities in Zea mays. *Nature plants, 3*(9), 715-723.

Lane, H. M., & Murray, S. C. High Throughput can produce better decisions than high accuracy when phenotyping plant populations. *Crop Science*.

Lane, H. M., Murray, S. C., Montesinos-López, O. A., Montesinos-López, A., Crossa, J., Rooney, D. K., . . . Morgan, C. L. S. (2020). Phenomic selection and prediction of maize grain yield from near-infrared reflectance spectroscopy of kernels. *The Plant Phenome Journal, 3*(1), e20002. doi:https://doi.org/10.1002/ppj2.20002

Larkin, M. A., Blackshields, G., Brown, N. P., Chenna, R., McGettigan, P. A., McWilliam, H., . . . Lopez, R. (2007). Clustal W and Clustal X version 2.0. *bioinformatics, 23*(21), 2947-2948.

Larsson, S. J., Lipka, A. E., & Buckler, E. S. (2013). Lessons from Dwarf8 on the strengths and weaknesses of structured association mapping. *PLoS Genetics, 9*(2), e1003246.

Lawit, S. J., Wych, H. M., Xu, D., Kundu, S., & Tomes, D. T. (2010). Maize DELLA proteins dwarf plant8 and dwarf plant9 as modulators of plant development. *Plant and Cell Physiology, 51*(11), 1854-1868.

Lazakis, C. M., Coneva, V., & Colasanti, J. (2011). ZCN8 encodes a potential orthologue of Arabidopsis FT florigen that integrates both endogenous and photoperiod flowering signals in maize. *Journal of experimental botany, 62*(14), 4833-4842.

Le Maire, G., Francois, C., & Dufrene, E. (2004). Towards universal broad leaf chlorophyll indices using PROSPECT simulated database and hyperspectral reflectance measurements. *Remote sensing of environment, 89*(1), 1-28.

Lee, B.-h., Johnston, R., Yang, Y., Gallavotti, A., Kojima, M., Travençolo, B. A., . . . Jackson, D. (2009). Studies of aberrant phyllotaxy1 mutants of maize indicate complex interactions between auxin and cytokinin signaling in the shoot apical meristem. *Plant physiology, 150*(1), 205-216.

Lee, E. A., & Tollenaar, M. (2007). Physiological Basis of Successful Breeding Strategies for Maize Grain Yield. *Crop science, 47*(S3), S-202-S-215. doi:https://doi.org/10.2135/cropsci2007.04.0010IPBS

Lee, I., Aukerman, M. J., Gore, S. L., Lohman, K. N., Michaels, S. D., Weaver, L. M., . . . Amasino, R. M. (1994). Isolation of LUMINIDEPENDENS: a gene involved in the control of flowering time in Arabidopsis. *The Plant Cell, 6*(1), 75-83.

Li, D., Wang, X., Zhang, X., Chen, Q., Xu, G., Xu, D., . . . Huang, C. (2016). The genetic architecture of leaf number and its genetic relationship to flowering time in maize. *New Phytologist, 210*(1), 256-268.

Li, H., Peng, Z., Yang, X., Wang, W., Fu, J., Wang, J., . . . Yang, N. (2013). Genome-wide association study dissects the genetic architecture of oil biosynthesis in maize kernels. *Nature genetics, 45*(1), 43-50.

Li, J., Essemine, J., Bunce, J. A., Shang, C., Zhang, H., Sun, D., . . . Qu, M. (2019). Roles of heat shock protein and reprogramming of photosynthetic carbon metabolism in thermotolerance under elevated CO2 in maize. *Environmental and Experimental Botany, 168*, 103869.

Li, J., Hu, E., Chen, X., Xu, J., Lan, H., Li, C., . . . Lu, Y. (2016). Evolution of DUF1313 family members across plant species and their association with maize photoperiod sensitivity. *Genomics, 107*(5), 199-207.

Li, P., Cao, W., Fang, H., Xu, S., Yin, S., Zhang, Y., . . . Xu, C. (2017). Transcriptomic profiling of the maize (Zea mays L.) leaf response to abiotic stresses at the seedling stage. *Frontiers in plant science, 8*, 290.

Li, X., Guo, T., Bai, G., Zhang, Z., See, D., Marshall, J., . . . Yu, J. (2022). Genetics-inspired data-driven approaches explain and predict crop performance fluctuations attributed to changing climatic conditions. *Molecular Plant*.

Li, X., Guo, T., Mu, Q., Li, X., & Yu, J. (2018). Genomic and environmental determinants and their interplay underlying phenotypic plasticity. *Proceedings of the National Academy of Sciences, 115*(26), 6679-6684.

Li, Y. x., Li, C., Bradbury, P. J., Liu, X., Lu, F., Romay, C. M., . . . Shi, Y. (2016). Identification of genetic variants associated with maize flowering time using an extremely large multi-genetic background population. *The Plant Journal, 86*(5), 391-402.

Li, Z., Gao, Q., Liu, Y., He, C., Zhang, X., & Zhang, J. (2011). Overexpression of transcription factor ZmPTF1 improves low phosphate tolerance of maize by regulating carbon metabolism and root growth. *Planta, 233*(6), 1129-1143.

Liang, Y., Liu, Q., Wang, X., Huang, C., Xu, G., Hey, S., . . . Wu, L. (2019). Zm MADS 69 functions as a flowering activator through the ZmRap2. 7-ZCN 8 regulatory module and contributes to maize flowering time adaptation. *New Phytologist, 221*(4), 2335-2347.

Lima, M. d. L. A., de Souza, C. L., Bento, D. A. V., De Souza, A. P., & Carlini-Garcia, L. A. (2006). Mapping QTL for grain yield and plant traits in a tropical maize population. *Molecular breeding, 17*(3), 227-239.

Lindsey, R. S. (2015). *Genetic analysis of nitrogen remobilization and kernel composition in Zea mays L. and Sorghum bicolor (L.) Moench.* Purdue University,

Lipka, A. E., Kandianis, C. B., Hudson, M. E., Yu, J., Drnevich, J., Bradbury, P. J., & Gore, M. A. (2015). From association to prediction: statistical methods for the dissection and selection of complex traits in plants. *Current Opinion in Plant Biology, 24*, 110-118.

Liu, J., Huang, J., Guo, H., Lan, L., Wang, H., Xu, Y., . . . Xiao, Y. (2017). The conserved and unique genetic architecture of kernel size and weight in maize and rice. *Plant physiology, 175*(2), 774-785.

Liu, K., Goodman, M., Muse, S., Smith, J. S., Buckler, E., & Doebley, J. (2003). Genetic structure and diversity among maize inbred lines as inferred from DNA microsatellites. *Genetics, 165*(4), 2117-2128.

Liu, L., Du, Y., Shen, X., Li, M., Sun, W., Huang, J., . . . Yan, J. (2015). KRN4 controls quantitative variation in maize kernel row number. *PLoS genetics, 11*(11), e1005670.

Liu, X., Huang, M., Fan, B., Buckler, E. S., & Zhang, Z. (2016). Iterative usage of fixed and random effect models for powerful and efficient genome-wide association studies. *PLoS genetics, 12*(2), e1005767.

López, O. A. M., López, A. M., & Crossa, J. (2022). *Multivariate Statistical Machine Learning Methods for Genomic Prediction*: Springer.

Louhaichi, M., Borman, M. M., & Johnson, D. E. (2001). Spatially located platform and aerial photography for documentation of grazing impacts on wheat. *Geocarto International, 16*(1), 65-70.

Lu, J., Miao, Y., Shi, W., Li, J., & Yuan, F. (2017). Evaluating different approaches to non-destructive nitrogen status diagnosis of rice using portable RapidSCAN active canopy sensor. *Scientific reports, 7*(1), 1-10.

Lyra, D. H., Virlet, N., Sadeghi-Tehran, P., Hassall, K. L., Wingen, L. U., Orford, S., . . . Slavov, G. T. (2020). Functional QTL mapping and genomic prediction of canopy height in wheat measured using a robotic field phenotyping platform. *Journal of experimental botany, 71*(6), 1885-1898.

Malambo, L., Popescu, S. C., Murray, S. C., Putman, E., Pugh, N. A., Horne, D. W., . . . Avant, R. (2018). Multitemporal field-based plant height estimation using 3D point clouds generated from small unmanned aerial systems high-resolution imagery. *International Journal of Applied Earth Observation and Geoinformation, 64*, 31-42.

Malcomber, S. T., Preston, J. C., Reinheimer, R., Kossuth, J., & Kellogg, E. A. (2006). Developmental gene evolution and the origin of grass inflorescence diversity. *Advances in Botanical Research, 44*, 425-481.

Maresma, Á., Ariza, M., Martínez, E., Lloveras, J., & Martínez-Casasnovas, J. A. (2016). Analysis of vegetation indices to determine nitrogen application and yield prediction in maize (Zea mays L.) from a standard UAV service. *Remote Sensing, 8*(12), 973.

Mascheretti, I., Turner, K., Brivio, R. S., Hand, A., Colasanti, J., & Rossi, V. (2015). Florigen-encoding genes of day-neutral and photoperiod-sensitive maize are regulated by different chromatin modifications at the floral transition. *Plant physiology, 168*(4), 1351-1363.

Matias, F. I., Caraza-Harter, M. V., & Endelman, J. B. (2020). FIELDimageR: an R package to analyze orthomosaic images from agricultural field trials. *The Plant Phenome Journal, 3*(1), e20005.

Matilla, A., & Radrizzani, M. (2005). The Anp32 family of proteins containing leucine-rich repeats. *The Cerebellum, 4*(1), 7-18.

Matsuoka, Y., Vigouroux, Y., Goodman, M. M., Sanchez, J., Buckler, E., & Doebley, J. (2002). A single domestication for maize shown by multilocus microsatellite genotyping. *Proceedings of the National Academy of Sciences, 99*(9), 6080-6084.

Mayfield, K., Betrán, F. J., Isakeit, T., Odvody, G., Murray, S. C., Rooney, W. L., & Landivar, J. C. (2012). Registration of maize germplasm lines Tx736, Tx739, and Tx740 for reducing preharvest aflatoxin accumulation. *Journal of plant registrations, 6*(1), 88-94.

Mayfield, K., Murray, S., Rooney, W., Isakeit, T., & Odvody, G. (2011). Confirmation of QTL reducing aflatoxin in maize testcrosses. *Crop science, 51*(6), 2489-2498.

McFarland, B. A., AlKhalifah, N., Bohn, M., Bubert, J., Buckler, E. S., Ciampitti, I., . . . Falcon, C. M. (2020). Maize genomes to fields (G2F): 2014–2017 field seasons: genotype, phenotype, climatic, soil, and inbred ear image datasets. *BMC research notes, 13*(1), 1-6.

McFarland, B. A., AlKhalifah, N., Bohn, M., Bubert, J., Buckler, E. S., Ciampitti, I., . . . de Leon, N. (2020). Maize genomes to fields (G2F): 2014–2017 field seasons: genotype, phenotype, climatic, soil, and inbred ear image datasets. *BMC Research Notes, 13*(1), 71. doi:10.1186/s13104-020-4922-8

Meng, L., Li, H., Zhang, L., & Wang, J. (2015). QTL IciMapping: integrated software for genetic linkage map construction and quantitative trait locus mapping in biparental populations. *The Crop Journal, 3*(3), 269-283.

Meng, X., Muszynski, M. G., & Danilevskaya, O. N. (2011). The FT-like ZCN8 gene functions as a floral activator and is involved in photoperiod sensitivity in maize. *The Plant Cell, 23*(3), 942-960.

Merzlyak, M. N., Gitelson, A. A., Chivkunova, O. B., & Rakitin, V. Y. (1999). Non-destructive optical detection of pigment changes during leaf senescence and fruit ripening. *Physiologia plantarum, 106*(1), 135-141.

Messina, C. D., Technow, F., Tang, T., Totir, R., Gho, C., & Cooper, M. (2018). Leveraging biological insight and environmental variation to improve phenotypic prediction: Integrating crop growth models (CGM) with whole genome prediction (WGP). *European Journal of Agronomy, 100*, 151-162.

Meuwissen, T. H., Hayes, B. J., & Goddard, M. E. (2001). Prediction of total genetic value using genome-wide dense marker maps. *Genetics, 157*(4), 1819-1829.

Meyer, G., Hindman, T., & Laksmi, K. (1998). MG (ed.), Deshazer JA, Machine vision detection parameters for plant species identification. *Precision agri540 culture and biological quality, Boston, Massachusetts, USA, 3*(4), 3543.

Meyer, G. E., & Neto, J. C. (2008). Verification of color vegetation indices for automated crop imaging applications. *Computers and electronics in agriculture, 63*(2), 282-293.

Miao, C., Xu, Y., Liu, S., Schnable, P. S., & Schnable, J. C. (2020). Increased power and accuracy of causal locus identification in time series genome-wide association in sorghum. *Plant Physiology, 183*(4), 1898-1909.

Minic, Z. (2008). Physiological roles of plant glycoside hydrolases. *Planta, 227*(4), 723-740.

Money, D., Gardner, K., Migicovsky, Z., Schwaninger, H., Zhong, G.-Y., & Myles, S. (2015). LinkImpute: fast and accurate genotype imputation for nonmodel organisms. *G3: Genes, Genomes, Genetics, 5*(11), 2383-2390.

Montesinos-López, O. A., Montesinos-López, A., Crossa, J., de Los Campos, G., Alvarado, G., Suchismita, M., . . . Burgueño, J. (2017). Predicting grain yield using canopy hyperspectral reflectance in wheat breeding data. *Plant methods, 13*(1), 1-23.

Monteverde, E., Rosas, J. E., Blanco, P., Pérez de Vida, F., Bonnecarrère, V., Quero, G., . . . McCouch, S. (2018). Multienvironment models increase prediction accuracy of complex traits in advanced breeding lines of rice. *Crop Science, 58*(4), 1519-1530.

Mu, Q., Guo, T., Li, X., & Yu, J. (2022). Phenotypic plasticity in plant height shaped by interaction between genetic loci and diurnal temperature range. *New Phytologist, 233*(4), 1768-1779. doi:https://doi.org/10.1111/nph.17904

Mu, X., Chen, Q., Chen, F., Yuan, L., & Mi, G. (2017). A RNA-seq analysis of the response of photosynthetic system to low nitrogen supply in maize leaf. *International journal of molecular sciences, 18*(12), 2624.

Mu, X., Li, J., Dai, Z., Xu, L., Fan, T., Jing, T., . . . Gou, M. (2021). Commonly and Specifically Activated Defense Responses in Maize Disease Lesion Mimic Mutants Revealed by Integrated Transcriptomics and Metabolomics Analysis. *Frontiers in Plant Science, 12*, 690.

Multani, D. S., Briggs, S. P., Chamberlin, M. A., Blakeslee, J. J., Murphy, A. S., & Johal, G. S. (2003). Loss of an MDR transporter in compact stalks of maize br2 and sorghum dw3 mutants. *Science, 302*(5642), 81-84.

Muraya, M. M., Chu, J., Zhao, Y., Junker, A., Klukas, C., Reif, J. C., & Altmann, T. (2017). Genetic variation of growth dynamics in maize (Zea mays L.) revealed through automated non-invasive phenotyping. *The Plant Journal, 89*(2), 366-380.

Murray, S., Malambo, L., Popescu, S., Cope, D., Anderson, S., Chang, A., . . . Walls, R. (2019). G2F Maize UAV Data, College Station, Texas 2017. *CyVerse Data Commons. doi, 10*.

Murray, S. C., Sharma, A., Rooney, W. L., Klein, P. E., Mullet, J. E., Mitchell, S. E., & Kresovich, S. (2008). Genetic improvement of sorghum as a biofuel feedstock: I. QTL for stem sugar and grain nonstructural carbohydrates. *Crop science, 48*(6), 2165-2179.

Murtas, G., Reeves, P. H., Fu, Y.-F., Bancroft, I., Dean, C., & Coupland, G. (2003). A nuclear protease required for flowering-time regulation in Arabidopsis reduces the abundance of SMALL UBIQUITIN-RELATED MODIFIER conjugates. *The Plant Cell, 15*(10), 2308-2319.

Muszynski, M. G., Dam, T., Li, B., Shirbroun, D. M., Hou, Z., Bruggemann, E., . . . Danilevskaya, O. N. (2006). Delayed flowering1 encodes a basic leucine zipper protein that mediates floral inductive signals at the shoot apex in maize. *Plant physiology, 142*(4), 1523-1536.

Myles, S., Peiffer, J., Brown, P. J., Ersoz, E. S., Zhang, Z., Costich, D. E., & Buckler, E. S. (2009). Association mapping: critical considerations shift from genotyping to experimental design. *The Plant Cell, 21*(8), 2194-2202.

Navabi, A., Iqbal, M., Strenzke, K., & Spaner, D. (2006). The relationship between lodging and plant height in a diverse wheat population. *Canadian Journal of Plant Science, 86*(3), 723-726.

Navarro, J. A. R., Willcox, M., Burgueño, J., Romay, C., Swarts, K., Trachsel, S., . . . Vidal, V. (2017). A study of allelic diversity underlying flowering-time adaptation in maize landraces. *Nature genetics, 49*(3), 476-480.

Neuffer, M., Jones, L., & Zuber, M. S. (1968). *The mutants of maize*. Retrieved from

Neumann, K., Zhao, Y., Chu, J., Keilwagen, J., Reif, J. C., Kilian, B., & Graner, A. (2017). Genetic architecture and temporal patterns of biomass accumulation in spring barley revealed by image analysis. *BMC plant biology, 17*(1), 1-12.

Ochs, B. A. (2005). *Evaluation of Argentine maize hybrids and exotic x temperate testcrosses across environments.* Texas A&M University,

Olivoto, T., & Lúcio, A. D. C. (2020). metan: An R package for multi-environment trial analysis. *Methods in Ecology and Evolution, 11*(6), 783-789.

Parish, F., Williams, W. P., Windham, G. L., & Shan, X. (2019). Differential expression of signaling pathway genes associated with aflatoxin reduction quantitative trait loci in maize (Zea mays L.). *Frontiers in microbiology, 10*, 2683.

Pauli, D., Andrade-Sanchez, P., Carmo-Silva, A. E., Gazave, E., French, A. N., Heun, J., . . . Strand, R. J. (2016). Field-based high-throughput plant phenotyping reveals the temporal patterns of quantitative trait loci associated with stress-responsive traits in cotton. *G3: Genes, Genomes, Genetics, 6*(4), 865-879.

Pauli, D., Chapman, S. C., Bart, R., Topp, C. N., Lawrence-Dill, C. J., Poland, J., & Gore, M. A. (2016). The quest for understanding phenotypic variation via integrated approaches in the field environment. *Plant Physiology, 172*(2), 622-634.

Peiffer, J. A., Romay, M. C., Gore, M. A., Flint-Garcia, S. A., Zhang, Z., Millard, M. J., . . . Bradbury, P. J. (2014). The genetic architecture of maize height. *Genetics, 196*(4), 1337-1356.

Peng, B., Guan, K., Pan, M., & Li, Y. (2018). Benefits of Seasonal Climate Prediction and Satellite Data for Forecasting U.S. Maize Yield. *Geophysical Research Letters, 45*(18), 9662-9671. doi:https://doi.org/10.1029/2018GL079291

Peng, B., Guan, K., Zhou, W., Jiang, C., Frankenberg, C., Sun, Y., . . . Philipp Köhler. (2020). Assessing the benefit of satellite-based Solar-Induced Chlorophyll Fluorescence in crop yield prediction. *International Journal of Applied Earth Observation and Geoinformation, 90*, 102126.

Peng, J., Richards, D. E., Hartley, N. M., Murphy, G. P., Devos, K. M., Flintham, J. E., . . . Pelica, F. (1999). 'Green revolution'genes encode mutant gibberellin response modulators. *Nature, 400*(6741), 256-261.

Peng, Y., & Gitelson, A. A. (2011). Application of chlorophyll-related vegetation indices for remote estimation of maize productivity. *Agricultural and Forest Meteorology, 151*(9), 1267-1276.

Pigliucci, M. (2005). Evolution of phenotypic plasticity: where are we going now? *Trends in ecology & evolution, 20*(9), 481-486.

Pin, P., & Nilsson, O. (2012). The multifaceted roles of FLOWERING LOCUS T in plant development. *Plant, cell & environment, 35*(10), 1742-1755.

Poland, J. A., & Rife, T. W. (2012). Genotyping-by-sequencing for plant breeding and genetics. *The Plant Genome, 5*(3).

Pugh, N. A., Horne, D. W., Murray, S. C., Carvalho Jr, G., Malambo, L., Jung, J., . . . Chu, T. (2018). Temporal estimates of crop growth in sorghum and maize breeding enabled by unmanned aerial systems. *The Plant Phenome Journal, 1*(1), 1-10.

Qi, J., Chehbouni, A., Huete, A. R., Kerr, Y. H., & Sorooshian, S. (1994). A modified soil adjusted vegetation index. *Remote sensing of environment, 48*(2), 119-126.

Qi, S., Chen, S., Wang, W., Li, W., Xu, X., Zhong, M., . . . Li, H. (2021). Alternative splicing and duplication of PI-like genes in maize. *Gene, 769*, 145064.

Qiu, C., Sawada, K., Zhang, X., & Cheng, X. (2002). The PWWP domain of mammalian DNA methyltransferase Dnmt3b defines a new family of DNA-binding folds. *Nature structural biology, 9*(3), 217-224.

Ramsay, N. A., & Glover, B. J. (2005). MYB–bHLH–WD40 protein complex and the evolution of cellular diversity. *Trends in plant science, 10*(2), 63-70.

Richardson, A. J., & Wiegand, C. (1977). Distinguishing vegetation from soil background information. *Photogrammetric engineering and remote sensing, 43*(12), 1541-1552.

Rincent, R., Charpentier, J.-P., Faivre-Rampant, P., Paux, E., Le Gouis, J., Bastien, C., & Segura, V. (2018). Phenomic selection is a low-cost and high-throughput method

based on indirect predictions: proof of concept on wheat and poplar. *G3: Genes, Genomes, Genetics, 8*(12), 3961-3972.

Rogers, A. R., Dunne, J. C., Romay, C., Bohn, M., Buckler, E. S., Ciampitti, I. A., . . . Gore, M. A. (2021). The importance of dominance and genotype-by-environment interactions on grain yield variation in a large-scale public cooperative maize experiment. *G3, 11*(2), jkaa050.

Rogers, A. R., & Holland, J. B. (2021). Environment-Specific Genomic Prediction Ability in Maize Using Environmental Covariates Depends on Environmental Similarity To Training Data. *G3 Genes| Genomes| Genetics*, jkab440.

Romay, M., Millard, M., Glaubitz, J., Peiffer, J., Swarts, K., Casstevens, T., & McMullen, M. (2013). & MD McMullen, 2013 Comprehensive genotyping of the USA national maize inbred seed bank. *Genome Biol, 14*, 55.

Rondeaux, G., Steven, M., & Baret, F. (1996). Optimization of soil-adjusted vegetation indices. *Remote sensing of environment, 55*(2), 95-107.

Roujean, J.-L., & Breon, F.-M. (1995). Estimating PAR absorbed by vegetation from bidirectional reflectance measurements. *Remote Sensing of Environment, 51*(3), 375-384.

Rutkoski, J., Poland, J., Mondal, S., Autrique, E., Pérez, L. G., Crossa, J., . . . Singh, R. (2016). Canopy temperature and vegetation indices from high-throughput phenotyping improve accuracy of pedigree and genomic selection for grain yield in wheat. *G3: Genes, Genomes, Genetics, 6*(9), 2799-2808.

Salvi, S., Castelletti, S., & Tuberosa, R. (2009). An updated consensus map for flowering time QTLs in maize. *Maydica, 54*(4), 501.

Salvi, S., Sponza, G., Morgante, M., Tomes, D., Niu, X., Fengler, K. A., . . . Bruggemann, E. (2007). Conserved noncoding genomic sequences associated with a flowering-time quantitative trait locus in maize. *Proceedings of the National Academy of Sciences, 104*(27), 11376-11381.

Sandham, L., & Zietsman, H. (1997). Surface temperature measurement from space: a case study in the south western cape of South Africa. *South African Journal of Enology and Viticulture, 18*(2), 25-30.

Sandhu, K. S., Mihalyov, P. D., Lewien, M. J., Pumphrey, M. O., & Carter, A. H. (2021). Combining genomic and phenomic information for predicting grain protein content and grain yield in spring wheat. *Frontiers in plant science, 12*, 170.

Sankaran, S., Khot, L. R., Espinoza, C. Z., Jarolmasjed, S., Sathuvalli, V. R., Vandemark, G. J., . . . Knowles, N. R. (2015). Low-altitude, high-resolution aerial imaging systems for row and field crop phenotyping: A review. *European Journal of Agronomy, 70*, 112-123.

Sari-Gorla, M., Krajewski, P., Di Fonzo, N., Villa, M., & Frova, C. (1999). Genetic analysis of drought tolerance in maize by molecular markers. II. Plant height and flowering. *Theoretical and Applied Genetics, 99*(1), 289-295.

Sawers, R. J., Linley, P. J., Farmer, P. R., Hanley, N. P., Costich, D. E., Terry, M. J., & Brutnell, T. P. (2002). elongated mesocotyl1, a phytochrome-deficient mutant of maize. *Plant Physiology, 130*(1), 155-163.

Scheben, A., Batley, J., & Edwards, D. (2017). Genotyping-by-sequencing approaches to characterize crop genomes: choosing the right tool for the right application. *Plant biotechnology journal, 15*(2), 149-161.

Schlüter, U., Mascher, M., Colmsee, C., Scholz, U., Bräutigam, A., Fahnenstich, H., & Sonnewald, U. (2012). Maize source leaf adaptation to nitrogen deficiency affects not only nitrogen and carbon metabolism but also control of phosphate homeostasis. *Plant Physiology, 160*(3), 1384-1406.

Schnable, P. S., Ware, D., Fulton, R. S., Stein, J. C., Wei, F., Pasternak, S., . . . Graves, T. A. (2009). The B73 maize genome: complexity, diversity, and dynamics. *science, 326*(5956), 1112-1115.

Segura, V., Vilhjálmsson, B. J., Platt, A., Korte, A., Seren, Ü., Long, Q., & Nordborg, M. (2012). An efficient multi-locus mixed-model approach for genome-wide association studies in structured populations. *Nature genetics, 44*(7), 825-830.

Setter, T. L., Yan, J., Warburton, M., Ribaut, J.-M., Xu, Y., Sawkins, M., . . . Gore, M. A. (2011). Genetic association mapping identifies single nucleotide polymorphisms in genes that affect abscisic acid levels in maize floral tissues during drought. *Journal of experimental botany, 62*(2), 701-716.

Shanahan, J. F., Schepers, J. S., Francis, D. D., Varvel, G. E., Wilhelm, W. W., Tringe, J. M., . . . Major, D. J. (2001). Use of remote-sensing imagery to estimate corn grain yield. *Agronomy Journal, 93*(3), 583-589.

Shi, Y., Thomasson, J. A., Murray, S. C., Pugh, N. A., Rooney, W. L., Shafian, S., . . . Neely, H. L. (2016). Unmanned aerial vehicles for high-throughput phenotyping and agronomic research. *PloS one, 11*(7), e0159781.

Shin, J.-H., Blay, S., McNeney, B., & Graham, J. (2006). LDheatmap: an R function for graphical display of pairwise linkage disequilibria between single nucleotide polymorphisms. *Journal of statistical software, 16*(3), 1-10.

Shukla, S., Felderhoff, T. J., Saballos, A., & Vermerris, W. (2017). The relationship between plant height and sugar accumulation in the stems of sweet sorghum (Sorghum bicolor (L.) Moench). *Field Crops Research, 203*, 181-191.

Sibov, S. T., De Souza Jr, C. L., Garcia, A. A. F., Silva, A. R., Garcia, A. F., Mangolin, C. A., . . . De Souza, A. P. (2003). Molecular mapping in tropical maize (Zea mays L.) using microsatellite markers. 2. Quantitative trait loci (QTL) for grain yield, plant heigth, ear height and grain moisture. *Hereditas, 139*(2), 107-115.

Simmons, C., Hantke, S., Grant, S., Johal, G. S., & Briggs, S. P. (1998). The maize lethal leaf spot 1 mutant has elevated resistance to fungal infection at the leaf epidermis. *Molecular plant-microbe interactions, 11*(11), 1110-1118.

Singh, D., Wang, X., Kumar, U., Gao, L., Noor, M., Imtiaz, M., . . . Poland, J. (2019). High-throughput phenotyping enabled genetic dissection of crop lodging in wheat. *Frontiers in plant science, 10*, 394.

Smith, M. R., Rao, I. M., & Merchant, A. (2018). Source-sink relationships in crop plants and their influence on yield development and nutritional quality. . *Frontiers in Plant Science,, 9*, 1889.

Smith, S. M., Steinau, M., Trick, H. N., & Hulbert, S. H. (2010). Recombinant Rp1 genes confer necrotic or nonspecific resistance phenotypes. *Molecular Genetics and Genomics, 283*(6), 591-602.

SONG, X.-h., Lei, T., WANG, S.-x., ZHOU, J.-l., Zhang, J., Zan, C., . . . CHEN, Y.-h. (2019). Integrating transcriptomic and proteomic analyses of photoperiod-sensitive in near isogenic maize line under long-day conditions. *Journal of Integrative Agriculture, 18*(6), 1211-1221.

Sripada, R. P., Heiniger, R. W., White, J. G., & Meijer, A. D. (2006). Aerial color infrared photography for determining early in-season nitrogen requirements in corn. *Agronomy Journal, 98*(4), 968-977.

Stratton, D. A. (1998). Reaction norm functions and QTL–environment interactions for flowering time in Arabidopsis thaliana. *Heredity, 81*(2), 144-155.

Sun, J., Poland, J. A., Mondal, S., Crossa, J., Juliana, P., Singh, R. P., . . . Velu, G. (2019). High-throughput phenotyping platforms enhance genomic selection for wheat grain yield across populations and cycles in early stage. *Theoretical and Applied Genetics, 132*(6), 1705-1720.

Swarts, K., Bauer, E., Glaubitz, J. C., Ho, T., Johnson, L., Li, Y., . . . Schön, C.-C. (2021). Joint analysis of days to flowering reveals independent temperate adaptations in maize. *Heredity, 126*(6), 929-941.

Tanger, P., Klassen, S., Mojica, J. P., Lovell, J. T., Moyers, B. T., Baraoidan, M., . . . Bush, D. R. (2017). Field-based high throughput phenotyping rapidly identifies genomic regions controlling yield components in rice. *Scientific reports, 7*(1), 1-8.

Tarter, J., & Holland, J. (2006). Gains from selection during the development of semiexotic inbred lines from Latin American maize accessions. *Maydica, 51*(1), 15.

Teixeira, J., Weldekidan, T., De Leon, N., Flint-Garcia, S., Holland, J., Lauter, N., . . . Kleintop, A. (2015). Hallauer's Tusón: a decade of selection for tropical-to-temperate phenological adaptation in maize. *Heredity, 114*(2), 229-240.

Thornsberry, J. M., Goodman, M. M., Doebley, J., Kresovich, S., Nielsen, D., & Buckler, E. S. (2001). Dwarf8 polymorphisms associate with variation in flowering time. *Nature genetics, 28*(3), 286-289.

Tirado, S. B., Hirsch, C. N., & Springer, N. M. (2020). UAV-based imaging platform for monitoring maize growth throughout development. *Plant direct, 4*(6), e00230.

Tucker, C. J. (1979). Red and photographic infrared linear combinations for monitoring vegetation. *Remote sensing of Environment, 8*(2), 127-150.

Untergasser, A., Cutcutache, I., Koressaar, T., Ye, J., Faircloth, B. C., Remm, M., & Rozen, S. G. (2012). Primer3—new capabilities and interfaces. *Nucleic acids research, 40*(15), e115-e115.

van Heerwaarden, J., Hufford, M. B., & Ross-Ibarra, J. (2012). Historical genomics of North American maize. *Proceedings of the National Academy of Sciences, 109*(31), 12420-12425.

Vaughan, M. M., Christensen, S., Schmelz, E. A., Huffaker, A., Mcauslane, H. J., Alborn, H. T., . . . Teal, P. E. (2015). Accumulation of terpenoid phytoalexins in maize roots is associated with drought tolerance. *Plant, cell & environment, 38*(11), 2195-2207.

Vidotti, M. S., Lyra, D. H., Morosini, J. S., Granato, Í. S. C., Quecine, M. C., Azevedo, J. L. d., & Fritsche-Neto, R. (2019). Additive and heterozygous (dis) advantage GWAS models reveal candidate genes involved in the genotypic variation of maize hybrids to Azospirillum brasilense. *PloS one, 14*(9), e0222788.

Vincini, M., Frazzi, E., & D'Alessio, P. (2008). A broad-band leaf chlorophyll vegetation index at the canopy scale. *Precision Agriculture, 9*(5), 303-319.

Wahl, N., Murray, S. C., Isakeit, T., Krakowsky, M., Windham, G. L., Williams, W. P., . . . Xu, W. (2017). Identification of resistance to aflatoxin accumulation and yield potential in maize hybrids in the Southeast Regional Aflatoxin Trials (SERAT). *Crop science, 57*(1), 202-215.

Walbot, V. (1991). Maize mutants for the 21st century. *The Plant Cell, 3*(9), 851.

Wallace, J. G., Zhang, X., Beyene, Y., Semagn, K., Olsen, M., Prasanna, B. M., & Buckler, E. (2016a). Genome-wide association for plant height and flowering time across 15 tropical maize populations under managed drought stress and well-watered conditions in Sub-Saharan Africa.

Wallace, J. G., Zhang, X., Beyene, Y., Semagn, K., Olsen, M., Prasanna, B. M., & Buckler, E. S. (2016b). Genome-wide Association for Plant Height and Flowering Time across 15 Tropical Maize Populations under Managed Drought Stress and Well-Watered Conditions in Sub-Saharan Africa. *Crop Science, 56*(5), 2365-2378.

Wang, B., Li, Z., Ran, Q., Li, P., Peng, Z., & Zhang, J. (2018). ZmNF-YB16 overexpression improves drought resistance and yield by enhancing photosynthesis and the antioxidant capacity of maize plants. *Frontiers in plant science, 9*, 709.

Wang, H., Xu, C., Liu, X., Guo, Z., Xu, X., Wang, S., . . . Xu, Y. (2017). Development of a multiple-hybrid population for genome-wide association studies: theoretical consideration and genetic mapping of flowering traits in maize. *Scientific Reports, 7*(1), 1-16.

Wang, J., Li, X., Guo, T., Dzievit, M. J., Yu, X., Liu, P., . . . Yu, J. (2021). Genetic dissection of seasonal vegetation index dynamics in maize through aerial based high-throughput phenotyping. *The Plant Genome*, e20155.

Wang, J., & Zhang, Z. (2021). GAPIT Version 3: boosting power and accuracy for genomic association and prediction. *Genomics, proteomics & bioinformatics*.

Wang, W., Yao, X., Yao, X., Tian, Y., Liu, X., Ni, J., . . . Zhu, Y. (2012). Estimating leaf nitrogen concentration with three-band vegetation indices in rice and wheat. *Field Crops Research, 129*, 90-98.

Wang, X., Wang, H., Liu, S., Ferjani, A., Li, J., Yan, J., . . . Qin, F. (2016). Genetic variation in ZmVPP1 contributes to drought tolerance in maize seedlings. *Nature genetics, 48*(10), 1233-1241.

Wang, X., Zhang, R., Song, W., Han, L., Liu, X., Sun, X., . . . Yang, H. (2019). Dynamic plant height QTL revealed in maize through remote sensing phenotyping using a high-throughput unmanned aerial vehicle (UAV). *Scientific reports, 9*(1), 1-10.

Wang, Y., Wang, Y., Wang, X., & Deng, D. (2020). Integrated meta-QTL and genome-wide association study analyses reveal candidate genes for maize yield. *Journal of Plant Growth Regulation, 39*(1), 229-238.

Warburton, M. L., Tang, J. D., Windham, G. L., Hawkins, L. K., Murray, S. C., Xu, W., . . . Williams, W. P. (2015). Genome-wide association mapping of Aspergillus flavus and aflatoxin accumulation resistance in maize. *Crop science, 55*(5), 1857-1867.

Ward, B., Brien, C., Oakey, H., Pearson, A., Negrão, S., Schilling, R. K., . . . Roy, S. J. (2019). High-throughput 3D modelling to dissect the genetic control of leaf elongation in barley (Hordeum vulgare). *The Plant Journal, 98*(3), 555-570.

Warrington, I., & Kanemasu, E. (1983a). Corn Growth Response to Temperature and Photoperiod I. Seedling Emergence, Tassel Initiation, and Anthesis 1. *Agronomy Journal, 75*(5), 749-754.

Warrington, I., & Kanemasu, E. (1983b). Corn Growth Response to Temperature and Photoperiod II. Leaf-Initiation and Leaf-Appearance Rates 1. *Agronomy Journal, 75*(5), 755-761.

Weber, V. S., Araus, J. L., Cairns, J. E., Sanchez, C., Melchinger, A. E., & Orsini, E. (2012). rediction of grain yield using reflectance spectra of canopy and leaves in maize plants grown under different water regimes. *Field Crops Research, 128*, 82-90.

Weiß, T. M., Zhu, X., Leiser, W. L., Li, D., Liu, W., Schipprack, W., . . . Würschum, T. (2022). Unraveling the potential of phenomic selection within and among diverse breeding material of maize (Zea mays L.). *G3 Genes|Genomes|Genetics, 12*(3). doi:10.1093/g3journal/jkab445

Weldekidan, T., Manching, H., Choquette, N., de Leon, N., Flint-Garcia, S., Holland, J., . . . Wisser, R. J. (2022). Registration of tropical populations of maize selected in parallel for early flowering time across the United States. *Journal of Plant Registrations, 16*(1), 100-108. doi:https://doi.org/10.1002/plr2.20181

Weng, J., Xie, C., Hao, Z., Wang, J., Liu, C., Li, M., . . . Li, X. (2011). Genome-wide association study identifies candidate genes that affect plant height in Chinese elite maize (Zea mays L.) inbred lines. *PLoS One, 6*(12), e29229.

Whittaker, J. C., Thompson, R., & Denham, M. C. (2000). Marker-assisted selection using ridge regression. *Genetics Research, 75*(2), 249-252.

Windhausen, V. S., Atlin, G. N., Hickey, J. M., Crossa, J., Jannink, J.-L., Sorrells, M. E., . . . Semagn, K. (2012). Effectiveness of genomic prediction of maize hybrid performance in different breeding populations and environments. *G3: Genes| genomes| genetics, 2*(11), 1427-1436.

Winkler, R. G., & Helentjaris, T. (1995). The maize Dwarf3 gene encodes a cytochrome P450-mediated early step in Gibberellin biosynthesis. *The Plant Cell, 7*(8), 1307-1317.

Wisser, R. J., Kolkman, J. M., Patzoldt, M. E., Holland, J. B., Yu, J., Krakowsky, M., . . . Balint-Kurti, P. J. (2011). Multivariate analysis of maize disease resistances suggests a pleiotropic genetic basis and implicates a GST gene. *Proceedings of the National Academy of Sciences, 108*(18), 7339-7344.

Woebbecke, D. M., Meyer, G. E., Von Bargen, K., & Mortensen, D. A. (1995). Color indices for weed identification under various soil, residue, and lighting conditions. *Transactions of the ASAE, 38*(1), 259-269.

Wong, A. Y., & Colasanti, J. (2007). Maize floral regulator protein INDETERMINATE1 is localized to developing leaves and is not altered by light or the sink/source transition. *J Exp Bot, 58*(3), 403-414. doi:10.1093/jxb/erl206

Wu, G., Miller, N. D., De Leon, N., Kaeppler, S. M., & Spalding, E. P. (2019a). Predicting Zea mays flowering time, yield, and kernel dimensions by analyzing aerial images. *Frontiers in plant science, 10*, 1251.

Wu, G., Miller, N. D., De Leon, N., Kaeppler, S. M., & Spalding, E. P. (2019b). Predicting Zea mays flowering time, yield, and kernel dimensions by analyzing aerial images. *Frontiers in plant science*, 1251.

Wu, R., Wang, Z., Zhao, W., & Cheverud, J. M. (2004). A mechanistic model for genetic machinery of ontogenetic growth. *Genetics, 168*(4), 2383-2394.

Wu, X., Li, Y., Shi, Y., Song, Y., Zhang, D., Li, C., . . . Wang, T. (2016). Joint-linkage mapping and GWAS reveal extensive genetic loci that regulate male inflorescence size in maize. *Plant Biotechnology Journal, 14*(7), 1551-1562.

Wu, Y., Zhang, D., Chu, J. Y., Boyle, P., Wang, Y., Brindle, I. D., . . . Després, C. (2012). The Arabidopsis NPR1 protein is a receptor for the plant defense hormone salicylic acid. *Cell reports, 1*(6), 639-647.

Würschum, T., Liu, W., Busemeyer, L., Tucker, M. R., Reif, J. C., Weissmann, E. A., . . . Maurer, H. P. (2014). Mapping dynamic QTL for plant height in triticale. *BMC genetics, 15*(1), 1-8.

Xavier, A., Hall, B., Hearst, A. A., Cherkauer, K. A., & Rainey, K. M. (2017). Genetic architecture of phenomic-enabled canopy coverage in Glycine max. *Genetics, 206*(2), 1081-1089.

Xu, J., Liu, Y., Liu, J., Cao, M., Wang, J., Lan, H., . . . Rong, T. (2012). The genetic architecture of flowering time and photoperiod sensitivity in maize as revealed by QTL review and meta analysis. *Journal of Integrative Plant Biology, 54*(6), 358-373.

Xu, Y., Li, P., Yang, Z., & Xu, C. (2017). Genetic mapping of quantitative trait loci in crops. *The Crop Journal, 5*(2), 175-184.

Xue, J., & Su, B. (2017). Significant Remote Sensing Vegetation Indices: A Review of Developments and Applications. *Journal of Sensors, 2017*, 1353691. doi:10.1155/2017/1353691

Yang, J., Mezmouk, S., Baumgarten, A., Buckler, E. S., Guill, K. E., McMullen, M. D., . . . Ross-Ibarra, J. (2017). Incomplete dominance of deleterious alleles contributes substantially to trait variation and heterosis in maize. *PLoS Genetics, 13*(9), e1007019.

Yang, Q., Li, Z., Li, W., Ku, L., Wang, C., Ye, J., . . . Zhong, T. (2013). CACTA-like transposable element in ZmCCT attenuated photoperiod sensitivity and accelerated the postdomestication spread of maize. *Proceedings of the National Academy of Sciences, 110*(42), 16969-16974.

Yin, X., McClure, M. A., Jaja, N., Tyler, D. D., & Hayes, R. M. (2011). In-season prediction of corn yield using plant height under major production systems. *Agronomy Journal, 103*(3), 923-929.

You, F. M., Huo, N., Gu, Y. Q., Luo, M.-c., Ma, Y., Hane, D., . . . Anderson, O. D. (2008). BatchPrimer3: a high throughput web application for PCR and sequencing primer design. *BMC bioinformatics, 9*(1), 1-13.

Youssef, M. S., Mira, M. M., Millar, J. L., Becker, M. G., Belmonte, M. F., Hill, R. D., & Stasolla, C. (2019). Spatial identification of transcripts and biological processes in laser micro-dissected sub-regions of waterlogged corn roots with altered expression of phytoglobin. *Plant Physiology and Biochemistry, 139*, 350-365.

Zaman-Allah, M., Vergara, O., Araus, J. L., Tarekegne, A., Magorokosho, C., Zarco-Tejada, P. J., . . . Cairns, J. (2015). Unmanned aerial platform-based multi-spectral

imaging for field phenotyping of maize. *Plant Methods, 11*(1), 35. doi:10.1186/s13007-015-0078-2

Zarco-Tejada, P. J., Berjón, A., López-Lozano, R., Miller, J. R., Martín, P., Cachorro, V., . . . De Frutos, A. (2005). Assessing vineyard condition with hyperspectral indices: Leaf and canopy reflectance simulation in a row-structured discontinuous canopy. *Remote Sensing of Environment, 99*(3), 271-287.

Zhang, X.-H., Rao, X.-L., Shi, H.-T., Li, R.-J., & Lu, Y.-T. (2011). Overexpression of a cytosolic glyceraldehyde-3-phosphate dehydrogenase gene OsGAPC3 confers salt tolerance in rice. *Plant Cell, Tissue and Organ Culture (PCTOC), 107*(1), 1-11.

Zhang, X., Huang, C., Wu, D., Qiao, F., Li, W., Duan, L., . . . Liu, Q. (2017). High-throughput phenotyping and QTL mapping reveals the genetic architecture of maize plant growth. *Plant physiology, 173*(3), 1554-1564.

Zhang, X., Zhang, F., Qi, Y., Deng, L., Wang, X., & Yang, S. (2019). New research methods for vegetation information extraction based on visible light remote sensing images from an unmanned aerial vehicle (UAV). *International Journal of Applied Earth Observation and Geoinformation, 78*, 215-226.

Zhang, Y., Yu, C., Lin, J., Liu, J., Liu, B., Wang, J., . . . Zhao, T. (2017). OsMPH1 regulates plant height and improves grain yield in rice. *PLoS one, 12*(7), e0180825.

Zhao, P., Begcy, K., Dresselhaus, T., & Sun, M.-X. (2017). Does early embryogenesis in eudicots and monocots involve the same mechanism and molecular players? *Plant Physiology, 173*(1), 130-142.

Zhao, X., Lu, Y., Bai, M., Li, W., Zhang, D., Li, G., & Zhong, Y. (2019). Genetic dissection of photosynthetic performances in maize under drought-stressed and well-watered environments. *Reseachsquare*.

Zhao, Y., Gowda, M., Liu, W., Würschum, T., Maurer, H. P., Longin, F. H., . . . Reif, J. C. (2012). Accuracy of genomic selection in European maize elite breeding populations. *Theoretical and Applied Genetics, 124*(4), 769-776.

Zheng, H., Yang, Z., Wang, W., Guo, S., Li, Z., Liu, K., & Sui, N. (2020). Transcriptome analysis of maize inbred lines differing in drought tolerance provides novel insights into the molecular mechanisms of drought responses in roots. *Plant Physiology and Biochemistry, 149*, 11-26.

Zheng, J., He, C., Qin, Y., Lin, G., Park, W. D., Sun, M., . . . Yeh, C. T. (2019). Co-expression analysis aids in the identification of genes in the cuticular wax pathway in maize. *The Plant Journal, 97*(3), 530-542.

Zhou, M.-L., Zhang, Q., Zhou, M., Sun, Z.-M., Zhu, X.-M., Shao, J.-R., . . . Wu, Y.-M. (2012). Genome-wide identification of genes involved in raffinose metabolism in Maize. *Glycobiology, 22*(12), 1775-1785.

Zhou, Z., Li, G., Tan, S., Li, D., Weiß, T. M., Wang, X., . . . Liu, W. (2020). A QTL atlas for grain yield and its component traits in maize (Zea mays). *Plant Breeding, 139*(3), 562-574.

Zhu, Q.-H., & Helliwell, C. A. (2011). Regulation of flowering time and floral patterning by miR172. *Journal of experimental botany, 62*(2), 487-495.

APPENDIX A

APPENDIX OF CHAPTER I

Table 1A The discovered markers for photoperiod associated flowering.

SNP	Chromosome	Position	P.value	MAF	Explained variation (%)	effect	Log	PAF	Region
S1_84550450	chr 1	84550450	7.95E-07	0.090909	0.09	2.076455	6	IA-TX(DTS)	region 1
S1_84550450	chr 1	84550450	9.02E-08	0.090909	0.10	2.28243	7	WI-TX(DTS)	region 1
S1_84550450	chr 1	84550450	8.52E-06	0.090909	0.07	1.649227	5	IA-TX(DTA)	region 1
S1_84550465	chr 1	84550465	4.44E-07	0.085664	0.09	2.170191	6	IA-TX(DTS)	region 1
S1_84550465	chr 1	84550465	1.06E-07	0.085664	0.10	2.316473	7	WI-TX(DTS)	region 1
S1_84550465	chr 1	84550465	1.03E-06	0.085664	0.09	1.854646	6	IA-TX(DTA)	region 1
S1_84550644	chr 1	84550644	1.11E-06	0.089161	0.09	2.01662	6	IA-TX(DTS)	region 1
S1_84550644	chr 1	84550644	3.77E-06	0.089161	0.08	1.931815	5	WI-TX(DTS)	region 1
S1_84550644	chr 1	84550644	1.72E-06	0.089161	0.08	1.750333	6	IA-TX(DTA)	region 1
S1_246318979	chr 1	2.46E+08	2.51E-08	0.066434	0.11	2.641109	8	IA-TX(DTS)	region 2
S1_246318979	chr 1	2.46E+08	2.64E-06	0.066434	0.08	2.232913	6	WI-TX(DTS)	region 2
S1_246318979	chr 1	2.46E+08	2.74E-06	0.066434	0.08	1.949582	6	IA-TX(DTA)	region 2
S1_246319812	chr 1	2.46E+08	1.25E-08	0.059441	0.12	2.8487	8	IA-TX(DTS)	region 2
S1_246319812	chr 1	2.46E+08	9.96E-06	0.059441	0.07	2.209735	5	WI-TX(DTS)	region 2
S1_246319812	chr 1	2.46E+08	1.75E-06	0.059441	0.08	2.097481	6	IA-TX(DTA)	region 2
S1_246319828	chr 1	2.46E+08	1.25E-08	0.059441	0.12	2.8487	8	IA-TX(DTS)	region 2
S1_246319828	chr 1	2.46E+08	9.96E-06	0.059441	0.07	2.209735	5	WI-TX(DTS)	region 2
S1_246319828	chr 1	2.46E+08	1.75E-06	0.059441	0.08	2.097481	6	IA-TX(DTA)	region 2
S1_246320639	chr 1	2.46E+08	1.13E-08	0.062937	0.12	2.792728	8	IA-TX(DTS)	region 2
S1_246320639	chr 1	2.46E+08	2.85E-06	0.062937	0.08	2.292944	6	WI-TX(DTS)	region 2
S1_246320639	chr 1	2.46E+08	1.84E-06	0.062937	0.08	2.044629	6	IA-TX(DTA)	region 2
S1_246331356	chr 1	2.46E+08	5.87E-08	0.066434	0.11	2.574775	7	IA-TX(DTS)	region 2
S1_246331356	chr 1	2.46E+08	1.75E-05	0.066434	0.07	2.041499	5	WI-TX(DTS)	region 2
S1_246331356	chr 1	2.46E+08	1.36E-05	0.066434	0.07	1.809441	5	IA-TX(DTA)	region 2
S1_246331987	chr 1	2.46E+08	4.34E-09	0.06993	0.13	2.729912	8	IA-TX(DTS)	region 2
S1_246331987	chr 1	2.46E+08	6.92E-07	0.06993	0.09	2.313443	6	WI-TX(DTS)	region 2
S1_246331987	chr 1	2.46E+08	2.24E-06	0.06993	0.08	1.924164	6	IA-TX(DTA)	region 2
S1_246332064	chr 1	2.46E+08	1.80E-05	0.062937	0.07	2.067867	5	IA-TX(DTS)	region 2

S1_246339162	chr 1	2.46E+08	2.96E-08	0.062937	0.11	2.699878	8	IA-TX(DTS)	region 2
S1_246339162	chr 1	2.46E+08	2.46E-05	0.062937	0.06	2.053432	5	WI-TX(DTS)	region 2
S1_246339162	chr 1	2.46E+08	8.29E-06	0.062937	0.07	1.90108	5	IA-TX(DTA)	region 2
S1_246346556	chr 1	2.46E+08	8.89E-06	0.055944	0.07	2.261426	5	IA-TX(DTS)	region 2
S1_246346633	chr 1	2.46E+08	9.82E-06	0.055944	0.07	2.247626	5	IA-TX(DTS)	region 2
S1_246346713	chr 1	2.46E+08	8.89E-06	0.055944	0.07	2.261426	5	IA-TX(DTS)	region 2
S1_246346738	chr 1	2.46E+08	7.69E-06	0.059441	0.07	2.209707	5	IA-TX(DTS)	region 2
S4_75985939	chr 4	75985939	1.52E-07	0.055944	0.10	2.683869	7	IA-TX(DTS)	region 1
S4_75985939	chr 4	75985939	1.57E-05	0.055944	0.07	1.936733	5	IA-TX(DTA)	region 1
S4_75986298	chr 4	75986298	1.42E-07	0.055944	0.10	2.687412	7	IA-TX(DTS)	region 1
S4_75986298	chr 4	75986298	1.21E-05	0.055944	0.07	1.960871	5	IA-TX(DTA)	region 1
S4_75997451	chr 4	75997451	2.29E-06	0.059441	0.08	2.324276	6	IA-TX(DTS)	region 1
S4_76000912	chr 4	76000912	2.87E-07	0.059441	0.10	2.54214	7	IA-TX(DTS)	region 1
S4_76001018	chr 4	76001018	6.73E-07	0.08042	0.09	2.116052	6	IA-TX(DTS)	region 1
S4_76001018	chr 4	76001018	1.49E-05	0.08042	0.07	1.622051	5	IA-TX(DTA)	region 1
S4_76001245	chr 4	76001245	4.41E-07	0.062937	0.09	2.4423	6	IA-TX(DTS)	region 1
S4_76001245	chr 4	76001245	2.16E-05	0.062937	0.06	1.804308	5	IA-TX(DTA)	region 1
S4_76001753	chr 4	76001753	5.12E-08	0.055944	0.11	2.766331	7	IA-TX(DTS)	region 1
S4_76074057	chr 4	76074057	6.02E-10	0.055944	0.14	3.191235	9	IA-TX(DTS)	region 1
S4_76074057	chr 4	76074057	1.22E-07	0.055944	0.10	2.732199	7	WI-TX(DTS)	region 1
S4_76074057	chr 4	76074057	1.35E-07	0.055944	0.10	2.381014	7	IA-TX(DTA)	region 1
S4_76077492	chr 4	76077492	1.19E-07	0.055944	0.10	2.713047	7	IA-TX(DTS)	region 1
S4_76077492	chr 4	76077492	7.36E-06	0.055944	0.07	2.016608	5	IA-TX(DTA)	region 1
S4_76099704	chr 4	76099704	5.39E-07	0.06993	0.09	2.290256	6	IA-TX(DTS)	region 1
S4_76101130	chr 4	76101130	1.41E-05	0.083916	0.07	1.805471	5	IA-TX(DTS)	region 1
S4_76104089	chr 4	76104089	3.20E-07	0.055944	0.09	2.61155	6	IA-TX(DTS)	region 1
S4_76104089	chr 4	76104089	1.25E-05	0.055944	0.07	1.961423	5	IA-TX(DTA)	region 1
S4_76104418	chr 4	76104418	1.09E-05	0.083916	0.07	1.834349	5	IA-TX(DTS)	region 1
S4_76112068	chr 4	76112068	3.90E-07	0.062937	0.09	2.472872	6	IA-TX(DTS)	region 1
S4_76112068	chr 4	76112068	2.88E-05	0.062937	0.06	1.789498	5	IA-TX(DTA)	region 1
S4_76143833	chr 4	76143833	3.76E-08	0.055944	0.11	2.808193	7	IA-TX(DTS)	region 1
S4_76143833	chr 4	76143833	1.46E-05	0.055944	0.07	2.213924	5	WI-TX(DTS)	region 1
S4_76143833	chr 4	76143833	5.00E-06	0.055944	0.07	2.043044	5	IA-TX(DTA)	region 1
S4_76144085	chr 4	76144085	1.43E-07	0.055944	0.10	2.689515	7	IA-TX(DTS)	region 1

S4_76144085	chr 4	76144085	6.58E-06	0.055944	0.07	2.024097	5	IA-TX(DTA)	region 1
S4_76151459	chr 4	76151459	7.93E-07	0.059441	0.09	2.435238	6	IA-TX(DTS)	region 1
S4_76151459	chr 4	76151459	2.14E-05	0.059441	0.06	1.843384	5	IA-TX(DTA)	region 1
S4_76154787	chr 4	76154787	1.42E-07	0.055944	0.10	2.687412	7	IA-TX(DTS)	region 1
S4_76154787	chr 4	76154787	1.21E-05	0.055944	0.07	1.960871	5	IA-TX(DTA)	region 1
S4_76154795	chr 4	76154795	8.52E-08	0.055944	0.10	2.740116	7	IA-TX(DTS)	region 1
S4_76154795	chr 4	76154795	5.44E-06	0.055944	0.07	2.04256	5	IA-TX(DTA)	region 1
S4_76155114	chr 4	76155114	2.52E-07	0.055944	0.10	2.650814	7	IA-TX(DTS)	region 1
S4_76155114	chr 4	76155114	1.18E-05	0.055944	0.07	1.978639	5	IA-TX(DTA)	region 1
S4_76207905	chr 4	76207905	1.46E-07	0.059441	0.10	2.611357	7	IA-TX(DTS)	region 1
S4_76207905	chr 4	76207905	3.00E-05	0.059441	0.06	1.816355	5	IA-TX(DTA)	region 1
S4_76208236	chr 4	76208236	4.95E-07	0.059441	0.09	2.482053	6	IA-TX(DTS)	region 1
S4_76208236	chr 4	76208236	2.74E-05	0.059441	0.06	2.079109	5	WI-TX(DTS)	region 1
S4_76208236	chr 4	76208236	1.75E-05	0.059441	0.07	1.863099	5	IA-TX(DTA)	region 1
S4_76228192	chr 4	76228192	2.47E-06	0.06993	0.08	2.161821	6	IA-TX(DTS)	region 1
S4_76228200	chr 4	76228200	2.47E-06	0.06993	0.08	2.161821	6	IA-TX(DTS)	region 1
S4_76248441	chr 4	76248441	5.18E-07	0.073427	0.09	2.238263	6	IA-TX(DTS)	region 1
S4_76248441	chr 4	76248441	2.59E-06	0.073427	0.08	2.113916	6	WI-TX(DTS)	region 1
S4_76253781	chr 4	76253781	1.45E-05	0.06993	0.07	1.978157	5	IA-TX(DTS)	region 1
S4_76255457	chr 4	76255457	1.42E-07	0.055944	0.10	2.687412	7	IA-TX(DTS)	region 1
S4_76255457	chr 4	76255457	1.21E-05	0.055944	0.07	1.960871	5	IA-TX(DTA)	region 1
S4_76255488	chr 4	76255488	1.28E-07	0.059441	0.10	2.630016	7	IA-TX(DTS)	region 1
S4_76255488	chr 4	76255488	2.25E-05	0.059441	0.06	2.114759	5	WI-TX(DTS)	region 1
S4_76255488	chr 4	76255488	1.26E-05	0.059441	0.07	1.90733	5	IA-TX(DTA)	region 1
S4_76255489	chr 4	76255489	1.28E-07	0.059441	0.10	2.630016	7	IA-TX(DTS)	region 1
S4_76255489	chr 4	76255489	2.25E-05	0.059441	0.06	2.114759	5	WI-TX(DTS)	region 1
S4_76255489	chr 4	76255489	1.26E-05	0.059441	0.07	1.90733	5	IA-TX(DTA)	region 1
S4_76258847	chr 4	76258847	7.82E-08	0.055944	0.10	2.751029	7	IA-TX(DTS)	region 1
S4_76258847	chr 4	76258847	9.00E-06	0.055944	0.07	1.994605	5	IA-TX(DTA)	region 1
S4_76258923	chr 4	76258923	7.82E-08	0.055944	0.10	2.751029	7	IA-TX(DTS)	region 1
S4_76258923	chr 4	76258923	9.00E-06	0.055944	0.07	1.994605	5	IA-TX(DTA)	region 1
S4_76287384	chr 4	76287384	7.96E-07	0.101399	0.09	1.892966	6	IA-TX(DTS)	region 1
S4_76287384	chr 4	76287384	8.08E-06	0.101399	0.07	1.723782	5	WI-TX(DTS)	region 1
S4_76287384	chr 4	76287384	7.98E-06	0.101399	0.07	1.508413	5	IA-TX(DTA)	region 1

S4_76289463	chr 4	76289463	3.69E-08	0.055944	0.11	2.839459	7	IA-TX(DTS)	region 1
S4_76289463	chr 4	76289463	1.53E-05	0.055944	0.07	2.231897	5	WI-TX(DTS)	region 1
S4_76289463	chr 4	76289463	4.31E-06	0.055944	0.08	2.079147	5	IA-TX(DTA)	region 1
S4_76289480	chr 4	76289480	1.14E-07	0.059441	0.10	2.648639	7	IA-TX(DTS)	region 1
S4_76289480	chr 4	76289480	2.59E-05	0.059441	0.06	2.104731	5	WI-TX(DTS)	region 1
S4_76289480	chr 4	76289480	1.08E-05	0.059441	0.07	1.928566	5	IA-TX(DTA)	region 1
S4_76289530	chr 4	76289530	1.28E-07	0.059441	0.10	2.630016	7	IA-TX(DTS)	region 1
S4_76289530	chr 4	76289530	2.25E-05	0.059441	0.06	2.114759	5	WI-TX(DTS)	region 1
S4_76289530	chr 4	76289530	1.26E-05	0.059441	0.07	1.90733	5	IA-TX(DTA)	region 1
S4_76292620	chr 4	76292620	1.28E-07	0.059441	0.10	2.630016	7	IA-TX(DTS)	region 1
S4_76292620	chr 4	76292620	2.25E-05	0.059441	0.06	2.114759	5	WI-TX(DTS)	region 1
S4_76292620	chr 4	76292620	1.26E-05	0.059441	0.07	1.90733	5	IA-TX(DTA)	region 1
S7_77675871	chr 7	77675871	6.58E-06	0.062937	0.07	2.196852	5	IA-TX(DTS)	region 1
S7_77795828	chr 7	77795828	9.00E-09	0.062937	0.12	2.829353	8	IA-TX(DTS)	region 1
S7_77795828	chr 7	77795828	2.95E-07	0.062937	0.09	2.53602	7	WI-TX(DTS)	region 1
S7_77795828	chr 7	77795828	4.91E-07	0.062937	0.09	2.174054	6	IA-TX(DTA)	region 1
S7_77957848	chr 7	77957848	2.52E-07	0.073427	0.10	2.349578	7	IA-TX(DTS)	region 1
S7_77957848	chr 7	77957848	2.11E-06	0.073427	0.08	2.177352	6	WI-TX(DTS)	region 1
S7_77957848	chr 7	77957848	5.45E-06	0.073427	0.07	1.822421	5	IA-TX(DTA)	region 1
S7_77964769	chr 7	77964769	3.99E-06	0.076923	0.08	2.069811	5	IA-TX(DTS)	region 1
S9_47452498	chr 9	47452498	9.93E-06	0.475524	0.07	1.670073	5	WI-TX(DTS)	region 1
S9_47482210	chr 9	47482210	1.90E-05	0.412587	0.07	1.78814	5	IA-TX(DTS)	region 1
S9_47582318	chr 9	47582318	2.86E-05	0.396853	0.06	1.805727	5	WI-TX(DTS)	region 1
S9_47582724	chr 9	47582724	2.61E-06	0.393357	0.08	2.18144	6	WI-TX(DTS)	region 1
S9_47582724	chr 9	47582724	1.12E-05	0.393357	0.07	1.778645	5	IA-TX(DTA)	region 1
S9_47582724	chr 9	47582724	9.00E-06	0.393357	0.07	1.855691	5	WI-TX(DTA)	region 1
S9_47584741	chr 9	47584741	5.26E-06	0.410839	0.07	2.031774	5	WI-TX(DTS)	region 1
S9_47584741	chr 9	47584741	1.69E-05	0.410839	0.07	1.675405	5	IA-TX(DTA)	region 1
S9_47584818	chr 9	47584818	7.32E-06	0.403846	0.07	1.949754	5	WI-TX(DTS)	region 1
S9_47584856	chr 9	47584856	1.51E-05	0.405594	0.07	1.864087	5	WI-TX(DTS)	region 1
S9_47584859	chr 9	47584859	7.71E-06	0.409091	0.07	1.903918	5	WI-TX(DTS)	region 1
S9_47585018	chr 9	47585018	2.58E-05	0.379371	0.06	1.802524	5	IA-TX(DTS)	region 1
S9_47585018	chr 9	47585018	1.97E-05	0.379371	0.06	1.85014	5	WI-TX(DTS)	region 1
S9_47585018	chr 9	47585018	6.90E-06	0.379371	0.07	1.761759	5	WI-TX(DTA)	region 1

S9_47589901	chr 9	47589901	2.82E-05	0.395105	0.06	1.90414	5	IA-TX(DTS)	region 1
S9_47589901	chr 9	47589901	1.64E-05	0.395105	0.07	1.734063	5	IA-TX(DTA)	region 1
S9_47599294	chr 9	47599294	2.46E-05	0.40035	0.06	1.890926	5	IA-TX(DTS)	region 1
S9_47599294	chr 9	47599294	8.31E-06	0.40035	0.07	1.770028	5	IA-TX(DTA)	region 1
S9_47600589	chr 9	47600589	1.55E-05	0.402098	0.07	1.960129	5	WI-TX(DTS)	region 1
S9_47600683	chr 9	47600683	2.91E-05	0.403846	0.06	1.648814	5	IA-TX(DTA)	region 1
S9_47601010	chr 9	47601010	1.86E-05	0.402098	0.07	1.934625	5	WI-TX(DTS)	region 1
S9_47601062	chr 9	47601062	1.42E-05	0.407343	0.07	1.932628	5	WI-TX(DTS)	region 1
S9_47601358	chr 9	47601358	2.24E-05	0.391608	0.06	1.725674	5	IA-TX(DTA)	region 1
S9_47601624	chr 9	47601624	2.67E-05	0.393357	0.06	1.68319	5	IA-TX(DTA)	region 1
S9_47601875	chr 9	47601875	6.04E-06	0.405594	0.07	2.039687	5	WI-TX(DTS)	region 1
S9_47601876	chr 9	47601876	6.10E-06	0.398601	0.07	2.07658	5	WI-TX(DTS)	region 1
S9_47601876	chr 9	47601876	1.68E-05	0.398601	0.07	1.7251	5	IA-TX(DTA)	region 1
S9_47601991	chr 9	47601991	1.87E-05	0.409091	0.07	1.927059	5	IA-TX(DTS)	region 1
S9_47601991	chr 9	47601991	2.44E-06	0.409091	0.08	2.153698	6	WI-TX(DTS)	region 1
S9_47601991	chr 9	47601991	8.33E-06	0.409091	0.07	1.776971	5	IA-TX(DTA)	region 1
S9_47601995	chr 9	47601995	1.87E-05	0.409091	0.07	1.927059	5	IA-TX(DTS)	region 1
S9_47601995	chr 9	47601995	2.44E-06	0.409091	0.08	2.153698	6	WI-TX(DTS)	region 1
S9_47601995	chr 9	47601995	8.33E-06	0.409091	0.07	1.776971	5	IA-TX(DTA)	region 1
S9_47602020	chr 9	47602020	1.13E-05	0.402098	0.07	2.027561	5	WI-TX(DTS)	region 1
S9_47602088	chr 9	47602088	2.07E-05	0.388112	0.06	1.77424	5	IA-TX(DTA)	region 1
S9_47602125	chr 9	47602125	2.36E-05	0.396853	0.06	1.940761	5	IA-TX(DTS)	region 1
S9_47602125	chr 9	47602125	8.83E-06	0.396853	0.07	2.066285	5	WI-TX(DTS)	region 1
S9_47602125	chr 9	47602125	7.56E-06	0.396853	0.07	1.820993	5	IA-TX(DTA)	region 1
S9_47602129	chr 9	47602129	1.88E-05	0.402098	0.07	1.931371	5	IA-TX(DTS)	region 1
S9_47602129	chr 9	47602129	1.20E-05	0.402098	0.07	1.999863	5	WI-TX(DTS)	region 1
S9_47602129	chr 9	47602129	1.70E-05	0.402098	0.07	1.717242	5	IA-TX(DTA)	region 1
S9_47607018	chr 9	47607018	3.17E-06	0.388112	0.08	1.973019	5	WI-TX(DTS)	region 1
S9_53023168	chr 9	53023168	3.35E-06	0.059441	0.08	2.322398	5	IA-TX(DTS)	region 1
S9_53023168	chr 9	53023168	2.94E-05	0.059441	0.06	2.103181	5	WI-TX(DTS)	region 1
S9_53113618	chr 9	53113618	3.33E-06	0.066434	0.08	2.237552	5	IA-TX(DTS)	region 1
S9_53113618	chr 9	53113618	2.54E-05	0.066434	0.06	1.786001	5	IA-TX(DTA)	region 1
S9_53113625	chr 9	53113625	3.32E-06	0.062937	0.08	2.291982	5	IA-TX(DTS)	region 1
S9_53113625	chr 9	53113625	2.03E-05	0.062937	0.06	1.851729	5	IA-TX(DTA)	region 1

S9_53118532	chr 9	53118532	1.10E-05	0.066434	0.07	2.108803	5	IA-TX(DTS)	region 1
S9_53118542	chr 9	53118542	7.67E-06	0.066434	0.07	2.149095	5	IA-TX(DTS)	region 1
S9_53118542	chr 9	53118542	3.75E-06	0.066434	0.08	1.966985	5	IA-TX(DTA)	region 1
S9_53135092	chr 9	53135092	9.51E-06	0.104895	0.07	1.494393	5	IA-TX(DTA)	region 1
S9_53152354	chr 9	53152354	2.62E-07	0.059441	0.10	2.59887	7	IA-TX(DTS)	region 1
S9_53152354	chr 9	53152354	2.43E-06	0.059441	0.08	2.09606	6	IA-TX(DTA)	region 1
S9_53152390	chr 9	53152390	2.21E-07	0.062937	0.10	2.54623	7	IA-TX(DTS)	region 1
S9_53152390	chr 9	53152390	6.64E-06	0.062937	0.07	1.946678	5	IA-TX(DTA)	region 1
S9_53189551	chr 9	53189551	1.09E-06	0.055944	0.09	2.51746	6	IA-TX(DTS)	region 1
S9_53189551	chr 9	53189551	5.34E-06	0.055944	0.07	2.072827	5	IA-TX(DTA)	region 1
S9_53354213	chr 9	53354213	4.49E-08	0.055944	0.11	2.846101	7	IA-TX(DTS)	region 1
S9_53354213	chr 9	53354213	1.19E-05	0.055944	0.07	2.281569	5	WI-TX(DTS)	region 1
S9_53354213	chr 9	53354213	4.69E-07	0.055944	0.09	2.308838	6	IA-TX(DTA)	region 1
S9_53359448	chr 9	53359448	6.39E-08	0.055944	0.11	2.792798	7	IA-TX(DTS)	region 1
S9_53359448	chr 9	53359448	5.11E-07	0.055944	0.09	2.285497	6	IA-TX(DTA)	region 1
S9_53360022	chr 9	53360022	3.56E-07	0.055944	0.09	2.61231	6	IA-TX(DTS)	region 1
S9_53360022	chr 9	53360022	4.00E-06	0.055944	0.08	2.083636	5	IA-TX(DTA)	region 1
S9_53361654	chr 9	53361654	9.33E-08	0.055944	0.10	2.778898	7	IA-TX(DTS)	region 1
S9_53361654	chr 9	53361654	1.20E-06	0.055944	0.09	2.22459	6	IA-TX(DTA)	region 1
S9_53390849	chr 9	53390849	4.13E-08	0.055944	0.11	2.858571	7	IA-TX(DTS)	region 1
S9_53390849	chr 9	53390849	1.95E-05	0.055944	0.06	2.226892	5	WI-TX(DTS)	region 1
S9_53390849	chr 9	53390849	2.84E-07	0.055944	0.10	2.358088	7	IA-TX(DTA)	region 1
S9_53391564	chr 9	53391564	9.33E-08	0.055944	0.10	2.778898	7	IA-TX(DTS)	region 1
S9_53391564	chr 9	53391564	1.20E-06	0.055944	0.09	2.22459	6	IA-TX(DTA)	region 1
S9_53391751	chr 9	53391751	4.13E-08	0.055944	0.11	2.858571	7	IA-TX(DTS)	region 1
S9_53391751	chr 9	53391751	1.95E-05	0.055944	0.06	2.226892	5	WI-TX(DTS)	region 1
S9_53391751	chr 9	53391751	2.84E-07	0.055944	0.10	2.358088	7	IA-TX(DTA)	region 1
S9_53392358	chr 9	53392358	4.41E-08	0.062937	0.11	2.67963	7	IA-TX(DTS)	region 1
S9_53392358	chr 9	53392358	1.14E-06	0.062937	0.09	2.094643	6	IA-TX(DTA)	region 1
S9_53392731	chr 9	53392731	1.67E-07	0.062937	0.10	2.568988	7	IA-TX(DTS)	region 1
S9_53392731	chr 9	53392731	1.06E-05	0.062937	0.07	1.898427	5	IA-TX(DTA)	region 1
S9_53392846	chr 9	53392846	1.08E-07	0.059441	0.10	2.683986	7	IA-TX(DTS)	region 1
S9_53392846	chr 9	53392846	3.09E-05	0.059441	0.06	2.107635	5	WI-TX(DTS)	region 1
S9_53392846	chr 9	53392846	2.72E-06	0.059441	0.08	2.084031	6	IA-TX(DTA)	region 1

S9_53392892	chr 9	53392892	1.08E-07	0.059441	0.10	2.683986	7	IA-TX(DTS)	region 1
S9_53392892	chr 9	53392892	3.09E-05	0.059441	0.06	2.107635	5	WI-TX(DTS)	region 1
S9_53392892	chr 9	53392892	2.72E-06	0.059441	0.08	2.084031	6	IA-TX(DTA)	region 1
S9_53454966	chr 9	53454966	2.34E-05	0.122378	0.06	1.494352	5	IA-TX(DTS)	region 1
S9_53459703	chr 9	53459703	4.80E-06	0.06993	0.07	2.093981	5	IA-TX(DTS)	region 1
S9_53459703	chr 9	53459703	2.92E-05	0.06993	0.06	1.687271	5	IA-TX(DTA)	region 1
S9_53461547	chr 9	53461547	3.50E-07	0.066434	0.09	2.459818	6	IA-TX(DTS)	region 1
S9_53461547	chr 9	53461547	2.89E-05	0.066434	0.06	2.026535	5	WI-TX(DTS)	region 1
S9_53461547	chr 9	53461547	3.20E-06	0.066434	0.08	1.981395	5	IA-TX(DTA)	region 1
S9_53461744	chr 9	53461744	1.14E-06	0.062937	0.09	2.392292	6	IA-TX(DTS)	region 1
S9_53461744	chr 9	53461744	8.68E-06	0.062937	0.07	1.92723	5	IA-TX(DTA)	region 1
S9_53461754	chr 9	53461754	8.60E-07	0.066434	0.09	2.372385	6	IA-TX(DTS)	region 1
S9_53461754	chr 9	53461754	5.66E-06	0.066434	0.07	1.928611	5	IA-TX(DTA)	region 1
S9_53461769	chr 9	53461769	8.60E-07	0.066434	0.09	2.372385	6	IA-TX(DTS)	region 1
S9_53461769	chr 9	53461769	5.66E-06	0.066434	0.07	1.928611	5	IA-TX(DTA)	region 1
S9_53488387	chr 9	53488387	1.31E-07	0.059441	0.10	2.652679	7	IA-TX(DTS)	region 1
S9_53488387	chr 9	53488387	1.84E-05	0.059441	0.07	2.159011	5	WI-TX(DTS)	region 1
S9_53488387	chr 9	53488387	1.28E-06	0.059441	0.08	2.144199	6	IA-TX(DTA)	region 1
S9_53500761	chr 9	53500761	1.31E-07	0.059441	0.10	2.652679	7	IA-TX(DTS)	region 1
S9_53500761	chr 9	53500761	1.84E-05	0.059441	0.07	2.159011	5	WI-TX(DTS)	region 1
S9_53500761	chr 9	53500761	1.28E-06	0.059441	0.08	2.144199	6	IA-TX(DTA)	region 1
S9_53500780	chr 9	53500780	1.31E-07	0.059441	0.10	2.652679	7	IA-TX(DTS)	region 1
S9_53500780	chr 9	53500780	1.84E-05	0.059441	0.07	2.159011	5	WI-TX(DTS)	region 1
S9_53500780	chr 9	53500780	1.28E-06	0.059441	0.08	2.144199	6	IA-TX(DTA)	region 1
S9_53501169	chr 9	53501169	5.40E-07	0.066434	0.09	2.38416	6	IA-TX(DTS)	region 1
S9_53501169	chr 9	53501169	2.46E-06	0.066434	0.08	1.97689	6	IA-TX(DTA)	region 1
S9_53507253	chr 9	53507253	1.42E-06	0.062937	0.08	2.333301	6	IA-TX(DTS)	region 1
S9_53507253	chr 9	53507253	1.05E-05	0.062937	0.07	1.879136	5	IA-TX(DTA)	region 1
S9_53508018	chr 9	53508018	1.50E-07	0.059441	0.10	2.631006	7	IA-TX(DTS)	region 1
S9_53508018	chr 9	53508018	3.94E-06	0.059441	0.08	2.032294	5	IA-TX(DTA)	region 1
S9_53597676	chr 9	53597676	1.52E-06	0.062937	0.08	2.345211	6	IA-TX(DTS)	region 1
S9_53597676	chr 9	53597676	6.69E-06	0.062937	0.07	1.937308	5	IA-TX(DTA)	region 1
S9_53651716	chr 9	53651716	4.43E-08	0.055944	0.11	2.838933	7	IA-TX(DTS)	region 1
S9_53651716	chr 9	53651716	1.35E-06	0.055944	0.08	2.203466	6	IA-TX(DTA)	region 1

S9_53679864	chr 9	53679864	7.27E-07	0.055944	0.09	2.551471	6	IA-TX(DTS)	region 1
S9_53679864	chr 9	53679864	3.08E-06	0.055944	0.08	2.119662	6	IA-TX(DTA)	region 1
S9_53686456	chr 9	53686456	5.24E-08	0.059441	0.11	2.763729	7	IA-TX(DTS)	region 1
S9_53686456	chr 9	53686456	2.82E-05	0.059441	0.06	2.12666	5	WI-TX(DTS)	region 1
S9_53686456	chr 9	53686456	1.69E-07	0.059441	0.10	2.343906	7	IA-TX(DTA)	region 1
S9_53703347	chr 9	53703347	1.50E-07	0.059441	0.10	2.634144	7	IA-TX(DTS)	region 1
S9_53703347	chr 9	53703347	2.91E-06	0.059441	0.08	2.063656	6	IA-TX(DTA)	region 1
S9_53703390	chr 9	53703390	1.36E-07	0.059441	0.10	2.643961	7	IA-TX(DTS)	region 1
S9_53703390	chr 9	53703390	2.45E-05	0.059441	0.06	2.120797	5	WI-TX(DTS)	region 1
S9_53703390	chr 9	53703390	1.03E-06	0.059441	0.09	2.159411	6	IA-TX(DTA)	region 1
S9_53703665	chr 9	53703665	1.08E-07	0.059441	0.10	2.683986	7	IA-TX(DTS)	region 1
S9_53703665	chr 9	53703665	3.09E-05	0.059441	0.06	2.107635	5	WI-TX(DTS)	region 1
S9_53703665	chr 9	53703665	2.72E-06	0.059441	0.08	2.084031	6	IA-TX(DTA)	region 1
S9_53703736	chr 9	53703736	1.83E-07	0.06993	0.10	2.442017	7	IA-TX(DTS)	region 1
S9_53703736	chr 9	53703736	5.81E-06	0.06993	0.07	1.865812	5	IA-TX(DTA)	region 1
S9_53704114	chr 9	53704114	4.58E-07	0.073427	0.09	2.316407	6	IA-TX(DTS)	region 1
S9_53704114	chr 9	53704114	1.65E-05	0.073427	0.07	1.738952	5	IA-TX(DTA)	region 1
S9_53707327	chr 9	53707327	7.09E-06	0.062937	0.07	2.168388	5	IA-TX(DTS)	region 1
S9_53744161	chr 9	53744161	1.38E-05	0.094406	0.07	1.712171	5	IA-TX(DTS)	region 1
S9_53744161	chr 9	53744161	1.20E-05	0.094406	0.07	1.744062	5	WI-TX(DTS)	region 1
S9_53746510	chr 9	53746510	2.60E-07	0.06993	0.10	2.405958	7	IA-TX(DTS)	region 1
S9_53746510	chr 9	53746510	8.99E-06	0.06993	0.07	1.823145	5	IA-TX(DTA)	region 1
S9_53766139	chr 9	53766139	1.61E-07	0.06993	0.10	2.432754	7	IA-TX(DTS)	region 1
S9_53766139	chr 9	53766139	1.14E-05	0.06993	0.07	1.78869	5	IA-TX(DTA)	region 1
S9_53766140	chr 9	53766140	1.61E-07	0.06993	0.10	2.432754	7	IA-TX(DTS)	region 1
S9_53766140	chr 9	53766140	1.14E-05	0.06993	0.07	1.78869	5	IA-TX(DTA)	region 1
S9_53778393	chr 9	53778393	2.84E-07	0.062937	0.10	2.510429	7	IA-TX(DTS)	region 1
S9_53778393	chr 9	53778393	6.37E-06	0.062937	0.07	1.94148	5	IA-TX(DTA)	region 1
S9_53778686	chr 9	53778686	1.31E-07	0.059441	0.10	2.652679	7	IA-TX(DTS)	region 1
S9_53778686	chr 9	53778686	1.84E-05	0.059441	0.07	2.159011	5	WI-TX(DTS)	region 1
S9_53778686	chr 9	53778686	1.28E-06	0.059441	0.08	2.144199	6	IA-TX(DTA)	region 1
S9_53778706	chr 9	53778706	2.84E-07	0.062937	0.10	2.510429	7	IA-TX(DTS)	region 1
S9_53778706	chr 9	53778706	6.37E-06	0.062937	0.07	1.94148	5	IA-TX(DTA)	region 1
S9_53883948	chr 9	53883948	1.41E-08	0.066434	0.12	2.734594	8	IA-TX(DTS)	region 1

S9_53883948	chr 9	53883948	2.68E-06	0.066434	0.08	2.267238	6	WI-TX(DTS)	region 1
S9_53883948	chr 9	53883948	9.63E-07	0.066434	0.09	2.073204	6	IA-TX(DTA)	region 1
S9_53884515	chr 9	53884515	1.70E-08	0.087413	0.12	2.400286	8	IA-TX(DTS)	region 1
S9_53884515	chr 9	53884515	1.73E-06	0.087413	0.08	2.041679	6	WI-TX(DTS)	region 1
S9_53884515	chr 9	53884515	2.96E-08	0.087413	0.11	2.084501	8	IA-TX(DTA)	region 1
S9_53888672	chr 9	53888672	2.65E-07	0.076923	0.10	2.30431	7	IA-TX(DTS)	region 1
S9_53888672	chr 9	53888672	1.56E-05	0.076923	0.07	1.942134	5	WI-TX(DTS)	region 1
S9_53888672	chr 9	53888672	4.50E-06	0.076923	0.08	1.807182	5	IA-TX(DTA)	region 1
S9_53892783	chr 9	53892783	8.03E-08	0.062937	0.10	2.647125	7	IA-TX(DTS)	region 1
S9_53892783	chr 9	53892783	6.76E-06	0.062937	0.07	2.227953	5	WI-TX(DTS)	region 1
S9_53892783	chr 9	53892783	3.36E-06	0.062937	0.08	2.014125	5	IA-TX(DTA)	region 1
S9_53892794	chr 9	53892794	8.03E-08	0.062937	0.10	2.647125	7	IA-TX(DTS)	region 1
S9_53892794	chr 9	53892794	6.76E-06	0.062937	0.07	2.227953	5	WI-TX(DTS)	region 1
S9_53892794	chr 9	53892794	3.36E-06	0.062937	0.08	2.014125	5	IA-TX(DTA)	region 1
S9_53892797	chr 9	53892797	8.03E-08	0.062937	0.10	2.647125	7	IA-TX(DTS)	region 1
S9_53892797	chr 9	53892797	6.76E-06	0.062937	0.07	2.227953	5	WI-TX(DTS)	region 1
S9_53892797	chr 9	53892797	3.36E-06	0.062937	0.08	2.014125	5	IA-TX(DTA)	region 1
S9_53893128	chr 9	53893128	5.69E-06	0.097902	0.07	1.843916	5	IA-TX(DTS)	region 1
S9_53978401	chr 9	53978401	8.47E-06	0.083916	0.07	1.936967	5	IA-TX(DTS)	region 1
S9_53979486	chr 9	53979486	5.63E-06	0.076923	0.07	2.029755	5	IA-TX(DTS)	region 1
S9_53979643	chr 9	53979643	6.48E-09	0.08042	0.12	2.568544	8	IA-TX(DTS)	region 1
S9_53979643	chr 9	53979643	3.79E-07	0.08042	0.09	2.256887	6	WI-TX(DTS)	region 1
S9_53979643	chr 9	53979643	2.09E-07	0.08042	0.10	2.019515	7	IA-TX(DTA)	region 1
S9_53979729	chr 9	53979729	1.51E-07	0.066434	0.10	2.524984	7	IA-TX(DTS)	region 1
S9_53979729	chr 9	53979729	1.77E-06	0.066434	0.08	2.022877	6	IA-TX(DTA)	region 1
S9_54071623	chr 9	54071623	2.34E-07	0.066434	0.10	2.46687	7	IA-TX(DTS)	region 1
S9_54071623	chr 9	54071623	1.56E-05	0.066434	0.07	1.809597	5	IA-TX(DTA)	region 1
S9_54072045	chr 9	54072045	9.71E-07	0.073427	0.09	2.22246	6	IA-TX(DTS)	region 1
S9_54114660	chr 9	54114660	4.60E-06	0.174825	0.08	1.39375	5	IA-TX(DTS)	region 1
S9_54200239	chr 9	54200239	8.23E-08	0.059441	0.10	2.722575	7	IA-TX(DTS)	region 1
S9_54200239	chr 9	54200239	1.31E-06	0.059441	0.08	2.161806	6	IA-TX(DTA)	region 1
S9_54200277	chr 9	54200277	5.23E-07	0.059441	0.09	2.511528	6	IA-TX(DTS)	region 1
S9_54200277	chr 9	54200277	2.95E-06	0.059441	0.08	2.062903	6	IA-TX(DTA)	region 1
S9_54200465	chr 9	54200465	1.21E-07	0.055944	0.10	2.740657	7	IA-TX(DTS)	region 1

S9_54200465	chr 9	54200465	2.52E-06	0.055944	0.08	2.144497	6	IA-TX(DTA)	region 1
S9_54200583	chr 9	54200583	6.43E-07	0.062937	0.09	2.439856	6	IA-TX(DTS)	region 1
S9_54200583	chr 9	54200583	3.62E-06	0.062937	0.08	2.001917	5	IA-TX(DTA)	region 1
S9_54200729	chr 9	54200729	1.50E-07	0.062937	0.10	2.571214	7	IA-TX(DTS)	region 1
S9_54200729	chr 9	54200729	1.06E-05	0.062937	0.07	2.164682	5	WI-TX(DTS)	region 1
S9_54200729	chr 9	54200729	3.51E-06	0.062937	0.08	1.997169	5	IA-TX(DTA)	region 1
S9_54200952	chr 9	54200952	1.43E-08	0.062937	0.12	2.785371	8	IA-TX(DTS)	region 1
S9_54200952	chr 9	54200952	3.48E-06	0.062937	0.08	2.28303	5	WI-TX(DTS)	region 1
S9_54200952	chr 9	54200952	1.38E-06	0.062937	0.08	2.080725	6	IA-TX(DTA)	region 1
S9_54201389	chr 9	54201389	8.93E-07	0.062937	0.09	2.397768	6	IA-TX(DTS)	region 1
S9_54201389	chr 9	54201389	2.95E-05	0.062937	0.06	2.048839	5	WI-TX(DTS)	region 1
S9_54201389	chr 9	54201389	7.89E-06	0.062937	0.07	1.920892	5	IA-TX(DTA)	region 1
S9_54202466	chr 9	54202466	4.37E-08	0.059441	0.11	2.758198	7	IA-TX(DTS)	region 1
S9_54202466	chr 9	54202466	2.95E-05	0.059441	0.06	2.103945	5	WI-TX(DTS)	region 1
S9_54202466	chr 9	54202466	1.32E-06	0.059441	0.08	2.141707	6	IA-TX(DTA)	region 1
S9_54203544	chr 9	54203544	9.44E-08	0.059441	0.10	2.673715	7	IA-TX(DTS)	region 1
S9_54203544	chr 9	54203544	1.66E-05	0.059441	0.07	2.162368	5	WI-TX(DTS)	region 1
S9_54203544	chr 9	54203544	1.00E-06	0.059441	0.09	2.157895	6	IA-TX(DTA)	region 1
S9_54203764	chr 9	54203764	3.73E-07	0.055944	0.09	2.633478	6	IA-TX(DTS)	region 1
S9_54203764	chr 9	54203764	1.12E-06	0.055944	0.09	2.2274	6	IA-TX(DTA)	region 1
S9_54205096	chr 9	54205096	2.35E-07	0.059441	0.10	2.602554	7	IA-TX(DTS)	region 1
S9_54205096	chr 9	54205096	1.35E-06	0.059441	0.08	2.145449	6	IA-TX(DTA)	region 1
S9_54206880	chr 9	54206880	6.33E-08	0.055944	0.11	2.811808	7	IA-TX(DTS)	region 1
S9_54206880	chr 9	54206880	2.42E-07	0.055944	0.10	2.368287	7	IA-TX(DTA)	region 1
S9_54207123	chr 9	54207123	5.24E-08	0.059441	0.11	2.763729	7	IA-TX(DTS)	region 1
S9_54207123	chr 9	54207123	2.82E-05	0.059441	0.06	2.12666	5	WI-TX(DTS)	region 1
S9_54207123	chr 9	54207123	1.69E-07	0.059441	0.10	2.343906	7	IA-TX(DTA)	region 1
S9_54207311	chr 9	54207311	1.99E-07	0.062937	0.10	2.559435	7	IA-TX(DTS)	region 1
S9_54207311	chr 9	54207311	3.16E-06	0.062937	0.08	2.018524	5	IA-TX(DTA)	region 1
S9_54223580	chr 9	54223580	7.23E-07	0.062937	0.09	2.417823	6	IA-TX(DTS)	region 1
S9_54223580	chr 9	54223580	7.90E-07	0.062937	0.09	2.130475	6	IA-TX(DTA)	region 1
S9_54224127	chr 9	54224127	8.23E-08	0.059441	0.10	2.722575	7	IA-TX(DTS)	region 1
S9_54224127	chr 9	54224127	1.31E-06	0.059441	0.08	2.161806	6	IA-TX(DTA)	region 1
S9_54224137	chr 9	54224137	8.23E-08	0.059441	0.10	2.722575	7	IA-TX(DTS)	region 1

S9_54224137	chr 9	54224137	1.31E-06	0.059441	0.08	2.161806	6	IA-TX(DTA)	region 1
S9_54224599	chr 9	54224599	1.08E-07	0.059441	0.10	2.683986	7	IA-TX(DTS)	region 1
S9_54224599	chr 9	54224599	3.09E-05	0.059441	0.06	2.107635	5	WI-TX(DTS)	region 1
S9_54224599	chr 9	54224599	2.72E-06	0.059441	0.08	2.084031	6	IA-TX(DTA)	region 1
S9_54225623	chr 9	54225623	7.46E-08	0.062937	0.11	2.666162	7	IA-TX(DTS)	region 1
S9_54225623	chr 9	54225623	2.92E-06	0.062937	0.08	2.32859	6	WI-TX(DTS)	region 1
S9_54225623	chr 9	54225623	7.94E-07	0.062937	0.09	2.154844	6	IA-TX(DTA)	region 1
S9_54232738	chr 9	54232738	2.51E-06	0.059441	0.08	2.35416	6	IA-TX(DTS)	region 1
S9_54242046	chr 9	54242046	1.08E-07	0.059441	0.10	2.683986	7	IA-TX(DTS)	region 1
S9_54242046	chr 9	54242046	3.09E-05	0.059441	0.06	2.107635	5	WI-TX(DTS)	region 1
S9_54242046	chr 9	54242046	2.72E-06	0.059441	0.08	2.084031	6	IA-TX(DTA)	region 1
S9_54242388	chr 9	54242388	4.49E-08	0.055944	0.11	2.846101	7	IA-TX(DTS)	region 1
S9_54242388	chr 9	54242388	1.19E-05	0.055944	0.07	2.281569	5	WI-TX(DTS)	region 1
S9_54242388	chr 9	54242388	4.69E-07	0.055944	0.09	2.308838	6	IA-TX(DTA)	region 1
S9_54243812	chr 9	54243812	1.61E-08	0.059441	0.12	2.848048	8	IA-TX(DTS)	region 1
S9_54243812	chr 9	54243812	3.26E-06	0.059441	0.08	2.350424	5	WI-TX(DTS)	region 1
S9_54243812	chr 9	54243812	4.65E-07	0.059441	0.09	2.23385	6	IA-TX(DTA)	region 1
S9_54245258	chr 9	54245258	1.05E-07	0.055944	0.10	2.761598	7	IA-TX(DTS)	region 1
S9_54245258	chr 9	54245258	2.25E-05	0.055944	0.06	2.204997	5	WI-TX(DTS)	region 1
S9_54245258	chr 9	54245258	1.07E-06	0.055944	0.09	2.231297	6	IA-TX(DTA)	region 1
S9_54247653	chr 9	54247653	4.49E-08	0.055944	0.11	2.846101	7	IA-TX(DTS)	region 1
S9_54247653	chr 9	54247653	1.19E-05	0.055944	0.07	2.281569	5	WI-TX(DTS)	region 1
S9_54247653	chr 9	54247653	4.69E-07	0.055944	0.09	2.308838	6	IA-TX(DTA)	region 1
S9_54248991	chr 9	54248991	5.80E-08	0.059441	0.11	2.731818	7	IA-TX(DTS)	region 1
S9_54248991	chr 9	54248991	9.88E-06	0.059441	0.07	2.230767	5	WI-TX(DTS)	region 1
S9_54248991	chr 9	54248991	5.80E-07	0.059441	0.09	2.216829	6	IA-TX(DTA)	region 1
S9_54289336	chr 9	54289336	1.83E-07	0.073427	0.10	2.39862	7	IA-TX(DTS)	region 1
S9_54289336	chr 9	54289336	9.39E-06	0.073427	0.07	1.789841	5	IA-TX(DTA)	region 1
S9_54289356	chr 9	54289356	9.94E-08	0.062937	0.10	2.615375	7	IA-TX(DTS)	region 1
S9_54289356	chr 9	54289356	4.00E-06	0.062937	0.08	1.989131	5	IA-TX(DTA)	region 1
S9_54306734	chr 9	54306734	4.49E-08	0.055944	0.11	2.846101	7	IA-TX(DTS)	region 1
S9_54306734	chr 9	54306734	1.19E-05	0.055944	0.07	2.281569	5	WI-TX(DTS)	region 1
S9_54306734	chr 9	54306734	4.69E-07	0.055944	0.09	2.308838	6	IA-TX(DTA)	region 1
S9_54381406	chr 9	54381406	9.33E-08	0.055944	0.10	2.778898	7	IA-TX(DTS)	region 1

S9_54381406	chr 9	54381406	1.20E-06	0.055944	0.09	2.22459	6	IA-TX(DTA)	region 1
S9_54381445	chr 9	54381445	4.49E-08	0.055944	0.11	2.846101	7	IA-TX(DTS)	region 1
S9_54381445	chr 9	54381445	1.19E-05	0.055944	0.07	2.281569	5	WI-TX(DTS)	region 1
S9_54381445	chr 9	54381445	4.69E-07	0.055944	0.09	2.308838	6	IA-TX(DTA)	region 1
S9_54400418	chr 9	54400418	1.35E-08	0.115385	0.12	2.122892	8	IA-TX(DTS)	region 1
S9_54400418	chr 9	54400418	1.98E-05	0.115385	0.06	1.592722	5	WI-TX(DTS)	region 1
S9_54400418	chr 9	54400418	1.03E-07	0.115385	0.10	1.752625	7	IA-TX(DTA)	region 1
S9_54527240	chr 9	54527240	8.23E-08	0.059441	0.10	2.722575	7	IA-TX(DTS)	region 1
S9_54527240	chr 9	54527240	1.31E-06	0.059441	0.08	2.161806	6	IA-TX(DTA)	region 1
S9_54539165	chr 9	54539165	1.08E-07	0.059441	0.10	2.683986	7	IA-TX(DTS)	region 1
S9_54539165	chr 9	54539165	3.09E-05	0.059441	0.06	2.107635	5	WI-TX(DTS)	region 1
S9_54539165	chr 9	54539165	2.72E-06	0.059441	0.08	2.084031	6	IA-TX(DTA)	region 1
S9_54541738	chr 9	54541738	4.49E-08	0.055944	0.11	2.846101	7	IA-TX(DTS)	region 1
S9_54541738	chr 9	54541738	1.19E-05	0.055944	0.07	2.281569	5	WI-TX(DTS)	region 1
S9_54541738	chr 9	54541738	4.69E-07	0.055944	0.09	2.308838	6	IA-TX(DTA)	region 1
S9_70776582	chr 9	70776582	1.16E-05	0.356643	0.07	2.050711	5	IA-TX(DTS)	region 2
S9_74139024	chr 9	74139024	8.37E-07	0.076923	0.09	2.182172	6	IA-TX(DTS)	region 2
S9_74139024	chr 9	74139024	4.64E-06	0.076923	0.08	2.045525	5	WI-TX(DTS)	region 2
S9_74168868	chr 9	74168868	1.13E-05	0.059441	0.07	2.148722	5	IA-TX(DTS)	region 2
S9_74404914	chr 9	74404914	9.36E-06	0.353147	0.07	2.04275	5	IA-TX(DTS)	region 2
S9_74411757	chr 9	74411757	1.89E-05	0.367133	0.07	1.918999	5	IA-TX(DTS)	region 2
S9_74630038	chr 9	74630038	2.00E-05	0.339161	0.06	1.920806	5	WI-TX(DTS)	region 2
S9_74647394	chr 9	74647394	1.40E-05	0.374126	0.07	1.83045	5	IA-TX(DTS)	region 2
S9_74647394	chr 9	74647394	6.80E-06	0.374126	0.07	1.919763	5	WI-TX(DTS)	region 2
S9_74652044	chr 9	74652044	5.73E-06	0.374126	0.07	1.962952	5	IA-TX(DTS)	region 2
S9_74652044	chr 9	74652044	1.52E-05	0.374126	0.07	1.889956	5	WI-TX(DTS)	region 2
S9_74652100	chr 9	74652100	2.02E-06	0.370629	0.08	2.110069	6	IA-TX(DTS)	region 2
S9_74652100	chr 9	74652100	8.87E-06	0.370629	0.07	1.990156	5	WI-TX(DTS)	region 2
S9_74652141	chr 9	74652141	2.31E-06	0.374126	0.08	2.039388	6	IA-TX(DTS)	region 2
S9_74652141	chr 9	74652141	4.88E-06	0.374126	0.07	1.992637	5	WI-TX(DTS)	region 2
S9_74652227	chr 9	74652227	5.32E-07	0.370629	0.09	2.217618	6	IA-TX(DTS)	region 2
S9_74652227	chr 9	74652227	8.87E-06	0.370629	0.07	1.977282	5	WI-TX(DTS)	region 2
S9_74652286	chr 9	74652286	1.99E-05	0.384615	0.06	1.805769	5	IA-TX(DTS)	region 2
S9_74652286	chr 9	74652286	1.09E-05	0.384615	0.07	1.884576	5	WI-TX(DTS)	region 2

S9_78461989	chr 9	78461989	1.72E-05	0.361888	0.07	1.898992	5	IA-TX(DTS)	region 2
S9_78461989	chr 9	78461989	2.61E-05	0.361888	0.06	1.877505	5	WI-TX(DTS)	region 2
S9_78461993	chr 9	78461993	1.72E-05	0.361888	0.07	1.898992	5	IA-TX(DTS)	region 2
S9_78461993	chr 9	78461993	2.61E-05	0.361888	0.06	1.877505	5	WI-TX(DTS)	region 2
S9_78462077	chr 9	78462077	2.14E-05	0.367133	0.06	1.869854	5	IA-TX(DTS)	region 2
S9_89222060	chr 9	89222060	2.61E-05	0.346154	0.06	-1.63086	5	WI-TX(DTS)	region 2
S9_89222088	chr 9	89222088	2.18E-06	0.358392	0.08	-1.80085	6	WI-TX(DTS)	region 2
S9_89222150	chr 9	89222150	1.95E-05	0.333916	0.06	-1.66382	5	WI-TX(DTS)	region 2
S9_89222423	chr 9	89222423	8.22E-06	0.328671	0.07	-1.74421	5	WI-TX(DTS)	region 2
S9_93804862	chr 9	93804862	1.10E-05	0.106643	0.07	1.762246	5	IA-TX(DTS)	region 2
S9_93804862	chr 9	93804862	2.02E-05	0.106643	0.06	1.725916	5	WI-TX(DTS)	region 2
S9_93804862	chr 9	93804862	2.84E-06	0.106643	0.08	1.663626	6	IA-TX(DTA)	region 2
S9_93815334	chr 9	93815334	1.73E-05	0.117133	0.07	1.476602	5	IA-TX(DTA)	region 2
S9_93815476	chr 9	93815476	2.85E-05	0.117133	0.06	1.6202	5	IA-TX(DTS)	region 2
S9_93815476	chr 9	93815476	7.72E-06	0.117133	0.07	1.754897	5	WI-TX(DTS)	region 2
S9_93815476	chr 9	93815476	5.61E-06	0.117133	0.07	1.558805	5	IA-TX(DTA)	region 2
S9_93815476	chr 9	93815476	2.34E-05	0.117133	0.06	1.494706	5	WI-TX(DTA)	region 2
S10_111768253	chr 10	1.12E+08	1.86E-05	0.089161	0.07	1.844335	5	IA-TX(DTS)	region 1
S10_111768253	chr 10	1.12E+08	1.01E-05	0.089161	0.07	1.925627	5	WI-TX(DTS)	region 1
S10_111837738	chr 10	1.12E+08	2.69E-07	0.096154	0.10	2.168484	7	IA-TX(DTS)	region 1
S10_111837738	chr 10	1.12E+08	1.58E-06	0.096154	0.08	2.040315	6	WI-TX(DTS)	region 1
S10_111837738	chr 10	1.12E+08	9.28E-07	0.096154	0.09	1.825276	6	IA-TX(DTA)	region 1
S10_111884305	chr 10	1.12E+08	1.48E-07	0.090909	0.10	2.231988	7	IA-TX(DTS)	region 1
S10_111884305	chr 10	1.12E+08	7.65E-06	0.090909	0.07	1.908814	5	WI-TX(DTS)	region 1
S10_111884305	chr 10	1.12E+08	3.13E-07	0.090909	0.09	1.91886	7	IA-TX(DTA)	region 1
S10_111884517	chr 10	1.12E+08	2.06E-07	0.096154	0.10	2.198075	7	IA-TX(DTS)	region 1
S10_111884517	chr 10	1.12E+08	1.26E-06	0.096154	0.08	2.067272	6	WI-TX(DTS)	region 1
S10_111884517	chr 10	1.12E+08	9.00E-07	0.096154	0.09	1.833689	6	IA-TX(DTA)	region 1
S10_111884547	chr 10	1.12E+08	1.46E-05	0.092657	0.07	1.84829	5	IA-TX(DTS)	region 1
S10_111884547	chr 10	1.12E+08	2.15E-05	0.092657	0.06	1.830955	5	WI-TX(DTS)	region 1
S10_111884704	chr 10	1.12E+08	2.06E-07	0.096154	0.10	2.198075	7	IA-TX(DTS)	region 1
S10_111884704	chr 10	1.12E+08	1.26E-06	0.096154	0.08	2.067272	6	WI-TX(DTS)	region 1
S10_111884704	chr 10	1.12E+08	9.00E-07	0.096154	0.09	1.833689	6	IA-TX(DTA)	region 1
S10_111884737	chr 10	1.12E+08	1.03E-07	0.09965	0.10	2.220947	7	IA-TX(DTS)	region 1

S10_11188473 7	chr 10	1.12E+08	7.25E-07	0.09965	0.09	2.083911	6	WI-TX(DTS)	region 1
S10_11188473 7	chr 10	1.12E+08	4.78E-07	0.09965	0.09	1.853409	6	IA-TX(DTA)	region 1
S10_11188474 6	chr 10	1.12E+08	2.06E-07	0.096154	0.10	2.198075	7	IA-TX(DTS)	region 1
S10_11188474 6	chr 10	1.12E+08	1.26E-06	0.096154	0.08	2.067272	6	WI-TX(DTS)	region 1
S10_11188474 6	chr 10	1.12E+08	9.00E-07	0.096154	0.09	1.833689	6	IA-TX(DTA)	region 1
S10_11189525 8	chr 10	1.12E+08	1.20E-05	0.124126	0.07	1.613496	5	IA-TX(DTS)	region 1
S10_11189544 9	chr 10	1.12E+08	4.13E-06	0.146853	0.08	1.580242	5	IA-TX(DTS)	region 1
S10_11189544 9	chr 10	1.12E+08	7.60E-07	0.146853	0.09	1.72135	6	WI-TX(DTS)	region 1
S10_11189544 9	chr 10	1.12E+08	1.18E-05	0.146853	0.07	1.369344	5	WI-TX(DTA)	region 1
S10_11191648 4	chr 10	1.12E+08	1.59E-06	0.075175	0.08	2.196564	6	IA-TX(DTS)	region 1
S10_11191648 4	chr 10	1.12E+08	8.37E-06	0.075175	0.07	2.055889	5	WI-TX(DTS)	region 1
S10_11191648 4	chr 10	1.12E+08	2.35E-06	0.075175	0.08	1.90903	6	IA-TX(DTA)	region 1
S10_13066720 0	chr 10	1.31E+08	1.23E-07	0.06993	0.10	2.553994	7	IA-TX(DTS)	region 2
S10_13066720 0	chr 10	1.31E+08	3.76E-07	0.06993	0.09	2.476336	6	WI-TX(DTS)	region 2
S10_13066720 0	chr 10	1.31E+08	1.16E-06	0.06993	0.09	2.068337	6	IA-TX(DTA)	region 2
S10_13075392 3	chr 10	1.31E+08	2.58E-07	0.059441	0.10	2.636171	7	IA-TX(DTS)	region 2
S10_13075392 3	chr 10	1.31E+08	1.75E-05	0.059441	0.07	2.206329	5	WI-TX(DTS)	region 2
S10_13075392 3	chr 10	1.31E+08	2.35E-06	0.059441	0.08	2.128284	6	IA-TX(DTA)	region 2
S10_13075399 1	chr 10	1.31E+08	8.92E-07	0.066434	0.09	2.409553	6	IA-TX(DTS)	region 2
S10_13075399 1	chr 10	1.31E+08	2.73E-05	0.066434	0.06	2.067592	5	WI-TX(DTS)	region 2
S10_13075399 1	chr 10	1.31E+08	4.04E-06	0.066434	0.08	1.99344	5	IA-TX(DTA)	region 2
S10_13075422 7	chr 10	1.31E+08	4.32E-06	0.08042	0.08	2.06061	5	IA-TX(DTS)	region 2
S10_13075422 7	chr 10	1.31E+08	1.37E-05	0.08042	0.07	1.967651	5	WI-TX(DTS)	region 2
S10_13075456 6	chr 10	1.31E+08	4.32E-06	0.08042	0.08	2.06061	5	IA-TX(DTS)	region 2
S10_13075456 6	chr 10	1.31E+08	1.37E-05	0.08042	0.07	1.967651	5	WI-TX(DTS)	region 2
S10_13075527 0	chr 10	1.31E+08	5.28E-06	0.083916	0.07	2.010012	5	IA-TX(DTS)	region 2
S10_13075527 0	chr 10	1.31E+08	1.27E-05	0.083916	0.07	1.945471	5	WI-TX(DTS)	region 2
S10_13075555 2	chr 10	1.31E+08	1.43E-06	0.073427	0.08	2.27531	6	IA-TX(DTS)	region 2
S10_13075555 2	chr 10	1.31E+08	2.98E-05	0.073427	0.06	1.982115	5	WI-TX(DTS)	region 2
S10_13075555 2	chr 10	1.31E+08	1.28E-05	0.073427	0.07	1.814393	5	IA-TX(DTA)	region 2
S10_13075599 4	chr 10	1.31E+08	8.06E-07	0.076923	0.09	2.27241	6	IA-TX(DTS)	region 2
S10_13075599 4	chr 10	1.31E+08	7.00E-06	0.076923	0.07	2.085134	5	WI-TX(DTS)	region 2
S10_13075599 4	chr 10	1.31E+08	8.64E-06	0.076923	0.07	1.804646	5	IA-TX(DTA)	region 2
S10_13075722 7	chr 10	1.31E+08	2.74E-06	0.08042	0.08	2.125688	6	IA-TX(DTS)	region 2

S10_130757227	chr 10	1.31E+08	5.09E-06	0.08042	0.07	2.088513	5	WI-TX(DTS)	region 2
S10_130757227	chr 10	1.31E+08	2.82E-05	0.08042	0.06	1.672018	5	IA-TX(DTA)	region 2
S10_130757352	chr 10	1.31E+08	2.74E-06	0.08042	0.08	2.125688	6	IA-TX(DTS)	region 2
S10_130757352	chr 10	1.31E+08	5.09E-06	0.08042	0.07	2.088513	5	WI-TX(DTS)	region 2
S10_130757352	chr 10	1.31E+08	2.82E-05	0.08042	0.06	1.672018	5	IA-TX(DTA)	region 2
S10_132866091	chr 10	1.33E+08	3.79E-08	0.083916	0.11	2.424389	7	IA-TX(DTS)	region 2
S10_132866091	chr 10	1.33E+08	3.03E-07	0.083916	0.09	2.274439	7	WI-TX(DTS)	region 2
S10_132866091	chr 10	1.33E+08	1.83E-06	0.083916	0.08	1.847157	6	IA-TX(DTA)	region 2
S10_134812153	chr 10	1.35E+08	1.38E-05	0.083916	0.07	1.925201	5	IA-TX(DTS)	region 2
S10_134812153	chr 10	1.35E+08	1.74E-05	0.083916	0.07	1.922688	5	WI-TX(DTS)	region 2
S10_134812280	chr 10	1.35E+08	5.29E-06	0.066434	0.07	2.248143	5	IA-TX(DTS)	region 2
S10_134812280	chr 10	1.35E+08	2.25E-05	0.066434	0.06	2.111429	5	WI-TX(DTS)	region 2
S10_134812280	chr 10	1.35E+08	1.85E-05	0.066434	0.07	1.865982	5	IA-TX(DTA)	region 2

APPENDIX B

APPENDIX OF CHAPTER II

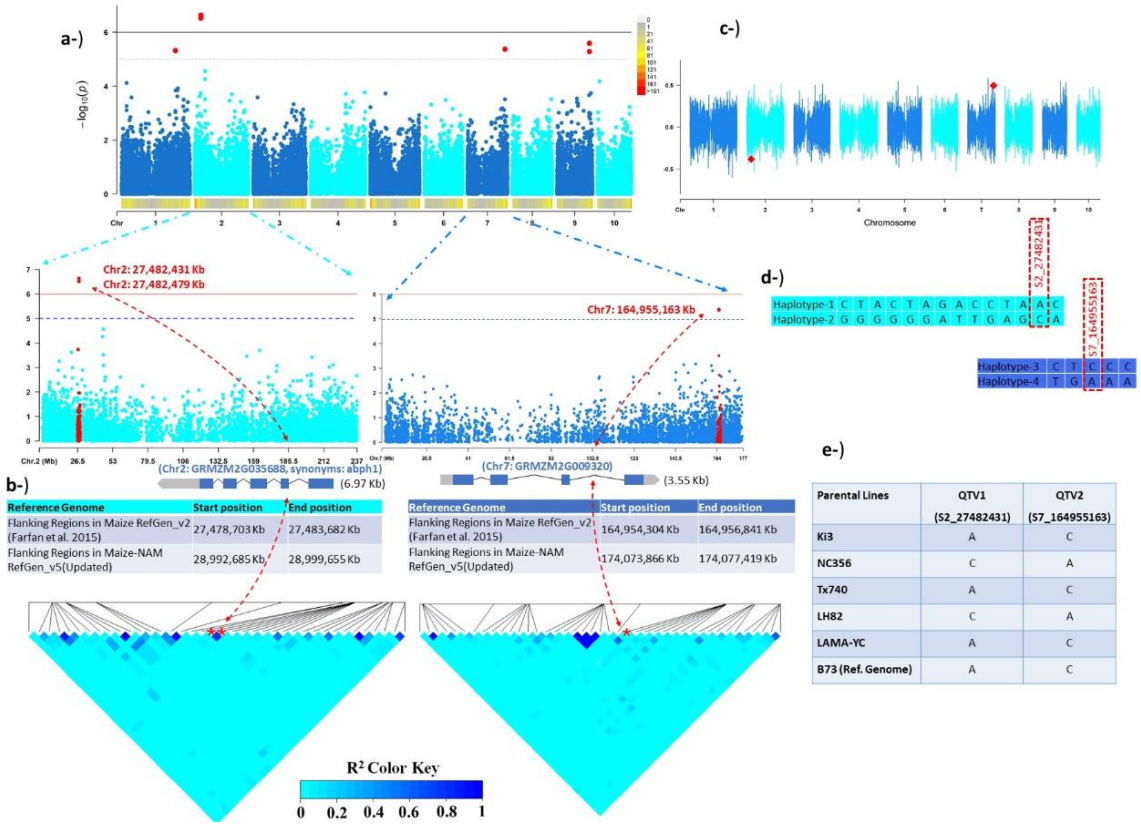

Figure S1. GWAS Manhattan plots, linkage disequilibrium of SNPs, allelic effects and parental sequences of previous work confirmed by this study. Previously, two SNPs were discovered for plant height as well as for yield using the plant height as a covariate in a GWAS study (Farfan *et al.* 2015) (a) Physical position of the two SNPs on Manhattan plot when plant height was included as a covariate in the model to predict yield. Zoom in figures of two SNPs on chromosomes 2 and 7 and lengths of the genes in kilobase pairs (Kb) (b) SNPs positions updated from maize-NAM reference genome version 5 were used to find linkage disequilibrium (LD) using R^2 values and flanking regions of the genes for the two SNPs. (c) Effects sizes for the two SNPs (tonne per hectare) (d) Polymorphic SNPs colocalized in LD blocks and haplotype variants based on two SNPs and (e) segregations of two SNPs in parental genotypes, advanced populations used in this study as follows: [LAMA (recurrent parent) x LH82], [Ki3 x NC356 (recurrent parent)], [Ki3 (recurrent parent) x NC356] and [Tx740 (recurrent parents) x NC356]. Reprinted from Adak, Conrad, et al., 2021.

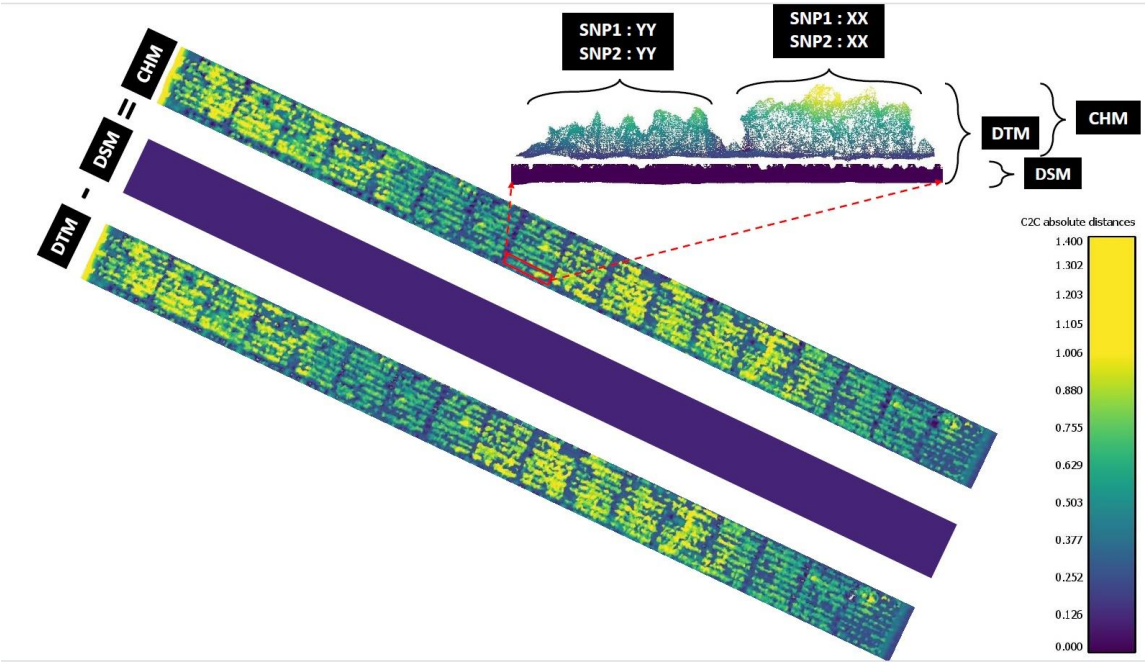

Figure S2. Illustrations of canopy height measurements (CHM) obtained by extracting the digital surface model (DSM) from digital terrain model (DTM). The orthomosaic obtained from the drone flight that was flown on 28.06.2019 is shown as an example in here. C2C (cloud to cloud) absolute distances (as meters unit) heatmap show the plant heights of HIFs in the point clouds of CHM after the extraction of point clouds of DSM from point clouds of DTM. Viridis color heatmap was used to illustrate the plant heights in the ranges and row plots as top view. The zoomed row plot illustrates the side view example of plant height differences between two heterogeneous inbred families developed from same population background comparatively; one of those has both favorable alleles (XX:XX; SNP1:SNP2), the other has unfavorable alleles (YY:YY; SNP1:SNP2). Reprinted from Adak, Conrad, et al., 2021.

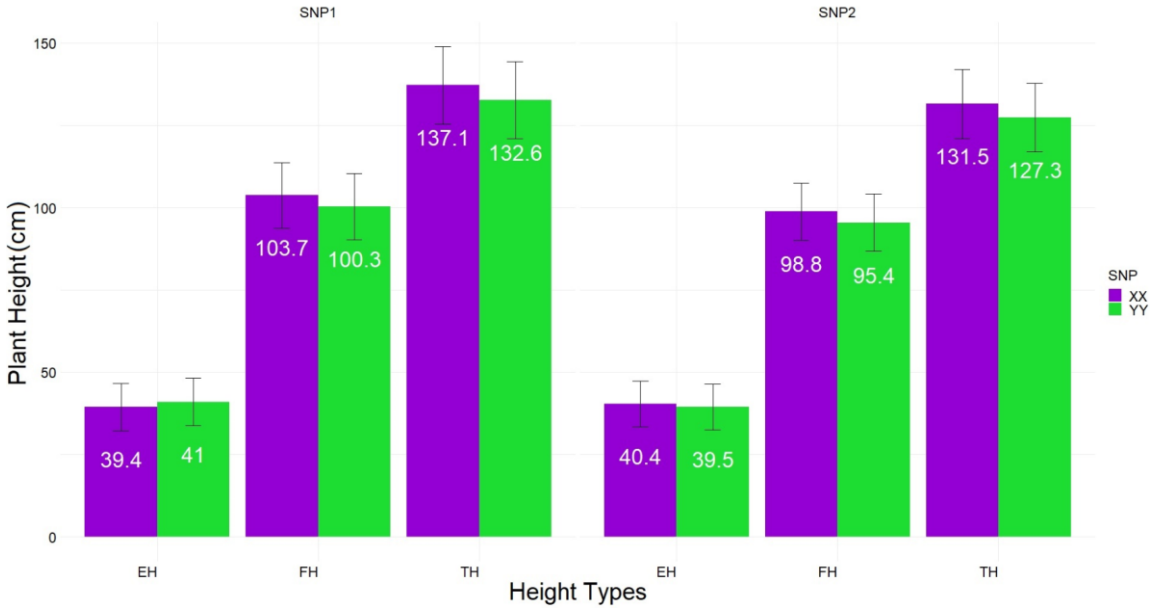

Figure S3. The BLUEs of SNP1 (left) and SNP2 (right) for all three ruler measures of plant height. BLUEs were obtained by Equation 2 ($SNP_j\ term$) demonstrating that favorable alleles (XX) contributed consistent taller height for all three ruler measures. TH, tip of tassel height; FH, flag leaf collar height; and EH, height of the first ear shank from ground on the x-axis. Whiskers represent the standard error. SNP1 was fixed as XX while SNP2 was segregating to be tested, SNP2 was fixed as XX while SNP1 was segregating to be tested in Equation 2. Reprinted from Adak, Conrad, et al., 2021.

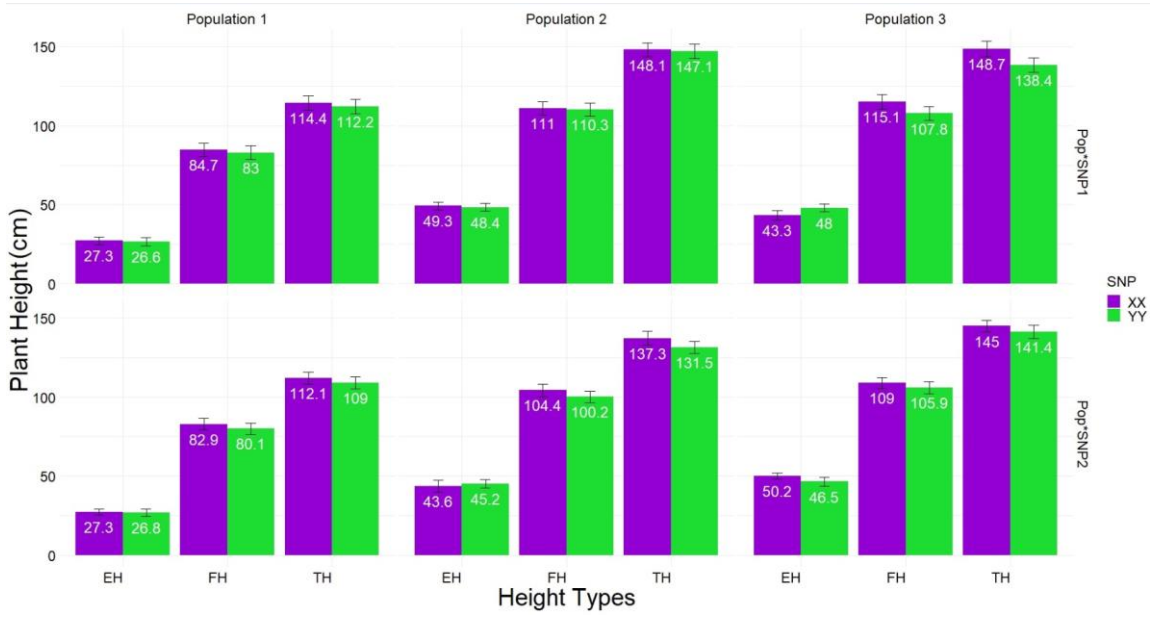

Figure S4. Interaction of SNP1*populations (top) and SNP2*populations (bottom) for three ruler measures of plant height. TH, tip of tassel height; FH, flag leaf collar height; and EH, height of the first ear shank from ground on the x-axis. Plant height was obtained from Equation 2 ($[Pop * SNP]_{ij}$ term) and show the largest differences for tassel height. Whiskers represent the standard error. Reprinted from Adak, Conrad, et al., 2021.

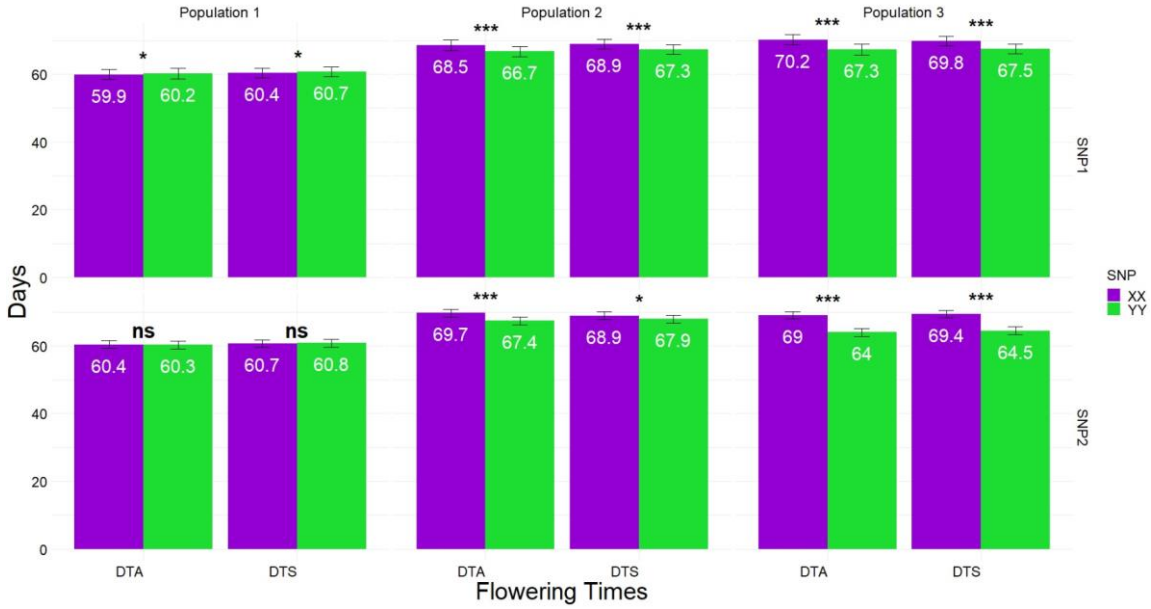

Figure S5. SNP1- and SNP2-population interactions for flowering DTA and DTS. Flowering BLUPs were obtained from Equation 2 ($[Pop * SNP]_{ij}$ term) for days after planting to 50% anthesis (DTA) and days to 50% silking (DTS). These demonstrated a much larger effect size on population 3. Each call of SNP1 and SNP2 were orthogonally contrasted within population for DTA and DTS. Whiskers represent the standard error. *, **, *** are the significance level of 0.05, 0.01 and 0.001 respectively. Reprinted from Adak, Conrad, et al., 2021.

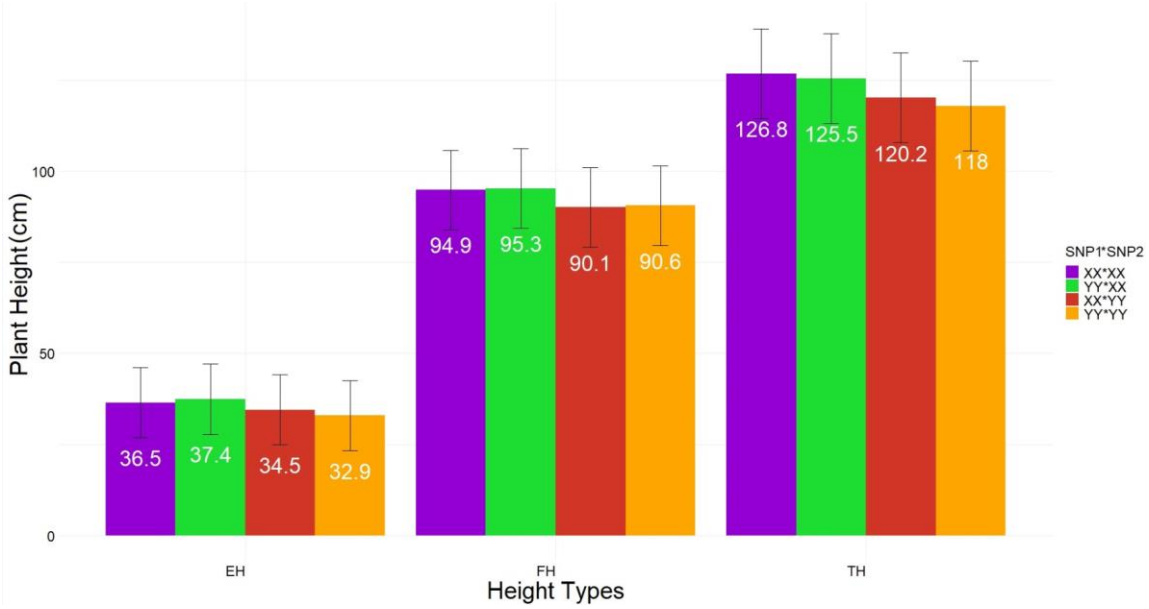

Figure S6. Interaction of SNP1-SNP2 $[SNP1 * SNP2]_{jk}$ estimated by Equation 3 for each of three ruler height measurements. TH, tip of tassel height; FH, flag leaf collar height; and EH, height of the first ear shank from ground on the x-axis. Combined favorable SNP1 and SNP2 loci (XX-XX) was taller than YY-YY combination in TH by as much as 8.8cm. Whiskers represent the standard error. Reprinted from Adak, Conrad, et al., 2021.

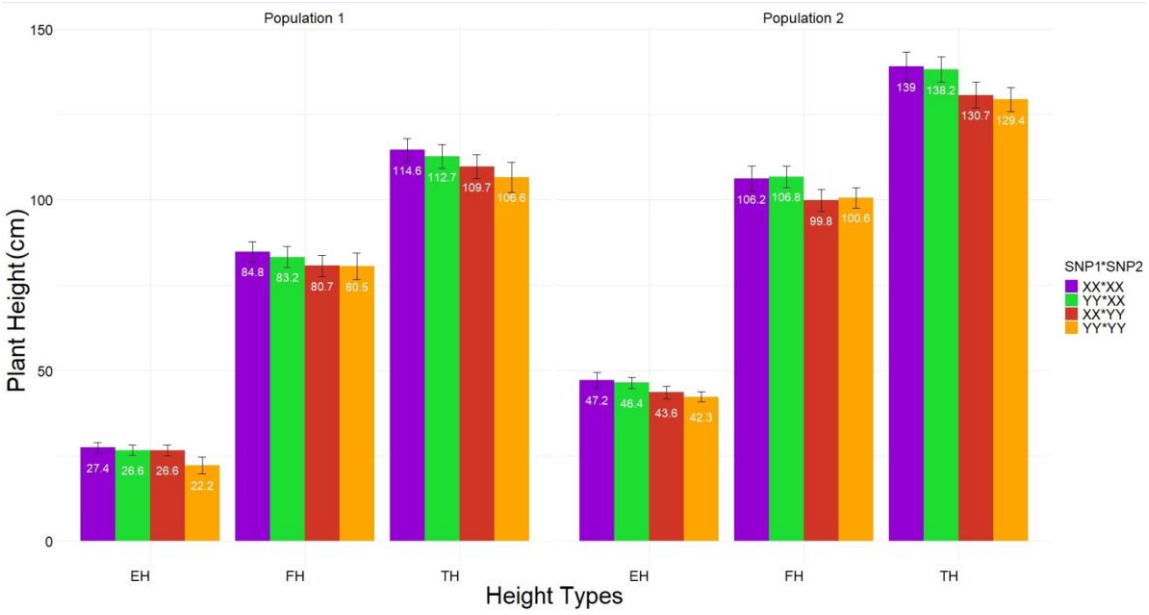

Figure S7. Combined interaction of SNPs with populations $[Pop * SNP1 * SNP2]_{ijk}$ for three ruler height measurements. TH, tip of tassel height; FH, flag leaf collar height;

and EH, height of the first ear shank from ground on the x-axis. Whiskers represent the standard error. Reprinted from Adak, Conrad, et al., 2021.

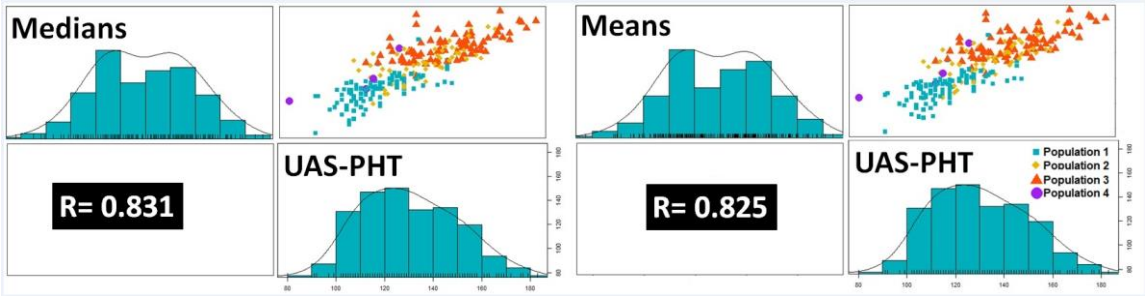

Figure S8. Pearson correlations (R) between UAS-PHT with ruler measured means (right) and medians (left) of HIF plots. Reprinted from Adak, Conrad, et al., 2021.

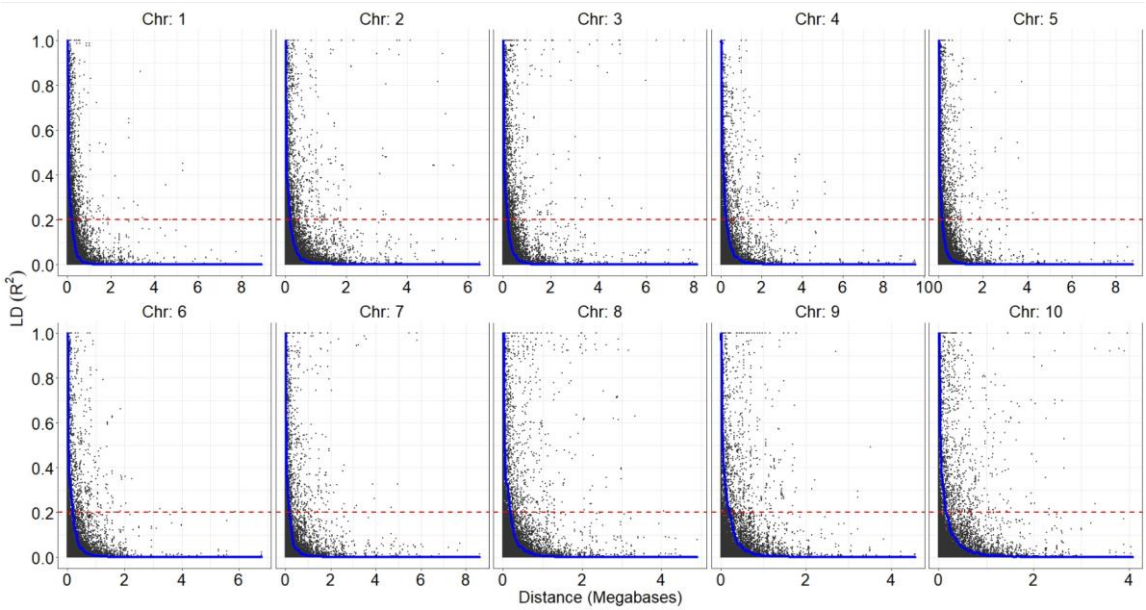

Figure S9. Linkage disequilibrium decay plots for each chromosome. Y axis represents the R^2 and x axis represents the distance as Megabases. Horizontal red dashed lines indicate the 0.2 R^2 that was used as cutoff value in determining the LD decay distances for all chromosomes. Blue line shows the LD decay through the distances. LD decay was found to be rapid for all chromosome and fluctuated between 1 to 6 kb. Reprinted from Adak, Conrad, et al., 2021.

APPENDIX C

APPENDIX OF CHAPTER III

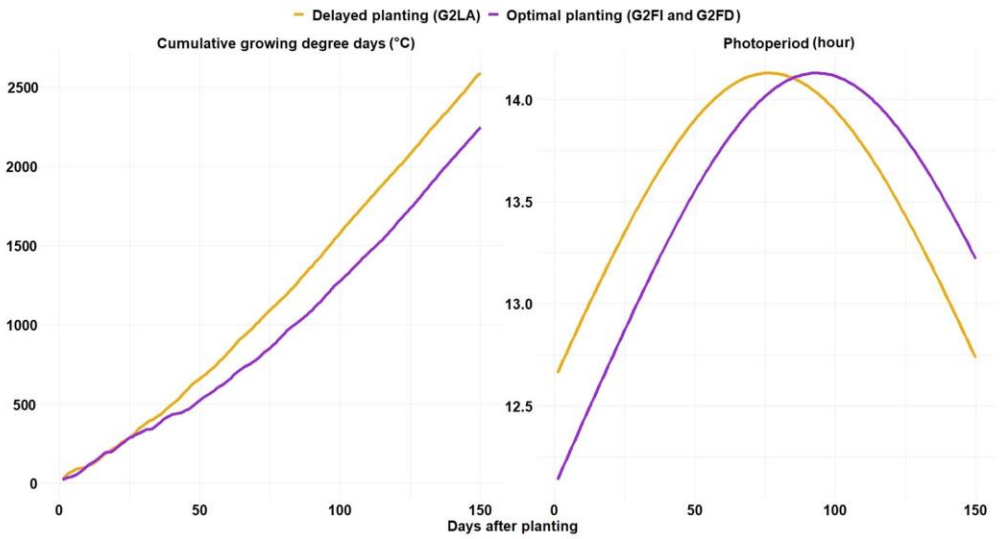

Supplemental Figure S1. Differences in growing degree day accumulation and photoperiod in the three trials. Reprinted from Adak, Murray, Anderson, et al., 2021.

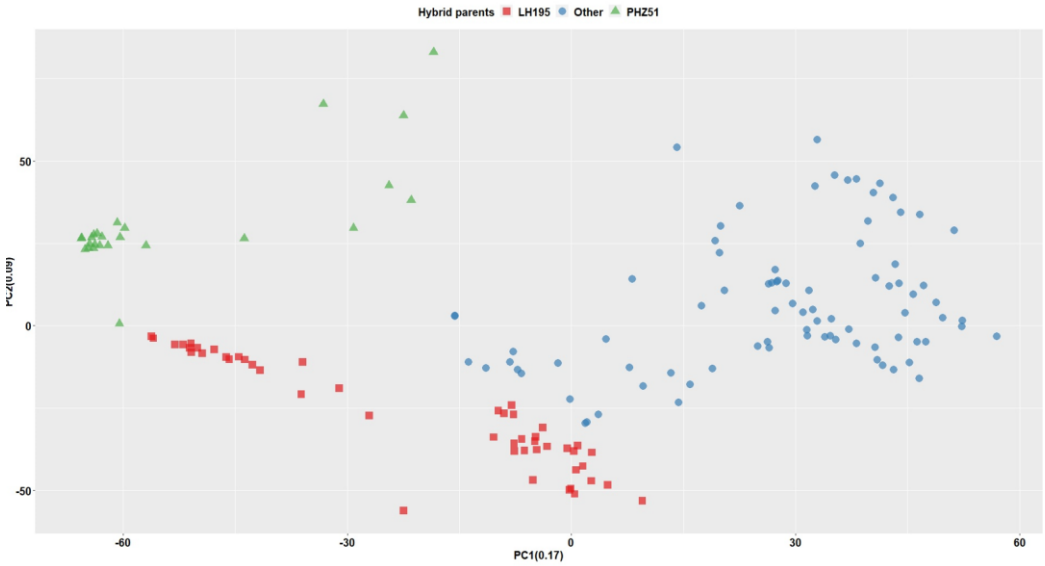

Supplemental Figure S2. Population structure of hybrids using 153,252 filtered SNPs belonging to the 158 hybrids with genotype information. Reprinted from Adak, Murray, Anderson, et al., 2021.

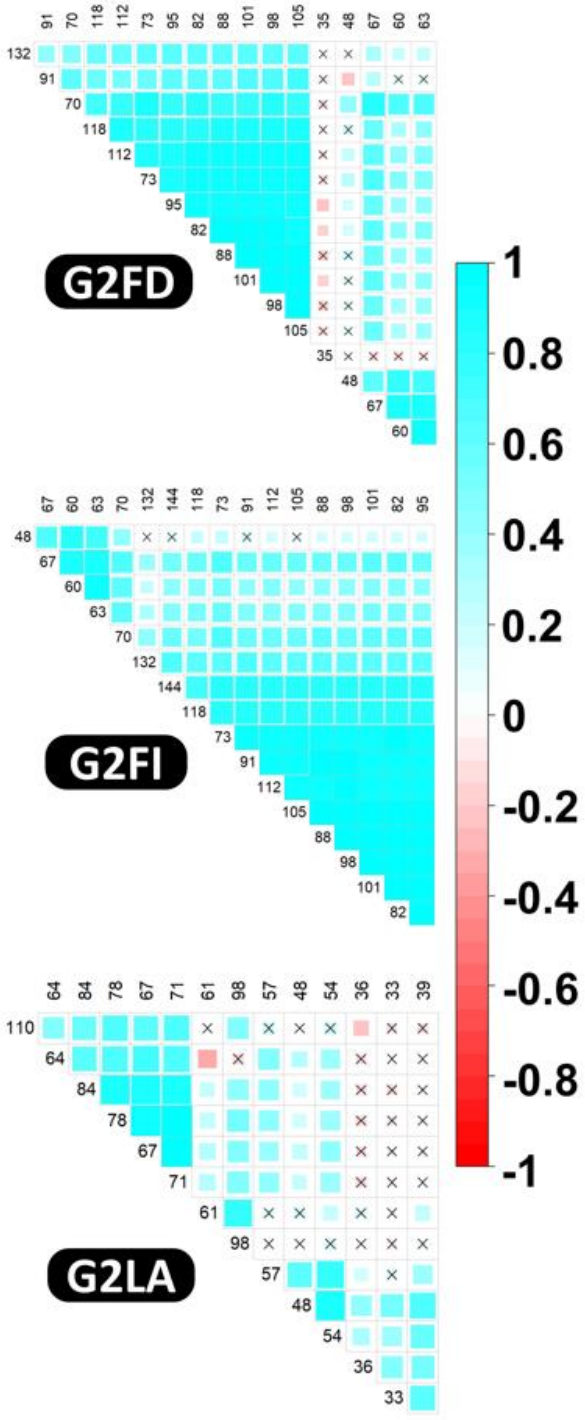

Supplemental Figure S3. Pearson correlation coefficients among the predicted plant heights (UAS_{PEBVs}) belonging to different flights of each trial. Reprinted from Adak, Murray, Anderson, et al., 2021.

Supplemental Table S1. contains the discovered SNPs (with p-values higher than FDR and Bonferonni threshold) in Manhattan plots in Figure 5 with their SNP names, chromosomes, physical positions (bp), p values, p values as -log100, minor allele frequencies (MAF), SNP effects, explained percent variances, flight times as DAP, trials, spanning regions, candidate genes and descriptions information respectively. Reprinted from Adak, Murray, Anderson, et al., 2021.

SNP name	Chromosome	Physicial position (bp)	P value	P Value (-log10)	Minor allele frequency (MAF)	Effect	Variance_Explained (percent)	Flight (DAS)	Trial	Spanning region of candidate gene	Candidate Gene	Description
S1_67250958	1	68394342	5.07E-10	9.29	0.34	-0.06	28.92	89	G2FD	(Chr1:68390923..68398129)	GRMZM2G004353	arginine/serine-rich 2
S1_74704365	1	76153056	6.85E-06	7.16	0.22	-0.06	68.05	95	G2FD	(Chr1:76150002..76162541)	GRMZM2G034442	Pathogenesis-related protein
S1_74704983	1	76153074	1.85E-12	11.73	0.22	0.08	53.34	73	G2FD	(Chr1:76150002..76162541)	GRMZM2G034442	Pathogenesis-related protein
S1_282688035	1	287796640	4.72E-09	8.33	0.41	-0.05	45.49	105	G2FD	(Chr1:287794751..287815169)	GRMZM2G022139	cytocolic purine 5-nucleotidase
S3_2276S3196	3	225334714	1.1E-25	24.96	0.06	0.00	0.01	35	G2FD	(Chr3: 225322949..225342279)	Zm00001d044329, brig1754	S-adenosyl-L-methionine-dependent methyltransferases superfamily protein
S4_18573017	4	18595623	2.77E-07	6.56	0.19	0.05	0.01	90	G2FD	(Chr4: 18595571..18598388)	GRMZM2G074924, wri2	VFIII transcription factor2
S5_4770003	5	4881308	1.43E-17	16.84	0.04	0.00	0.01	35	G2FD	(Chr5: 4875257..4880327)	GRMZM2G029370	unknown
S5_39820707	5	41053181	1.69E-29	28.72	0.03	0.00	0.01	35	G2FD	(Chr5: 41048500..41055727)	GRMZM2G048549	Calcium-binding EF-hand family protein
S7_5134206	7	5392803	2.39E-08	7.62	0.47	0.02	46.12	63	G2FD	(Chr7: 5386978..5400827)	GRMZM2G051114	IAP-like protein 1
S8_17108666	8	17625946	1.5E-11	10.81	0.23	-0.09	24.79	89	G2FD	(Chr8: 17625736..17626570)	GRMZM2G379035[pco008246 -]	Putative bifunctional inhibitor/L TP/seed storage protein family
S9_103070230	9	106870224	5.93E-09	7.23	0.13	0.06	0.21	73	G2FD	(Chr9: 106877295..106921620)	Zm00001d048807	unknown
S9_133736900	9	136190811	3.16E-08	7.50	0.41	-0.04	42.84	60	G2FD	(Chr9: 136190068..136193752)	Zm00001d047580	NAD(P)-binding Rossmann-fold superfamily protein
S9_139762759	9	142389817	6.79E-10	9.17	0.18	0.06	10.92	73	G2FD	(Chr9: 142387475..142394903)	GRMZM2G011426	Clustered-basidia protein-related protein 3B
S10_88760141	10	88844463	3.22E-23	22.49	0.04	0.00	0.00	35	G2FD	(Chr10: 88842539..88849374)	GRMZM2G422090	Probable GTP-binding protein DEGM mitochondrial
S10_88760038	10	88844460	3.22E-23	22.49	0.04	0.00	0.00	35	G2FD	(Chr10: 88842539..88849374)	GRMZM2G422090	Probable GTP-binding protein DEGM mitochondrial
S10_121647902	10	122398538	1.89E-23	22.74	0.01	0.66	96.66	91	G2FD	(Chr10:122395909..122920307)	GRMZM2G007426	Isotrim-related
S10_125905536	10	127077709	3.22E-23	22.49	0.04	0.00	0.01	35	G2FD	(Chr10: 127073834..127109248)	GRMZM2G162640	BTB/POZ domain-containing protein
S1_12645498	1	13867341	2.19E-07	6.68	0.22	0.04	41.09	95	G2FL	(Chr1: 13861800..13868602)	GRMZM2G004641, lsb64	BEL1-like homeodomain protein 2
S1_90905918	1	91893867	2.32E-11	10.63	0.25	-0.07	12.05	91	G2FL	(Chr1: 91889867..91892367)	GRMZM5G806839	AP2-EREBP-transcription factor 44
S1_90905918	1	91893893	3.32E-15	14.48	0.25	-0.08	15.21	101	G2FL	(Chr1: 91889867..91892367)	GRMZM5G806839	AP2-EREBP-transcription factor 44
S1_90074400	1	92056014	2.49E-09	8.60	0.24	0.06	10.57	89	G2FL	(Chr1: 91889867..91892367)	GRMZM5G806839	AP2-EREBP-transcription factor 44
S1_205638265	1	204145649	2.69E-09	8.70	0.46	0.05	43.09	90	G2FL	(Chr1: 204143639..204151448)	GRMZM2G016276	NEP-interacting protein 1
S1_205638265	1	204145649	3.69E-09	7.43	0.46	0.04	2.16	105	G2FL	(Chr1: 204143639..204151448)	GRMZM2G016276	NEP-interacting protein 1
S1_250667041	1	254169450	6.29E-09	8.20	0.27	-0.03	32.88	49	G2FL	(Chr1: 254163670..254170345)	GRMZM2G157470	methyl binding domain115
S1_28144189	1	286738454	2.2E-09	8.66	0.49	0.05	7.28	91	G2FL	(Chr1: 286736942..286743976)	GRMZM2G029286	Probable xyloglucan glycosyltransferase 12
S1_28144498	1	286738763	3.66E-09	7.44	0.09	-0.06	40.33	82	G2FL	(Chr1: 286736942..286743976)	GRMZM2G029286	Probable xyloglucan glycosyltransferase 12
S1_28144498	1	286738763	5.29E-12	11.28	0.09	-0.09	9.92	101	G2FL	(Chr1: 286736942..286743976)	GRMZM2G029286	Probable xyloglucan glycosyltransferase 12
S3_132394105	3	132997092	2.09E-08	7.70	0.16	0.04	53.15	63	G2FL	(Chr3: 132995199..132999807)	GRMZM2G064015	unknown
S3_168449495	3	169072334	4.1E-08	7.39	0.32	-0.01	30.06	79	G2FL	(Chr3: 169070073..169076750)	GRMZM2G184873	bHLH transcription factor 132
S3_23577991	3	223245535	5.11E-08	7.29	0.08	-0.06	7.89	91	G2FL	(Chr3: 223240508..223247569)	GRMZM2G077693, umc2152	Protein indeterminate-domain 9
S4_166295252	4	168809396	2.09E-07	6.70	0.19	-0.05	9.71	91	G2FL	(Chr4: 168805861..168812355)	GRMZM2G394528	Probable methyltransferase PMT15
S4_218940914	4	223205547	2.3E-08	7.64	0.16	0.05	11.31	105	G2FL	(Chr4:223202432..223206669)	LOC103654675,GRMZM2G187126	unknown
S5_4499406	5	4605467	5.11E-08	7.29	0.01	0.14	30.59	101	G2FL	(Chr5: 4599612..4607469)	GRMZM2G007260	Ubiquitin-conjugating enzyme E2 2
S5_53943433	5	60955783	7.53E-08	7.12	0.19	0.05	63.78	119	G2FL	(Chr5: 60953111..60958937)	GRMZM2G105570	Peptidyl-prolyl cis-trans isomerase CYP20-1
S5_19588809	5	19938639	1.03E-09	8.99	0.26	0.05	29.09	132	G2FL	(Chr5: 19523979..19534194)	GRMZM2G154428 [pip2d - plasma membrane intrinsic protein2]	Aquaporin PIP2-4
S5_21384268	5	21971868	2.09E-07	6.68	0.40	-0.04	14.73	89	G2FL	(Chr5: 21971868..21972092)	GRMZM2G075978 (mcm5 - minichromosome maintenance5)	DNA replication licensing factor MCM5
S6_31708395	6	33194331	9.51E-06	7.02	0.12	-0.05	0.54	73	G2FL	(Chr6: 33192023..33196650)	GRMZM2G059412 (jac1 - jacalin1)	Expressed protein; Mannose-specific jacalin-related lectin; protein
S6_105159728	6	106552216	1.41E-09	8.85	0.05	-0.09	12.36	89	G2FL	(Chr6: 106546395..106550411)	Zm00001d036394	Protein trichome birefringence-like 16
S6_105159728	6	106552216	6.00E-13	12.22	0.05	-0.09	11.22	105	G2FL	(Chr6: 106546395..106550411)	Zm00001d036394	Protein trichome birefringence-like 16
S6_105159728	6	106552216	3.2E-08	7.49	0.05	-0.09	2.94	112	G2FL	(Chr6: 106546395..106550411)	Zm00001d036394	Protein trichome birefringence-like 16
S6_109613392	6	114214670	1.79E-07	6.75	0.45	-0.04	13.71	112	G2FL	(Chr6: 114213941..114218713)	GRMZM2G009958 (gbp#10 - GeBP-transcription factor 10)	GeBP-transcription factor 10
S7_65707706	7	68533723	7.99E-11	10.10	0.45	-0.05	5.11	95	G2FL	(Chr7: 68531502..68551160)	GRMZM2G126170	Protein SAVADEE HOMEODOMAIN HOMOLOG 2
S7_92393340	7	95253631	1.39E-12	11.86	0.23	-0.07	0.01	95	G2FL	(Chr7: 95250565..95255556)	GRMZM2G031915 (wrky37 - WRKY-transcription factor 37)	WRKY74-superfamily of TFs having WRKY and zinc finger domains
S7_112625307	7	115913254	3.46E-09	8.46	0.35	0.03	13.98	48	G2FL	(Chr7: 115910023..115922358)	GRMZM2G071112	Mini zinc finger 3
S7_14114206	7	14604206	2.23E-06	7.65	0.25	-0.04	6.88	112	G2FL	(Chr7: 14603705..14604007)	GRMZM2G066946 (ereb115 - AP2-EREBP-transcription factor 115)	Dehydration-responsive element-binding protein 1B
S9_143940859	9	144518146	5.29E-09	7.27	0.12	0.08	8.23	132	G2FL	(Chr9: 144505373..144514252)	GRMZM2G445763	65-kDa microtubule-associated protein 1
S10_150107267	10	150847940	5.17E-10	9.29	0.16	0.07	3.35	105	G2FL	(Chr10: 150823979..150835283)	GRMZM2G178025	Glycoside transferase/s2C sle-hairpin/s2C subgroup
S1_14603778	1	15010061	3.17E-08	7.50	0.02	0.16	70.49	71	G2LA	(Chr1: 15010049..15015396)	GRMZM2G052807	Ribosomal L18p/L5e family protein
S1_37778525	1	38082539	9.09E-10	9.04	0.01	-0.15	78.79	49	G2LA	(Chr1: 38078922..38092626)	GRMZM2G087251, ereb4	Ethylene-responsive transcription factor ERF094
S1_74704983	1	76153074	3.56E-09	8.02	0.22	0.09	41.77	67	G2LA	(Chr1: 76150002..76162541)	GRMZM2G034442	Pathogenesis-related protein
S1_282688035	1	287796640	1.61E-12	11.79	0.41	-0.09	14.76	67	G2LA	(Chr1: 287794751..287815169)	GRMZM2G022139	cytocolic purine 5-nucleotidase
S1_295691579	1	300608847	2.95E-06	7.53	0.05	-0.47	46.26	61	G2LA	(Chr1: 300600139..300611199)	GRMZM2G122148 [cl35795_1 -]	S-adenosyl-L-methionine-dependent methyltransferases superfamily protein
S4_193350893	4	197684625	1.47E-07	6.83	0.36	-0.32	0.16	61	G2LA	(Chr4: 197663764..197670265)	GRMZM2G036805	Probable protein S-acyltransferase 7
S5_77436213	5	79757266	3.44E-09	8.46	0.07	0.03	13.04	36	G2LA	(Chr5: 60953111..60958937)	GRMZM5G805495	leucine-rich repeat/extensin 2
S6_112004339	6	115048918	1.53E-15	14.82	0.11	-0.17	3.65	94	G2LA	(Chr6: 115046518..115053902)	GRMZM2G073700	Probable RNA-binding protein ARP1
S6_130286758	6	142627909	1.30E-07	6.88	0.07	0.03	22.34	36	G2LA	(Chr6: 142625143..142629759)	GRMZM2G447480	unknown
S6_162133980	6	166326767	1.85E-08	7.73	0.08	0.72	15.62	61	G2LA	(Chr6: 166323183..166339150)	GRMZM2G174749 (rcc4 - regulator of chromosome condensation 4)	Putative regulator of chromosome condensation (RCC1) family protein
S8_157300725	8	162948889	7.06E-10	9.15	0.15	-0.10	9.07	84	G2LA	(Chr8: 162141480..162147756)	GRMZM2G178836	Bzip transcription factor-like protein
S8_22782253	9	22643943	2.44E-10	9.61	0.09	0.12	16.16	84	G2LA	(Chr9: 22639403..22644985)	GRMZM2G033208	translocase 1
S9_103956817	9	107407460	1.03E-06	7.99	0.20	0.07	31.78	84	G2LA	(Chr9: 107403627..107409503)	GRMZM2G054093	unknown
S10_120792271	10	121898523	1.69E-14	13.80	0.04	0.66	2.02	61	G2LA	(Chr10: 121894503..121899804)	GRMZM5G859456	Fucosyltransferase 7
S10_139079346	10	140334316	5.47E-09	8.26	0.15	0.14	17.03	110	G2LA	(Chr10: 140332412..140338285)	Zm00001d026170 (sbp21 - SBP-transcription factor 21)	Squamosa promoter-binding protein-like (SBP domain) transcription factor family protein
S10_142824823	10	143602491	2.28E-09	8.64	0.41	0.47	0.01	61	G2LA	(Chr10:143599892..143602669)	GRMZM2G029478	F-box domain containing protein

APPENDIX D

APPENDIX OF CHAPTER V

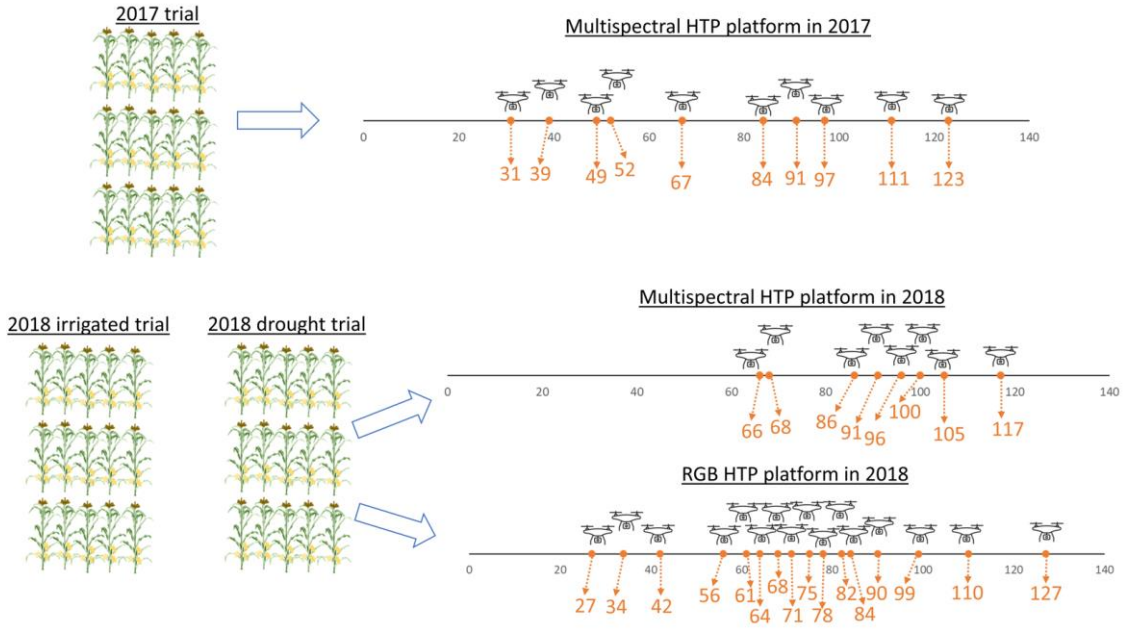

Supplementary Figure 1 The high throughput phenotyping platforms (HTP) that were conducted in 2017 and 2018 (both irrigated and drought). Drones equipped with RGB camera was flown over 2018 drought and irrigated trials with 16 flights. Drones equipped with multispectral camera was flown over 2017 with 10 flights and 8 flights over 2018 (both irrigated and drought) trials. Timeline of HTP shows the flight dates as days after planting times indicated by orange points with orange numbers.

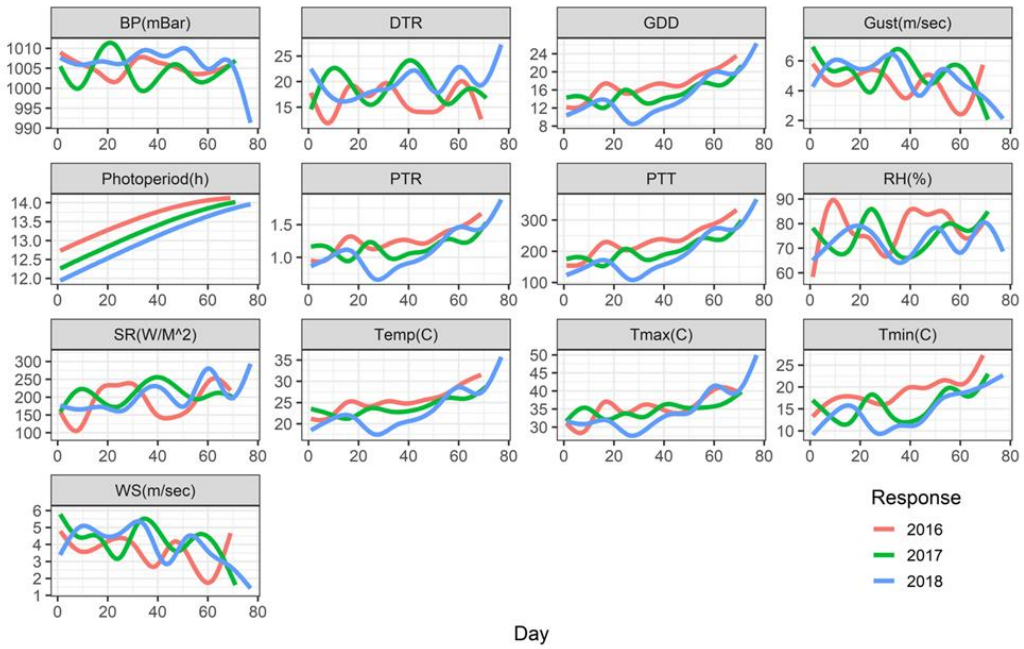

Supplementary Figure 2 shows the 13 environmental parameters belonging to planting times to mean days to anthesis belonging to trials grown in 2016, 2017 and 2018. The X axis represents the days after planting, the Y axis represents the value of the environmental paramants that were collected at 10-minute increments. A smoothing function was applied to all environmental parameters to reveal the trend across growth.

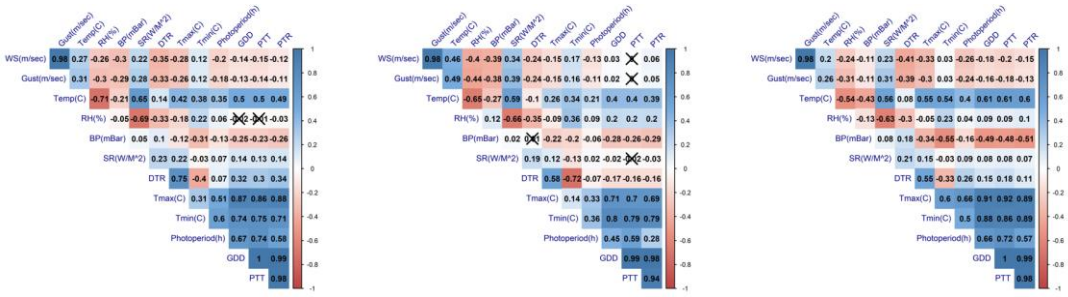

Supplementary Figure 3 correlation of the 13 environmental parameters for trials grown in 2016 (left), 2017 (middle) and 2018 (right). No significant correlation according to the 0.05 level is marked with an '×'.

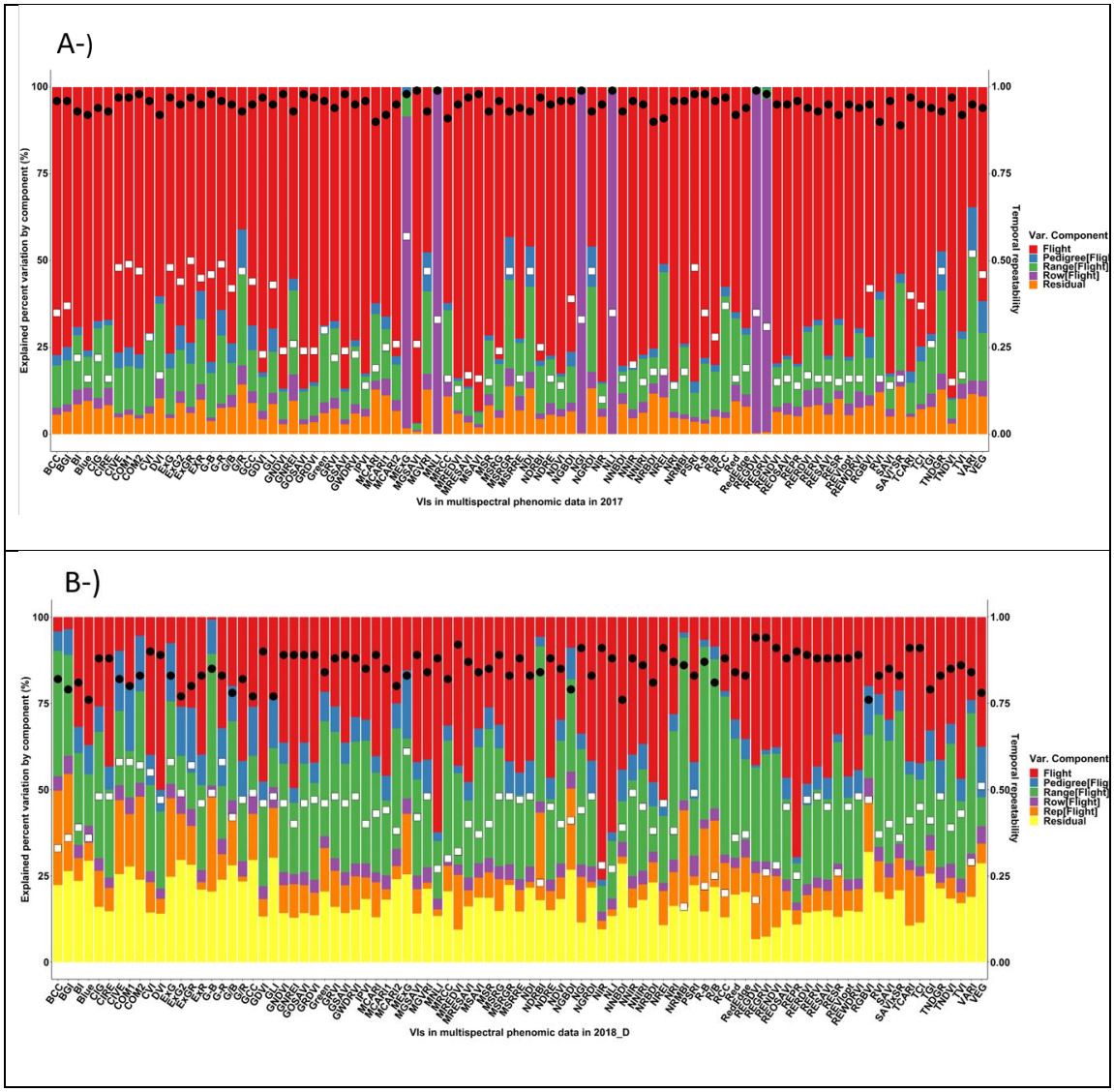
A-)
Explained percent variation by component (%)
Temporal repeatability
Var. Component
Flight
Pedigree[Flig
Range[Flight]
Row[Flight]
Residual
VIs in multispectral phenomic data in 2017
B-)
Explained percent variation by component (%)
Temporal repeatability
Var. Component
Flight
Pedigree[Flig
Range[Flight]
Row[Flight]
Rep[Flight]
Residual
VIs in multispectral phenomic data in 2018_D

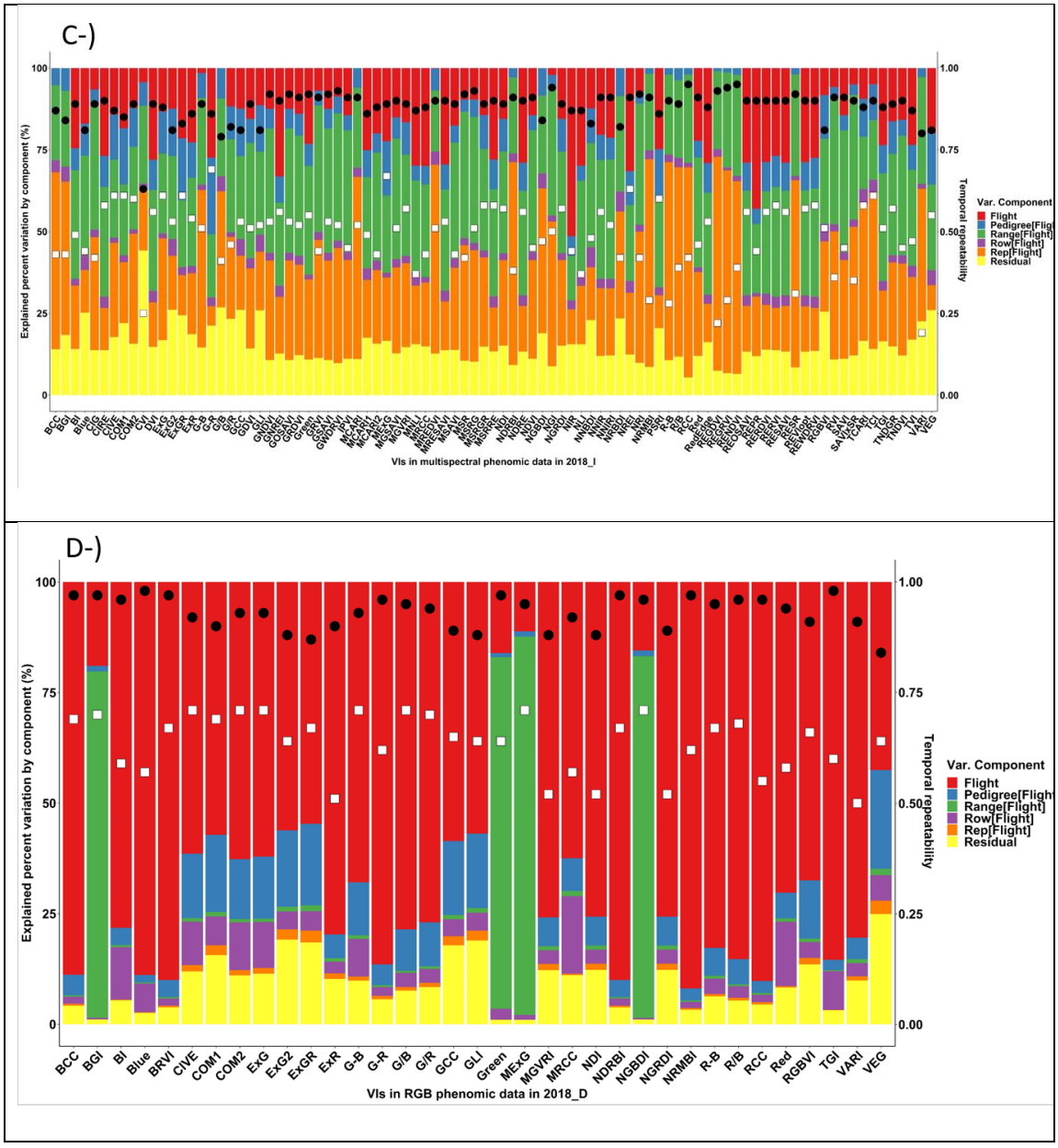
C-)
Explained percent variation by component (%)
Temporal repeatability
Var. Component
Flight
Pedigree[Flig
Range[Flight]
Row[Flight]
Rep[Flight]
Residual
VIs in multispectral phenomic data in 2018_I
D-)
Explained percent variation by component (%)
Temporal repeatability
Var. Component
Flight
Pedigree[Flight
Range[Flight]
Row[Flight]
Rep[Flight]
Residual
BCC BGI BI Blue BRVI CIVE COM1 COM2 ExG ExG2 ExGR ExR G-B G-R G/B G/R GCC GLI Green MExG MGVRI MRCC NDI NDRBI NGBDI NGRDI NRMBI R-B R/B RCC Red RGBVI TGI VARI VEG
VIs in RGB phenomic data in 2018_D

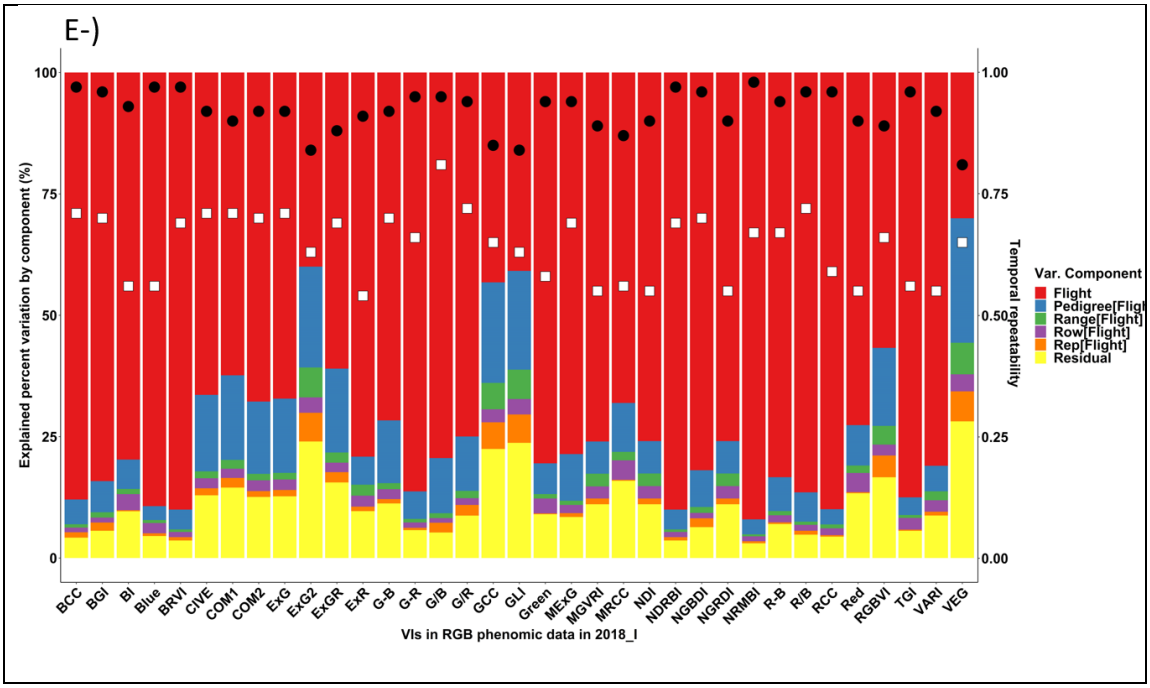

Supplementary data 1. Stack bar plot shows the explained percent variation by each component in the nested design (equation 1, Eq. 1) for the RGB and multispectral phenomic data in 2017 and 2018. Left Y axis show the explained percent variation and right Y axis show the R-squared (black round) and temporal heritability (white square). X axis show the vegetation indices. A-) results of the multispectral data in 2017 trial, (B) the results of the multispectral data in 2018_D trial, (C) the results of the multispectral data in 2018_I trial, (D) the results of the RGB phenomic data in 2018_D and (E) the results of the RGB phenomic data in 2018_I.

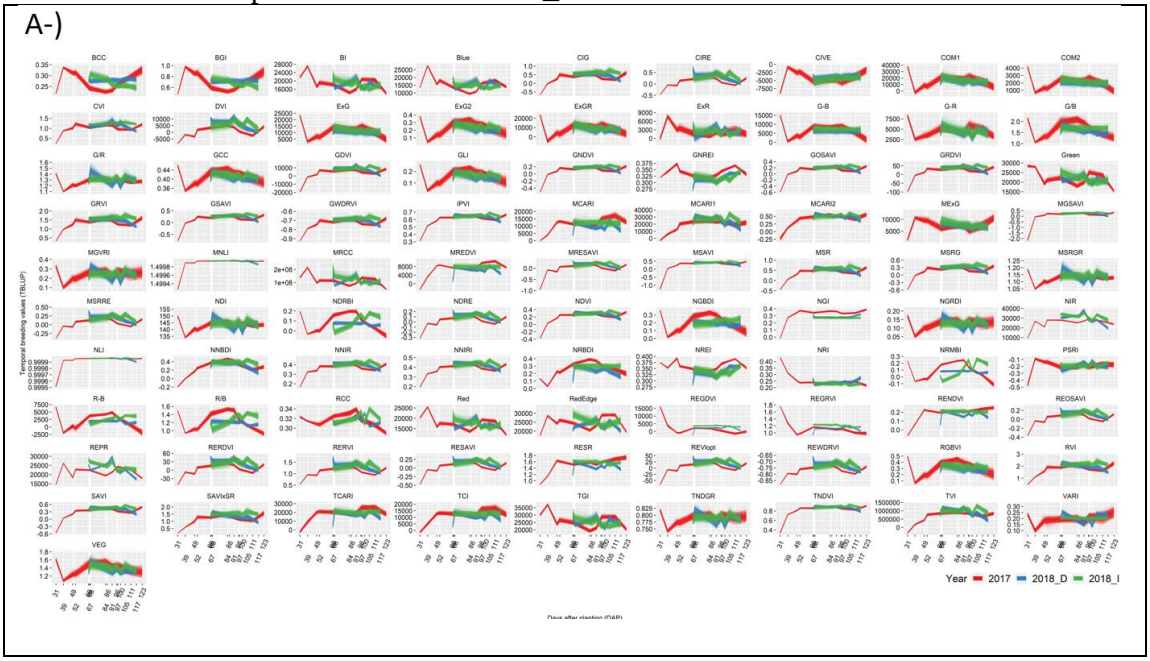

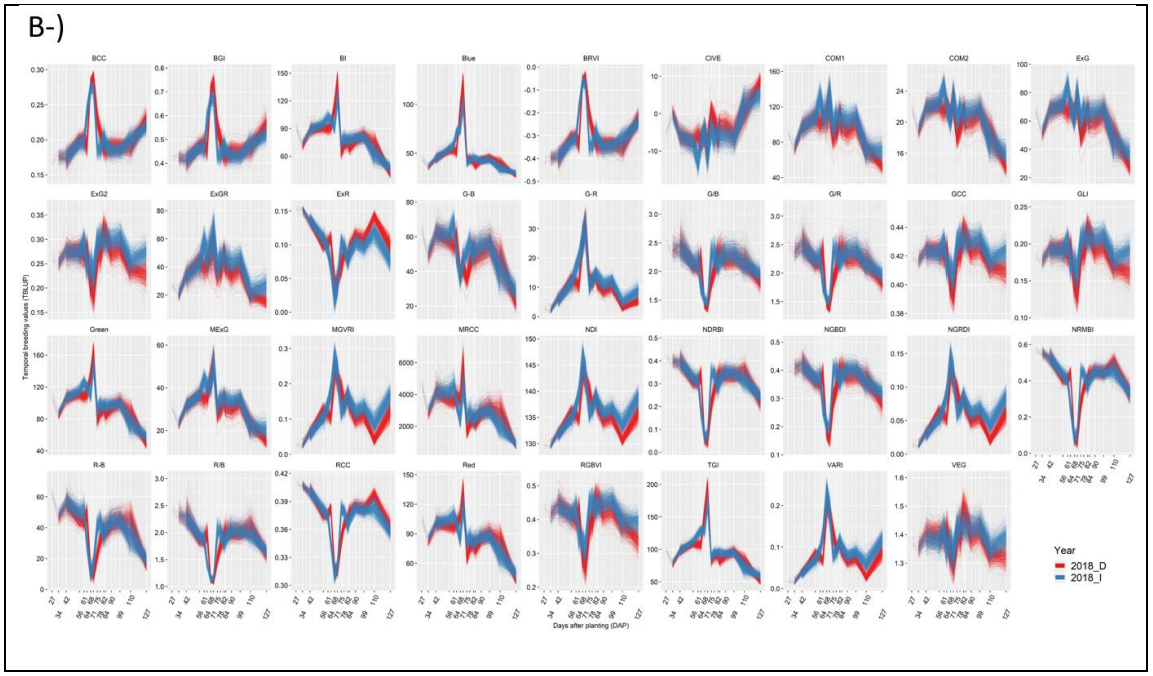

Supplementary data 2. Temporal breeding values for each RIL predicted by the pedigree nested within flight component in nested design (equation 1, Eq. 1). (A) Temporal breeding values of RILs for each VI in multispectral phenomic data in 2017, 2018_D and 2018_I. (B) temporal breeding values of RILs for each VI in RGB phenomic data in 2018_I and 2018_D.

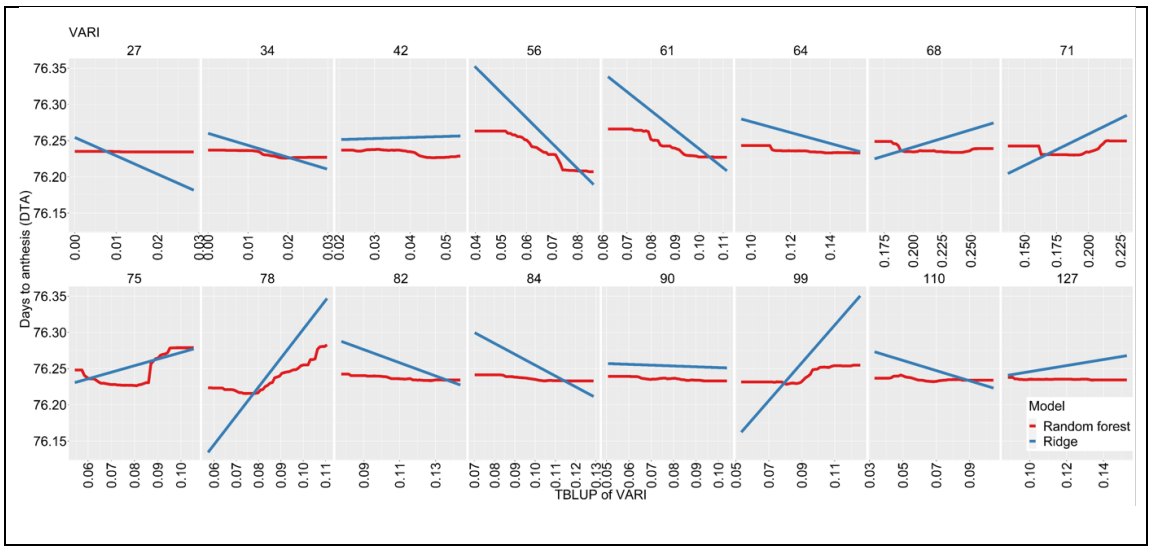

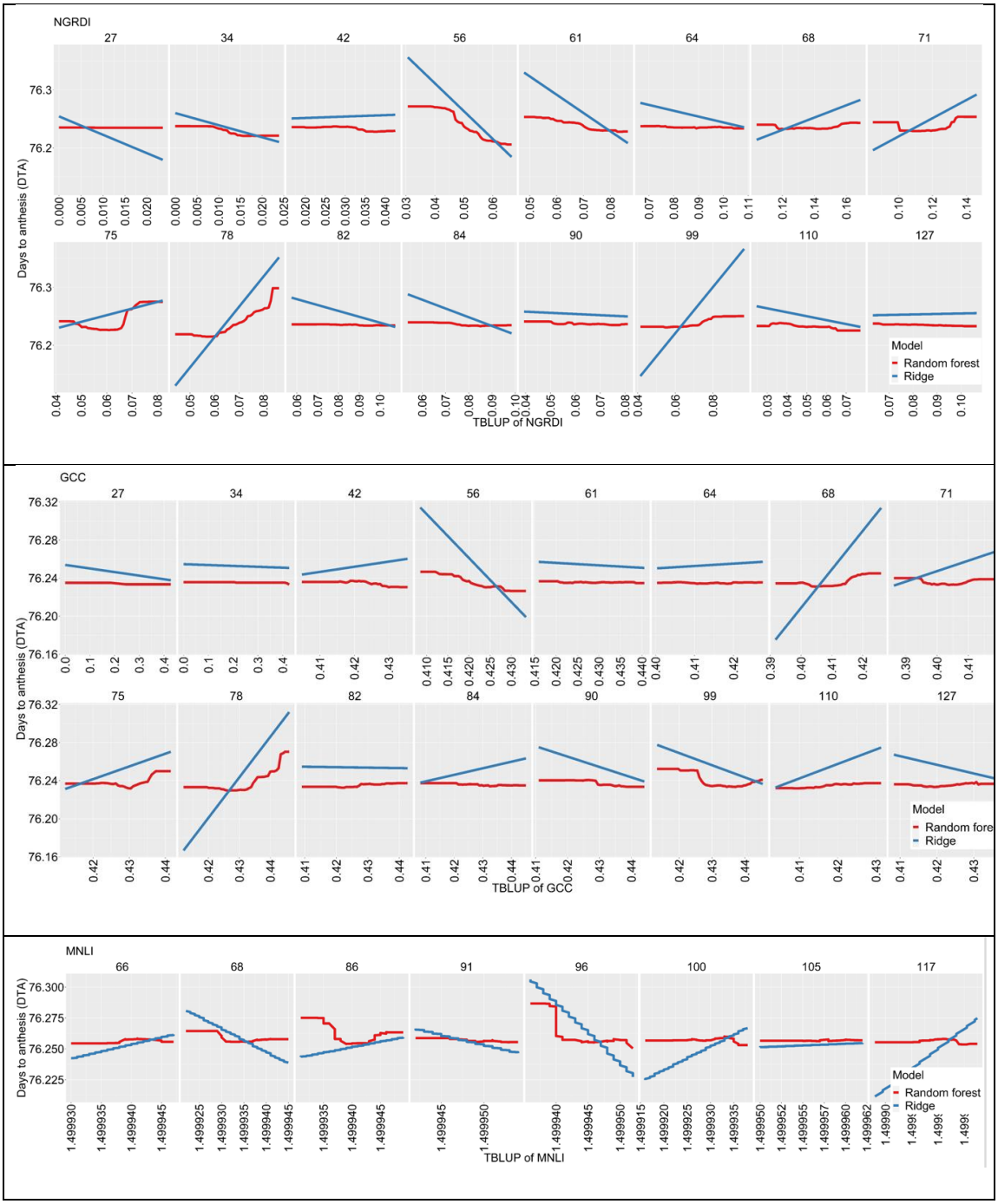

Supplementary data 3. Partial dependence plots between each temporal value (from 27 to 127 days after planting) of GCC, NGRDI, VARI in RGB phenomic data and predicted days to anthesis (DTA) by ridge (blue line) and random forest (red line) regressions. Partial dependence plots between each temporal value (from 66 to 117 days after planting) of MNLI in multispectral phenomic data and predicted days to anthesis (DTA) by ridge (blue line) and random forest (red line) regressions.

Supplementary table 1 shows the vegetation indices used and their formulas along with references.

Vegetation index	Ratios	References
VIs derived from RGB bands		
Blue chromatic coordinate index (BCC)	$B/(R+G+B)$	(Woebbecke et al., 1995)
Blue green pigment index (BGI)	B/G	(Zarco-Tejada et al., 2005)
Brightness index (BI)	$sqrt((R\hat{}2+G\hat{}2+B\hat{}2)/3)$	(Richardson & Wiegand, 1977)
Blue-red vegetation index (BRVI)	$(B-R)/(B+R)$	(Hunt et al., 2005)
Color index of vegetation extraction (CIVE)	$0.441R-0.811G+0.385B+18.78745$	(Kataoka, Kaneko, Okamoto, & Hata, 2003)
Combined indices 1 (COM1)	$EXG+CIVE+EXGR+VEG$	(Guijarro et al., 2011)
Combined indices 2 (COM2)	$0.36EXG+0.47CIVE+0.17VEG$	(Guerrero, Pajares, Montalvo, Romeo, & Guijarro, 2012)
Excessive green (EXG)	$2G-R-B$	(Woebbecke et al., 1995)
Normalized Excess green index (EXG2)	$\frac{2G-R-B}{G+R+B}$	(Woebbecke et al., 1995)
Excess green minus excess red index (EXGR)	$3G-2.4R-B$	(G. E. Meyer & Neto, 2008)
Excessive red (EXR)	$1.4R-G$	(G. Meyer, Hindman, & Laksmi, 1998)
Green minus blue index (G-B)	$G-B$	(Woebbecke et al., 1995)
Green minus red index (G-R)	$G-R$	(Woebbecke et al., 1995)
Green blue simple ratio index (G/B)	G/B	(Woebbecke et al., 1995)
Green red simple ratio index (G/R)	G/R	(Woebbecke et al., 1995)
Green chromatic coordinate index (GCC)	$G/(R+G+B)$	(Woebbecke et al., 1995)
Green leaf index (GLI)	$(2G-R-B)/(2G+R+B)$	(Louhaichi et al., 2001)
Modified excess green index (MExG)	$1.262G-0.884R-0.311B$	(Burgos-Artizzu, Ribeiro, Guijarro, & Pajares, 2011)
Modified green red index (MGVRI)	$(G\hat{}2-R\hat{}2)/(G\hat{}2+R\hat{}2)$	(Bendig et al., 2015)
Modified red chromatic coordinate index (MRCC)	$R\hat{}3/(R+G+B)$	Created in this study
Normalized difference index (NDI)	$128*((((G-R))/((G+R)))+1)$	(G. E. Meyer & Neto, 2008)
Normalized difference red blue index (NDRBI)	$(R-B)/(R+B)$	(Golzarian & Frick, 2011)
Normalized green-blue difference index (NGBDI)	$(G-B)/(G+B)$	(Hunt et al., 2005)
Normalized green red difference index (NGRDI)	$(G-R)/(G+R)$	(Tucker, 1979)
Normalized red minus blue index (NRMBI)	$(R-B)/G$	Created in this study
Red minus blue index (R-B)	$R-B$	(Woebbecke et al., 1995)
Red blue simple ratio index (R/B)	R/B	(Woebbecke et al., 1995)
Red chromatic coordinate index (RCC)	$R/(R+G+B)$	(Woebbecke et al., 1995)
Red green blue index (RGBVI)	$(G\hat{}2-R*B)/(G\hat{}2+R*B)$	(Bendig et al., 2015)
Triangular greenery index (TGI)	$G-(0.39R-0.69B)$	(Hunt, Daughtry, Eitel, & Long, 2011)

Visible atmospherically resistant index (VARI)	$(G - R)/(G + R - B)$	(Gitelson et al., 2002)
Vegetativen (VEG)	$G/(R\text{^}0.667 * B\text{^}0.334)$	(Hague et al., 2006)
VIs derived from multispectral bands (RGB, red-edge and NIR bands)		
Chlorophyll vegetation index-green (CIG)	$NIR/G - 1$	(Gitelson, Vina, Ciganda, Rundquist, & Arkebauer, 2005)
Chlorophyll vegetation index-red edge (CIRE)	$NIR/RE - 1$	(Gitelson et al., 2005)
Chlorophyll vegetation index (CVI)	$(NIR * R)/G\text{^}2$	(Vincini, Frazzi, & D'Alessio, 2008)
Difference vegetation index (DVI)	$NIR - RE$	(Tucker, 1979)
Enhanced normalized difference vegetation index (ENDVI)	$(NIR + G - 2B)/(NIR + G + 2B)$	Maxmax 2015 (http://www.maxmax.com/endvi.htm)
Enhanced vegetation index (EVI)	$2.5(NIR - R)/(NIR + 6R - 7.5B + 1)$	(A. Huete et al., 2002)
Green difference vegetation index (GDVI)	$NIR - G$	(Tucker, 1979)
Green normalized difference vegetation index (GNDVI)	$(NIR - G)/(NIR + G)$	(Gitelson, Kaufman, & Merzlyak, 1996)
GNREI		
Green optimal soil adjusted vegetation index (GOSAVI)	$(1 + 0.16)(NIR - G)/(NIR + G + 0.16)$	(Rondeaux, Steven, & Baret, 1996)
Green re-normalized different vegetation index (GRDVI)	$(NIR - G)/sqrt(NIR + G)$	(Roujean & Breon, 1995)
Green ratio vegetation index (GRVI)	NIR/G	(Buschmann & Nagel, 1993)
Green soil adjusted vegetation index (GSAVI)	$1.5((NIR - G)/(NIR + G + 0.5))$	(Sripada, Heiniger, White, & Meijer, 2006)
Green wide dynamic range vegetation index (GWDRVI)	$(0.12NIR - G)/(0.12NIR + G)$	(Gitelson, 2004)
IPVI		
Modified Chlorophyll Absorption in Reflectance Index (MCARI)	$((RE - R) - 0.2 * (RE - G)) * (RE/R)$	(Daughtry, Walthall, Kim, De Colstoun, & McMurtrey Iii, 2000)
Modified chlorophyll absorption in reflectance index 1(MCARI1)	$((NIR - RE) - 0.2 * (NIR - G)) * (NIR/RE)$	(Daughtry et al., 2000)
Modified chlorophyll absorption in reflectance index 2(MCARI2)	$(1.5(NIR - RE) - 1.3(NIR - G))/\sqrt{((2NIR + 1)\text{^}2 - (6NIR - 5\sqrt{RE}) - 0.5)}$	(Haboudane, Miller, Pattey, Zarco-Tejada, & Strachan, 2004)
Modified Nonlinear Index (MNLI)	$1.5(NIR\text{^}2 - R)/(NIR\text{^}2 + R + 0.5)$	(P. Gong, Pu, Biging, & Larrieu, 2003)
Modified Red Edge Difference Vegetation Index (MREDVI)	$RE - R$	(Q. Cao et al., 2013)
Modified RESAVI (MRESAVI)	$0.5(2NIR + 1 - sqrt((2NIR + 1)^2 - 8(NIR - RE)))$	(J. Qi, Chehbouni, Huete, Kerr, & Sorooshian, 1994)
Modified Soil-adjusted Vegetation Index (MSAVI)	$0.5\ (2NIR + 1 - sqrt((2NIR + 1)^2 - 8(NIR - R)))$	(J. Qi et al., 1994)
Modified GSAVI (MGSAVI)	$0.5[2NIR + 1 - sqrt((2NIR + 1)\text{^}2 - 8(NIR - G))]$	(J. Qi et al., 1994)
Modified Simple Ratio (MSR)	$(NIR/R - 1)/sqrt(NIR/R + 1)$	(J. M. Chen, 1996)
Modified green simple ratio (MSRG)	$((NIR/G - 1))/\sqrt{((NIR/G + 1))}$	(J. M. Chen, 1996)

Modified Simple Ratio Green and Red (MSRGR)	$\sqrt{(G/R)}$	(Tucker, 1979)
Modified green simple ratio (MSRRE)	$((\mathrm{NIR}/\mathrm{RE}-1))/\sqrt{((\mathrm{NIR}/\mathrm{RE}+1)}$)	(J. M. Chen, 1996)
Normalized difference red edge (NDRE)	$(\mathrm{NIR}-\mathrm{RE})/(\mathrm{NIR}+\mathrm{RE})$	(Barnes et al., 2000)
Normalized difference vegetation index (NDVI)	$(\mathrm{NIR}-\mathrm{R})/(\mathrm{NIR}+\mathrm{R})$	(Tucker, 1979)
Nonlinear Index (NLI)	$(\mathrm{NIR}^2-R)/(\mathrm{NIR}^2+R)$	(Goel & Qin, 1994)
Modified normalized difference index (MNDI)	$(\mathrm{NIR}-\mathrm{RE})/(\mathrm{NIR}-\mathrm{G})$	(Datt, 1999)
Modified normalized difference red edge (MNDRE)	$[\mathrm{NIR}-(\mathrm{RE}-2\mathrm{G})]/[\mathrm{NIR}+(\mathrm{RE}-2\mathrm{G})]$	(W. Wang et al., 2012)
Normalized NIR-blue difference index (NNBDI)	$(\mathrm{NIR}-\mathrm{B})/(\mathrm{NIR}+\mathrm{B})$	In this study
Normalized NIR index (NNIR)	$\mathrm{NIR}/(\mathrm{NIR}+\mathrm{RE}+\mathrm{G})$	(Sripada et al., 2006)
Normalized Near Infrared Index (NNIRI)	$\mathrm{NIR}/(\mathrm{NIR}+\mathrm{RE}+\mathrm{R})$	(Lu, Miao, Shi, Li, & Yuan, 2017)
Normalized red edge index (NREI)	$\mathrm{RE}/(\mathrm{NIR}+\mathrm{RE}+\mathrm{G})$	(Sripada et al., 2006)
Normalized Red Index (NRI)	$\mathrm{R}/(\mathrm{NIR}+\mathrm{RE}+\mathrm{R})$	(Lu et al., 2017)
Plant senescence reflectance index (PSRI)	$(\mathrm{R}-\mathrm{G})/\mathrm{RE}$	(Merzlyak, Gitelson, Chivkunova, & Rakitin, 1999)
Red edge green difference vegetation index (REGDVI)	$\mathrm{RE}-\mathrm{G}$	(Tucker, 1979)
Red edge green ratio vegetation index (REGRVI)	RE/G	(Q. Cao et al., 2013)
Red edge normalized difference vegetation index (RENDVI)	$(\mathrm{RE}-\mathrm{R})/(\mathrm{RE}+\mathrm{R})$	(Elsayed, Rischbeck, & Schmidhalter, 2015)
Red edge optimal soil adjusted vegetation index (REOSAVI)	$(1+0.16)(\mathrm{NIR}-\mathrm{RE})/(\mathrm{NIR}+\mathrm{RE}+0.16)$	(Rondeaux et al., 1996)
Red Edge Point Reflectance (REPR)	$(\mathrm{R}+\mathrm{NIR})/2$	(Dash & Curran, 2004)
Renormalized difference vegetation index (RERDVI)	$(\mathrm{NIR}-\mathrm{RE})/\sqrt{(\mathrm{NIR}+\mathrm{RE})}$	(Roujean & Breon, 1995)
Red Edge Ratio Vegetation Index (RERVI)	NIR/RE	(Gitelson et al., 1996)
Red edge soil adjusted vegetation index (RESAVI)	$1.5[(\mathrm{NIR}-\mathrm{RE})/(\mathrm{NIR}+\mathrm{RE}+0.5)]$	(Sripada et al., 2006)
Red Edge Simple Ratio (RESR)	RE/R	(Erdle, Mistele, & Schmidhalter, 2011)
Optimized Red Edge Vegetation Index ($\mathrm{REVI}_{\mathrm{opt}}$)	$100*(ln(\mathrm{NIR})-ln(\mathrm{RE}))$	(Jasper, Reusch, & Link, 2009)
Red edge wide dynamic range vegetation index (REWDRVI)	$(0.12\mathrm{NIR}-\mathrm{RE})/(0.12\mathrm{NIR}+\mathrm{RE})$	(Gitelson, 2004)
Ratio vegetation index (RVI)	NIR/R	(Jordan, 1969)
Soil-adjusted vegetation index (SAVI)	$1.5(\mathrm{NIR}-\mathrm{R})/(\mathrm{NIR}+\mathrm{R}+0.5)$	(A. R. Huete, 1988)
SAVI*SR	(NIR^2-R)/[(NIR+R+0.5)*R]	(P. Gong et al., 2003)
Transformed Chlorophyll Absorption in Reflectance Index (TCARI)	3((RE-R)-0.2(RE-G)*(RE/R))	(Haboudane, Miller, Tremblay, Zarco-Tejada, & Dextraze, 2002)

Triangular Chlorophyll Index (TCI)	1.2((RE-G)-1.5(RE-G)*sqrt(RE/R))	(Haboudane, Tremblay, Miller, & Vigneault, 2008)
Transformed Normalized Vegetation Index (TNDVI)	$\mathrm{sqrt}((\mathrm{NIR}-\mathrm{R})/(\mathrm{NIR}+\mathrm{R})+0.5)$	(Sandham & Zietsman, 1997)
Triangular vegetation index (TVI)	$0.5*(120*(\mathrm{NIR}-\mathrm{G})-200*(\mathrm{R}-\mathrm{G}))$	(Broge & Leblanc, 2001)

Supplementary data 4 is not included here as it is a very large table, includes GWAS results for each VI and is provided upon request by Texas A&M University Quantitative Genetic and Maize Breeding Program.

Phenomic data and weather data are also very large excel files containing thousands of columns and rows and ~21,000 KB and ~3,259 KB. So that two files are also provided based provided upon request by Texas A&M University Quantitative Genetic and Maize Breeding Program.

APPENDIX E

APPENDIX OF CHAPTER VI

Supporting Information(SI) Materials and Methods

Phenomic data extraction pipeline

Detailed function settings of R/UAStools::plotshpcreate were set as follows: (i) nrowplot was set 2 since two consecutive row plots represent the one hybrid pedigree, multirowind was also set TRUE (T) to define two consecutive row plots indicates one pedigree; (ii) dimension of each polygon was defined by setting the functions of rangespc and rowspc as 7.62 and 0.76 meters respectively; (iii) buffer polygon was obtained by removing the alley distances from left, right, top and bottom sides using rangebuf and rowbuf functions; buffer polygon was obtained by setting rangebuf (for top and bottom sides) and rowbuf (for left and right sides) as 0.61 and 0.05 meters respectively. Buffer polygons covering each plot were used as shape files in data extraction pipelines to obtain better accuracy since walking alleys surrounding the plots were excluded (https://github.com/andersst91/UAStools/wiki/plotshpcreate.R). As a result, a shape file containing 594 buffer polygons (each contain two row plots) were created with the unique plot number in each. After constructing the shape file, each buffer polygon was visualized with tiff files for each time point in QGIS software (https://qgis.org/en/site) and checked manually; occasionally a small percentage of polygons was required to move slightly around the row plots to make each cover the row plots accurately because of the minor overlap issue for certain region of the mosaicked tiff files.

To extract the VIs, first, the tiff files were clipped into a trial level in QGIS, then the extraction pipeline was applied to each clipped tiff file in R. Extraction pipeline were explained briefly as follows: (i) aggregate function was first implemented to each tiff file consistently to reduce the computational time requirement by setting fact as 4 [aggregate("input tiff file", fact = 4]; (ii) soil was removed from the tiff files by using the Hue index in R/FIELDImageR::fieldMask function; (ESCADAFAL 1993); (iii) additional VIs for both HTP platforms were defined in R/FIELDImageR::fieldndex function using the output tiff file of second step; (iv) previously constructed shape files were combined with the output of the third step to obtain the values of each VI for each row plot. The VIs calculated by using RGB bands were extracted from the images in first HTP platform while VIs calculated by using RGB, red edge and NIR bands were extracted from the images in second HTP platform.

To construct the canopy height model (CHM), each 3D point cloud file (.las) was first clipped into trial level then the following steps of the custom batch code was applied to each point cloud to extract the plot based temporal plant height as follows: (i) sorting the clipped point clouds to facilitate further processing steps (LAStools/lasssort.exe); (ii) removing excessively noise points (blunders) located below ground and above canopy (LAStools/lasnoise.exe) of row plots; (iii) using the hierarchical robust interpolation algorithm (HRI) (KRAUS AND PFEIFER 1998) to determine the ground points (FUSION\GroundFilter.exe); (iv) detecting the key points from the ground filter to outline digital terrain model (DTM) (LAStools\lasthin.exe); (v) creating the DTM model using the key points from the previous step

(FUSION\GridSurfaceCreate.exe); (vi) generating the canopy surface model by extracting the digital terrain model (output of step v) from the digital surface model (output of step ii) (LAStools\lasheight.exe). Adjusting 'Z' values that account for plant height in the canopy surface model, merging with the ESRI shape file to clip the canopy surface model into plots (FUSION/PolyClipData.exe). As a last step, statistical metrics (e.g., plant height values based on different percentiles) for each clipped plot (pedigree row) were calculated (FUSION/CloudMetrics.exe). Predicted CHM for each pedigree by equation 2 (Eq. 2) was fit based on the Weibull sigmoidal growth model as follows:

$$Weibull\ sigmoidal\ growth = a\left(1 - Exp\left(-\left(\frac{flight\ date}{x}\right)^{b}\right)\right)\ Equation\ 1; Eq.1$$

Where, a is the asymptote; flight date is numeric values as days after planting of each flight date; x is the inflection point and b is the growth rate. Weibull fit CHM was used in further analysis.

Experimental Design and Nested Model for Phenomic Data

Following extraction of plot based temporal vegetation indices and CHM, a nested design predicted the temporal breeding values for each of 280 pedigrees to assess the temporal phenomic data jointly for optimal management (OM) and stressed management (SM, no irrigation, low fertilizer) using the "lmer" function in the "lme4" package in R. Each temporal vegetation index and temporal plant height was modelled for both HTP platform as follows:

$$Y_{ijklm} = \mu + \beta_i + \Omega_{i(j)} + \delta_{i(k)} + \Psi_{i(l)} + \theta_{i(m)} + \varepsilon_{ijklm}\ (Equation\ 2; Eq.2)$$

where, μ = overall mean; β_i = the random effect of ith flight time (as days after planting time, DAP) with $\beta_i \overset{iid}{\sim} N(0, \sigma^2_{\beta_i})$, $i \in$ [27, 34, 41, 48, 55, 59, 63, 69, 77, 82, 88, 97, 103, 105, 118; rotary-wing with RGB camera HTP platform] and $i \in$ [27, 34, 52, 60, 70, 73, 88, 105, 112, 118, 132, 144; tuffwing with multispectral camera HTP platform]; $\Omega_{i(j)}$= the random effect of jth pedigree (maize hybrid) within the ith flight time with $\Omega_{i(j)} \overset{iid}{\sim} N(0, \sigma^2_{\Omega_{i(j)}})$, $j \in [1, \ldots, 280]$; $\delta_{i(k)}$ = the random effect of kth range within the ith flight time with $\delta_{i(k)} \overset{iid}{\sim} N(0, \sigma^2_{\delta_{i(k)}})$, $k \in [1, \ldots, 18]$; $\Psi_{i(l)}$= the random effect of lth row within the ith flight time with $\Psi_{i(l)} \overset{iid}{\sim} N(0, \sigma^2_{\Psi_{i(l)}})$, $l \in [1, \ldots, 33]$; $\theta_{i(m)}$= the random effect of mth replication within the ith flight time with $\theta_{i(m)} \overset{iid}{\sim} N(0, \sigma^2_{\theta_{i(m)}})$, $m \in [1, 2]$; ε_{ijklm} is pooled error with $\varepsilon_{ijklm} \overset{iid}{\sim} N\left(0, \sigma^2_{\varepsilon_{ijklm}}\right)$.

Temporal repeatability (TR) was calculated using the genotypic variance containing the variation of the trait belonging to all flight times. *Eq. 3* was applied to each vegetation index and canopy height separately.

$$Temporal\ repeatability\ (TR) = \frac{\sigma^2_{\Omega_{i(j)}}}{\sigma^2_{\Omega_{i(j)}} + \frac{\sigma^2_{\varepsilon_{ijklm}}}{no.of\ replications}} \quad (Equation\ 3; Eq. 3)$$

Where, $\sigma^2_{\Omega_{i(j)}}$ is genotypic variance containing joint genotypic variation occurring across the flights; $\sigma^2_{\varepsilon_{ijklm}}$ is residual variance containing unexplained error.

Grain yield (GY) was collected from each two adjacent row plots (per hybrid) via a plot combine harvester; days to anthesis (DTA) and silking (DTS) were collected when

fifty percent of plots displayed anthesis and silking emergence; manually measured terminal plant height was calculated from the ground to the tip of tassel.

GY, DTA, DTS, PHT were used as predicted variables and modelled according to *Eq. 2* without flight time (denoted as β in *Eq. 2*) component as follows:

$$Y_{jklm} = \mu + \Omega_j + \delta_k + \Psi_l + \theta_m + \varepsilon_{jklm} \ (Equation\ 4; Eq. 4)$$

Traditional repeatability was calculated for all cumulative traits (GY, DTA, DTS, PHT) based on *Eq. 3* with the nested effect by flight time removed (denoted as β in *Eq. 2*) as follows:

$$Repeatability = \frac{\sigma^2_{\Omega_j}}{\sigma^2_{\Omega_j} + \frac{\sigma^2_{\varepsilon_{jklm}}}{no.of\ replications}} \ (Equation\ 5; Eq. 5)$$

As a result of $\Omega_{i(j)}$ component in $Eq. 2$, 35 VIs and Weibull_CHM belonging to fifteen time points in TPP_RGB, and 89 VIs and Weibull_CHM belonging to twelve time points in TPP_Multi were predicted, resulting in 540 and 1080 phenomic data belonging to 280 maize hybrids respectively. Pearson correlation coefficients between each phenotype data at each time point of each temporal trait with GY were calculated using the "*corrplot*" package in R.

Machine Learning Based Phenomic Prediction Models

Caret package was used in R to run the prediction models. "Caret::trainControl()" function was used to set repeated cross validation (method="repeatedcv") with 10 folds and 3 repeats; this cross validation was used for

every model consistently inside the loop. Brief steps of the single loop were explained as follows: (i) partitioning the whole data set as 70 percent training and remainders test data set in TPP_RGB and TPP_Multi phenomic data belonging to optimal (OM) and stress (SM) managements, which were different in each loop, using the "caret::createDataPartition()" function, (ii) training the all prediction models using the train data set of OM (tested environment) in the "caret::train()" function, (iii) predicting the train data set in OM (cross validation 1; tested genotypes in tested environment; CV1), test data set in OM (cross validation 2; untested genotypes in tested environment; CV2), train data set in SM (cross validation 3; tested genotypes in untested environment; CV3) and test data set in OM (cross validation 4; untested genotypes in untested environment; CV4) using the trained model to obtain the predicted data using the "caret::predict()" function for each model, (iv) computing the correlation between actual data and predicted data to evaluate the prediction accuracy ($\bar{r}$) for four cross validation schemes in each model and (v) saving the correlation results along with the R-squared (R2), root mean square error (RMSE) and mean absolute error (MAE) as well as the variable importance scores of the predictors belonging to each model in each loop. Number of loops was set to 500. To define the prediction model inside the "caret::train()" function, method was set as "lm" for the linear model, method was set as "glmnet" for elastic net, lasso and ridge models and model was set as "rf" for random forest (RF) model separately. To tune the parameters of the elastic net, lasso and ridge regressions, "alpha" value was set as 0 for ridge and 1 for lasso regression while sequential numbers between 0 and 1 by ten equal increment numbers were searched to

find the best alpha for elastic net regression. Sequential "lambda" value between 0 and 1 by ten equal increment numbers were also empirically searched to find the best "lambda" values for lasso, ridge, and elastic net regressions. To tune the parameters of RF model, "ntree" (number of trees to grow in the model) was set as 1000 while sequential "mtry" (number of variables randomly tested as candidates at each split) value between 1 and 50 by five equal increment number were empirically searched to find the best "mtry" based on highest accuracy metric of RF model.

Association Mapping for Phenomic Data

Cumulative AUC were calculated by using the below formula for each pedigree and each VI and Weibull_CHM:

$$Cumulative\ AUC_i = \sum_{t=1}^{n-1} \left(\frac{V_t + V_{t+1}}{2}\right)(F_{t+1} - F_t)\ (Equation\ 6;\ Eq.6)$$

Where, n is the number of total observations referring to the fifteen flights times in TPP_RGB, $Cumulative\ AUC_i$ is the cumulative AUC value based on the total number of flights belonging to ith pedigree for each trait, $i \in [1, \dots, 280]$; V_t is the value at tth flight time as DAP, $t \in$ $[27, 34, 41, 48, 55, 59, 63, 69, 77, 82, 88, 97, 103, 105, 118]$; F_t is the tth flight time as number of DAP at which value of interest was taken in first HTP platform.

The imputed ZeaGBSv2.7 with AGPv4 coordinates was used in this study, available in Panzea (https://www.panzea.org/genotypes) and Cyverse (Bridget A McFarland et al., 2020) platforms. In the genome wide association mapping study, 158

maize hybrids with genotyping by sequencing (GBS) data of their parental lines were available in MaizeGBSv2.7 (Glaubitz et al., 2014), generated via the method based on digestion the DNA with the *ApeKI* restriction enzyme (Elshire et al., 2011). ZeaGBSv2.7 was called in Tassel 5 software (Bradbury et al., 2007). Before association mapping, GBS data of the hybrid maize was created based on following step: (i) heterozygote calls belonging to any parental lines of the hybrids were set as missing, (ii) "*create_hybrid_genotype*" function in Tassel 5 software was used to create the GBS data of hybrid maize by merging the GBS data of parental lines of each hybrid and (iii) polymorphic markers were obtained by filtering the missing data that is more than ten percent and minor allele frequency that is lower than five percent. LD *k*-nearest neighbor algorithm (LD *KNNi* imputation) was implemented to GBS data to impute the missing calls in Tassel software (version 5) (Money et al., 2015). Finally, 101,100 polymorphic SNPs (single nucleotide polymorphism) remained and were used in the association mapping analysis.

To control the population structure of the hybrid population, the first five principal components, which explained 49% of total variation, and kinship matrix were used in each model. Bonferroni corrections [$-log_{10}(p\ values) > 6.3$; 0.01/(no. of markers)] were considered as threshold in determining the GWAS hits in Manhattan plots, in addition to Bonferroni threshold, false-positive discovery rate was set [$-log_{10}(p\ values) > 5$] to detect same loci (if any) that were associated with multiple traits with between the values of [$-log_{10}(p\ values) > 5$] and [$-log_{10}(p\ values) > 6.3$]. MaizeGBD (http://www.maizegdb.org/) and the Gramene database

(http://www.gramene.org) were used to determine corresponding candidate genes of the discovered SNPs and functions of genes. LD decay pattern was investigated in Tassel 5 (LD windows size = 10 markers) and visualized in R for each chromosome separately (**Fig. S1**). Linkage disequilibrium (LD) was visualized using the *LDheatmap* package in R (Shin et al., 2006) to identify the candidate genes within the LD blocks ($R^2 \geq 0.8$) of colocalized SNPs.

Genomic Prediction for Phenomic Data

153,252 SNPs belonging to 158 maize hybrids were obtained merging the GBS data of their parental lines in Tassel software as described in the "*Association mapping for phenomic data"* section. After obtaining the hybrid GBS, SNPs were filtered if minor allele frequency was lower than 0.01 and missing values were higher than 10 percent per marker resulting in 153,252 SNPs. Missing values of 153,252 SNPs were imputed using the *rrBLUP::Amat()* function in R. Temporal genomic prediction for phenomic data in TPP_RGB was modeled using the rrBLUP package (Endelman, 2011) in R as follows:

$$y = 1\mu + Z\Phi + \varepsilon \; (Equation\ 7; Eq.7)$$

Where, y = is the vector $(n \times 1)$ of single phenotype data of n maize hybrids (n = is training data set of each loop) belonging to each single time point of each phenotype data in TPP_RGB , $\begin{bmatrix} 0.6 \\ 0.9 \\ \vdots \\ n \end{bmatrix}$; $1 =$ vector of ones that are equal to numbers of n, $\begin{bmatrix} 1 \\ 1 \\ \vdots \\ n \end{bmatrix}$; μ = overall mean of training data set; Z = the incidence matrix $(n \times p)$ of allelic states of p number of SNPs (153,252 SNPs) belonging to n number of maize hybrids,

$\begin{bmatrix} 0 & 1\cdots & 0 \\ \vdots & \ddots & \vdots \\ -1 & 0\cdots & n \times p \end{bmatrix}$; Φ = vector of calculated SNP effects $(p \times 1)$, $\begin{bmatrix} 4e-05 \\ -5e-05 \\ \vdots \\ p \end{bmatrix}$; ε = vector of random residuals. RR-BLUP assumes $\Phi \sim MVN(0, \sigma_\Phi^2)$ indicating that marker effects are normally distributed with equal marker variance (σ_Φ^2) throughout the genome.

Genomic prediction was modelled using training data accounting for seventy percent of total data while the remaining thirty percent data was used as validation data. The genomic prediction model ($Equation\ 7, Eq.7$) evaluated 500 iterations applied to each phenotype of 158 maize hybrids belonging to each VI and Weibull_CHM at fifteen time points (totally 540 phenotype data) in TPP_RGB; base R function called "*sample()*"was used to randomly determine training and test data set in each iteration. During the prediction, the same training and test data set for each phenotype of each trait at each time point was needed to obtain fair comparison of the genomic prediction accuracy. Genomic prediction accuracy was calculated based on correlation results between the genetic estimated breeding values and the true breeding value of test data set in each iteration.

Phenomic Prediction versus Genomic Prediction

118 maize hybrids whose parental lines had GBS info in MaizeGBSv2.7 (Glaubitz et al., 2014) and grown in optimal (OM) and stressed (SM) managements were used. In genomic prediction, GBS data (GP) containing 153.252 SNPs that was

described in the "*Genomic prediction for phenomic data"* was used to predict grain yield (GY) using rrBLUP package in R (Endelman, 2011). TPP_RGB containing 540 phenomic data, and TPP_Multi containing 1080 phenomic data were used to predict GY using the ridge regression in the *caret* package in R. Prediction accuracy was obtained from 1000 bootstraps for each model where the same training and test data set were used for genomic and phenomic prediction within each bootstrap. Genomic prediction and phenomic prediction steps were explained in the *"Genomic prediction for phenomic data"* and *"Machine learning based phenomic prediction models"* respectively. Four cross validation schemes, which were explained in *"Machine learning based phenomic prediction models"***,** were applied in this section as well to compare the prediction accuracies of two phenomic predictions and genomic prediction.

Table S1 shows the calendar days between March to July, 2017 containing the flight dates for rotary-wing UAS with RGB camera (above) and TuffWing UAS with multispectral camera (below) high throughput phenotyping platforms. Flight dates were shown under the months with corresponding days after planting times in parenthesis. Reprinted from Adak, Murray, & Anderson, 2021.

Rotary-wing with RGB camera														
March	April					May					June			
29th (27)	5th (34)	12th (41)	19th (48)	26th (55)	30th (59)	4th (63)	10th (69)	18th (77)	23rd (82)	29th (88)	7th (97)	13th (103)	15th (105)	28th (118)

TuffWing with multispectral camera											
March	April		May				June			July	
29th (27)	5th (34)	23rd (52)	1st (60)	11th (70)	14th (73)	29th (88)	15th (105)	22nd (112)	28th (118)	12th (132)	24th (144)

Table S2 shows the vegetation indices used and their formulas along with references. Reprinted from Adak, Murray, & Anderson, 2021.

Vegetation index	Ratios	References
VIs derived from RGB bands		
Blue chromatic coordinate index (BCC)	$\frac{B}{R+G+B}$	(Woebbecke et al., 1995)
Blue green pigment index (BGI)	$\frac{B}{G}$	(Zarco-Tejada et al., 2005)
Brightness index (BI)	$\mathrm{sqrt}(\frac{R^2+G^2+B^2}{3})$	(Richardson & Wiegand, 1977)
Color index of vegetation extraction (CIVE)	$0.441R-0.811G+0.385B+18.78745$	(Kataoka et al., 2003)
Combined indices 1 (COM1)	$EXG+CIVE+EXGR+VEG$	(Guijarro et al., 2011)
Combined indices 2 (COM2)	$0.36EXG+0.47CIVE+0.17VEG$	(Guerrero et al., 2012)
Additional blue index (EBI)	$\frac{B-G}{B-R}$	(Golzarian & Frick, 2011)
Additional green index (EGI)	$\frac{G-R}{R-B}$	(Golzarian & Frick, 2011)
Green-red index (ERI)	$\frac{R-G}{R-B}$	(Golzarian & Frick, 2011)
Excessive green (EXG)	$2G-R-B$	(Woebbecke et al., 1995)
Normalized Excess green index (EXG2)	$\frac{2G-R-B}{G+R+B}$	(Woebbecke et al., 1995)
Excess green minus excess red index (EXGR)	$3G-2.4R-B$	(G. E. Meyer & Neto, 2008)
Excessive red (EXR)	$1.4R-G$	(G. Meyer et al., 1998)
Green minus blue index (G-B)	$G-B$	(Woebbecke et al., 1995)
Green minus red index (G-R)	$G-R$	(Woebbecke et al., 1995)
Green blue simple ratio index (G/B)	$\frac{G}{B}$	(Woebbecke et al., 1995)
Green red simple ratio index (G/R)	$\frac{G}{R}$	(Woebbecke et al., 1995)
Green chromatic coordinate index (GCC)	$\frac{G}{R+G+B}$	(Woebbecke et al., 1995)
Green leaf index (GLI)	$\frac{2G-R-B}{2G+R+B}$	(Louhaichi et al., 2001)
Modified excess green index (MEXG)	$1.262G-0.884R-0.311B$	(Burgos-Artizzu et al., 2011)
Modified green red index (MGVRI)	$\frac{G^2-R^2}{G^2+R^2}$	(Bendig et al., 2015)
Normalized difference index (NDI)	$128*[(\frac{(G-R)}{(G+R)})+1]$	(G. E. Meyer & Neto, 2008)
Normalized difference red blue index (NDRBI)	$\frac{R-B}{R+B}$	(Golzarian & Frick, 2011)
Normalized green-blue difference index (NGBDI)	$\frac{G-B}{G+B}$	(Hunt et al., 2005)
Normalized green red difference index (NGRDI)	$\frac{G-R}{G+R}$	(Tucker, 1979)

Red minus blue index (R-B)	$R - B$	(Woebbecke et al., 1995)
Red blue simple ratio index (R/B)	$\frac{R}{B}$	(Woebbecke et al., 1995)
Red chromatic coordinate index (RCC)	$\frac{R}{R+G+B}$	(Woebbecke et al., 1995)
Red green blue index (RGBVI)	$\frac{G^2 - R * B}{G^2 + R * B}$	(Bendig et al., 2015)
Triangular greenery index (TGI)	$G - (0.39R - 0.69B)$	(Hunt et al., 2011)
Visible atmospherically resistant index (VARI)	$\frac{G - R}{G + R - B}$	(Gitelson et al., 2002)
Vegetativen (VEG)	$\frac{G}{R^{0.667} * B^{0.334}}$	(Hague et al., 2006)
VIs derived from multispectral bands (RGB, red-edge and NIR bands)		
Modified chlorophyll absorption in reflectance index 1(MCARI1)	$[(NIR - RE) - 0.2 * (NIR - G)] * \left(\frac{NIR}{RE}\right)$	(Daughtry et al., 2000)
Modified chlorophyll absorption in reflectance index 2(MCARI2)	$\frac{1.5(NIR - RE) - 1.3(NIR - G)}{\sqrt{(2NIR + 1)^2 - (6NIR - 5\sqrt{RE}) - 0.5}}$	(Haboudane et al., 2004)
Chlorophyll vegetation index-green (CIG)	$\frac{NIR}{G} - 1$	(Gitelson et al., 2005)
Chlorophyll vegetation index-red edge (CIRE)	$\frac{NIR}{RE} - 1$	(Gitelson et al., 2005)
Chlorophyll vegetation index (CVI)	$\frac{NIR * R}{G^2}$	(Vincini et al., 2008)
Difference vegetation index (DVI)	$NIR - RE$	(Tucker, 1979)
Enhanced normalized difference vegetation index (ENDVI)	$\frac{NIR + G - 2B}{NIR + G + 2B}$	Maxmax 2015 (http://www.maxmax.com/endvi.htm)
Enhanced vegetation index (EVI)	$\frac{2.5(NIR - R)}{NIR + 6R - 7.5B + 1}$	(A. Huete et al., 2002)
Green difference vegetation index (GDVI)	$NIR - G$	(Tucker, 1979)
Green infrared percentage vegetation index (GIPVI)	$\frac{NIR}{NIR + G}$	(Crippen, 1990)
Green normalized difference vegetation index (GNDVI)	$\frac{NIR - G}{NIR + G}$	(Gitelson et al., 1996)
Green optimal soil adjusted vegetation index (GOSAVI)	$\frac{(1 + 0.16)(NIR - G)}{NIR + G + 0.16}$	(Rondeaux et al., 1996)
Green re-normalized different vegetation index (GRDVI)	$\frac{NIR - G}{sqrt(NIR + G)}$	(Roujean & Breon, 1995)
Green ratio vegetation index (GRVI)	$\frac{NIR}{G}$	(Buschmann & Nagel, 1993)
Green soil adjusted vegetation index (GSAVI)	$1.5\left(\frac{NIR - G}{NIR + G + 0.5}\right)$	(Sripada et al., 2006)
Green wide dynamic range vegetation index (GWDRVI)	$\frac{0.12NIR - G}{0.12NIR + G}$	(Gitelson, 2004)
Modified double difference index (MDD)	$(NIR - RE) - (RE - G)$	(Le Maire, Francois, & Dufrene, 2004)

Modified GSAVI (MGSAVI)	$0.5[2\mathrm{NIR} + 1 - \mathrm{sqrt}((2\mathrm{NIR} + 1)^2 - 8(\mathrm{NIR} - \mathrm{G}))]$	(J. Qi et al., 1994)
Modified normalized difference index (MNDI)	$(\mathrm{NIR} - \mathrm{RE})/(\mathrm{NIR} - \mathrm{G})$	(Datt, 1999)
Modified normalized difference red edge (MNDRE)	$\frac{[\mathrm{NIR} - (\mathrm{RE} - 2\mathrm{G})]}{[\mathrm{NIR} + (\mathrm{RE} - 2\mathrm{G})]}$	(W. Wang et al., 2012)
Modified RESAVI (MRESAVI)	$0.5\ [2\mathrm{NIR} + 1 - \mathrm{sqrt}((2\mathrm{NIR} + 1)^2 - 8(\mathrm{NIR} - \mathrm{RE}))]$	(J. Qi et al., 1994)
Modified RETVI (MRETVI)	$1.2[1.2(\mathrm{NIR} - \mathrm{G}) - 2.5(\mathrm{RE} - \mathrm{G})]$	(Haboudane et al., 2004)
Modified simple ratio (MSR)	$\frac{\left(\frac{\mathrm{NIR}}{\mathrm{R}} - 1\right)}{\sqrt{\left(\frac{\mathrm{NIR}}{\mathrm{R}} + 1\right)}}$	(J. M. Chen, 1996)
Modified green simple ratio (MSR_G)	$\frac{\left(\frac{\mathrm{NIR}}{\mathrm{G}} - 1\right)}{\sqrt{\left(\frac{\mathrm{NIR}}{\mathrm{G}} + 1\right)}}$	(J. M. Chen, 1996)
Modified green simple ratio (MSR_RE)	$\frac{\left(\frac{\mathrm{NIR}}{\mathrm{RE}} - 1\right)}{\sqrt{\left(\frac{\mathrm{NIR}}{\mathrm{RE}} + 1\right)}}$	(J. M. Chen, 1996)
Modified transformed CARI (MTCARI)	$3\left[(\mathrm{NIR} - \mathrm{RE}) - 0.2(\mathrm{NIR} - \mathrm{G})\left(\frac{\mathrm{NIR}}{\mathrm{RE}}\right)\right]$	(Haboudane et al., 2002)
Normalized difference red edge (NDRE)	$\frac{\mathrm{NIR} - \mathrm{RE}}{\mathrm{NIR} + \mathrm{RE}}$	(Barnes et al., 2000)
Normalized difference vegetation index (NDVI)	$\frac{\mathrm{NIR} - \mathrm{R}}{\mathrm{NIR} + \mathrm{R}}$	(Tucker, 1979)
Normalized NIR index (NNIR)	$\frac{\mathrm{NIR}}{\mathrm{NIR} + \mathrm{RE} + \mathrm{G}}$	(Sripada et al., 2006)
Normalized red edge index (NREI)	$\frac{\mathrm{RE}}{\mathrm{NIR} + \mathrm{RE} + \mathrm{G}}$	(Sripada et al., 2006)
Normalized green index (NGI)	$\frac{\mathrm{G}}{\mathrm{NIR} + \mathrm{RE} + \mathrm{G}}$	(Sripada et al., 2006)
Optimized soil-adjusted vegetation index (OSAVI)	$\frac{\mathrm{NIR} - \mathrm{R}}{\mathrm{NIR} + \mathrm{R} + 0.16}$	(Rondeaux et al., 1996)
Plant senescence reflectance index (PSRI)	$\frac{\mathrm{R} - \mathrm{G}}{\mathrm{RE}}$	(Merzlyak et al., 1999)
Red edge green difference vegetation index (REGDVI)	$\mathrm{RE} - \mathrm{G}$	(Tucker, 1979)
Red edge GNDVI (REGNDVI)	$\frac{\mathrm{RE} - \mathrm{G}}{\mathrm{RE} + \mathrm{G}}$	(Gitelson et al., 1996)
Red edge green ratio vegetation index (REGRVI)	$\frac{\mathrm{RE}}{\mathrm{G}}$	(Q. Cao et al., 2013)
Red edge optimal soil adjusted vegetation index (REOSAVI)	$\frac{(1 + 0.16)(\mathrm{NIR} - \mathrm{RE})}{\mathrm{NIR} + \mathrm{RE} + 0.16}$	(Rondeaux et al., 1996)
Renormalized difference vegetation index (RERDVI)	$\frac{\mathrm{NIR} - \mathrm{RE}}{\sqrt{\mathrm{NIR} + \mathrm{RE}}}$	(Roujean & Breon, 1995)
Red edge soil adjusted vegetation index (RESAVI)	$1.5\left[\frac{NIR - RE}{NIR + RE + 0.5}\right]$	(Sripada et al., 2006)

Red edge transformed vegetation index (RETVI)	$0.5[120(\mathrm{NIR}-\mathrm{G})-200(\mathrm{RE}-\mathrm{G})]$	(Broge & Leblanc, 2001)
Red edge wide dynamic range vegetation index (REWDRVI)	$\frac{0.12\mathrm{NIR}-\mathrm{RE}}{0.12\mathrm{NIR}+\mathrm{RE}}$	(Gitelson, 2004)
Ratio vegetation index (RVI)	$\frac{\mathrm{NIR}}{\mathrm{R}}$	(Jordan, 1969)
Soil-adjusted vegetation index (SAVI)	$\frac{1.5(\mathrm{NIR}-\mathrm{R})}{\mathrm{NIR}+\mathrm{R}+0.5}$	(A. R. Huete, 1988)
Triangular vegetation index (TVI)	$0.5[120(\mathrm{NIR}-\mathrm{G})-200(\mathrm{R}-\mathrm{G})]$	(Broge & Leblanc, 2001)
Optimized vegetation index 1 (VIopt1)	$100(\ln\mathrm{NIR}-\ln\mathrm{RE})$	(Jasper et al., 2009)
Transformed Normalized Vegetation Index (TNDVI)	$\mathrm{sqrt}\left(\frac{\mathrm{NIR}-\mathrm{R}}{\mathrm{NIR}+\mathrm{R}}+0.5\right)$	(Sandham & Zietsman, 1997)
Modified Nonlinear Index (MNLI)	$\frac{1.5(NIR^2-R)}{NIR^2+R+0.5}$	(P. Gong et al., 2003)
Red Edge Simple Ratio (RESR)	$\frac{RE}{\mathrm{R}}$	(Erdle et al., 2011)
Red edge normalized difference vegetation index (RENDVI)	$\frac{\mathrm{RE}-\mathrm{R}}{\mathrm{RE}+\mathrm{R}}$	(Elsayed et al., 2015)
Normalized NIR index2 (NNIR2)	$\frac{\mathrm{NIR}}{\mathrm{NIR}+\mathrm{RE}+\mathrm{R}}$	(Sripada et al., 2006)
Normalized red edge index2 (NREI2)	$\frac{\mathrm{RE}}{\mathrm{NIR}+\mathrm{RE}+\mathrm{R}}$	(Sripada et al., 2006)
Normalized red index (NRI)	$\frac{\mathrm{R}}{\mathrm{NIR}+\mathrm{RE}+\mathrm{R}}$	(Sripada et al., 2006)

R, G, B, RE and NIR represent the red, green, blue, red-edge and near infrared reflectance bands respectively. Red, green, blue, red edge and NIR reflectance bands were also used in this study singly.

SI Results

Genome Wide Association Mapping Results

Two close large effect locus 39,906,105 bp (*chr2_2*) and 39,906,547 bp (*chr2_3*) genomic locations was discovered for EXG2, GLI, RGBVI, VEG, Blue, GCC and NDRBI by all three GWAS models consistently and explained between 6 and 51 percent phenotypic variation depending on the traits and GWAS models (**Dataset S1**). *GRMZM2G129493* (chr2: 39906034 to 39907044 bp) candidate gene covers *chr2_2* (39906105 bp) and *chr2_3* (39906547 bp) GWAS peaks in its genomic region; known as polygalacturonase-inhibiting proteins (*PGIPs*) these encode plant defense related proteins (Ferrari, Vairo, Ausubel, Cervone, & De Lorenzo, 2003). Another candidate

gene (~2kb away from *chr2_2 and chr2_3*), *GRMZM2G362362* (chr2: 39893309 to 39904028), belongs to a family of glycoside hydrolases that hydrolase the glycosidic bonds in polysaccharide in cell wall (Minic, 2008).

The 50,705,765 bp (*chr2_4*) genomic location in chromosome 2 was discovered for TGI, Blue, BI, Green and Red by all three models consistently and explained 6 to 7 percent variation depending on the traits and models (**Dataset S1**). GRMZM2G018059 (chr2: 50696420 to 50706825) candidate gene contains the *chr2_4* GWAS peak in its genomic region and its function is related to U-box domain-containing protein kinase family protein that was discovered in previous association mapping studies as drought responsive genes (He et al., 2020; Xianglan Wang et al., 2016) as well as for yield related traits in maize (Z. Zhou et al., 2020).

203,544,095 bp (*chr4_1*) genomic location in chromosome 4 was discovered for TGI, BCC, BGI, G/B, G/R, GCC, NDRBI, NGBDI, R/B, COM1, EXG2, GLI and RGBVI and explained between 3 to 44 percent variation depending on the traits and models (**Dataset S1**). The *GRMZM2G001541* (chr4: 203544095 to 203547230 bp) candidate gene is closest \and ~30 base pairs away from the *chr4_1* (203544095 bp). The homolog of this gene in *Arabidopsis* is responsible for encoding the inflorescence and root apices receptor-like kinase (IRK) protein that is crucial for maintaining the differentiation of meristem (Hattan, Kanamoto, Takemura, Yokota, & Kohchi, 2004). *GRMZM2G001541* has been discovered by meta-QTL and GWAS analysis consistently and found to be highly expressed in developing tissues (e.g. primordia, developing leaves and ear) closely related to inflorescence development (X. Wu et al., 2016)

influencing yield performance directly in maize (Y. Wang, Wang, Wang, & Deng, 2020). *GRMZM2G001541* governs the expression level of *Unbranched3* (UB3), which regulates the quantitative variation of kernel row number in maize (L. Liu et al., 2015).

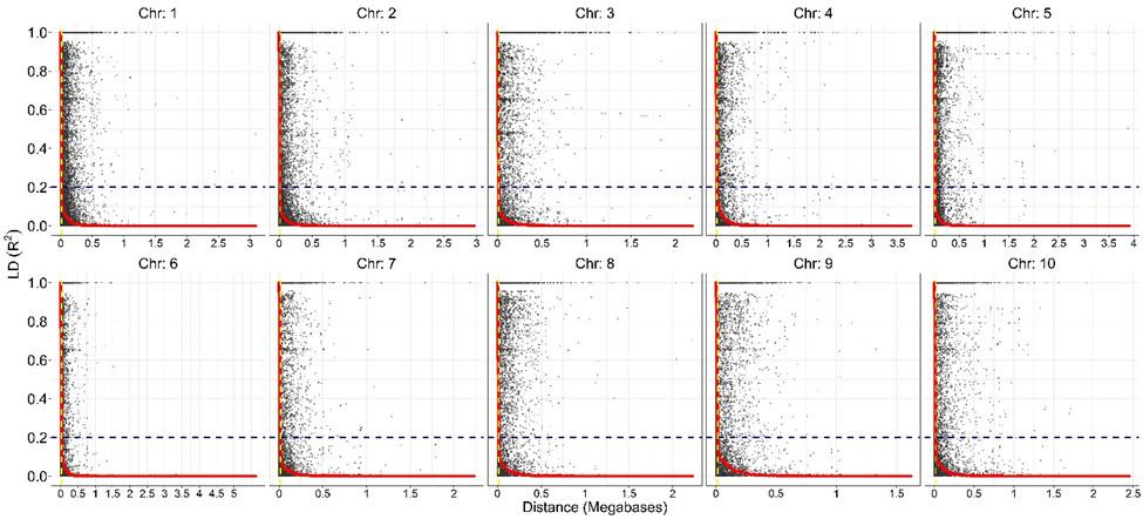

Figure S1 shows linkage disequilibrium decay (LD) patterns for each chromosome. The Y axis represents the R^2 while X axis shows the distance as Megabases. Horizontal dashed line shows the 0.2 R^2 LD while the vertical yellow color dashed line shows the 15 kilo base pair (kb) threshold in each chromosome. LD decay was found to be rapid for all chromosome and changing between 1 to 15 kb. Reprinted from Adak, Murray, & Anderson, 2021.

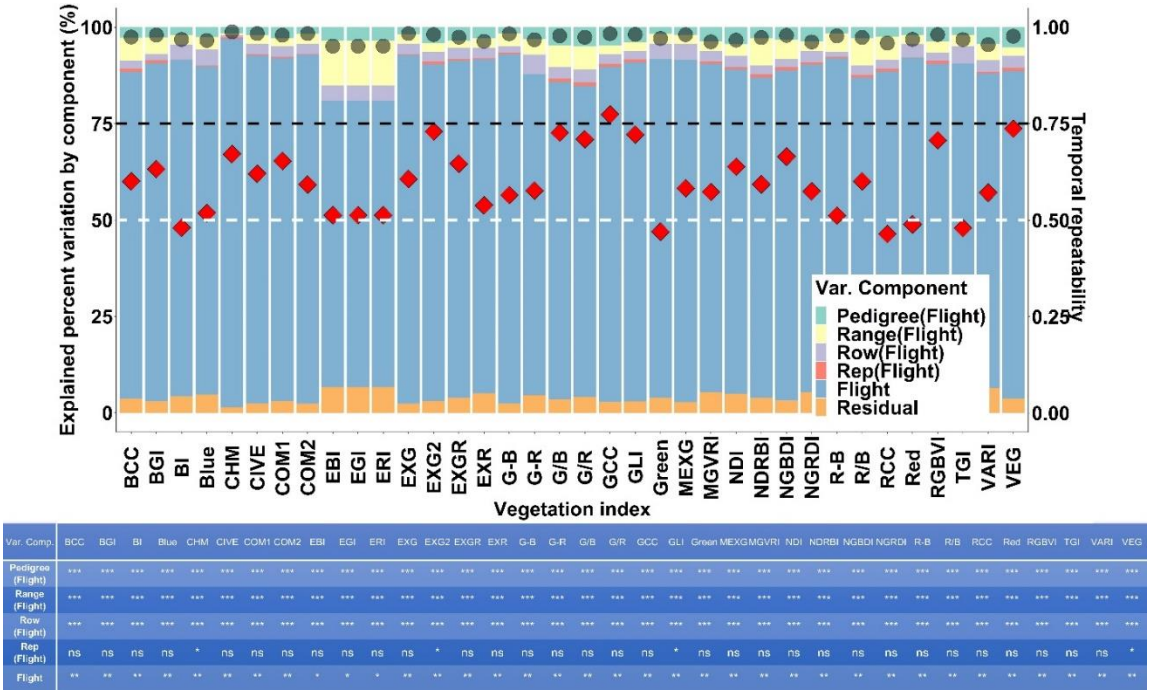

Var. Comp.	BCC	BGI	BI	Blue	CHM	CIVE	COM1	COM2	EBI	EGI	ERI	EXG	EXG2	EXGR	EXR	G-B	G-R	G/B	G/R	GCC	GLI	Green	MEXG	MGVRI	NDI	NDRBI	NGBDI	NGRDI	R-B	R/B	RCC	Red	RGBVI	TGI	VARI	VEG
Pedigree (Flight)	***	***	***	***	***	***	***	***	***	***	***	***	***	***	***	***	***	***	***	***	***	***	***	***	***	***	***	***	***	***	***	***	***	***	***	***
Range (Flight)	***	***	***	***	***	***	***	***	***	***	***	***	***	***	***	***	***	***	***	***	***	***	***	***	***	***	***	***	***	***	***	***	***	***	***	***
Row (Flight)	***	***	***	***	***	***	***	***	***	***	***	***	***	***	***	***	***	***	***	***	***	***	***	***	***	***	***	***	***	***	***	***	***	***	***	***
Rep (Flight)	ns	ns	ns	ns	*	ns	ns	ns	ns	ns	ns	ns	*	ns	ns	ns	ns	ns	ns	ns	*	ns	ns	ns	ns	ns	ns	ns	ns	ns	ns	ns	ns	ns	*
Flight	**	**	**	**	**	**	**	**	*	*	*	**	**	**	**	**	**	**	**	**	**	**	**	**	**	**	**	**	**	**	**	**	**	**	**	**

Figure S2 stacked bar plots show the explained percent variation by each component in *Eq. 2* for each temporal trait in TPP_RGB. Left y axis corresponds to the explained percent variation of the components in the stacked bar plots while the right y axis shows the temporal repeatability (red diamonds calculated by Eq 3) and R^2 values (black round symbols). Gray and black horizontal dashed lines represent the values of 0.50 and 0.75 where most of the temporal repeatability values of temporal traits accumulated. The table below shows the significance values of each component in *Eq. 2* for each temporal trait; ***, **, * are the 0.001, 0.01 and 0.05 significance levels respectively while ns is not statistically significant. Reprinted from Adak, Murray, & Anderson, 2021.

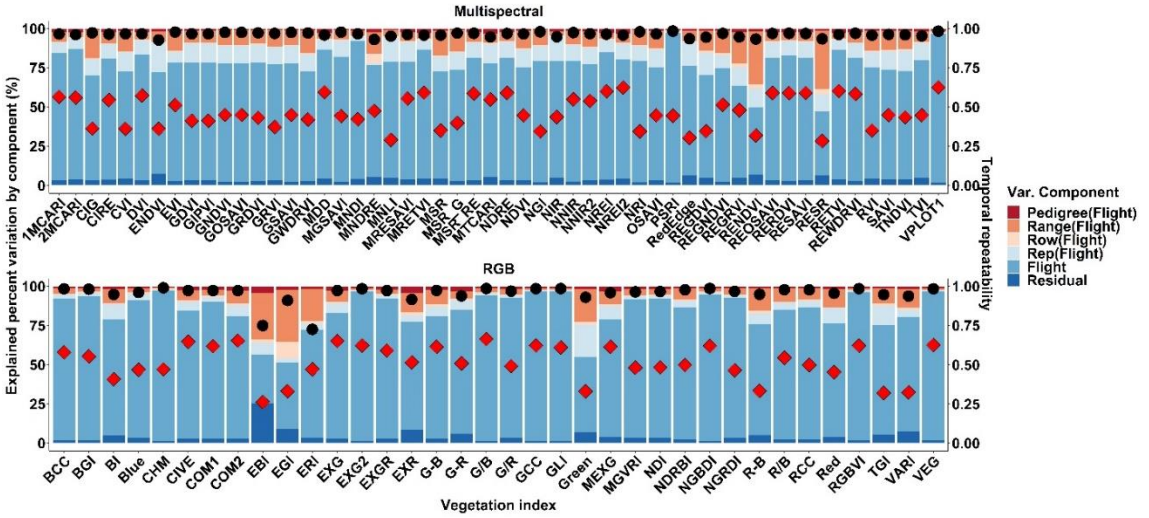

Figure S3 stacked bar plots represent the explained percent variation by each component in *Eq. 2* for each temporal trait in TPP_Multi. Left y axis corresponds to the explained percent variation of the components while right y axis shows the temporal repeatability (red diamonds calculated by *Eq. 3*) and R^2 values (black round symbols). Reprinted from Adak, Murray, & Anderson, 2021.

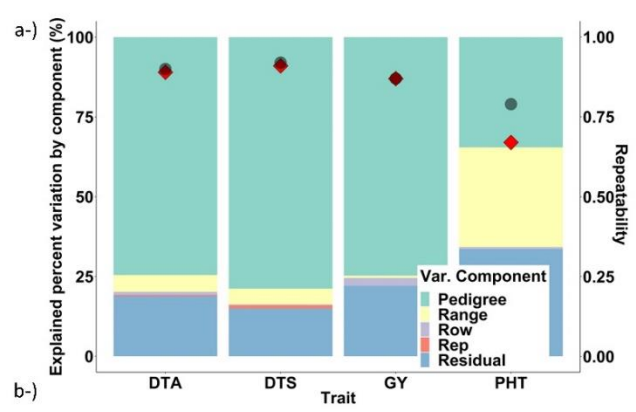

b-)

Var. Component of Equation 3	DTA (Day)	DTS (Day)	GY (t/ha)	PHT (cm)
Pedigree	***	***	***	***
Range	ns	ns	ns	**
Row	ns	ns	ns	*
Rep	ns	ns	ns	ns

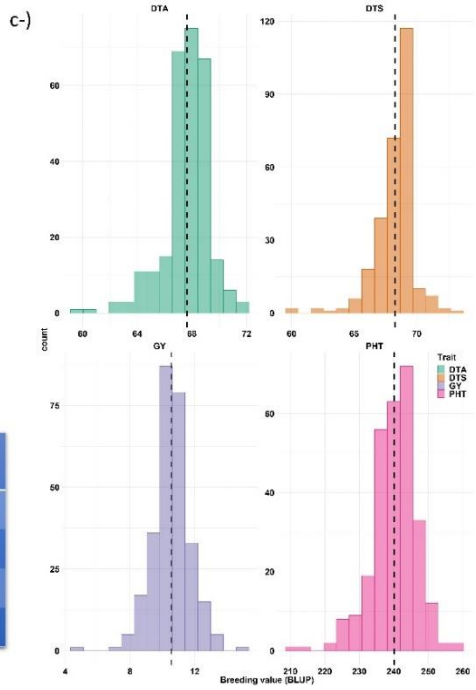

Figure S4 a-) stacked bar plots shows the explained percent variation by each component in *Eq. 4* for each trait. Left y axis represents the explained percent variation of the components while left y axis shows the temporal repeatability (red diamonds calculated by *Eq. 5*) and Rsquared values (black round symbols). b-) The table shows the significance values of each component in *Eq. 4* for each temporal trait; ***, **, * are the 0.001, 0.01 and 0.05 significance levels respectively while ns is not statistically significant. c-) shows the histograms of the breeding values of each trait with their means represented by vertical black lines. Reprinted from Adak, Murray, & Anderson, 2021.

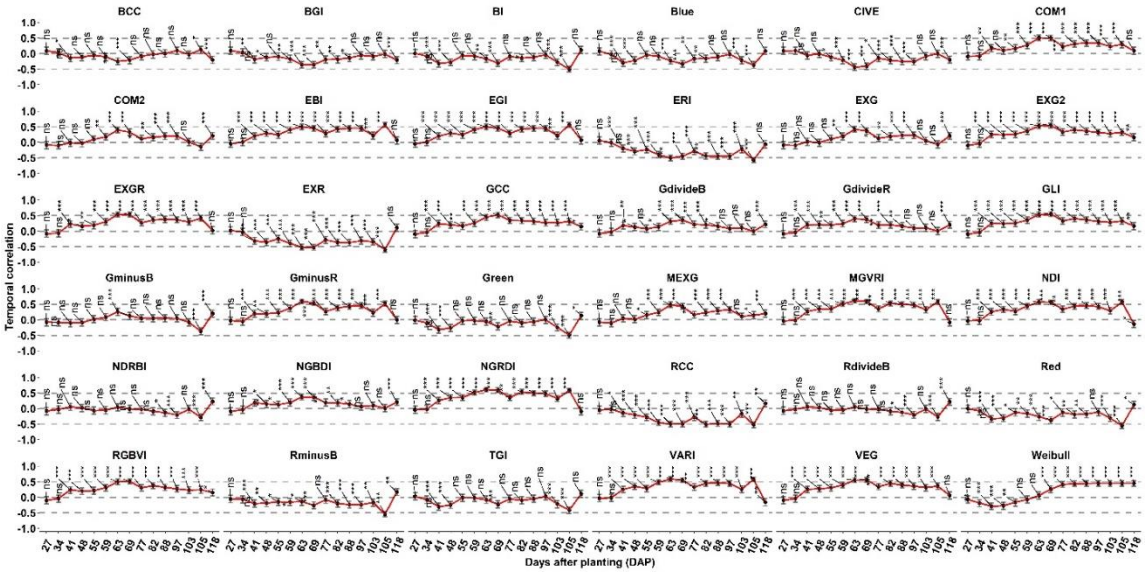

Figure S5 Pearson correlation coefficients between the phenotype values at each flight time point of the VIs in TPP_RGB. Whiskers shows upper and lower confident intervals of temporal correlation based on 95 percent confidence level. Above, middle, and below dashed lines represent the 0.5, 0 and -0.5 temporal correlation values. ***, **, * are the 0.001, 0.01 and 0.05 significance levels respectively while ns is not statistically significant. Reprinted from Adak, Murray, & Anderson, 2021.

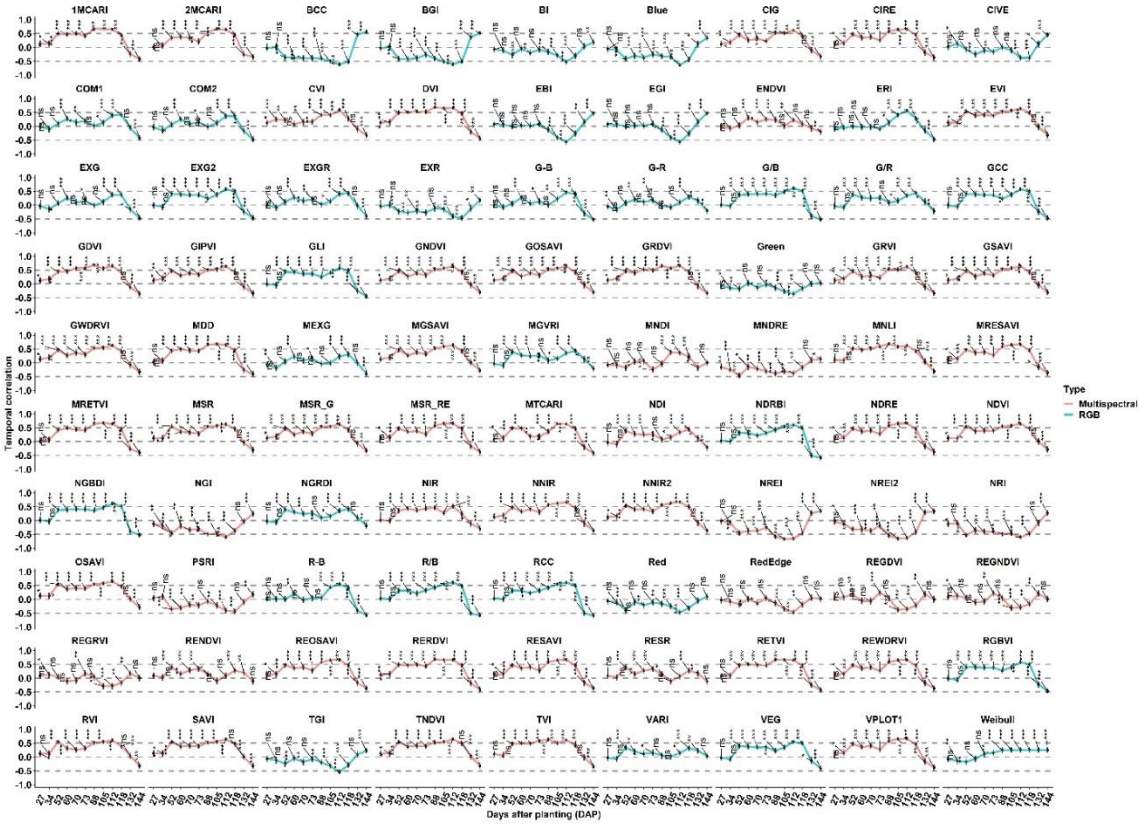

Figure S6 Pearson correlation between the phenotype values at each flight time point of the VIs in TPP_Multi. The title separated vegetation indices according to their derivation from multispectral bands and RGB bands. Whiskers show upper and lower confidence intervals of temporal correlation based on 95 percent confidence level. Above, middle, and below dashed lines represent the 0.5, 0 and -0.5 temporal correlation values. ***, **, * are the 0.001, 0.01 and 0.05 significance levels respectively; ns is not statistically significant. Reprinted from Adak, Murray, & Anderson, 2021.

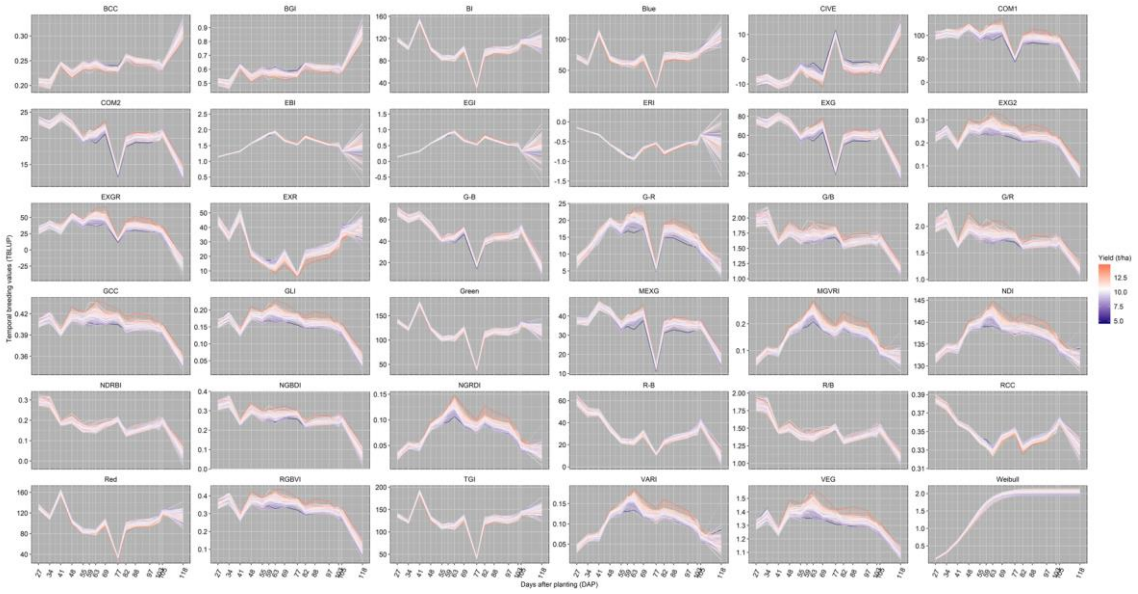

Figure S7 temporal pedigree values of 280 maize hybrids predicted by Eq. 2 belonging to each vegetation indices and Weibull_CHM in TPP_RGB of optimal management. Each hybrid was colored according to their yield values that are low, average, and high yield values representing blue, white, and red respectively in the heatmap scale. Average yield was 10.5 t/ha. Reprinted from Adak, Murray, & Anderson, 2021.

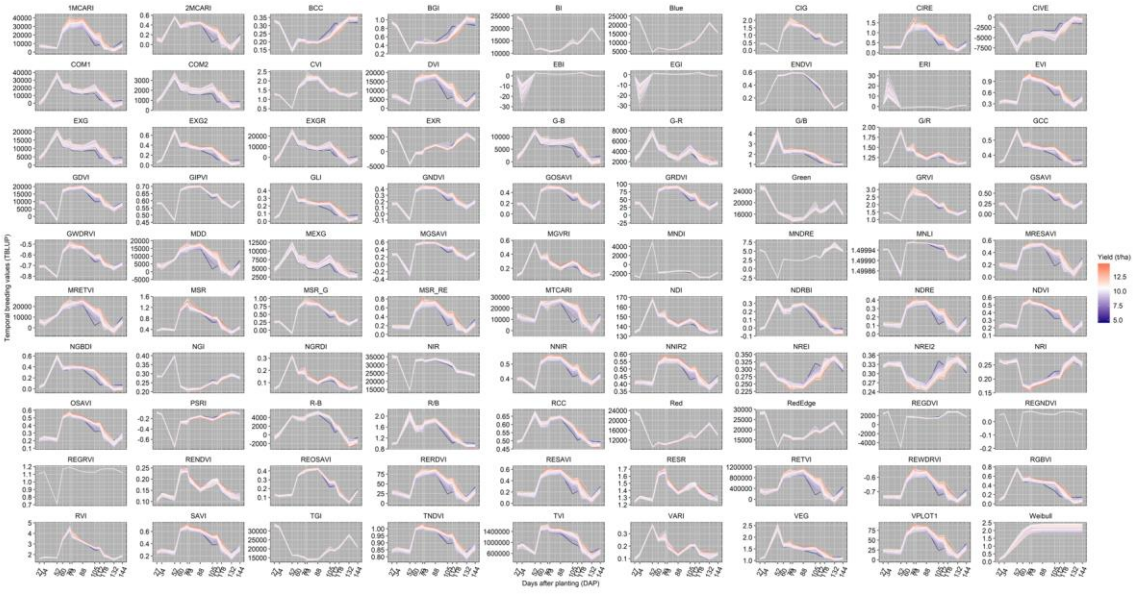

Figure S8 temporal pedigree values of 280 maize hybrids predicted by *Eq. 2* belonging to each vegetation indices in TPP_Multi of optimal management. Each hybrid was colored according to their yield values that are low, average, and high yield values

representing blue, white, and red respectively in the heatmap scale. Average yield was 10.5 t/ha. Reprinted from Adak, Murray, & Anderson, 2021.

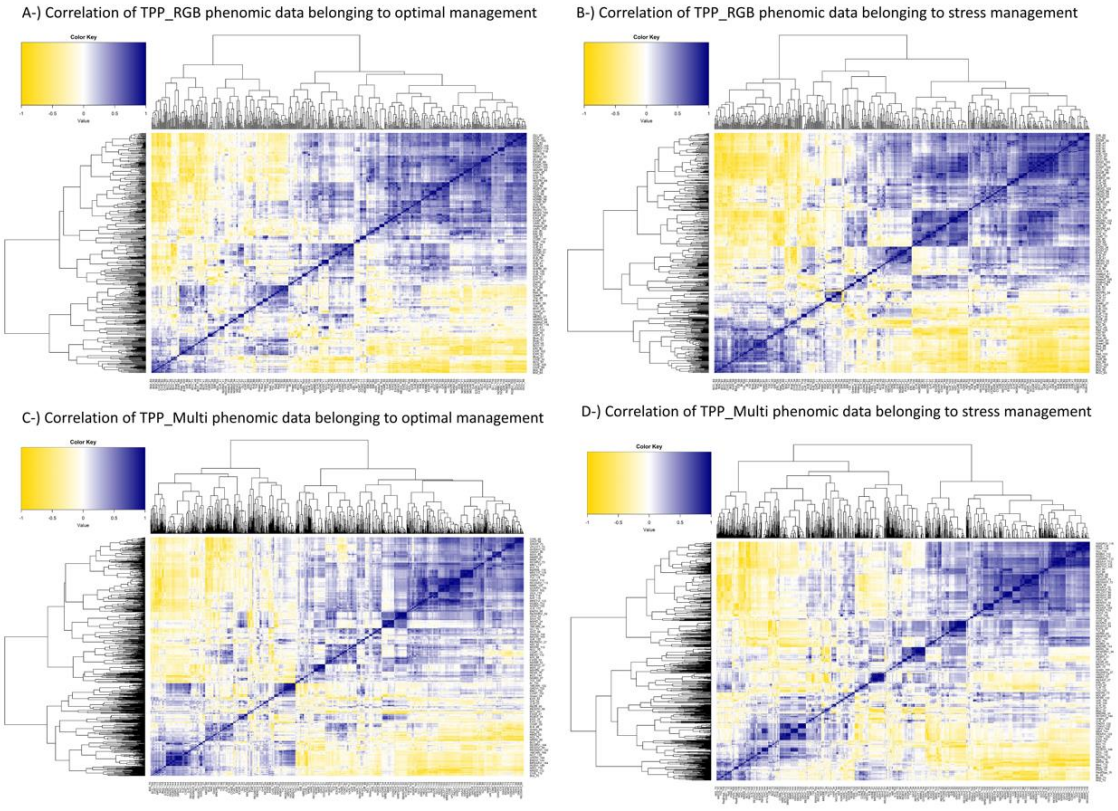

Figure S9 Heatmap illustration of correlation matrix of each phenomic data used in phenomic prediction. A-) correlation of the phenomic data of optimal management derived from RGB (red-green-blue) high throughput phenotyping(HTP) platform. B-) Correlation of the phenomic data of stress management derived from RGB HTP plant from. C-) Correlation of the phenomic data of optimal management derived from multispectral HTP platform. D-) Correlation of the phenomic data of stress management derived from multispectral HTP platform. Reprinted from Adak, Murray, & Anderson, 2021.

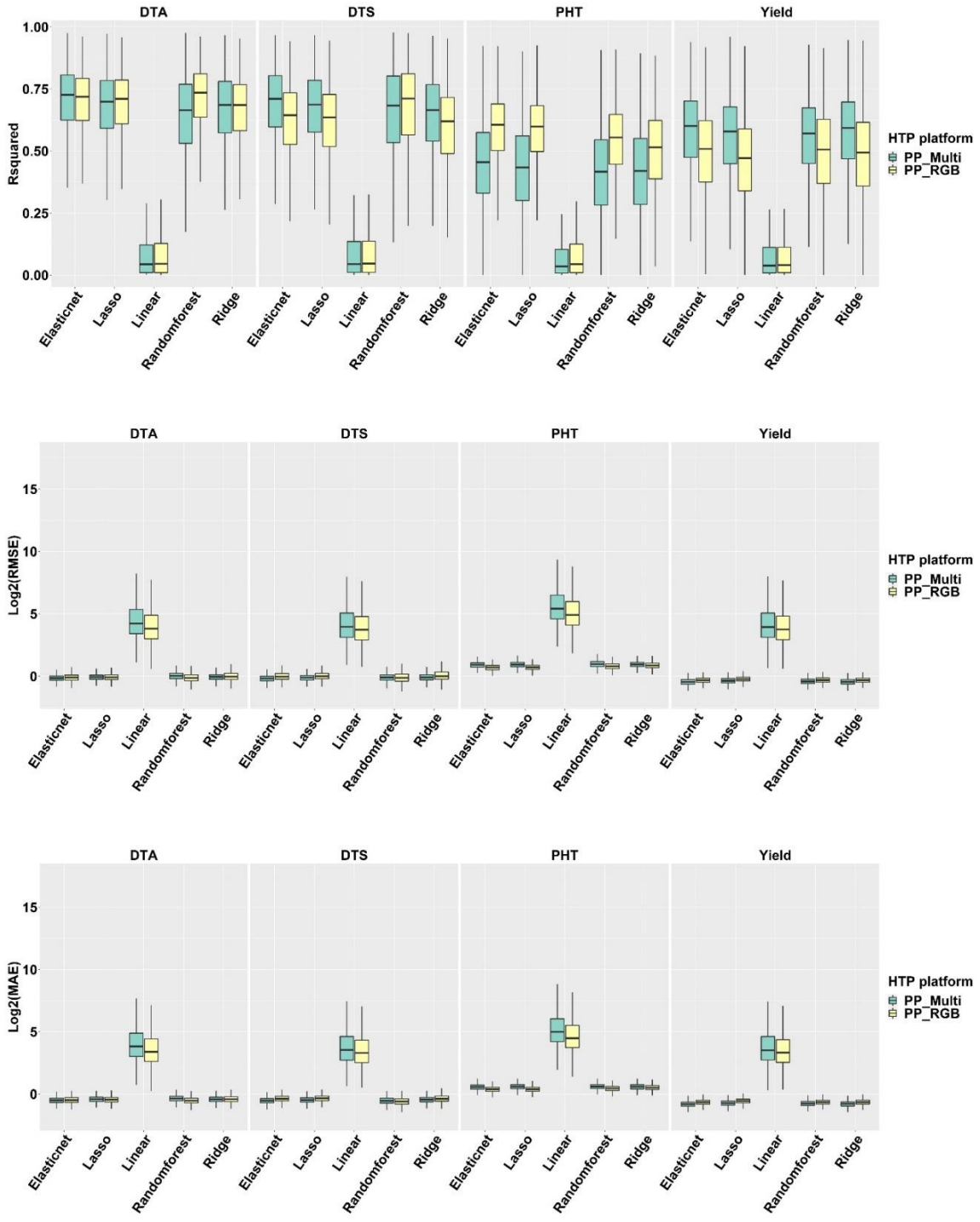

Figure S10 R-squared, root mean square error (RMSE), and mean absolute error (MAE) values from top to bottom belonging to each model (on the x axis) and each predicted variable (from left to right). $Log_2()$ transformation was applied to RMSE and MAE

values to show the excessive values belonging to linear model. Reprinted from Adak, Murray, & Anderson, 2021.

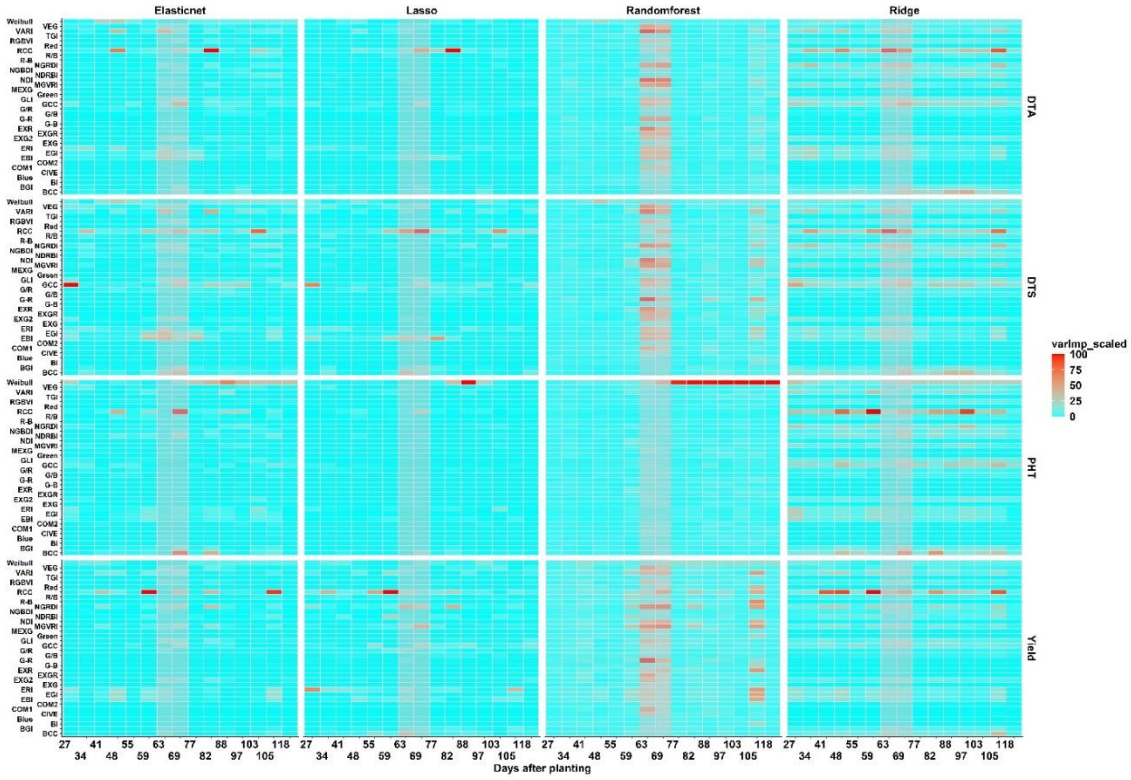

Figure S11 Variable importance scores belonging to each predicted variable (from top to bottom) and model (from left to right) when TPP_RGB phenomic data was used. X axis shows the VIs as well as Weibull_CHM and X axis shows the flight dates as days after planting times. The highlighted grey columns correspond to the range of flowering dates in this population. Reprinted from Adak, Murray, & Anderson, 2021.

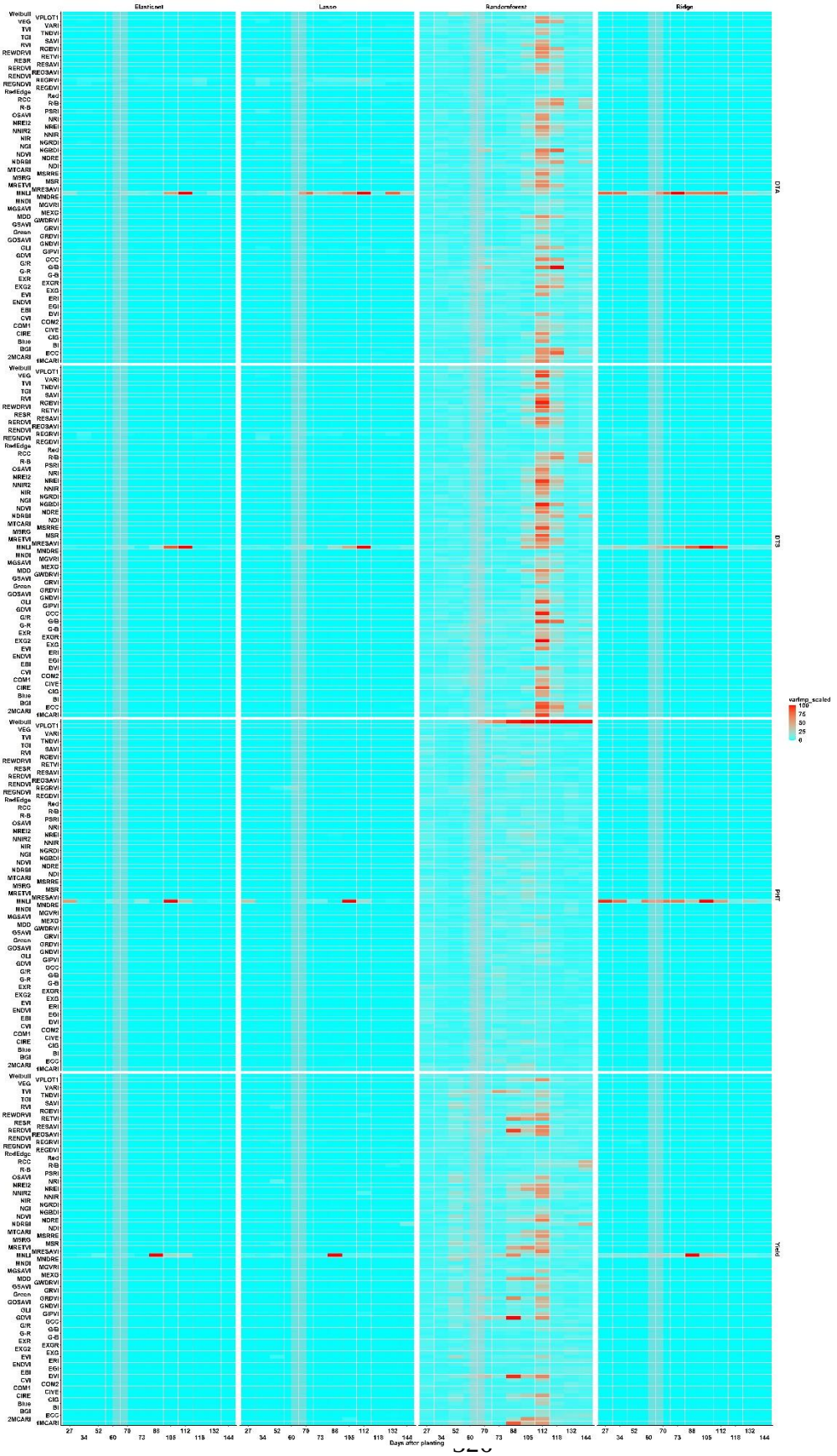
Elasticnet
Lasso
Randomforest
Ridge
DTA
DTS
PHT
PHV
varimp_scaled
100
75
50
25
0
Days after planting

Figure S12 Variable importance scores belonging to each predicted variable (from top to bottom) and model (from left to right) when TPP_Multi phenomic data was used. X axis shows the VIs as well as Weibull _CHM and X axis shows the flight dates as days after planting times. The highlighted grey columns correspond to the range of flowering dates in this population. Reprinted from Adak, Murray, & Anderson, 2021.

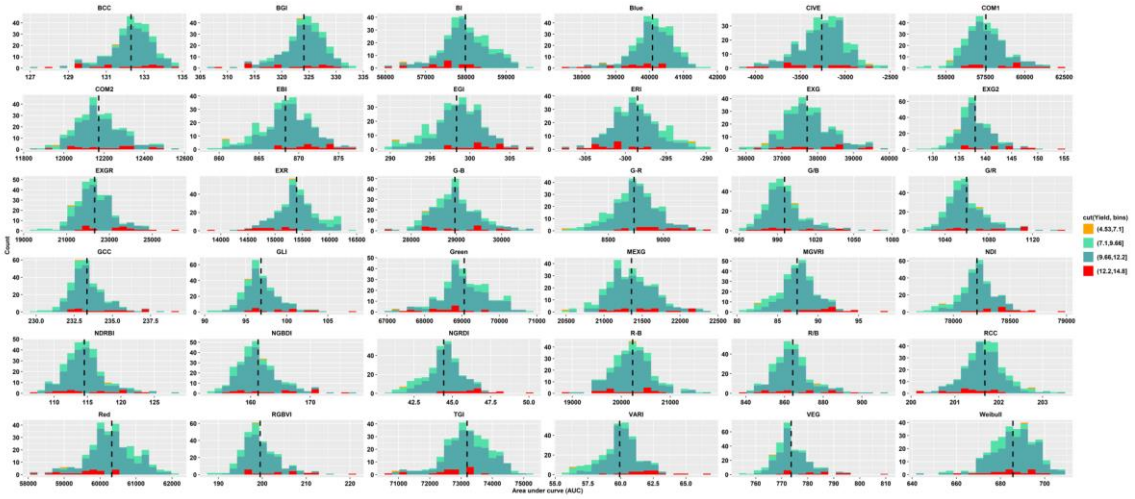

Figure S13 Histograms of area under curve value of each VI and Weibull _CHM for each genotype calculated by *Eq. 6* in TPP_RGB phenomic data belonging to optimal management. Area under curve values were divided into four equal bin categories based on yield value as shown in the legend and each histogram was colored based on these bins. Vertical dashed lines in each histogram show the mean values. Reprinted from Adak, Murray, & Anderson, 2021.

Figure S14 Combined Manhattan plots for each VI and Weibull _CHM (based on the right y-axis) in TPP_RGB. Below x-axis shows the genomic position of each chromosome (based on the above x-axis). Left y-axis shows the probability (-log10) of GWAS peaks between 6 to 26. Round, triangle and squares represent the Blink, FarmCPU and MLMM models results respectively. Reprinted from Adak, Murray, & Anderson, 2021.

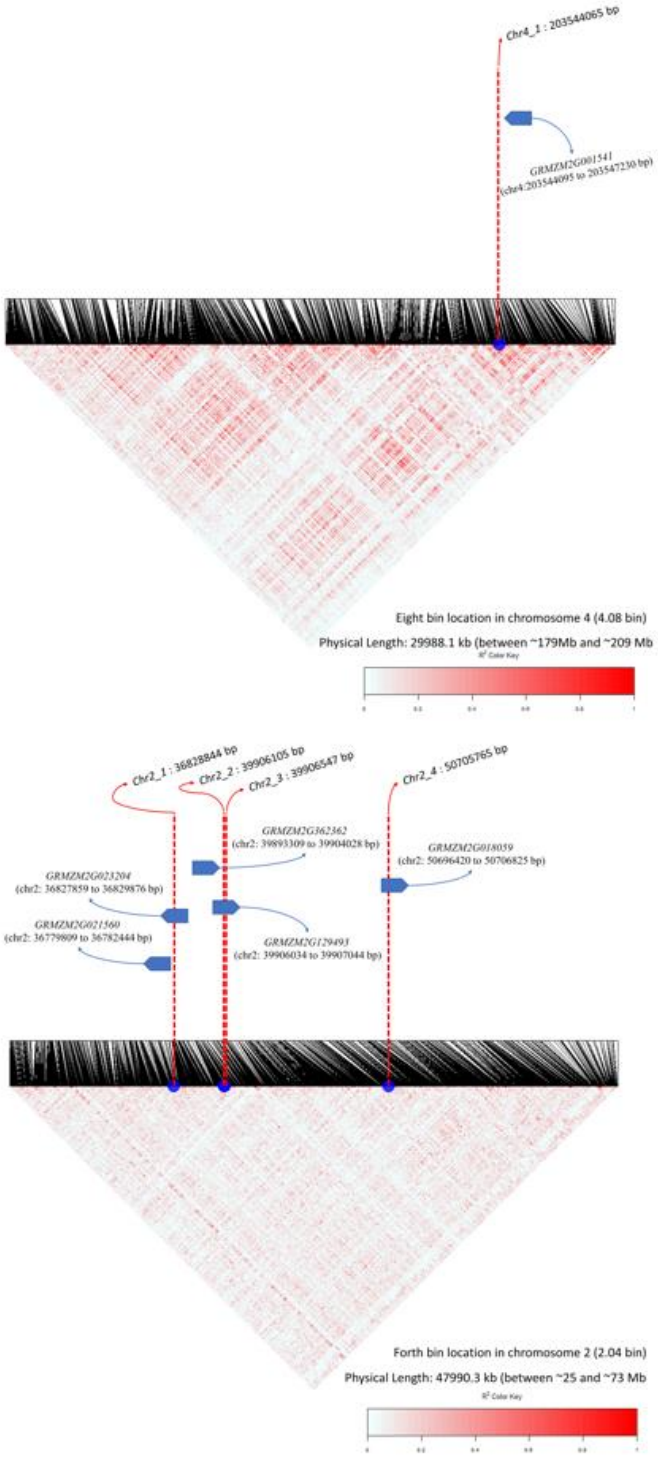

Figure S15 LD blocks around Chromosome two loci, *chr2_1*, *chr2_2*, *chr2_3*, *chr2_4* (below) and *chr4_1* (above) loci, nearby LD blocks of these loci within the 2.04 and 4.08 genomic bin locations and candidate gene annotations. Reprinted from Adak, Murray, & Anderson, 2021.

APPENDIX F

APPENDIX OF CHAPTER VII

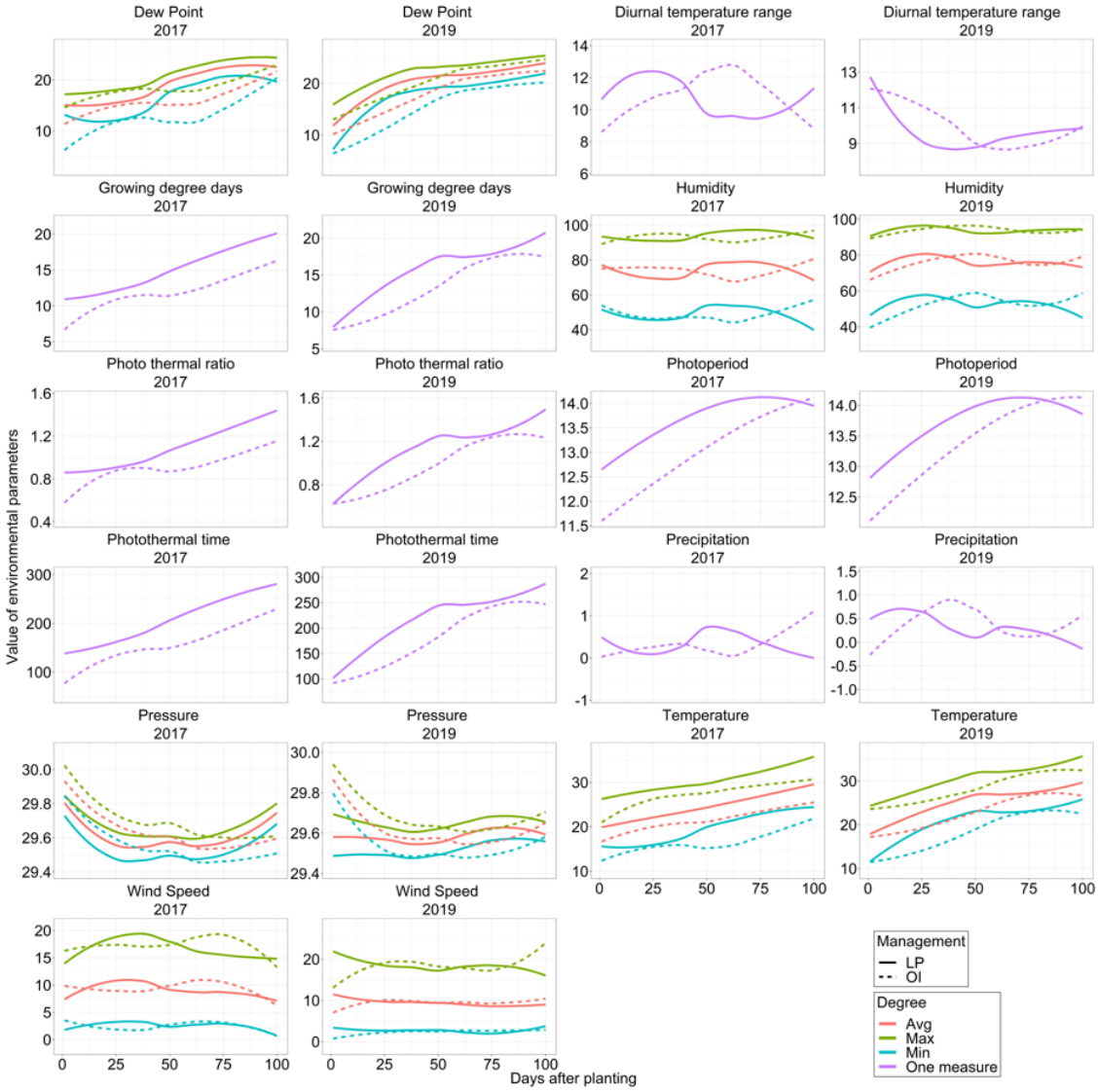

Supplementary Figure 1 shows the 100 days after planting window of environmental parameters belonging to managements (late planting; LP and optimal planting; OI) in 2017 and 2019. Note that LP is the same as OI but shifted based on the difference in planting date.

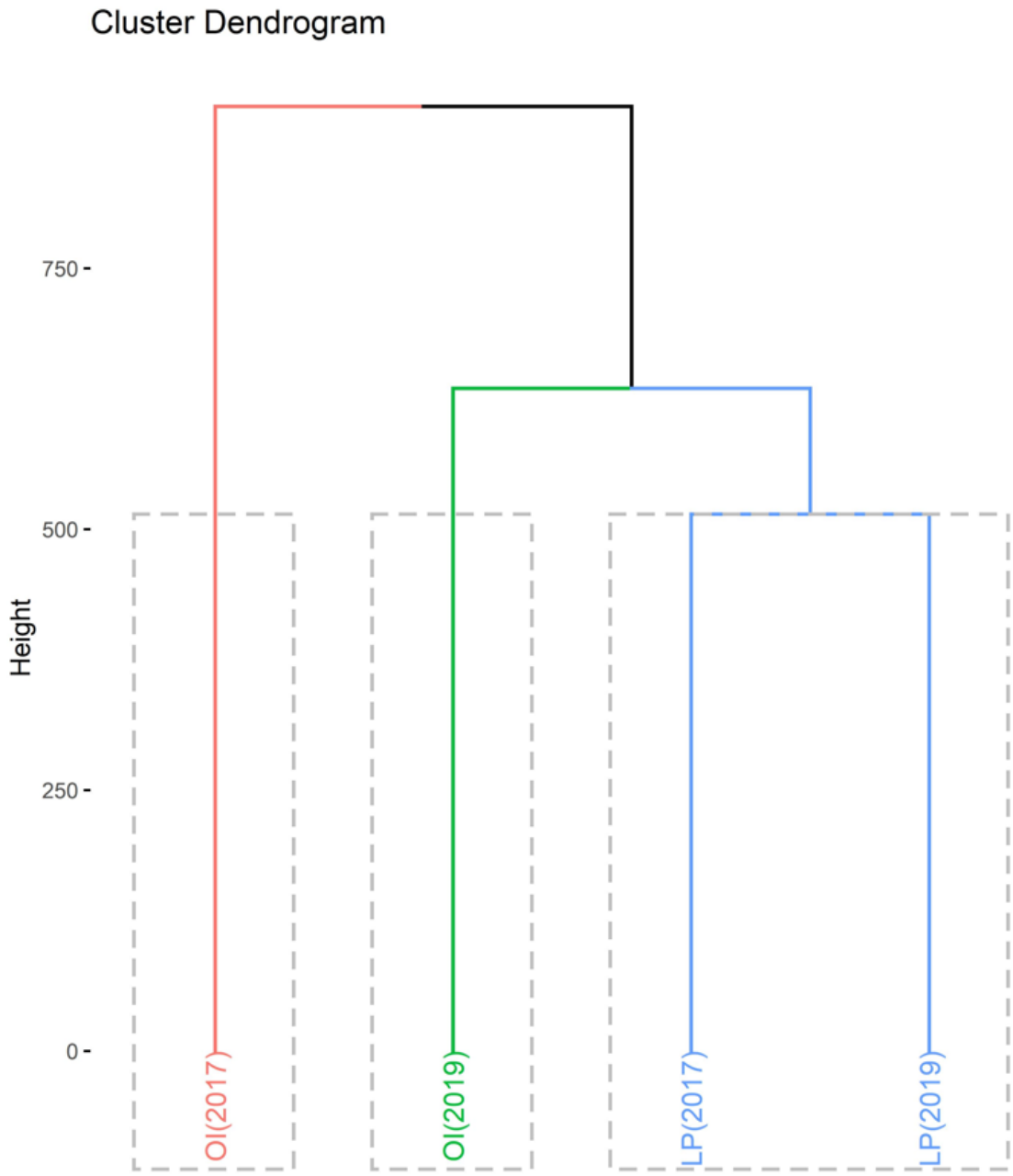

Supplementary Figure 2 shows the hierarchical clustering results of optimal (OI) and late (LP) planting trials in 2017 and 2019. Hierarchical clustering dendrogram revealed that similarity between optimal planting (tested environment) and late planting (untested environment) trials in 2017 is less than those in 2019.